UC San Diego

UC San Diego Electronic Theses and Dissertations

Title

Sensor data analysis and information extraction for structural health monitoring

Permalink

https://escholarship.org/uc/item/9j40r7qm

Author

Yan, Linjun

Publication Date

2006

Peer reviewed|Thesis/dissertation

eScholarship.org Powered by the California Digital Library
University of California

UNIVERSITY OF CALIFORNIA, SAN DIEGO

Sensor Data Analysis and Information Extraction for Structural Health Monitoring

A dissertation submitted in partial satisfaction of the

requirements for the degree Doctor of Philosophy

in

Structural Engineering

by

Linjun Yan

Committee in charge:

Professor Ahmed Elgamal, Chair
Professor Joel P. Conte
Professor Garrison W. Cottrell
Professor Charles Elkan
Professor Michael D. Todd

2006

Copyright

Linjun Yan, 2006

All rights reserved.

The dissertation of Linjun Yan is approved, and it is acceptable in quality and form for publication on microfilm:

_____

_____

_____

_____

_____

_____

Chair

University of California, San Diego

2006

TABLE OF CONTENTS

Signature Page ……..……...……. iii

Table of Contents ……...……. iv

List of Figures ……. ix

List of Tables ….……. xiii

Acknowledgements ……. xv

Vita and Publications ……..... xvii

Abstract ……... xix

1 Introduction ……. 1
1.1 Structural Health Monitoring ……. 1
1.2 Research Scope …….. 3
1.3 Data Used in the Studies ……..…….. 4
1.3.1 Lotung Seismic Downhole Data …… 4
1.3.2 Los Alamos Experimental Data …… 5
1.3.3 Virtual Bridge Testbed and Simulation Data …….…… 5
1.3.4 UCSD Bridge-Deck Testbed and Strain-Video Data ……..… 6
1.4 Organization of the Dissertation …… 6
1.5 Tables ….…… 8
1.6 Figures ….…….. 9
1.7 References …….. 16

2 A Substructure Identification and Monitoring Approach Based on Acceleration Measurements ……..……..…… 18
2.1 Introduction …… 18
2.2 Lotung Seismic Downhole Data …… 18
2.3 Analysis Framework ……..…… 20
2.3.1 Scenario 1 ……...…… 20
2.3.2 Scenario 2 ……...…… 22
2.4 Applications ……...…...……. 25
2.4.1 Scenario 1 ……...…… 25
2.4.1.1 Application to Numerical Simulation Data ...…… 25
2.4.1.2 Application to Lotung Seismic Downhole Data …... 26
2.4.2 Scenario 2 ……...…… 28
2.4.2.1 Application to Numerical Simulation Data …...……. 28
2.4.2.2 Application to Lotung Seismic Downhole Data …… 29
2.5 Summary and Conclusions ……...…..……. 31
2.6 Tables ……..……...…….…… 33

2.7 Figures 40
2.8 References 68

3 A Statistical Inference Approach for Structural Damage Detection Using NARX Neural Network 69
3.1 Introduction 69
3.2 Analysis Framework 71
3.3 NARX Neural Network 73
3.3.1 Network Configuration 73
3.3.2 Network Training 75
3.4 Damage Indicator 76
3.5 Application Example 1: 8-DOF Mass-Spring System 78
3.5.1 Experimental Setup 78
3.5.2 Application 80
3.6 Application Example 2: 3-Story Frame Structure 83
3.6.1 Experimental Setup 83
3.6.2 Application 84
3.7 Summary and Conclusions 86
3.8 Acknowledgements 87
3.9 Tables 88
3.10 Figures 94
3.11 References 106

4 A Neural-Network-Based Statistical Inference Approach for Bridge Pier Damage Identification 110
4.1 Introduction 110
4.2 Virtual Bridge Testbed 112
4.2.1 PEER Humboldt Bay Middle Channel Bridge Testbed 112
4.2.2 Bridge Modeling 113
4.2.3 Damage Simulation Using Staged Analysis 114
4.2.4 Data Generation 115
4.3 Analysis Framework 116
4.4 Substructure Identification Using NARX Neural Networks 117
4.4.1 Network Configuration 117
4.4.2 Network Training 118
4.4.3 Network Prediction 119
4.5 Damage Indicator 119
4.6 Results and Discussions 121
4.6.1 Quantification of Simulated Damage 121
4.6.2 Damage Identification Results 122
4.7 Summary and Conclusions 123
4.8 Acknowledgements 124
4.9 Tables 125
4.10 Figures 128
4.11 References 140

5 A PCA-Based Neural Network Approach for Bridge Pier Damage Identification 143
5.1 Introduction 143
5.2 Analysis Framework 145
5.3 Virtual Bridge Testbed 147
5.3.1 PEER Humboldt Bay Middle Channel Bridge Testbed 147
5.3.2 Model I 148
5.3.2.1 Bridge Modeling 148
5.3.2.2 Damage Simulation Using Staged Analysis 149
5.3.2.1 Data Generation 151
5.3.3 Model II 151
5.3.3.1 Bridge Modeling 151
5.3.3.2 Model Calibration 152
5.3.3.3 Damage Simulation 152
5.3.3.4 Data Generation 152
5.4 Feature Extraction Using PCA 153
5.5 Neural Network for Damage Identification 155
5.6 Test Results and Discussion 157
5.6.1 Damage Patterns Generated Using Model II 157
5.6.2 Damage Patterns Generated Using Model I 157
5.6.2.1 Quantification of Damage in Model I 157
5.6.2.2 Patterns with a Single Damaged Pier 158
5.6.2.3 Patterns with Multi Damaged Piers 159
5.7 Summary and Conclusions 159
5.8 Acknowledgements 160
5.9 Tables 161
5.10 Figures 167
5.11 References 179

6 Neural Networks and Principal Components Analysis for Strain-Based Vehicle Classification 182
6.1 Introduction 182
6.2 UCSD Bridge-Deck Testbed and Strain-Video Database 183
6.3 Preliminary Analysis 185
6.3.1 Characteristics of Traffic-Induced Strain Response 185
6.3.2 Vehicle Classification Based on Bayesian Inference 186
6.4 Analysis Procedure 187
6.5 Feature Extraction Using PCA 189
6.5.1 Computational Procedure 189
6.5.2 PCA Representation 191
6.6 Neural Network Development 192
6.6.1 Network Configuration 192
6.6.2 Network Training 193
6.7 Neural Network Results 194

6.7.1 Discussion 195
6.7.2 Application to the Entire Database 196
6.8 Summary and Conclusions 196
6.9 Acknowledgements 197
6.10 Tables 199
6.11 Figures 207
6.12 References 218

7 Summary and Conclusions 220
7.1 Structural Damage Identification 220
7.1.1 Approach A 220
7.1.2 Approach B 222
7.1.3 Approach C 223
7.1.4 Comparison of Approaches A, B, and C 224
7.1.5 Suggestions for Future Research 225
7.2 Traffic Pattern Recognition 226
7.3 Tables 227
7.4 Figures 228
7.5 References 229

Appendix A Three-Dimensional Bridge-Foundation-Ground System:
Part I. Computational Model 230
A.1 Introduction 230
A.2 Case History of Ground-Bridge Damage 232
A.3 PEER Humboldt Bay Middle Channel Bridge Testbed 233
A.4 Finite Element Analysis Framework/Platform: OpenSees 234
A.5 Finite Element Model 235
A.5.1 Bridge Superstructure 236
A.5.2 Bridge Piers 236
A.5.3 Pile Groups 237
A.5.4 Abutment and Soil Domain 238
A.5.4.1 Soil Constitutive Model 239
A.5.5 Boundary Conditions 240
A.5.5.1 Lateral Mesh Boundaries 240
A.5.5.2 Along Model Base 240
A.6 Definition of Input Excitation 241
A.7 Solution Procedure 242
A.7.1 Stage I. Application of Self Weight 243
A.7.2 Stage II. Earthquake Dynamic Analysis 243
A.8 Free-Field Ground Response 244
A.9 Summary and Conclusions 244
A.10 Acknowledgements 246
A.11 Appendix I 246
A.12 Tables 248
A.13 Figures 253

A.14 References …….. 274

Appendix B Three-Dimensional Bridge-Foundation-Ground System:
Part II. Seismic Response ……..…….. 278
B.1 Introduction …… 278
B.2 Global Response Behavior of the Bridge-Foundation-Ground System ……...……. 279
B.3 Spatial Ground Motion Variability …… 280
B.4 Soil Response ……..…… 280
B.4.1 Free Field Response ...…… 280
B.4.2 Ground Response near Abutments ….…… 281
B.5 Response of Bridge Structure ……...……. 281
B.6 Response of Bridge Piers ……...…… 283
B.7 Response of Bridge Pile Foundations ……...……. 285
B.8 Response of Bridge Superstructure ……...……. 287
B.9 Summary and Conclusions ……...…. 289
B.10 Acknowledgements ……...……. 290
B.11 Figures ……...……..…… 292
B.12 References ……...…….. 309

LIST OF FIGURES

Fig. 1.1 Integrated structural health monitoring system ……..... 9
Fig. 1.2 Configuration of Lotung site …..……...……... 10
Fig. 1.3 An 8-DOF mass-spring system attached to a shaker ..……... 11
Fig. 1.4 Experimental setup of the 3-story frame structural model …… 12
Fig. 1.5 Overhead view of Humboldt Bay Middle Channel Bridge ..…….. 13
Fig. 1.6 3D nonlinear FE model of the HBB bridge-foundation-soil system . 14
Fig. 1.7 UCSD bridge-deck panels testbed ……. 15

Fig. 2.1 Configurations of Lotung site ……..……... 40
Fig. 2.2 Configuration of the monitoring system and soil layer property estimation (scenario 1) ……...……..... 41
Fig. 2.3 Configuration of the monitoring system and soil layer property estimation (scenario 2) ……...……..... 42
Fig. 2.4 Prediction of the intact SDOF system (scenario 1) response to earthquake 5 ..……. 43
Fig. 2.5 Prediction of the intact SDOF system (scenario 1) response to earthquake 6 ..……. 44
Fig. 2.6 Prediction of the damaged SDOF system (scenario 1) response to earthquake 16 ..……..……. 45
Fig. 2.7 Transfer functions of the soil system between DHB-11 and FA1-5 .. 46
Fig. 2.8 Response time histories of the soil system between DHB-11 and FA1-5 for earthquake 5 ……...……..... 47
Fig. 2.9 Response time histories of the soil system between DHB-11 and FA1-5 for earthquake 6 ……...……..... 48
Fig. 2.10 Response time histories of the soil system between DHB-11 and FA1-5 for earthquake 16 ……...……..... 49
Fig. 2.11 Identification of the soil system between DHB-11 and FA1-5 based on windowed data of earthquake 5 ……..... 50
Fig. 2.12 Identification of the soil system between DHB-11 and FA1-5 based on windowed data of earthquake 6 ……..... 51
Fig. 2.13 Identification of the soil system between DHB-11 and FA1-5 based on windowed data of earthquake 16 ……..... 52
Fig. 2.14 Prediction of the ground surface response to earthquake 5 ……... 53
Fig. 2.15 Prediction of the ground surface response to earthquake 6 ……... 54
Fig. 2.16 Prediction of the ground surface response to earthquake 16 ……..... 55
Fig. 2.17 Prediction of the intact SDOF system (scenario 2) response to earthquake 5 ..……. 56
Fig. 2.18 Prediction of the intact SDOF system (scenario 2) response to earthquake 6 ..……. 57
Fig. 2.19 Prediction of the damaged SDOF system (scenario 2) response to earthquake 16 ..……..……. 58
Fig. 2.20 Response time histories of the soil system between DHB-17 and FA1-5 for earthquake 5 ……...……..... 59

Fig. 2.21 Response time histories of the soil system between DHB-17 and FA1-5 for earthquake 6 60
Fig. 2.22 Response time histories of the soil system between DHB-17 and FA1-5 for earthquake 16 61
Fig. 2.23 Identification of the soil system between DHB-17 and FA1-5 based on windowed data of earthquake 5 62
Fig. 2.24 Identification of the soil system between DHB-17 and FA1-5 based on windowed data of earthquake 6 63
Fig. 2.25 Identification of the soil system between DHB-17 and FA1-5 based on windowed data of earthquake 16 64
Fig. 2.26 Prediction of the ground response at the DHB-11 station to earthquake 5 65
Fig. 2.27 Prediction of the ground response at the DHB-11 station to earthquake 6 66
Fig. 2.28 Prediction of the ground response at the DHB-11 station to earthquake 16 67

Fig. 3.1 Analysis framework 94
Fig. 3.2 An 8-DOF mass-spring system attached to a shaker 95
Fig. 3.3 A typical bumper used to simulate nonlinear damage 96
Fig. 3.4 Substructures defined in the 8-DOF system 97
Fig. 3.5 Comparison of network predictions and sensor measurements of structural response of the 8-DOF system 98
Fig. 3.6 Neighboring prediction errors display very weak correlation 99
Fig. 3.7 Comparison of the histogram of p and the theoretical normal distribution 100
Fig. 3.8 Distributions of p at the baseline state (scenario 1) and q at scenarios 2, 8, 9, and 10, for substructure 7. 101
Fig. 3.9 Damage indicators computed for scenarios 2-10 of the 8-DOF mass-spring system 102
Fig. 3.10 Experimental setup of the 3-story frame structure model 103
Fig. 3.11 Comparison of network predictions and sensor measurements of structural response of the 3-story frame structure 104
Fig. 3.12 Damage indicators computed for scenarios 2-10 of the 3-story frame structure 105

Fig. 4.1 Damage at bridge pier bases during Kobe earthquake 128
Fig. 4.2 Plastic hinge formation at pier bases of Mingchou Bridge 129
Fig. 4.3 Sky view of Humboldt Bay Middle Channel Bridge 130
Fig. 4.4 3D FE model of bridge 131
Fig. 4.5 Modeling of piers and pile groups 132
Fig. 4.6 32 patterns with a single damaged pier 133
Fig. 4.7 Comparison of network predictions and corresponding actual record of structural response 134

Fig. 4.8 Correlation between the damage-induced peak bending curvature and corresponding reduction in gross flexural stiffness …… 135
Fig. 4.9 Damage identification results for scenarios U2-U4 ……... 136
Fig. 4.10 Damage identification results for scenarios S1-S32 …….. 137
Fig. 4.11 Damage identification results for scenarios M1-M21 ..…….. 138

Fig. 5.1 Damage at bridge pier bases during Kobe earthquake ...……..……... 167
Fig. 5.2 Plastic hinge formation at pier bases of Mingchou Bridge ……... 168
Fig. 5.3 Analysis framework ……..…….…..... 169
Fig. 5.4 Sky view of Humboldt Bay Middle Channel Bridge …….…..... 170
Fig. 5.5 3D FE model of bridge ……..…….. 171
Fig. 5.6 Modeling of piers and pile groups …… 172
Fig. 5.7 32 patterns with a single damaged pier …….. 173
Fig. 5.8 Baseline acceleration response comparison of Models I and II ……. 174
Fig. 5.9 Test results of the test set generated using Model II …….……. 175
Fig. 5.10 Comparison of network predictions and corresponding actual record of structural response ……..…… 176
Fig. 5.11 Test results of the 32 patterns with a single damaged pier generated using Model I ……..…… 177
Fig. 5.12 Test results of the 28 patterns with multi damaged piers generated using Model I ……. 178

Fig. 6.1 UCSD bridge-deck panels testbed ...…….…… 207
Fig. 6.2 Strain gage locations on the bridge-deck panels ……...…….…..... 208
Fig. 6.3 Examples of vehicle types in each class ……...…..... 209
Fig. 6.4 Characteristics of traffic-induced strain response…….…….. 210
Fig. 6.5 Histograms of maximum peak strain and event duration …….…. 211
Fig. 6.6 Flowchart of analysis procedure …… 212
Fig. 6.7 Original and normalized strain time histories …… 213
Fig. 6.8 PCA of the training set of scenario 1 ……. 214
Fig. 6.9 Computed **f** vectors of the 8 representative vehicle records ...……. 215
Fig. 6.10 Reconstructed strain time histories using the first 5 and 27 PCs …... 216
Fig. 6.11 Histograms of classification confidence for successes and failures .. 217

Fig. 7.1 Prototype smart sensors ……..... 228

Fig. A.1 Damage to the Toyokoro wooden bridge ……... 253
Fig. A.2 Damaged east abutment of bridge crossing the Rio Valdivia …… 254
Fig. A.3 Settlement at east abutment of bridge across Rio Valdivia ……... 255
Fig. A.4 Abutment settlement, at Nordhoff Way Bridge ……. 256
Fig. A.5 Sky view of Humboldt Bay Middle Channel Bridge ……. 257
Fig. A.6 Close-up photo of Humboldt Bay Middle Channel Bridge ……... 258
Fig. A.7 Global elevation view of bridge superstructure, piers, and foundation system …….. 259
Fig. A.8 3D FE model of bridge and idealized soil profile …….. 260

Fig. A.9 Modeling of pier and pile group using fiber-section beam-column element with uni-axial material constitutive models ……. 261
Fig. A.10 Cyclic moment-curvature response of pier cross-section …….. 262
Fig. A.11 Cyclic moment-curvature response of circular pile cross-section …. 263
Fig. A.12 Idealized soil shear wave velocity profile and measured soil shear wave velocity ……. 264
Fig. A.13 Details of abutment and approach ramp zone …… 265
Fig. A.14 Yield surfaces and hysteretic shear response of soil model …….. 266
Fig. A.15 Deconvolution of rock outcrop motion using Shake91 ……. 267
Fig. A.16 Shear modulus reduction and damping curves of rock …….. 268
Fig. A.17 Shear modulus reduction and damping curves of sand …….. 269
Fig. A.18 Results of deconvolution ……..……. 270
Fig. A.19 Schematic of updated boundary condition ……. 271
Fig. A.20 Free-field ground motion comparison …… 272
Fig. A.21 Amplification response spectrum of ground motion at location 1 …. 273

Fig. B.1 Residual deformation of the bridge-foundation-ground system after earthquake shaking …….……..…….. 292
Fig. B.2 Ground surface acceleration time history comparison for locations 1-3 ……..……..……..... 293
Fig. B.3 Linear elastic acceleration response spectra comparison for locations 1-3……...……. 294
Fig. B.4 Shear Stress-Strain Response of locations 1 and 4 …….……... 295
Fig. B.5 Elevation and plan views of the bridge, pier, pile foundation, and abutments after earthquake shaking ……... 296
Fig. B.6 Linear elastic acceleration response spectra comparison for 3 representative locations of bridge piers and abutments ……..……... 297
Fig. B.7 Global elevation view of bridge superstructure, piers, and foundation system ……..…… 298
Fig. B.8 Acceleration time histories at 3 locations along the bridge superstructure ……..……..……..... 299
Fig. B.9 Linear elastic acceleration response spectra comparison for 3 representative locations along the bridge superstructure …...……... 300
Fig. B.10 Displacement time histories at bridge pier tops and bases ……. 301
Fig. B.11 Moment-curvature response at pier bases …….…. 302
Fig. B.12 Shear force time histories at pier tops …...……. 303
Fig. B.13 Pier-base axial force time histories ……...…… 304
Fig. B.14 Axial force response of piers in group 4 …….……... 305
Fig. B.15 Axial force response at the top of single representative piles …… 306
Fig. B.16 Moment-curvature response at the top of single representative piles 307
Fig. B.17 Correlation between abutment displacement and bridge response … 308

LIST OF TABLES

Table 1.1	Organization of the Dissertation ……	8
Table 2.1	Information on the Three Studied Earthquakes …….	33
Table 2.2	Properties of the numerical SDOF model (Scenario 1) …….	34
Table 2.3	Identification of the numerical SDOF system (scenario 1) …..…….	35
Table 2.4	Identification of the equivalent SDOF system for the soil system between FA1-5 and DHB-11 …….	36
Table 2.5	Properties of the numerical SDOF model (Scenario 2) …….	37
Table 2.6	Identification of the numerical SDOF system (scenario 2) ……	38
Table 2.7	Identification of the equivalent SDOF system for the soil system between FA1-5 and DHB-17 …….	39
Table 3.1	Basic Information of the Ten Experimental Scenarios of the 8-DOF System ……..……...	88
Table 3.2	Numbering of Sensors ……..……...	89
Table 3.3	Definition of Substructures in the 8-DOF System ……..……...	90
Table 3.4	Parameters of the 8-DOF System Application …..…….	91
Table 3.5	Information of the Ten Experimental Scenarios of the 3-Story Frame Studied ……...……	92
Table 3.6	Parameters of the 3-Story Frame Structure Application …...…….	93
Table 4.1	Model Parameters of 3D Linear Elastic Beam-Column Elements	125
Table 4.2	Constitutive Model Parameters for Concrete Materials …….	126
Table 4.3	Constitutive Model Parameters for Steel Materials ……...……...	127
Table 5.1	Model Parameters of 3D Linear Elastic Beam-Column Elements	161
Table 5.2	Constitutive Model Parameters for Concrete Materials …….	162
Table 5.3	Constitutive Model Parameters for Steel Materials ……...……...	163
Table 5.4	Model Parameters of the 3D Linear Elastic Beam-Column Elements of Piers and Piles in Model II …….	164
Table 5.5	Comparison of Natural Frequencies of Models I and II ……...……	165
Table 5.6	Number of Damage Patterns Generated Using Model II ……...…...	166
Table 6.1	Definition of Vehicle Classes …….....	199
Table 6.2	Numbers of Labeled Records …….	200
Table 6.3	Preliminary Classification Results for the Test Set Using Bayesian Inference …….....	201
Table 6.4	Classification Results for the Test Set (Scenario 1) ……...	202
Table 6.5	Classification Results for the Test Set (Scenario 2) ……...	203
Table 6.6	Classification Results for the Test Set (Scenario 3) ……...	204
Table 6.7	Classification Results for the Entire Database ……...……...	205
Table 6.8	Random Check of Classification Results for the Entire Database ….	206

Table 7.1 Comparison of Damage Identification Approaches A, B, and C ….. 227

Table A.1 Model Parameters of Linear Elastic Beam-Column Element ……... 248
Table A.2 Constitutive Model Parameters for Concrete Material Used in Fiber Beam-Column Element ……...…..... 249
Table A.3 Constitutive Model Parameters for Steel Material Used in Fiber Beam-Column Element ...……... 250
Table A.4 Pile Spacing of the Idealized 2×2 Pile Groups ….……. 251
Table A.5 Soil Layer Properties …….……. 252

ACKNOWLEDGMENTS

I would like to express my gratitude to everyone who helped make completion of this dissertation possible. There are a few specific names I would like to mention.

Ahmed Elgamal has been my advisor for about five years, the entire time I have been at UCSD. Throughout this time, he has been a consistent source of feedback and good advice. From his example of hands on hard work, I have learned some key elements essential for good research. Through working with Ahmed, I have been exposed to a wide range of research frontiers (more than the materials included in this dissertation), and for that I am certainly better off. I could not have had a better advisor, and I have enjoyed working with him.

Zhouhui Yang and Joel P. Conte have also played a vital role in my work related to the numerical simulation of structural systems using OpenSees. Tony Fountain at the San Diego Supercomputer Center has provided insightful feedback for my research on the applications of artificial intelligence techniques. In fact, I would like to thank all of the members of my Ph.D. Committee (Joel P. Conte, Garrison W. Cottrell, Ahmed Elgamal, Charles Elkan, and Michael Todd) for their help in formulating and carrying out my research plan.

My fellow students and peers also played an important role throughout my time at UCSD. Zhaohui Yang, Tao Lai, Liangcai He, Jinchi Lu, Yuyi Zhang, Quan Gu, Xianfei He, Warrasak Jakrapiyanun, and Teerawut Juirnarongrit have been great officemates in the CADD laboratory and provided numerous discussions to elucidate many problems. Michael Fraser has also provided valuable friendship over the years

and significant help in improving my skills in English writing. For all these friends, I am grateful.

This work has been supported by the U.S. National Science Foundation, the Pacific Earthquake Engineering Research Center, the California Institute for Telecommunications and Information Technology, and the University of California, San Diego. These sources of support are highly appreciated.

I would also like to thank my family, especially my parents Ketan Yan and Liyu Lin, who have been supportive of everything I have done. Finally, I want to thank all my friends at the San Diego Chinese Evangelical Church, the San Diego Chinese Bible Study Church, and the San Diego H.O.P.E Church for their unending love and encouragement.

VITA

1994 – 1998	B.S., Structural Engineering (Major), Tianjin University
	B.S., Engineering Economics (Minor), Tianjin University
1998 – 2001	M.S., Structural Engineering, Tianjin University
2001 – 2006	Ph.D., Structural Engineering, University of California, San Diego

PUBLICATIONS

Yan, L., and Elgamal, A. (2006). "A Vibration-Based Statistical Inference Approach for Structural Damage Detection." *Proc. of the 4th World Conference on Structural Control and Monitoring*, July 11-13, 2006, San Diego, California, USA.

Elgamal, A., Fraser, M., Yan, L., and Conte, J.P. (2006). "Civil Infrastructure Damage Detection: Sensor Networks, Video Monitoring, and Assessment." *Proc. of International Conference on Bridge Management Systems: Monitoring, Assessment and Rehabilitation*, March 21-23, 2006, Cairo, Egypt.

Yan. L., Fraser, M., Oliver, K., Elgamal, A., Conte, J.P., and T. Fountain (2005). "Traffic Pattern Recognition using an Active Learning Neural Network and Principal Components Analysis." *Proc. of the Eighth International Conference on the Application of Artificial Intelligence to Civil, Structural and Environmental Engineering*, August 30 – September 2, Rome, Italy.

Elgamal, A., Yan, L., Fraser, M., Lu, J., and Conte, J.P. (2005). "Large-Scale Simulation and Data Analysis." *Proc. of International Conference on Computing in Civil Engineering*, July 12-15, 2005, Cancun, Mexico.

Bulut, A., Singh, A., Shin, P., Jasso, H., Fountain, T., Yan, L., and Elgamal, A. (2005). "Real-time Nondestructive Structural Health Monitoring using Support Vector Machines and Wavelets." *Proc. of the SPIE Conference on Advanced Sensor Technologies for Nondestructive Evaluation and Structural Health Monitoring (NDE05)*, March 2005, San Diego, California, USA.

Yan, L., Elgamal, A., Fountain, T., Conte, J.P., and Masri, S.F. (2004). "A PCA-Based Neural Network Approach for Multi-Storey Building Damage Identification." *Proc. of International Conference on Future Vision and Challenges for Urban Development*, December 20-22, 2004, Cairo, Egypt.

Yan, L., Elgamal, A., Yang, Z., and Conte, J.P. (2004). "Bridge-Foundation-Ground System: A 3D Seismic Response Model." *Proc. of the 3rd International Conference on Earthquake Engineering*, October 19-20, 2004, Nanjing, China.

Elgamal, A., Conte, J.P., Yan, L., Fraser, M., Masri, S.F., El Zarki, M., Fountain, T., and Trivedi, M. (2004). "A Framework for Monitoring Bridges and Civil Infrastructure." (Invited Paper) *Proc. of the 3rd China-Japan-US Symposium on Structural Health Monitoring and Control*, October 13-16, 2004, Dalian, China.

Yan, L., Fraser, M., Elgamal, A., and Conte, J.P. (2004). "Applications of Neural Networks in Structural Health Monitoring." *Proc. of the 3rd China-Japan-US Symposium on Structural Health Monitoring and Control*, October 13-16, 2004, Dalian, China.

Fraser, M., Yan, L., He, X., Elgamal, A., Conte, J.P., and Fountain, T. (2004). "Simple Neural Network Application for Traffic Monitoring." *Proc. of the International Conference on Computaional & Experimental Engineering and Sciences (ICCES'04)*, July 26-29, 2004, Madeira, Portugal.

Yan, L., Elgamal, A., Fountain, T., Conte, J.P., and Masri, S.F. (2004). "System Identification for Bridge Foundation Integrity." *Proc. of the International Conference on Geotechnical Engineering*, May 2004, Beirut, Lebanon.

Liang, J., Yan, L., and Lee, V.W. (2003). "Diffraction of Plane SV Waves by a Circular-Arc Layered Alluvial Valley: Analytical Solution." *ACTA Mechanica Solida Sinica* (Chinese), 24, 235-243.

Liang, J., Yan, L., and Lee, V.W. (2002). "Scattering of Incident Plane P Waves by A Circular-Arc Canyon with A Covering Layer." *ACTA Mechanica Solida Sinica* (Chinese), 23(4), 397-411.

Liang, J., Yan, L., and Lee, V.W. (2001). "Effects of a Covering Layer in a Circular-Arc Canyon on Incident Plane SV Waves." *ACTA Seismologica Sinica*, 14(6), 660-675.
Liang, J., Yan, L., Li, J. and Lee, V.W. (2001). "Response of Circular-Arc Alluvial Valleys under Incident Plane P Waves." *Rock and Soil Mechanics* (Chinese), 22(2), 138-143.

Liang, J., Yan, L., and Lee, V.W. (2001). "Scattering of Plane P Waves by Circular-Arc Layered Alluvial Valleys: An Analytical Solution." *ACTA Seismologica Sinica*, 14(2), 176-195.

ABSTRACT OF THE DISSERTATION

Sensor Data Analysis and Information Extraction for

Structural Health Monitoring

by

Linjun Yan

Doctor of Philosophy in Structural Engineering

University of California, San Diego, 2006

Professor Ahmed Elgamal, Chair

Recently, advances in sensing techniques, internet technologies, and wireless communications are increasingly facilitating and allowing practical deployment of large and dense sensor networks for structural health monitoring. Thus, it is vital to develop efficient techniques to process and analyze the massive amount of sensor data in order to extract essential information on the monitored structures. The efforts in this dissertation are mainly dedicated to this direction, including studies on structural damage identification and traffic pattern recognition. In these studies, traditional analysis tools for structural engineering (e.g., finite element (FE) based simulation) are utilized, and the potential of machine learning techniques is extensively explored.

Using different strategies, three structural damage identification approaches (referred to as approach A, B, and C, respectively) are developed in this dissertation. Both approaches A and B adopt decentralized analysis frameworks, which define substructures in the monitored system according to the sensor spatial distribution. Within approach A, each substructure is represented by a dynamic model, and the system properties are periodically identified based on sensor measurements for monitoring purposes. Herein, approach A is applied to seismic downhole data to monitor changes in soil layer properties. As for approach B, a neural network is developed for each substructure to predict the dynamic response at a selected sensor location from measurements of neighboring sensors. Thus, the dynamic characteristics of the substructure are represented by the network, and changes in the statistical distribution of network prediction error are evaluated and utilized as a damage indicator. Three applications of approach B are presented, two based on experimental data and one of bridge pier damage identification based on simulation data. Approach C adopts a statistical pattern recognition paradigm. Within this framework, a range of damage patterns of interest is provided by numerical simulation, the Principal Components Analysis (PCA) technique is employed for feature extraction, and a neural network is developed for damage pattern identification. Herein, approach C is also applied to the bridge pier damage identification problem. Finally, the combination of neural networks and PCA is also employed to develop a strain-based vehicle classification approach, based on a unique strain-video dataset.

1 INTRODUCTION

Advances in sensing techniques, internet technologies, and wireless communications are increasingly facilitating and allowing practical deployment of large and dense sensor networks for structural health monitoring purposes. In view of the increase in amount of sensor data, much useful information can be extracted through machine learning techniques. For instance, following an extreme loading event, the structural condition of a building or bridge may be assessed. An assessment of available residual strength may be the basis for important decisions related to post-event rescue and recovery strategies, cost of repair versus replacement, insurance considerations, and so forth.

In this chapter, the general background of structural health monitoring is first provided. Motivation and scope of this dissertation research is then described. The subsequent section introduces the source of each utilized dataset. Finally, the dissertation organization is outlined.

1.1 Structural Health Monitoring

The deterioration of the civil infrastructure has recently become a worldwide issue (Aktan et al. 2001; Catbas et al. 2001). In the United States, 50 percent of all bridges were built before the 1940's and about 27 percent are structurally deficient (Klaiber et al. 1987; Stalling et al. 2000; Aktan et al. 2001; Catbas et al. 2001; USDT 2004). These deficiencies may be due to an initial design based on old codes/provisions as well as structural degradation caused by harsh environments (Mazurek and DeWolf 1990). Since civil structures are among the most valuable

assets in any country, are of long service life, and prohibitive replacement cost, it is desirable to develop a cost-efficient structural health monitoring (SHM) system to detect damage at the earliest possible stage (Doebling et al. 1996; Chang 1997 and 2005; Sohn et al. 2003a).

Similarly, after major catastrophic events (e.g., earthquake, hurricane, terrorism attack, etc.), such a diagnosis system capable of rapid structural damage assessment is vital for a near-real-time post-disaster rescue response (Kiremidjian et al. 1997). Furthermore, some recently reported incidents of structural failures (e.g., Paris Charles de Gaulle Airport roof collapse on May 23, 2004) also highlight the emergent requirement of continuous health monitoring for critical public facilities with serious life safety concerns, especially those constructed of novel materials and/or designs.

A SHM system requires essential components, including a sensor network, data acquisition, communication, data storage and management, and a data analysis toolbox (Kiremidjian et al. 1997). For instance, Fig. 1.1 shows an integrated framework for SHM being developed and implemented by researchers at the University of California, San Diego (UCSD, Elgamal et al. 2003).

Since the occurrence of the 1994 Northridge, California earthquake and the 1995 Kobe, Japan earthquake, there has been a quantum jump in the number of civil structures that have been instrumented for monitoring purposes. However, in most of these SHM systems, the deployed sensor networks are relatively small and sparse. In view of the large and complex nature of civil structures, such simple systems may not provide sufficient information for monitoring purposes.

More recently, advances in sensing techniques, internet technologies, and wireless communications are increasingly facilitating and allowing practical deployment of large, dense, and heterogeneous sensor networks. Plans are underway to install a variety of strong-motion vibration sensors in many civil structures (in some cases many hundreds of sensors in a single structure).

1.2 Research Scope

Clearly, the main issue facing the SHM community is not the lack of measurements per se, but rather how to benefit from a large and dense sensor network once it becomes available. Thus, it is vital to develop efficient techniques to process and analyze the massive amount of sensor data in order to extract essential information on the monitored structures (e.g., damage location and severity, traffic loading condition on bridges, and so on). The efforts in this dissertation are primarily dedicated to this direction, including studies on structural damage identification and traffic pattern recognition. In these studies, traditional analysis tools for structural engineering (e.g., finite element based simulation) are utilized, and the potential of machine learning techniques (also called artificial intelligence, statistical learning, and data mining, Hastie et al. 2001) is also extensively explored.

Using different strategies, three structural damage identification approaches (referred to as approach A, B, and C, respectively) are developed in this dissertation. Both approaches A and B adopt decentralized analysis frameworks, which define substructures in the monitored system according to the sensor spatial distribution. Within approach A, each substructure is represented by a dynamic model, and the system properties are periodically identified based on sensor measurements for

monitoring purposes. Herein, approach A is applied to seismic downhole data to monitor changes in soil layer properties.

As for approach B, a neural network (Bishop 1995) is developed for each substructure to predict the dynamic response at a selected sensor location from measurements of neighboring sensors. Thus, the dynamic characteristics of the substructure are represented by the network, and changes in the statistical distribution of network prediction error are evaluated and utilized as a damage indicator. Three applications of approach B are presented, two based on experimental data and one of bridge pier damage identification based on simulation data.

Approach C adopts a statistical pattern recognition paradigm. Within this framework, a range of damage patterns of interest is provided by numerical simulation, the Principal Components Analysis (PCA, Jolliffe 1986) technique is employed for feature extraction, and a neural network is developed for damage pattern identification. Herein, approach C is also applied to the bridge pier damage identification problem.

Finally, the combination of neural networks and PCA is also employed to develop a strain-based vehicle classification approach, which may be used to provide information on traffic loading condition. Using this approach, vehicles crossing a bridge deck are classified based on traffic-induced changes in the measured deck strain response.

1.3 Data Used in the Studies

1.3.1 Lotung Seismic Downhole Data

The Electric Power Research Institute (EPRI) in cooperation with the Taiwan Power Company (TPC) conducted a large-scale seismic test (LSST) at a site near

Lotung, Taiwan. The LSST involved installation of an extensive array of strong motion instruments to monitor structural and site response (Tang 1987). The ground instrumentation (Fig. 1.2) includes three linear surface arrays, and two downhole arrays. Eighteen earthquakes were recorded during the period 1985-86. Herein, approach A is applied to the Lotung seismic downhole data in order to identify and monitor changes in soil layer properties.

1.3.2 Los Alamos Experimental Data

An eight-degree-of-freedom (8-DOF) system (Fig. 1.3) and a three-story frame structure model (Fig. 1.4) have been designed and constructed to study the structural damage identification problem at the Los Alamos National Laboratory (Sohn and Farrar 2001; Sohn et al. 2003b). Herein, data from these two experiments are utilized to verify the feasibility and efficiency of approach B.

1.3.3 Virtual Bridge Testbed and Simulation Data

In order to verify the efficiency of a damage identification approach for large scale civil structural systems, it is desirable to test it using data from actual damaged structures. However, such data are typically unavailable or scarce due to the long and gradual degradation progress. In this regard, finite element (FE) based modeling may provide the means for simulating damage patterns and generating the necessary data.

The Humboldt Bay Middle Channel Bridge (HBB, near Eureka in northern California, Fig. 1.5) was selected by the Pacific Earthquake Engineering Research Center as a research testbed (http://peer.berkeley.edu/peertestbeds/humboldt.htm, Porter 2003). This testbed has motivated a wide range of studies on advanced numerical simulation and seismic analysis. For instance, based on the structural

configuration and local soil conditions of HBB, a three-dimensional (3D) FE bridge-foundation-ground model (Fig. 1.6) has been developed by the author for seismic soil-bridge interaction study.

Herein, this refined bridge model is employed as a virtual bridge testbed for structural damage identification studies. Under the condition of destructive earthquake excitation, plastic hinges may form at the pier bases. In view of this, such damage is simulated using the bridge model, and both approaches B and C are applied for structural condition assessment purposes.

1.3.4 UCSD Bridge-Deck Testbed and Strain-Video Data

A large database has been compiled of traffic crossing over a set of bridge-deck panels on campus at UCSD (Fig. 1.7, http://healthmonitoring.ucsd.edu, Fraser et al. 2002; Fraser 2006). Deck strains caused by traffic, along with synchronized video clips have been archived (over 400,000 records). As such, this dataset allows for relating a measured strain signal to the corresponding vehicle characteristics. In view of this, the dataset is employed to develop a strain-based vehicle classification approach, as a machine learning application.

1.4 Organization of the Dissertation (Table 1.1)

In this dissertation, each chapter is prepared and formatted as a freestanding paper. As shown in Table 1.1, Chapter 2 describes approach A and the application to the Lotung seismic downhole data. Chapter 3 describes the analysis framework of approach B and the two applications based on the Los Alamos experimental data. Chapter 4 describes the application of approach B for bridge pier damage identification, based on numerical simulation data generated using the virtual bridge

testbed. Chapter 5 describes the analysis framework of approach C and the application to the same bridge pier damage identification problem. Chapter 6 describes the strain-based vehicle classification approach developed based on the UCSD bridge-deck strain-video data. Thereafter, summary and conclusions are given in Chapter 7. Finally, in appendixes A and B, the 3D FE model of the bridge-foundation-soil system (of Chapters 4 and 5) is described, including detailed information on numerical modeling and the results of performed seismic response analyses.

1.5 Tables

Table 1.1 Organization of Chapters 2-6

	Employed approach	Utilized Data
Chapter 2	Structural damage identification approach A	Lotung seismic downhole data
Chapter 3	Structural damage identification approach B	Los Alamos experimental data
Chapter 4	Structural damage identification approach B	Simulation data generated using the virtual bridge testbed
Chapter 5	Structural damage identification approach C	Simulation data generated using the virtual bridge testbed
Chapter 6	Vehicle classification approach	UCSD bridge-deck strain-video data

1.6 Figures

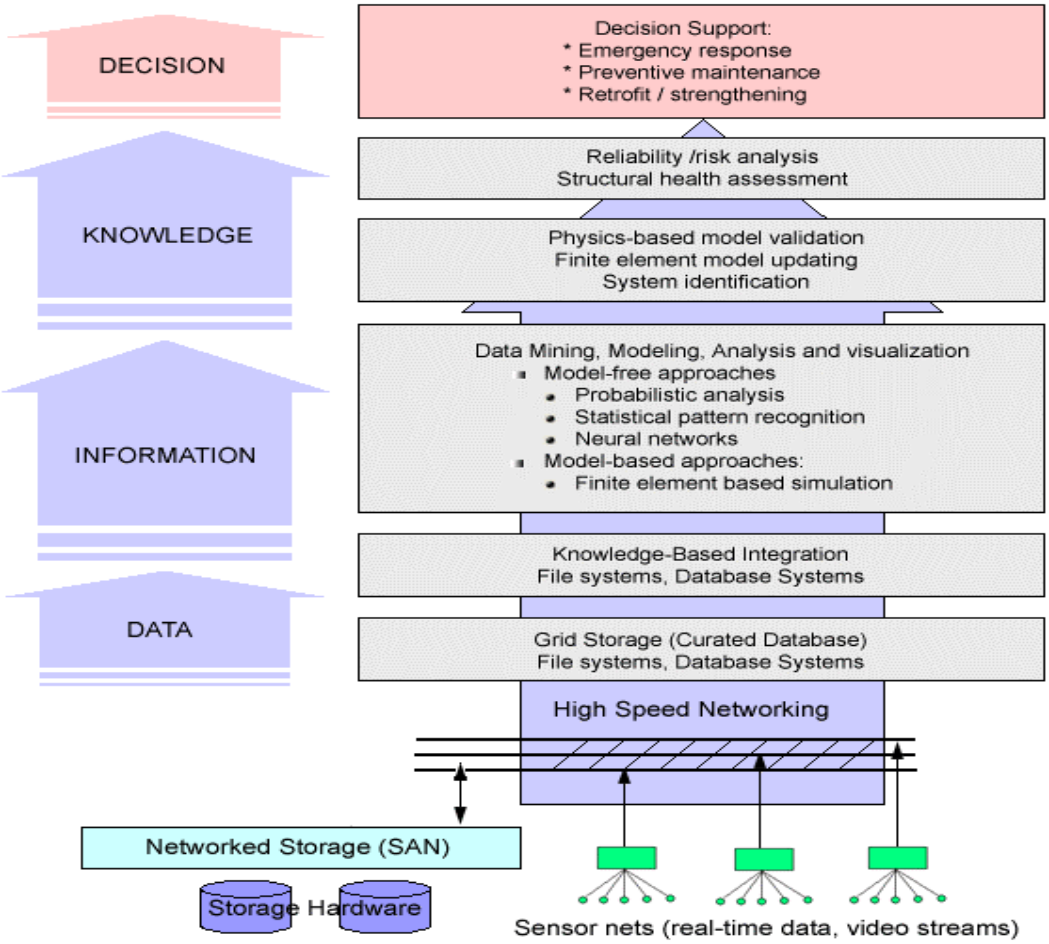


Fig. 1.1 Knowledge discovery hierarchy in an integrated structural health monitoring system (Elgamal et al. 2003).

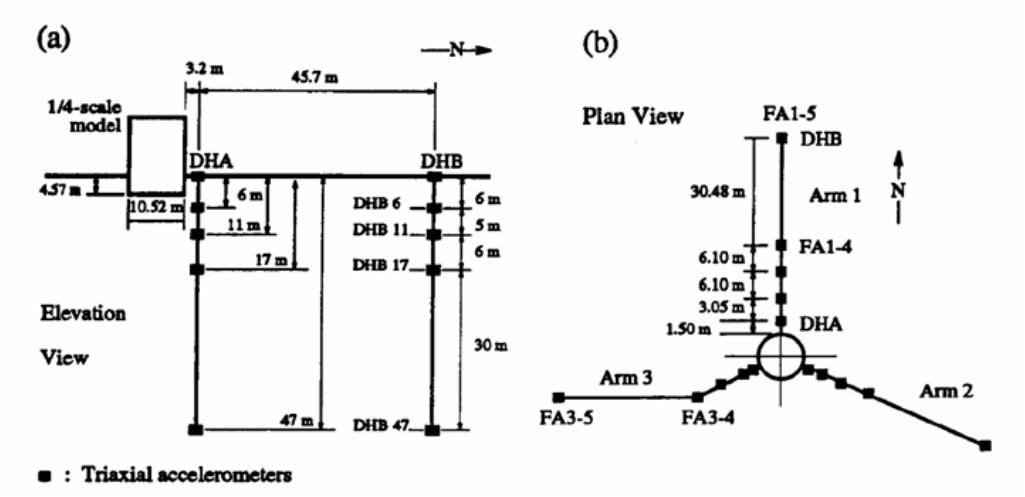


Fig. 1.2 Configuration of Lotung site: (a) downhole instrument arrays (b) surface instrument arrays (Elgamal et al. 1995).

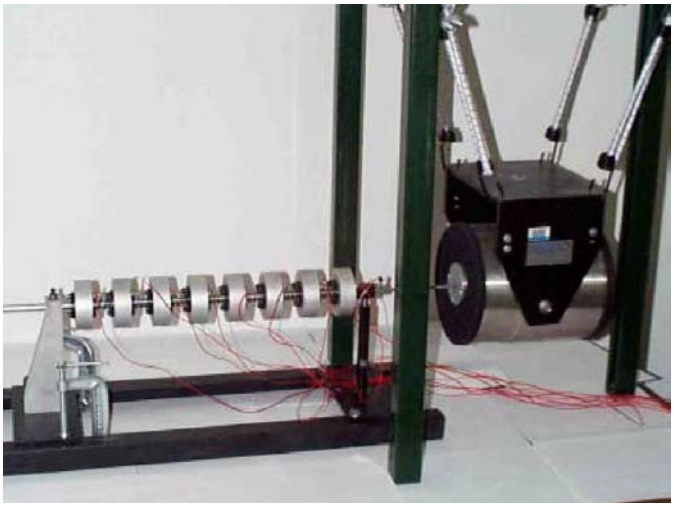
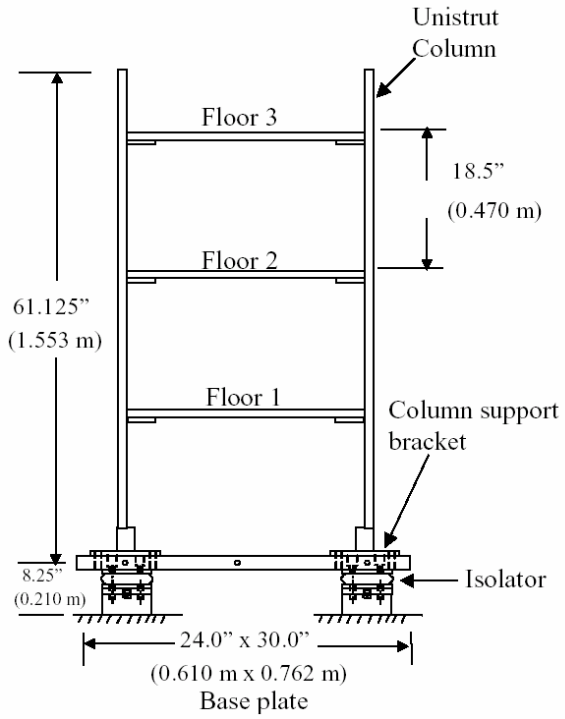
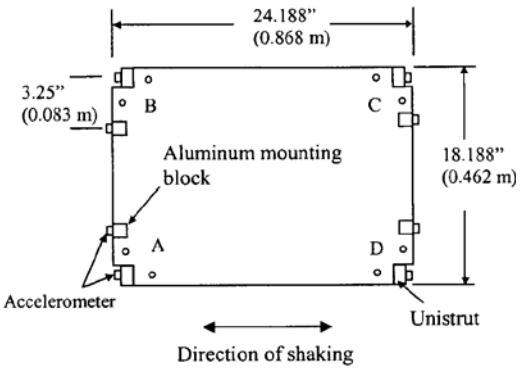


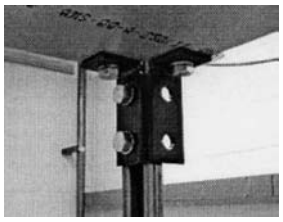
Fig. 1.3 An 8-DOF mass-spring system attached to a shaker with accelerometers mounted on each mass (Sohn and Farrar 2001).



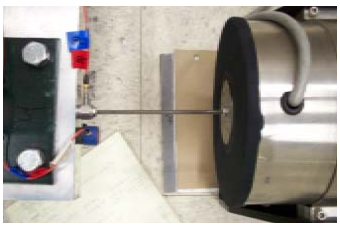
(a) Side view of the structure



(b) Top view of the floor layout



(c) A floor-column joint



(d) The attached shaker

Fig. 1.4 Experimental setup of the 3-story frame structural model (Sohn et al. 2003b).



Fig. 1.5 Overhead view of Humboldt Bay Middle Channel Bridge (HBB, Courtesy of Caltrans).

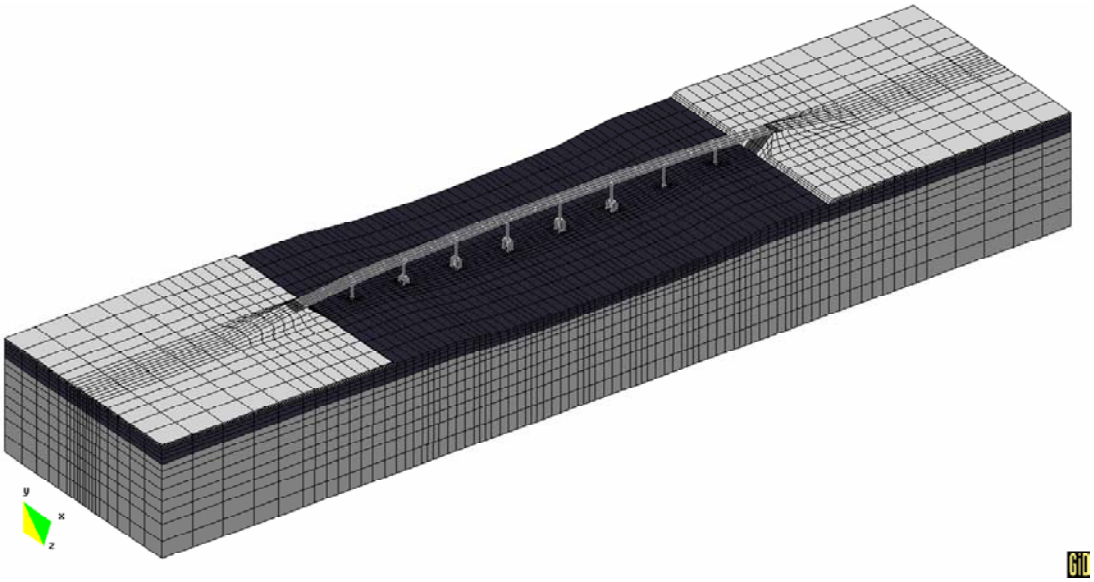


Fig. 1.6 3D nonlinear FE model of the HBB bridge-foundation-soil system.



Fig. 1.7 UCSD bridge-deck panels testbed (Fraser et al. 2002; Fraser 2006).

1.7 References

Aktan, E., Chase, S., Inman, D., and Pines, D. (2001). "Monitoring and Managing the Health of Infrastructure Systems." *Proc. of the 2001 SPIE Conference on Health Monitoring of Highway Transportation Infrastructure*, SPIE, March 6-8, 2001.

Bishop, C.M. (1995). *Neural Networks for Pattern Recognition*, Oxford University Press.

Catbas, N., Ciloglu, K., Celebioglu, A., Popovics, J., and Aktan. E. (2001). "Fleet Health Monitoring of Large Populations: Aged Concrete T-Beam Bridges in *Pennsylvania*." *Proc. of the 6th Annual Int'l Symposium on NDE for Health Monitoring and Diagnostics, SPIE*, March 4-8, 2001, Newport Beach, CA, USA.

Chang, F.K. (ed.) (1997). *Proc. of the First International Workshop on Structural Health Monitoring: Current Status and Perspectives*, September 18-20, 1997, Stanford, CA, USA.

Chang, F.K. (ed.) (2005). *Proc. of the 5th International Workshop on Structural Health Monitoring: Advancement and Challenge for Implementation*, September 12-14, 2005, Stanford, CA, USA.

Doebling, S.W., Farrar, C.R., Prime, M.B., and Shevitz, D.W. (1996). "Damage Identification and Health Monitoring of Structural and Mechanical Systems from Changes in Their Vibration Characteristics: A Literature Review." *Report No: LA-13070-MS*, Los Alamos National Laboratory.

Elgamal, A., Zeghal, M., Tang, H. T., and Stepp, J. C. (1995). "Lotung Downhole Array. I: Evaluation of Site Dynamic Properties." *Journal of Geotechnical Engineering*, 121(4), 350-362.

Elgamal, A., Conte J. P., Masri, S., Fraser, M., Fountain, T., Gupta, A., Trivedi, M., and El Zarki, M. (2003). "Health Monitoring Framework for Bridges and Civil Infrastructure." *Proc. of the 4th International Workshop on Structural Health Monitoring*, Stanford University, Stanford, CA, September 15 - 17, 2003.

Fraser, M., Elgamal, A., Conte, J. P., Karbhari, V., Zhao, L., and Seible, F. (2002). "Pilot Health Monitoring for Composite Bridge-deck Panels." *Proc. of the Third Middle East Symposium on Structural Composites for Infrastructure Applications*, Aswan, Egypt. December 17-20.

Fraser, M. (2006). "Development and Implementation of an Integrated Framework for Structural Health Monitoring." *Ph.D. Dissertation*, Department of Structural Engineering, University of California, San Diego, La Jolla, CA.

Hastie, T., Tibshirani, R., and Friedman, J. (2001). *The Elements of Statistical Learning: Data Ming, Inference, and Prediction*, Spring-Verlag, New York.

Jolliffe, I. T. (1986). *Principal Components Analysis*, Spring-Verlag, New York.

Kiremidjian, A.S., Straser, E.G., Meng, T., Law, K., and Soon, H. (1997). "Structural Damage Monitoring for Civil Structures." *Proc. of the First International Workshop on Structural Health Monitoring: Current Status and Perspectives*, 371-382, September 18-20, 1997, Stanford, CA, USA.

Klaiber, F.W., Dunker, K.F., Wipf, T.J., and Sanders, W.W. (1987). "Methods of Strengthening Existing Highway Bridges." *NCHRP Rep.293*, Transportation Research Board, National Research Council, Washington, D.C.

Mazurek, D.F., and DeWolf, J.T. (1990). "Experimental Study of Bridge Monitoring Technique." *ASCE, Journal of Structural Engineering*, 116(9), 2532-2549.

Porter, K. A. (2003). "An Overview of PEER's Performance-Based Earthquake Engineering Methodology." *Proc. of the Ninth International Conference on Applications of Statistics and Probability in Civil Engineering (ICASP9)*, Civil Engineering Risk and Reliability Association (CERRA), San Francisco, CA.

Sohn, H., Allen, D. W., Worden, K., and Farrar, C. R. (2003a). "Statistical Damage Classification Using Sequential Probability Ratio Tests." *Structural Health Monitoring*, 2(1), 57-74.

Sohn, H., and Farrar, C.R. (2001). "Damage Diagnosis Using Time Series Analysis of Vibration Signals." *Smart Materials and Structures*, 2001(10), 446-451.

Sohn, H., Farrar, C.R., Hemez, F., Czarnecki, J.J., Shunk, D., Stinemates, D., and Nadler, B. (2003b). "A Review of Structural Health Monitoring Literature from 1996-2001." *Report No: LA-13976-MS*, Los Alamos National Laboratory.

Stalling, J.M., Tedesco, J.W., El-Mihilmy, M., and McCauley, M. (2000). "Field Performance of FRP Bridge Repair." *ASCE, Journal of Bridge Engineering*, 5(2), 107-113.

Tang, H. (1987). "Large-Scale Soil Structure Interaction." *Rep. No. NP-5513-SR*, Electric Power Research Institute, Palo Alto, CA.

U.S. Department of Transportation (USDT) (2004). "2004 Status of the Nation's Highways, Bridges, and Transit: Conditions & Performance." *Report to Congress*.

2 A SUBSTRUCTURE IDENTIFICATION AND MONITORING APPROACH BASED ON ACCELERATION MEASUREMENTS

2.1 Introduction

In this chapter, a simple approach for substructure identification and monitoring (approach A in Chapter 1) is proposed. For this approach, substructures in a monitored structural system of interest are defined according to the sensor spatial distribution. Each substructure is then represented by a dynamic model (e.g., a single-degree-of-freedom (SDOF) model is herein employed), and the model properties are periodically identified based on measurements of structural acceleration response for monitoring purposes. This approach is developed for dense closely-spaced sensor network configurations, aiming to localize the condition assessment process, with only a limited set of sensors involved at any given time.

Herein, this conceptual analysis framework is applied to the Lotung seismic downhole data (Tang 1987) to monitor changes in soil layer properties. In the next section, detailed information on the Lotung seismic downhole data is provided. The analysis framework for soil layer identification is then described, including two different sub-layer scenarios. In the subsequent section, the proposed approach is first verified using simulation data, and the application of this approach to the Lotung seismic downhole data is presented. Finally, summary and conclusions are provided.

2.2 Lotung Seismic Downhole Data

Site seismic response measured by a downhole array provides valuable information on the soil properties. EPRI (Electric Power Research Institute) in

cooperation with TPC (Taiwan Power Company) conducted a large-scale seismic test (LSST) at the site near Lotung, Taiwan. The LSST involved construction of 1/4 and 1/2 scale model of a nuclear plant containment structure, and installation of an extensive array of strong motion instruments to monitor structural and site response (Tang 1987). The LSST site is located within the SMART-1 strong motion array in Taiwan. It is situated on a plat plain in a basin of triangular shaper that is 15km wide and 8km long (ERPI 1993). Geological material at the site generally consists of recent alluvium and Pleistocene over a Miocene basement. Field explorations showed the ground-water level was at or within 1m of ground surface.

Extensive instrumentation was deployed to record seismic structural and ground response, and to monitoring soil pore-water pressure buildup (Tang 1987). The ground instrumentation (Fig. 2.1) includes three linear surface arrays (Arms 1, 2, and 3), and two downhole arrays (DHA and DHB) that extended to a depth of 47m below ground surface. Downhole triaxial accelerometers were installed at depths of 6m, 11m, 17m, and 47m, oriented in the north-south (N-S), east-west (E-W), and vertical (V) directions. Eighteen earthquakes were recorded during the period 1985-86. These earthquakes were found to vary in peak acceleration, shaking duration, and frequency content bandwidth, providing a valuable a source of information on the site behavior over a broad range of excitations (Elgamal et al. 1995).

In this study, attention is focused on the site seismic response measured by the downhole array DHB and the overlying surface station (FA1-5). The N-S shaking records of three selected earthquakes (Table 1) are utilized in the analysis. It is seen

that Earthquakes 5 and 6 were relatively small and have similar peak accelerations, and Earthquake 16 induced significantly stronger shaking.

2.3 Analysis Framework

Near ground surface, soil response to earthquake motion is assumed to be predominantly caused by vertically propagating shear waves and closely match that of a conventional shear-beam (Kramer 1996). Thus, as a vertical array of downhole and surface accelerometers is available, the soil layer between selected sensors may be modeled crudely as an equivalent lumped mass single-degree-of-freedom (SDOF) system. Herein, two scenarios are investigated: (1) soil layer between a selected downhole sensor and the surface sensor (Fig. 2.2), and (2) soil layer within the range of three neighboring sensors (Fig. 2.3). Note that, for other structural forms (e.g., a bending beam response scenario), more sensors (e.g., 5-7) may be needed to define a substructure in order to provide sufficient information on structural response.

2.3.1 Scenario 1

The soil layer between a selected downhole sensor and the surface sensor (Fig. 2.2) may be modeled crudely as an equivalent lumped mass SDOF system characterized by the equation of motion shown below:

$$a_i + (c/m)(v_i - v_i^g) + (k/m)(d_i - d_i^g) = 0 \tag{2.1}$$

or

$$a_i + 2\xi\omega(v_i - v_i^g) + \omega^2(d_i - d_i^g) = 0 \tag{2.2}$$

where a_i, v_i, and d_i denote the absolute acceleration, velocity, and displacement of time step i at the ground surface, respectively; a_i^g, v_i^g, and d_i^g denote the absolute

acceleration, velocity, and displacement of time step i at the base, respectively; m, k, and c denote the equivalent mass, shear stiffness, and damping, respectively; ω and ξ denote the natural frequency and damping ratio, respectively. Defining $x = c/m = 2\xi\omega$, $y = k/m = \omega^2$, $v_i^R = v_i - v_i^g$, and $d_i^R = d_i - d_i^g$, Eq. 2.2 may be rewritten as:

$$a_i + xv_i^R + yd_i^R = 0 \tag{2.3}$$

Within this simple framework, the equivalent SDOF system can be identified based on recorded ground motions. First, initial acceleration, velocity, and displacement at all locations are assumed as zero. Using the Newmark method (Newmark 1959), ground velocity and displacement can be predicted based on the corresponding measured ground acceleration (average acceleration or trapezoidal rule):

$$\begin{aligned} v_{i+1} &= v_i + (\Delta t/2)(a_i + a_{i+1}) \\ d_{i+1} &= d_i + v_i\Delta t + (\Delta t^2/4)(a_i + a_{i+1}) \end{aligned} \tag{2.4}$$

and

$$\begin{aligned} v_{i+1}^g &= v_i^g + (\Delta t/2)(a_i^g + a_{i+1}^g) \\ d_{i+1}^g &= d_i^g + v_i^g\Delta t + (\Delta t^2/4)(a_i^g + a_{i+1}^g) \end{aligned} \tag{2.5}$$

where Δt is the time step size. Thereafter, v_i^R and d_i^R can be computed and used to predict ground surface acceleration using Eq. 2.3.

Herein, the measured absolute ground surface acceleration of time step i is denoted by a_i, and the corresponding predictor is denoted by $\tilde{a}_i$. Thus, the values of x and y can be identified by minimizing the sum squared error of a_i and $\tilde{a}_i$

$$E = \sum_i (a_i - \tilde{a}_i)^2 = \sum_i (a_i + xv_i^R + yd_i^R)^2 \tag{2.6}$$

Defining $A=\sum_i (a_i)^2$, $B=\sum_i (v_i^R)^2$, $D=\sum_i (d_i^R)^2$, $F=\sum_i (a_i v_i^R)$, $G=\sum_i (a_i d_i^R)$, and $H=\sum_i (v_i^R d_i^R)$, Eq. 2.6 may be rewritten as:

$$E = A + Bx^2 + Dy^2 + 2Fx + 2Gy + 2Hxy \tag{2.7}$$

Taking the partial derivative of Eq. 2.7 with respect to x and y yields:

$$\begin{aligned} \frac{\partial E}{\partial x} &= 2Bx + 2F + 2Hy = 0 \\ \frac{\partial E}{\partial y} &= 2Dy + 2G + 2Hx = 0 \end{aligned} \tag{2.8}$$

Solving this equation system results in:

$$\begin{aligned} x &= \frac{GH - DF}{BD - H^2} \\ y &= \frac{FH - BG}{BD - H^2} \end{aligned} \tag{2.9}$$

Thus, the values of ω and ξ can be computed based on x and y. Further, the identified equivalent SDOF system can be employed to predict the ground surface motion from the acceleration recorded by the downhole sensor using the Newmark method (Newmark 1959).

2.3.2 Scenario 2

The soil layer within the range of three neighboring sensors (Fig. 2.3) may be modeled crudely as an equivalent lumped mass SDOF system characterized by the equation of motion shown below:

$$a_i^N + \frac{c_1}{m}(v_i^N - v_i^{N-1}) + \frac{k_1}{m}(d_i^N - d_i^{N-1}) + \frac{c_2}{m}(v_i^N - v_i^{N+1}) + \frac{k_2}{m}(d_i^N - d_i^{N+1}) = 0 \tag{2.10}$$

where a_i^N, v_i^N, and d_i^N denote the absolute acceleration, velocity, and displacement of time step i at the accelerometer N location, respectively; a_i^{N-1}, v_i^{N-1}, and d_i^{N-1} denote the absolute acceleration, velocity, and displacement of time step i at the accelerometer N-1 location (base), respectively; a_i^{N+1}, v_i^{N+1}, and d_i^{N+1} denote the absolute acceleration, velocity, and displacement of time step i at the accelerometer N+1 location (top), respectively; m denotes the equivalent mass; k_1 and k_2 denotes equivalent shear stiffness parameters; c_1 and c_2 denotes equivalent damping parameters. Defining $x_1 = c_1/m$, $y_1 = k_1/m$, $x_2 = c_2/m$, $y_2 = k_2/m$, $v_i^{R1} = v_i^N - v_i^{N-1}$, $v_i^{R2} = v_i^N - v_i^{N+1}$, $d_i^{R1} = d_i^N - d_i^{N-1}$, $d_i^{R2} = d_i^N - d_i^{N+1}$, Eq. 2.10 may be rewritten as:

$$a_i^N + x_1 v_i^{R1} + y_1 d_i^{R1} + x_2 v_i^{R2} + y_2 d_i^{R2} = 0 \tag{2.11}$$

Within this simple framework, the equivalent SDOF systems can be identified based on recorded ground motions. First, initial acceleration, velocity, and displacement at all locations are assumed as zero. Using the Newmark method (Newmark 1959), ground velocity and displacement can be predicted based on the corresponding measured ground acceleration:

$$\begin{aligned} v_{i+1}^{N-1} &= v_i^{N-1} + (\Delta t/2)(a_i^{N-1} + a_{i+1}^{N-1}) \\ d_{i+1}^{N-1} &= d_i^{N-1} + v_i^{N-1}\Delta t + (\Delta t^2/4)(a_i^{N-1} + a_{i+1}^{N-1}) \end{aligned} \tag{2.12}$$

$$\begin{aligned} v_{i+1}^{N} &= v_i^{N} + (\Delta t/2)(a_i^{N} + a_{i+1}^{N}) \\ d_{i+1}^{N} &= d_i^{N} + v_i^{N}\Delta t + (\Delta t^2/4)(a_i^{N} + a_{i+1}^{N}) \end{aligned} \tag{2.13}$$

and

$$\begin{aligned} v_{i+1}^{N+1} &= v_i^{N+1} + (\Delta t/2)(a_i^{N+1} + a_{i+1}^{N+1}) \\ d_{i+1}^{N+1} &= d_i^{N+1} + v_i^{N+1}\Delta t + (\Delta t^2/4)(a_i^{N+1} + a_{i+1}^{N+1}) \end{aligned} \tag{2.14}$$

where Δt is the time step size. Thereafter, v_i^{R1}, d_i^{R1}, v_i^{R2}, and d_i^{R2} can be computed and used to predict ground acceleration at the accelerometer *N* location using Eq. 2.11.

Herein, the measured absolute acceleration of time step i at the accelerometer *N* location is denoted by a_i^N, and the corresponding predictor is denoted by $\tilde{a}_i^N$. Thus, the values of x_1, x_2, y_1, and y_2 can be identified by minimizing the sum squared error of a_i and $\tilde{a}_i$

$$E = \sum_i (a_i^N - \tilde{a}_i^N)^2 = \sum_i (a_i^N + x_1 \cdot v_i^{R1} + y_1 \cdot d_i^{R1} + x_2 \cdot v_i^{R2} + y_2 \cdot d_i^{R2})^2 \tag{2.15}$$

Defining $A_0 = \sum_i (a_i^N)^2$, $V_{11} = \sum_i (v_i^{R1})^2$, $D_{11} = \sum_i (d_i^{R1})^2$, $V_{22} = \sum_i (v_i^{R2})^2$, $D_{22} = \sum_i (d_i^{R2})^2$, $A_{v1} = \sum_i (a_i^N v_i^{R1})$, $A_{d1} = \sum_i (a_i^N d_i^{R1})$, $A_{v2} = \sum_i (a_i^N v_i^{R2})$, $A_{d2} = \sum_i (a_i^N d_i^{R2})$, $M_{11} = \sum_i (v_i^{R1} d_i^{R1})$, $V_{12} = \sum_i (v_i^{R1} v_i^{R2})$, $M_{12} = \sum_i (v_i^{R1} d_i^{R2})$, $M_{21} = \sum_i (v_i^{R2} d_i^{R1})$, $D_{12} = \sum_i (d_i^{R1} d_i^{R2})$, and $M_{22} = \sum_i (v_i^{R2} d_i^{R2})$, Eq. 2.15 may be rewritten as

$$\begin{aligned} E = {} & A_0 + V_{11}x_1^2 + D_{11}y_1^2 + V_{22}x_2^2 + D_{22}y_2^2 + 2A_{v1}x_1 + 2A_{d1}y_1 + 2A_{v2}x_2 + 2A_{d2}y_2 \\ & + 2M_{11}x_1y_1 + 2V_{12}x_1x_2 + 2M_{12}x_1y_2 + 2M_{21}x_2y_1 + 2D_{12}y_1y_2 + 2M_{22}x_2y_2 \end{aligned} \tag{2.16}$$

Taking the partial derivative of Eq. 2.16 with respect to x_1, y_1, x_2, and y_2 yields:

$$\begin{aligned} \frac{\partial E}{\partial x_1} &= 2V_{11}x_1 + 2M_{11}y_1 + 2V_{12}x_2 + 2M_{12}y_2 + 2A_{v1} = 0 \\ \frac{\partial E}{\partial y_1} &= 2M_{11}x_1 + 2D_{11}y_1 + 2M_{21}x_2 + 2D_{12}y_2 + 2A_{d1} = 0 \\ \frac{\partial E}{\partial x_2} &= 2V_{12}x_1 + 2M_{21}y_1 + 2V_{22}x_2 + 2M_{22}y_2 + 2A_{v2} = 0 \\ \frac{\partial E}{\partial y_2} &= 2M_{12}x_1 + 2D_{12}y_1 + 2M_{22}x_2 + 2D_{22}y_2 + 2A_{d2} = 0 \end{aligned} \tag{2.17}$$

Solving this system of equations yields the values of x_1, y_1, x_2, and y_2. Thus, the identified equivalent SDOF system can be employed to predict the ground motion at the accelerometer *N* location from the acceleration recorded by accelerometers *N*-1 and *N*+1 using the Newmark method (Newmark 1959).

2.4 Applications

In order to verify the proposed analysis framework, the approaches for both scenarios 1 and 2 are first applied to numerical data generated from SDOF models (Figs. 2.2 and 2.3). Thereafter, the Lotung seismic downhole array data is employed.

2.4.1 Scenario 1

2.4.1.1 Application to Numerical Simulation Data

For scenario 1, the system properties of the SDOF model (Fig. 2.2) are summarized in Table 2.2. In the simulations, N-S seismic motions measured at the Lotung DHB-11 station (at a depth of 11.5m) are employed as the base excitation. Three simulations are performed, two small tremors (earthquakes 5 and 6) and one strong motion (earthquake 16). In addition, it is assumed that the strong earthquake induces damage in the system, which is formulated as 10% reduction in the stiffness.

Following the aforementioned procedure, three system identification scenarios are studied based on the simulation data of earthquakes 5, 6, and 16, respectively. Table 2.3 shows that the system properties can be properly identified for all cases. For earthquakes 5 and 6 (no damage in the system), the identified natural frequency and damping ratio appear to match the actual values (Table 2.2). As to earthquake 16, the 10% induced stiffness reduction is also identified, reflecting in the decrease of ω^2.

In addition, the system properties identified from earthquake 5 data are employed to predict the SDOF system response to earthquakes 5, 6, and 16. The results are shown in Figs. 2.4-2.6. In these figures, the upper part shows the comparison of the predicted and simulated response along with the residual error (normalized by the maximum peak response) in time domain, and the lower part shows the comparison in frequency domain.

It is seen that for no damage cases (earthquakes 5 and 6), the predicted response can match the actual measurement well in both time and frequency domains and the residual error remains at a very low level (Figs. 2.4 and 2.5). However, the system response to earthquake 16 cannot be well predicted because of the induced damage. Fig. 2.6 shows that the residual error of prediction is significant, reaching about 50% of the maximum peak response. In other words, the prediction error is a good damage indicator (very sensitive to the damage).

2.4.1.2 Application to Lotung Seismic Downhole Data

The proposed analysis procedure of scenario 1 is applied to the Lotung seismic downhole array data. Excitations in the form of N-S shaking at the DHB-11 (11.5m depth) and FA1-5 (ground surface) stations for earthquakes 5, 6, and 16 are utilized.

Fig. 2.7 shows the computed transfer functions of the soil system between DHB-11 and FA1-5 for these three earthquakes. It is seen that as both earthquakes 5 and 6 are small tremors, they did not cause significant changes in the soil properties. Thus, their transfer functions present a similar pattern, with the first resonance frequency around 3-4Hz and the second one around 8.5Hz. In addition, as expected, the transfer function for earthquake 16 shows great difference as the strong motion

induces significant nonlinear soil response and temporarily changes the soil properties (Elgamal et al. 1995). Since the proposed approach only focuses on the first natural frequency, a bandpass filter is herein applied to all data to cut off frequency components lower than 2Hz or higher than 5Hz.

Figs. 2.8-2.10 show the a, v^R, and d^R time histories for earthquake 5, 6, and 16. Four soil property estimations are performed (Table 2.4) based on data of earthquake 5, earthquake 6, both earthquakes 5 and 6, and earthquake 16, respectively. It is seen that as expected, the results of the first three identifications (all based on small tremor data) are very close to each other, with the natural frequency around 3.2-3.4Hz. As to the strong earthquake 16 inducing nonlinear response, the identified value for ω^2 is much lower along with a much higher damping ratio (Table 2.4).

Further, in order to monitor the change with earthquake shaking, the natural frequency and damping ratio of the soil layer are also identified based on windowed data of earthquakes 5, 6, and 16, using a moving time window of 2.5 second width. The results are shown in Figs. 2.11-2.13, where the horizontal axis indicates window start time. It is seen that for earthquakes 5 and 6 (Figs. 2.11 and 2.12), the identified value for natural frequency is relatively stable, around 3.3Hz (the dashed line), indicating no significant change induced by these small tremors. However, the strong shaking of earthquake 16 significantly reduces the soil layer stiffness, causing the corresponding decrease of natural frequency (Fig. 2.13).

Thereafter, the equivalent SDOF system identified from earthquake 5 data (Table 2.4) is employed to predict the ground surface response from the motions recorded at the DHB11 station. Figs. 2.14 and 2.15 show that for earthquakes 5 and 6,

the amplitude of the predicted response is of the same order as the measurement. The maximum prediction error is about 40-60% of the maximum peak response. Fig. 2.16 shows the prediction for earthquake 16. It is seen that the predicted response is much higher than the actual measurement, which is limited by the nonlinear soil response induced by the strong motion. Compared with Figs. 2.14 and 2.15, the prediction error is much higher, reaching 300%. Based on this, changes in the soil properties can be inferred.

2.4.2 Scenario 2

2.4.2.1 Application to Numerical Simulation Data

The system properties of the SDOF model for scenario 2 (Fig. 2.3) are summarized in Table 2.5. In the simulations, N-S seismic motions measured at the Lotung DHB-17 (17m depth) and FA1-5 stations are employed as the base and top excitation, respectively. Three simulations are performed, two small tremors (earthquakes 5 and 6) and one strong motion (earthquake 16). In addition, it is assumed that the strong earthquake induces damage in the system, which is formulated as 10% reduction in the value of k_2 / m.

Following the proposed procedure, three system identifications are performed based on the simulation data of earthquakes 5, 6, and 16, respectively. Table 2.6 shows that the system properties can be properly identified for all cases. For earthquakes 5 and 6 (no damage in the system), the identified system properties match the actual values (Table 2.5) well. As to earthquake 16, the 10% reduction in k_2 / m is also identified.

In addition, the system properties identified from earthquake 5 data are employed to predict the SDOF system response to earthquakes 5, 6, and 16. The results are shown in Figs. 2.17-2.19. It is seen that for no damage cases (earthquakes 5 and 6), the predicted response can match the actual measurement well in both time and frequency domains and the residual error remains at a very low level (Figs. 2.17 and 2.18). However, the system response to earthquake 16 cannot be well predicted due to the induced damage. Fig. 2.19 shows that the residual error of prediction is significant, reaching about 10% of the maximum peak response.

2.4.2.2 Application to Lotung Seismic Downhole Data

The proposed analysis procedure of scenario 2 is applied to the Lotung seismic downhole array data to identify and monitor the soil system between DHB-17 and FA1-5. Excitations in the form of N-S shaking at the DHB-17, DHB-11, and FA1-5 stations for earthquakes 5, 6, and 16 are utilized. A bandpass filter is herein applied to all data to cut off frequency components lower than 2Hz or higher than 5Hz.

Figs. 2.20-2.22 show the a, v^{R1}, d^{R1}, v^{R2}, and d^{R2} time histories for earthquake 5, 6, and 16. Three times of soil layer property estimation are performed (Table 2.7) based on data of earthquakes 5, 6, and 16, respectively. It is seen that as expected, the results of the first two identifications (all based on small tremor data) are very close to each other. As to the strong earthquake 16 inducing nonlinear response, the identified values for k_1 / m and k_2 / m are significantly lower along with a much higher value for c_2 / m (a term related to damping, Table 2.7).

Further, in order to monitor the change with earthquake shaking, the soil layer properties are also identified based on windowed data of earthquakes 5, 6, and 16, using a moving time window of 2.5 second width (Figs. 2.23-2.25). Note that in these figures, only identification results corresponding to the strong shaking phase are presented in view of: 1) the early part of each record is dominated by P-wave, and 2) later in the record, surface wave contributions might be of significance.

It is seen that for earthquakes 5 and 6 (Figs. 2.23 and 2.24), the identified value for k_1/m and k_2/m is relatively stable, around the dashed lines, indicating no significant change induced by these small tremors. However, the strong shaking of earthquake 16 significantly reduces the soil layer stiffness, causing the corresponding decrease of k_1/m and k_2/m (Fig. 2.25).

Thereafter, the equivalent SDOF system identified from earthquake 5 (Table 2.7) is employed to predict the ground motion at the DBH-11 station from the measurements of DHB-17 and FA1-5. Figs. 2.26 and 2.27 show that for earthquakes 5 and 6, the amplitude of the predicted response is of the same order as the measurement. The maximum prediction error is about 50% of the maximum peak response. Fig. 2.28 shows the prediction for earthquake 16. It is seen that the predicted response is much higher than the actual measurement, which is limited by the nonlinear soil response induced by the strong motion. Compared with Figs. 2.26 and 2.27, the prediction error is much higher, reaching 100%. Based on this, changes in the soil properties can be inferred.

2.5 Summary and Conclusions

A simple approach for substructure identification and monitoring was proposed. For this approach, substructures in a monitored structural system of interest are first defined according to the sensor spatial distribution. Each substructure is then represented by a dynamic model, and the model properties are periodically identified based on measurements of structural acceleration response for monitoring purposes. Herein, this conceptual analysis framework was applied to the Lotung seismic downhole data (Tang 1987) to monitor changes in soil layer properties.

In the presence of a vertical array of downhole and surface accelerometers, the soil layer between selected sensors may be modeled crudely as an equivalent lumped mass SDOF system. In this paper, two scenarios were investigated: (1) soil layer between a selected downhole sensor and the surface sensor (Fig. 2.2), and (2) soil layer within the range of three neighboring sensors (Fig. 2.3). For each scenario, an analysis framework based on Newmark time integration (Newmark 1959) is then developed to identify the equivalent SDOF system based on measured seismic response.

Herein, the proposed approach is first verified using simulation data generated from numerical SDOF models and then applied to the Lotung seismic downhole data. Promising results are achieved, showing that strong earthquake induced changes in soil layer properties can be captured using the proposed identification technique. In addition, using the equivalent SDOF model identified from small earthquake data, seismic ground response at a selected sensor location can be crudely predicted from

the measurements of neighboring sensors. The prediction error is a sensitive damage indicator and may be utilized to monitor changes in the soil layer properties.

2.6 Tables

Table 2.1 Information on the Three Studied Earthquakes

Event	Date	Magnitude (M_l)	Peak Acceleration (g)		
			E-W	N-S	V
Earthquake 5	3/29/86	N/A	0.04	0.03	0.03
Earthquake 6	4/8/86	5.4	0.04	0.03	0.01
Earthquake 16	11/14/86	7.0	0.13	0.17	0.10

Table 2.2 Properties of the numerical SDOF model (Scenario 1)

Resonance frequency, f (Hz)	Damping ratio, ξ	$2\xi\omega$	ω^2
3.5	0.05	2.1991	483.6106

Table 2.3 Identification of the numerical SDOF system (scenario 1)

	Identified system properties			
Utilized simulation data	f (Hz)	ξ	$2\xi\omega$	ω^2
Earthquake 5	3.4999	0.0500	2.1986	483.5730
Earthquake 6	3.4991	0.0500	2.1999	483.3553
Earthquake 16	3.3203	0.0527	2.1991	435.2143

Table 2.4 Identification of the equivalent SDOF system for the soil system between the FA1-5 and DHB-11 stations

	Identified system properties			
Utilized seismic data	f (Hz)	ξ	$2\xi\omega$	ω^2
Earthquake 5 (small tremor)	3.3225	0.0207	0.8639	435.7805
Earthquake 6 (small tremor)	3.2443	0.0070	0.2837	415.5155
Earthquakes 5 and 6 (small tremors)	3.2592	0.0096	0.3931	419.3274
Earthquake 16 (strong motion)	2.2815	0.0645	1.8488	205.4802

Table 2.5 Properties of the numerical SDOF model (Scenario 2)

c_1 / m	k_1 / m	c_2 / m	k_2 / m
1	50	2	100

Table 2.6 Identification of the numerical SDOF system (scenario 2)

	Identified system properties			
Utilized simulation data	c_1/m	k_1/m	c_2/m	k_2/m
Earthquake 5	1.0016	50.0004	1.9992	100.0008
Earthquake 6	0.9992	49.9863	1.9999	99.9725
Earthquake 16	1.0016	49.9885	2.0003	89.9795

Table 2.7 Identification of the equivalent SDOF system for the soil system between the FA1-5 and DHB-17 stations

	Identified system properties			
Utilized seismic data	c_1 / m	k_1 / m	c_2 / m	k_2 / m
Earthquake 5 (small tremor)	4.7418	522.4231	0.3037	192.6565
Earthquake 6 (small tremor)	6.6423	602.0427	1.6886	211.7880
Earthquake 16 (strong motion)	4.6251	351.3066	2.1473	116.5453

2.7 Figures

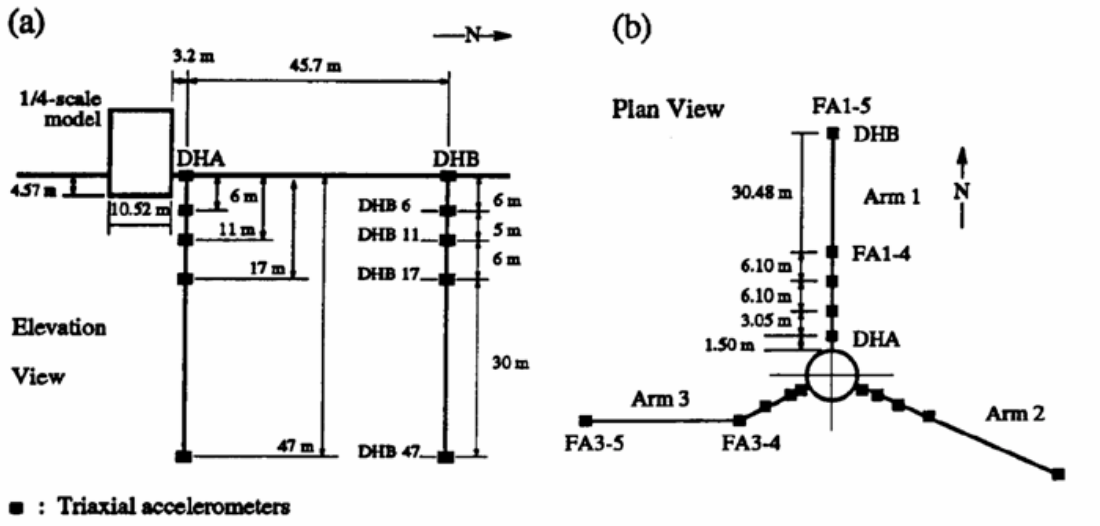


Fig. 2.1 Configurations of Lotung site: (a) downhole instrument arrays (b) surface instrument arrays (Elgamal et al. 1995).

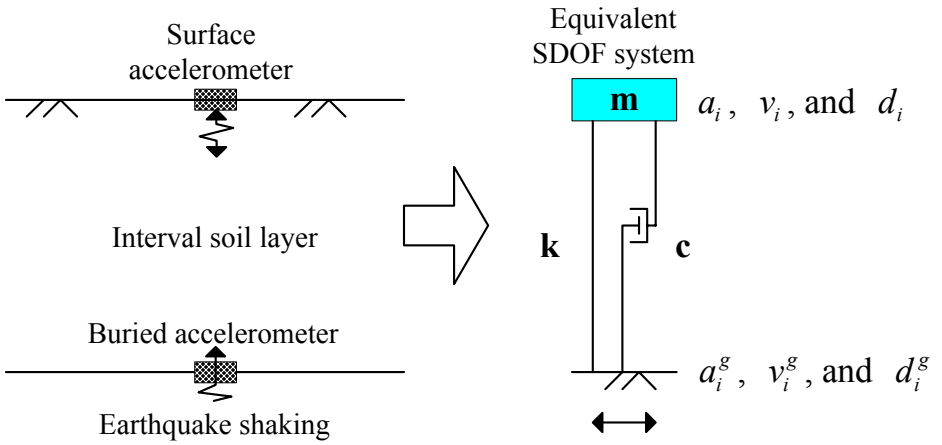


Fig. 2.2 Configuration of the monitoring system and property estimation for the soil layer between a selected downhole sensor and a surface sensor (scenario 1).

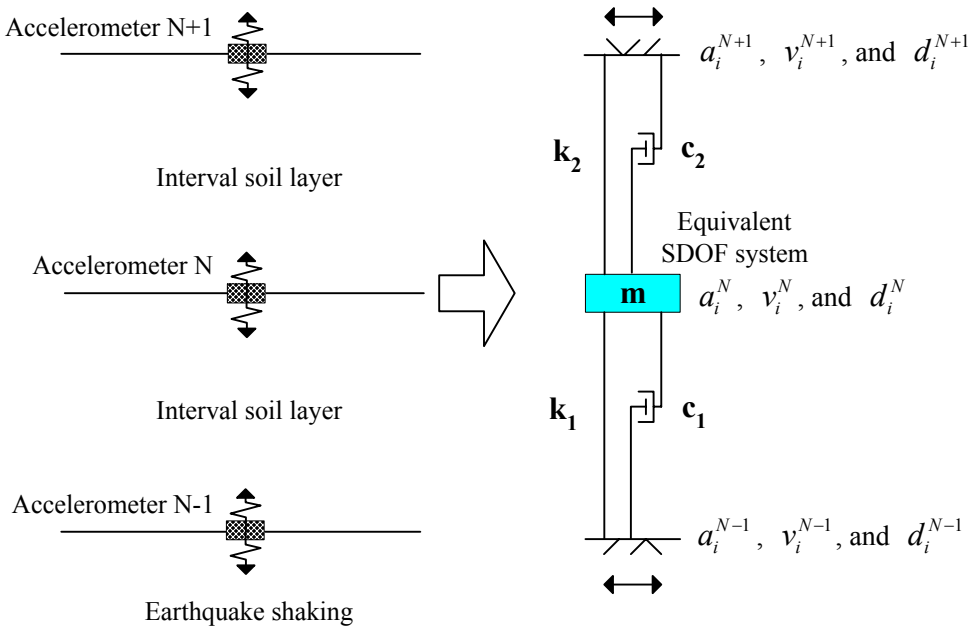


Fig. 2.3 Configuration of the monitoring system and property estimation for the soil layer within the range of three neighboring sensors (scenario 2).

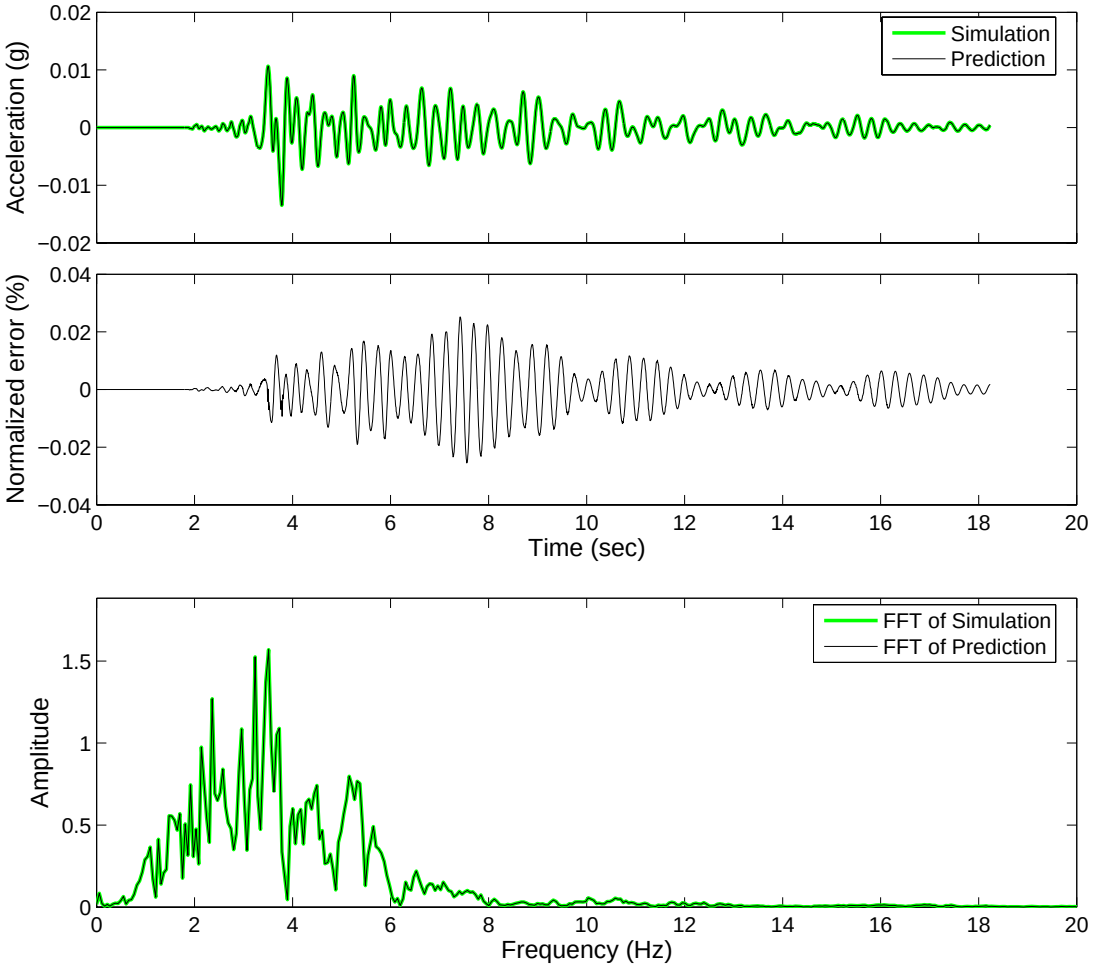


Fig. 2.4 Prediction of the intact SDOF system (scenario 1) response to earthquake 5.

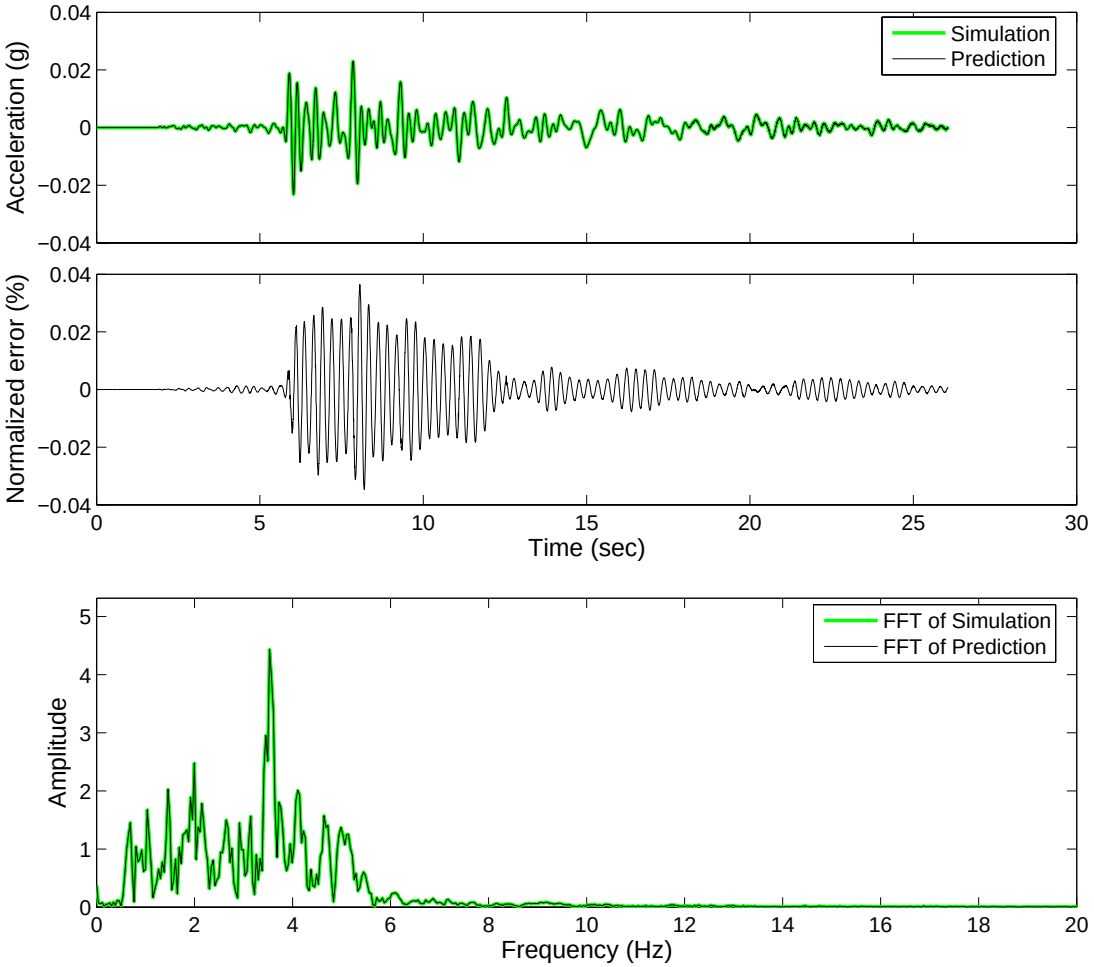


Fig. 2.5 Prediction of the intact SDOF system (scenario 1) response to earthquake 6.

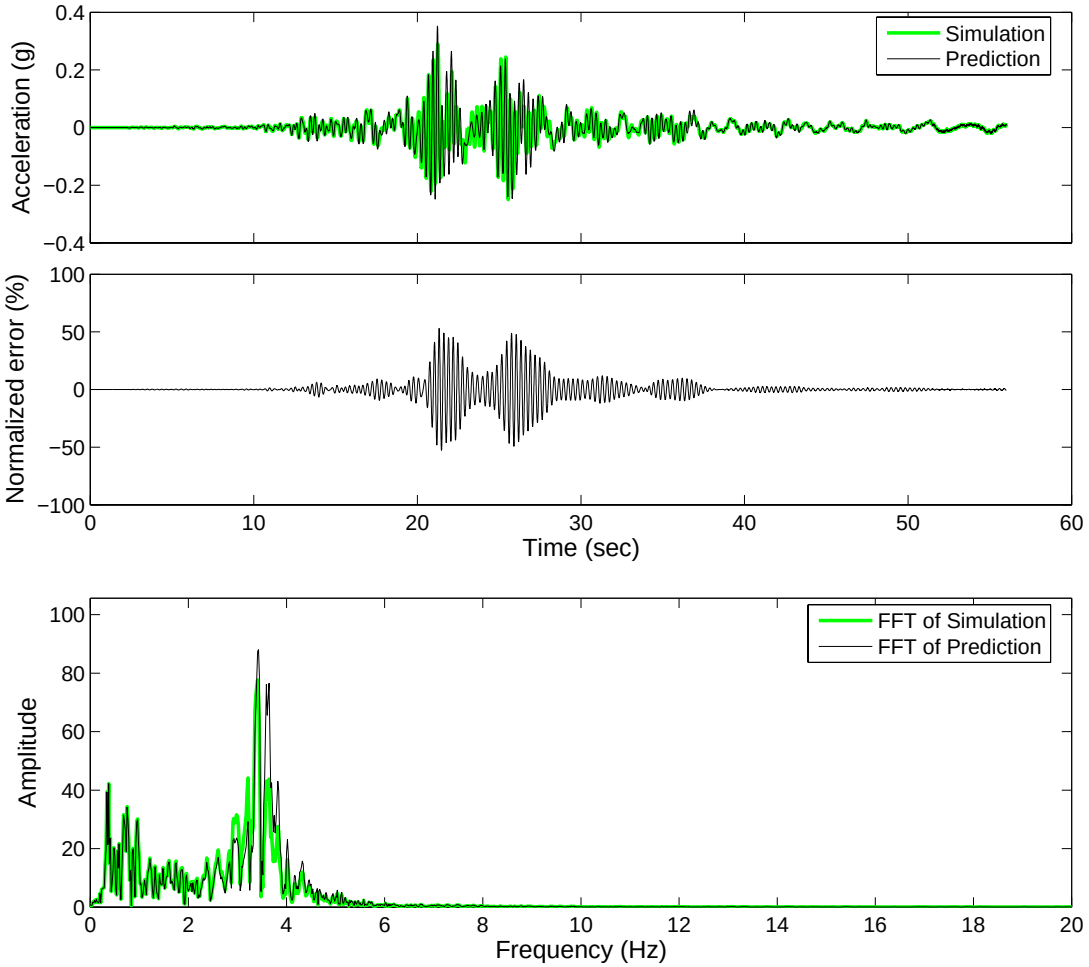


Fig. 2.6 Prediction of the damaged SDOF system (scenario 1) response to earthquake 16.

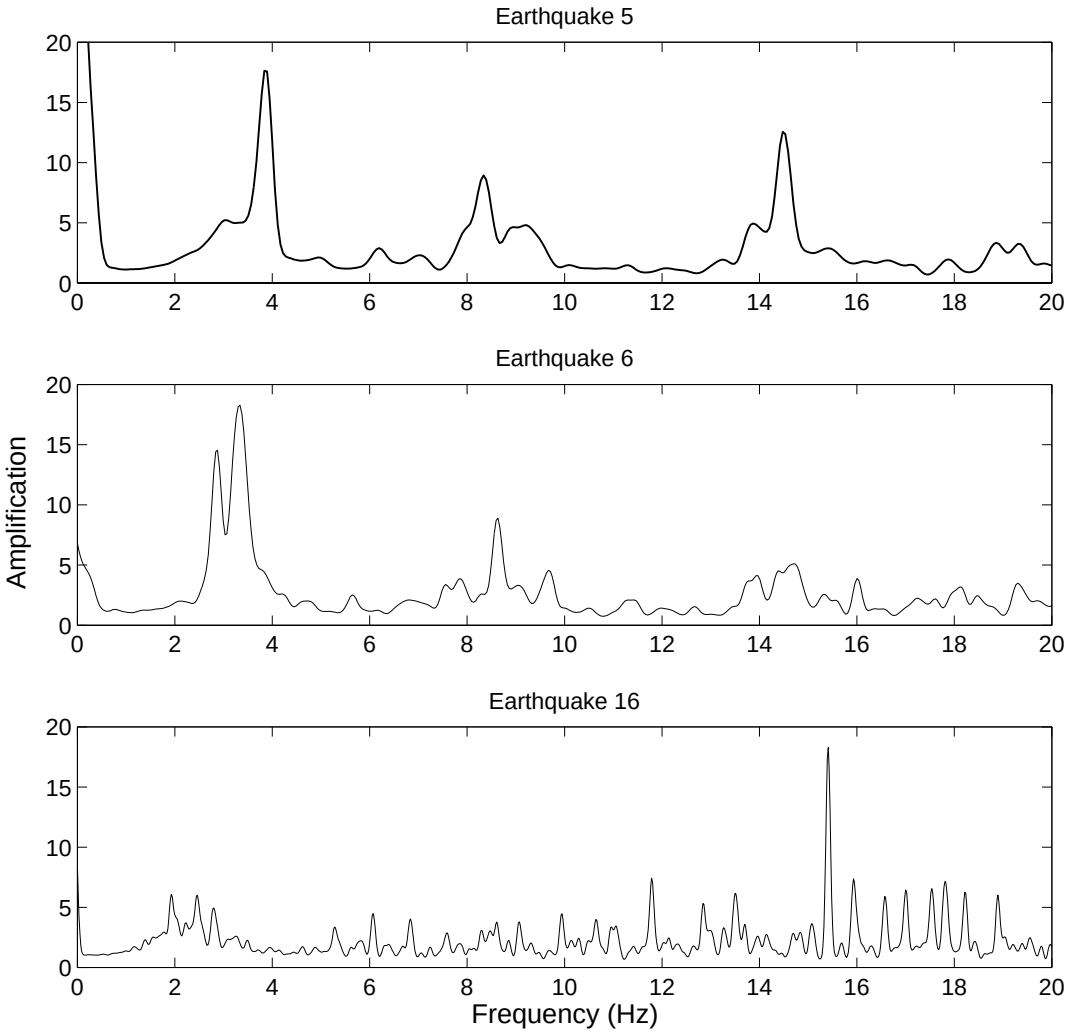


Fig. 2.7 Transfer functions of the soil system between DHB-11 and FA1-5 for earthquakes 5, 6, and 16.

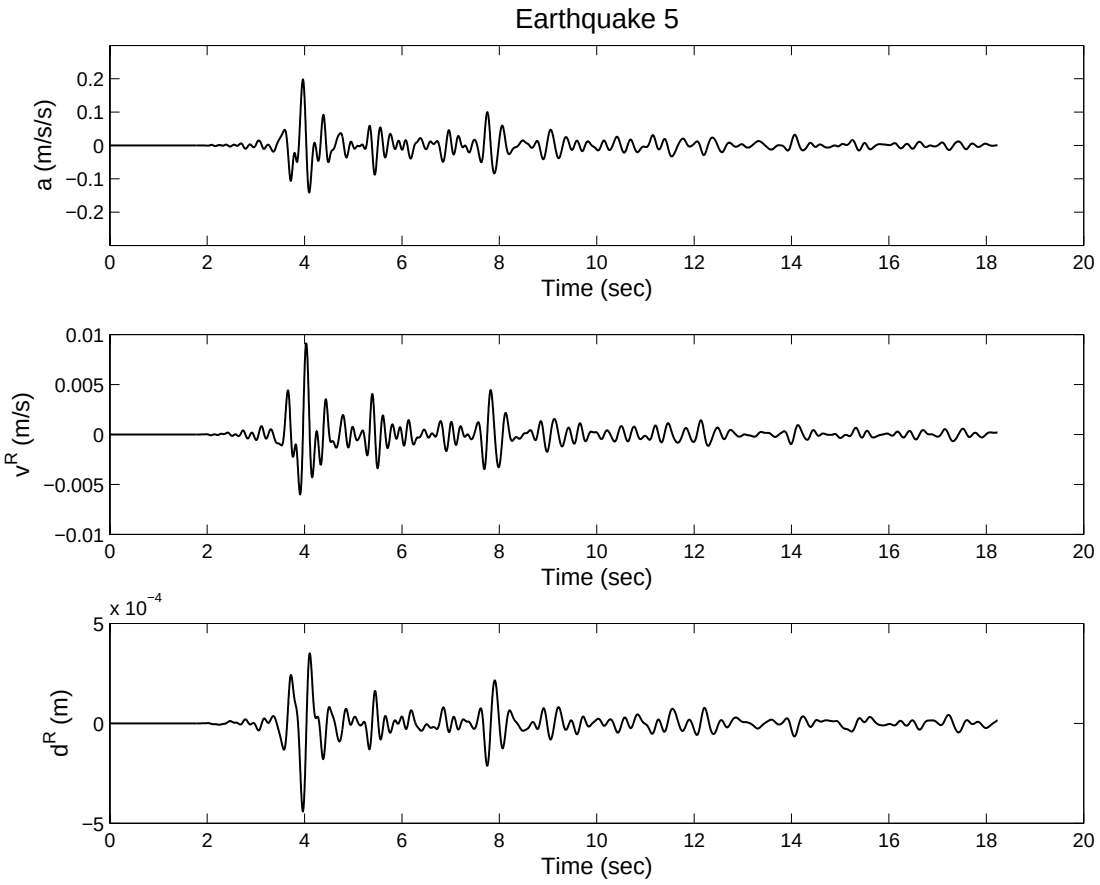


Fig. 2.8 a, v^R, and d^R time histories of the soil system between DHB-11 and FA1-5 for response to earthquake 5.

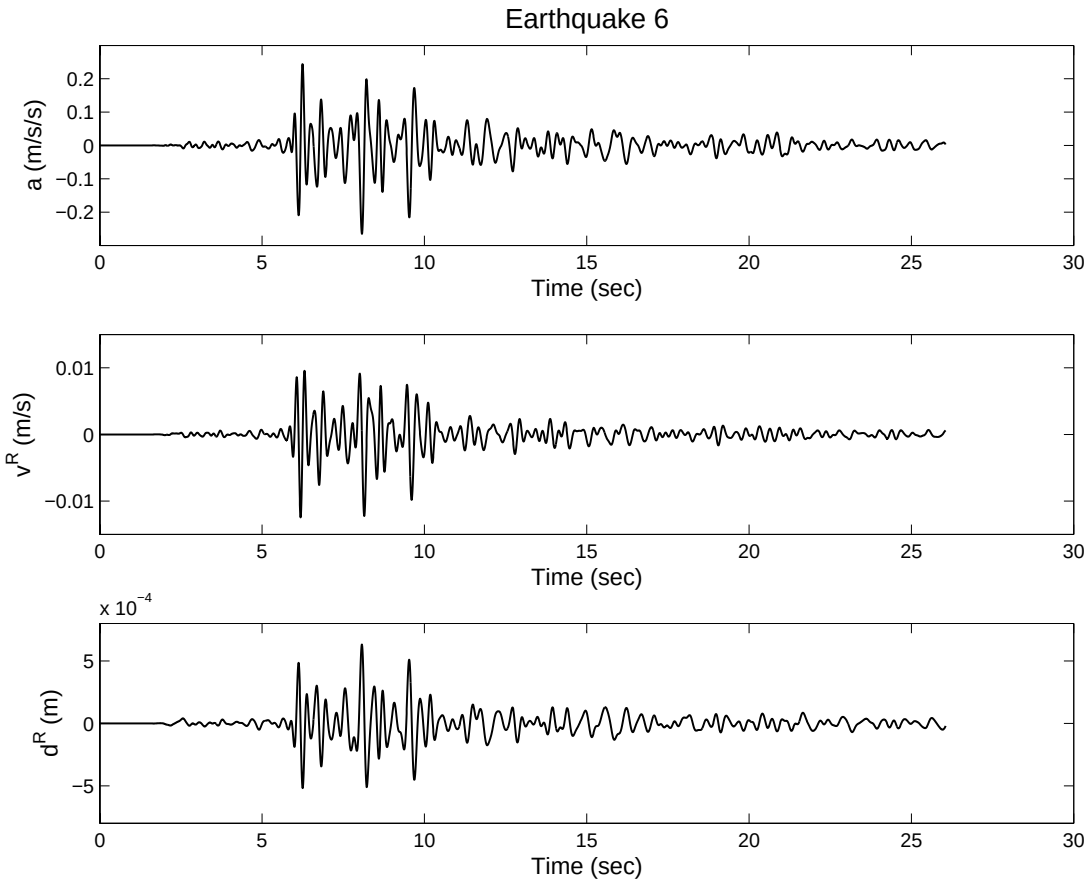


Fig. 2.9 a, v^R, and d^R time histories of the soil system between DHB-11 and FA1-5 for response to earthquake 6.

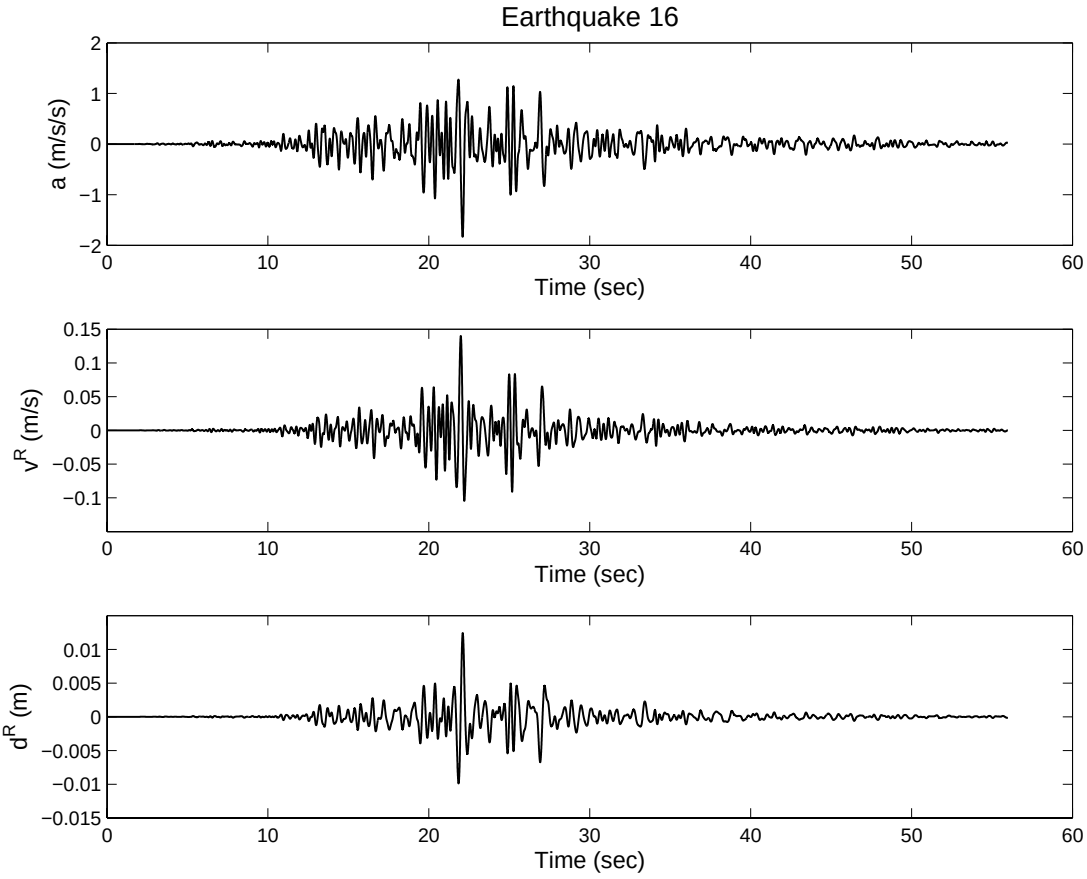


Fig. 2.10 a, v^R, and d^R time histories of the soil system between DHB-11 and FA1-5 for response to earthquake 16.

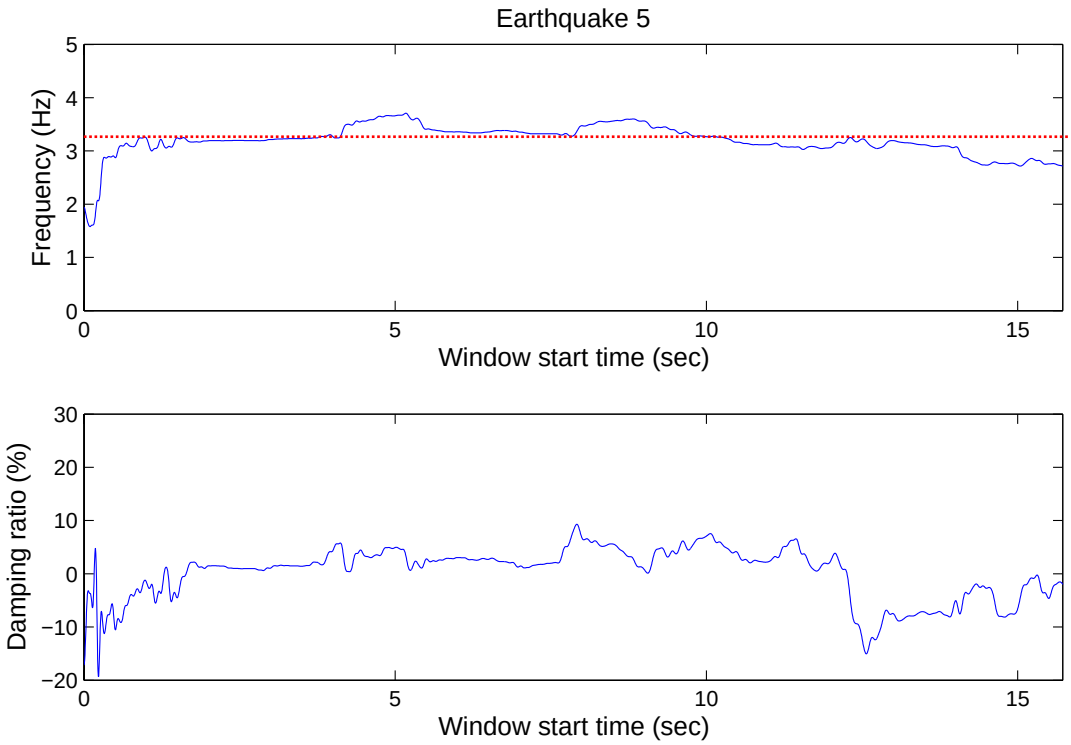


Fig. 2.11 Natural frequency and damping ratio identification of the soil system between DHB-11 and FA1-5 using the analysis framework of scenario 1 and a moving time window of 2.5 second width, based on data of earthquake 5.

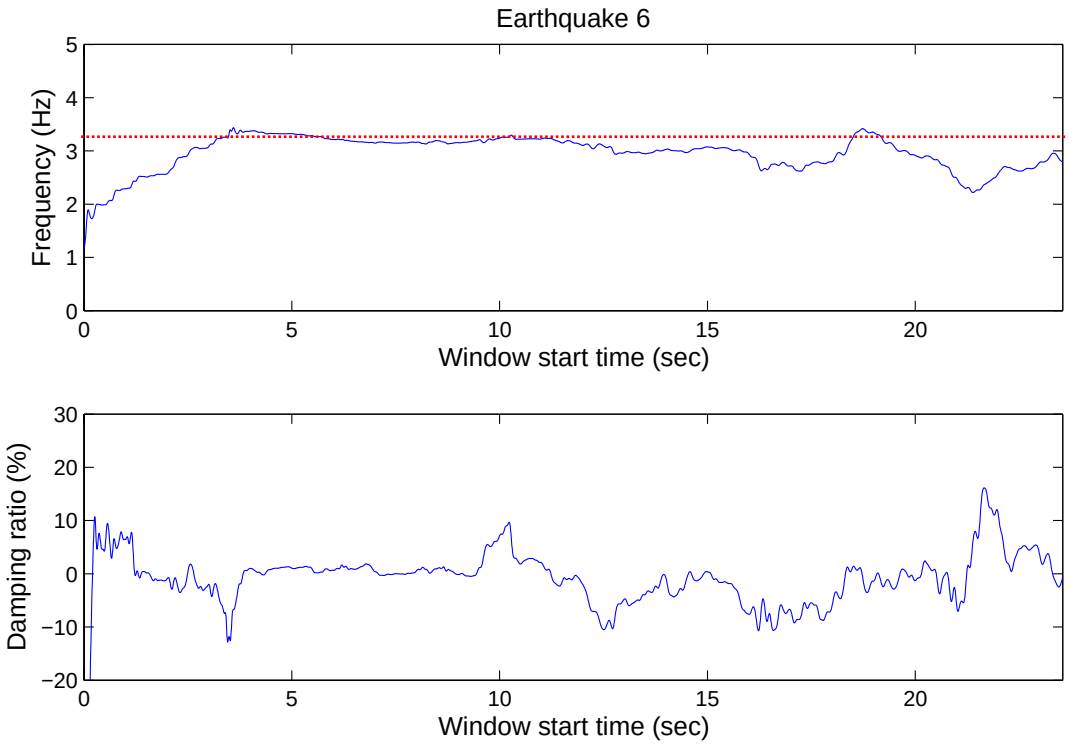


Fig. 2.12 Natural frequency and damping ratio identification of the soil system between DHB-11 and FA1-5 using the analysis framework of scenario 1 and a moving time window of 2.5 second width, based on data of earthquake 6.

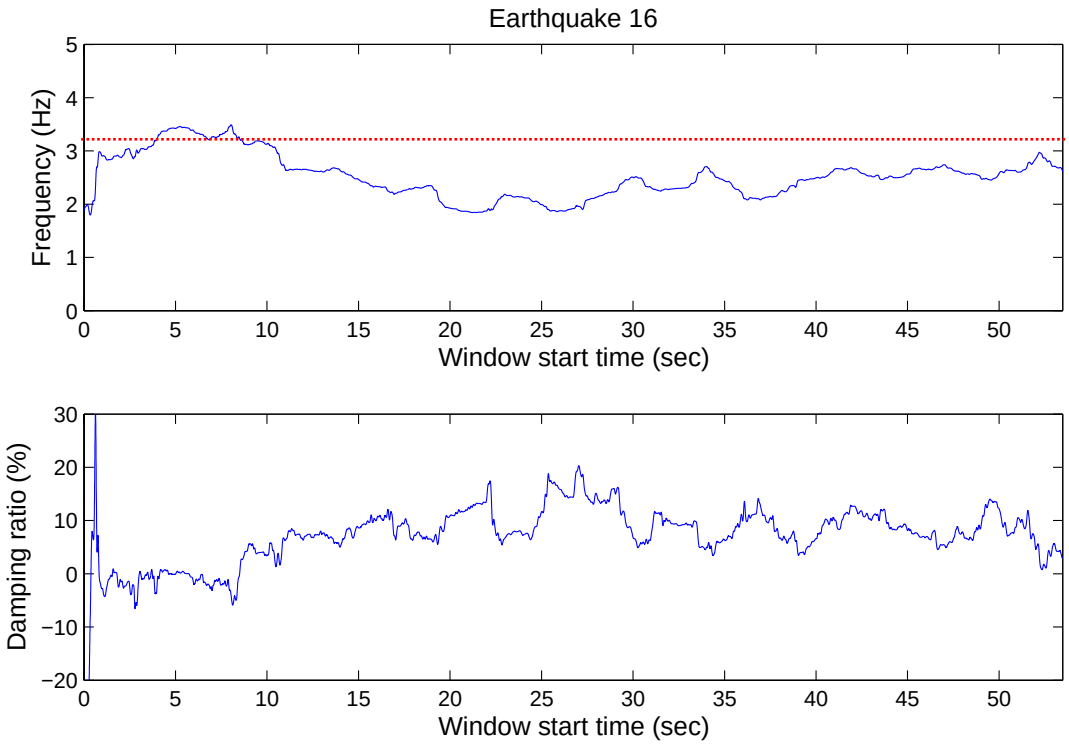


Fig. 2.13 Natural frequency and damping ratio identification of the soil system between DHB-11 and FA1-5 using the analysis framework of scenario 1 and a moving time window of 2.5 second width, based on data of earthquake 16.

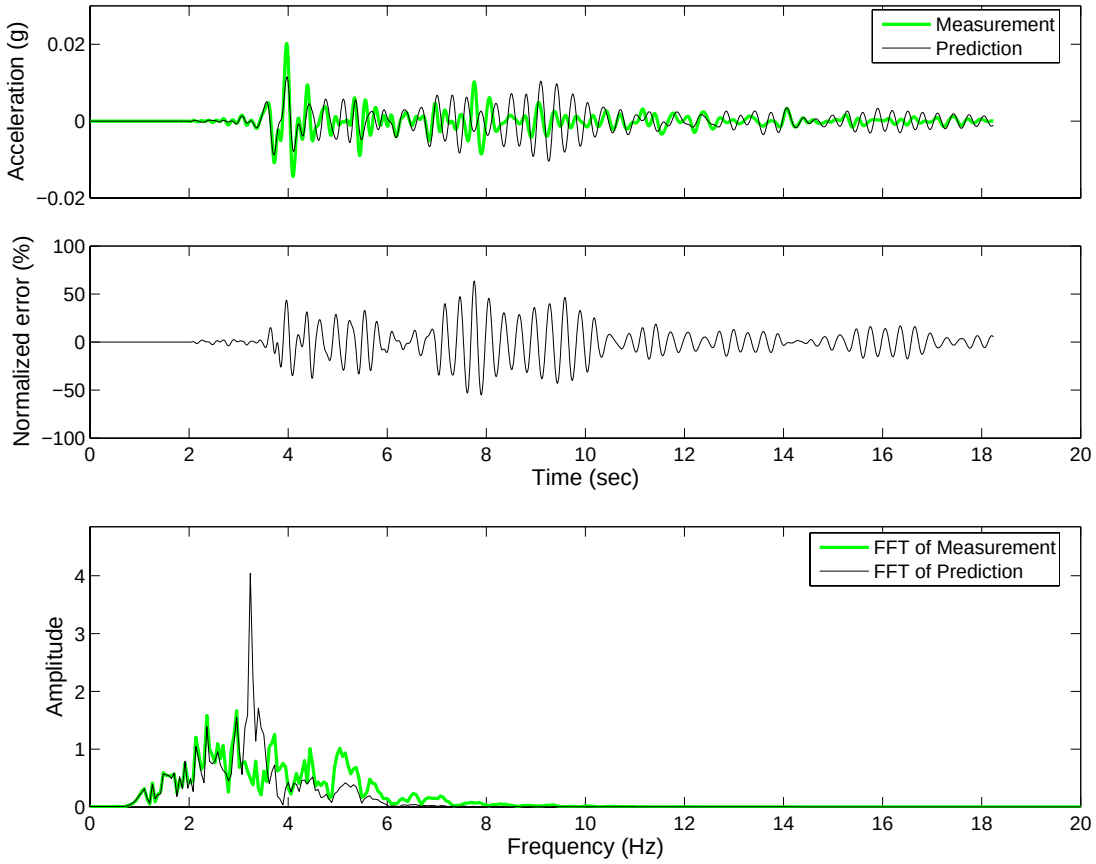


Fig. 2.14 Prediction of the ground surface response to earthquake 5.

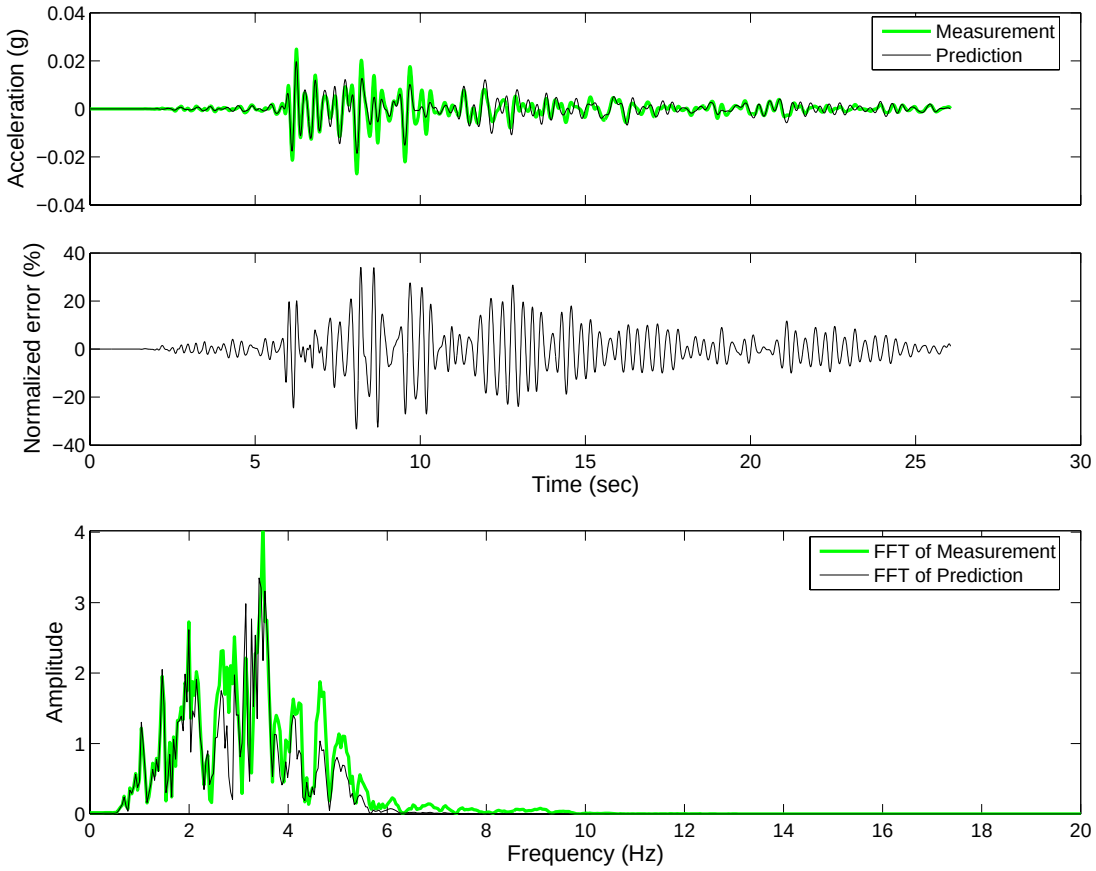


Fig. 2.15 Prediction of the ground surface response to earthquake 6.

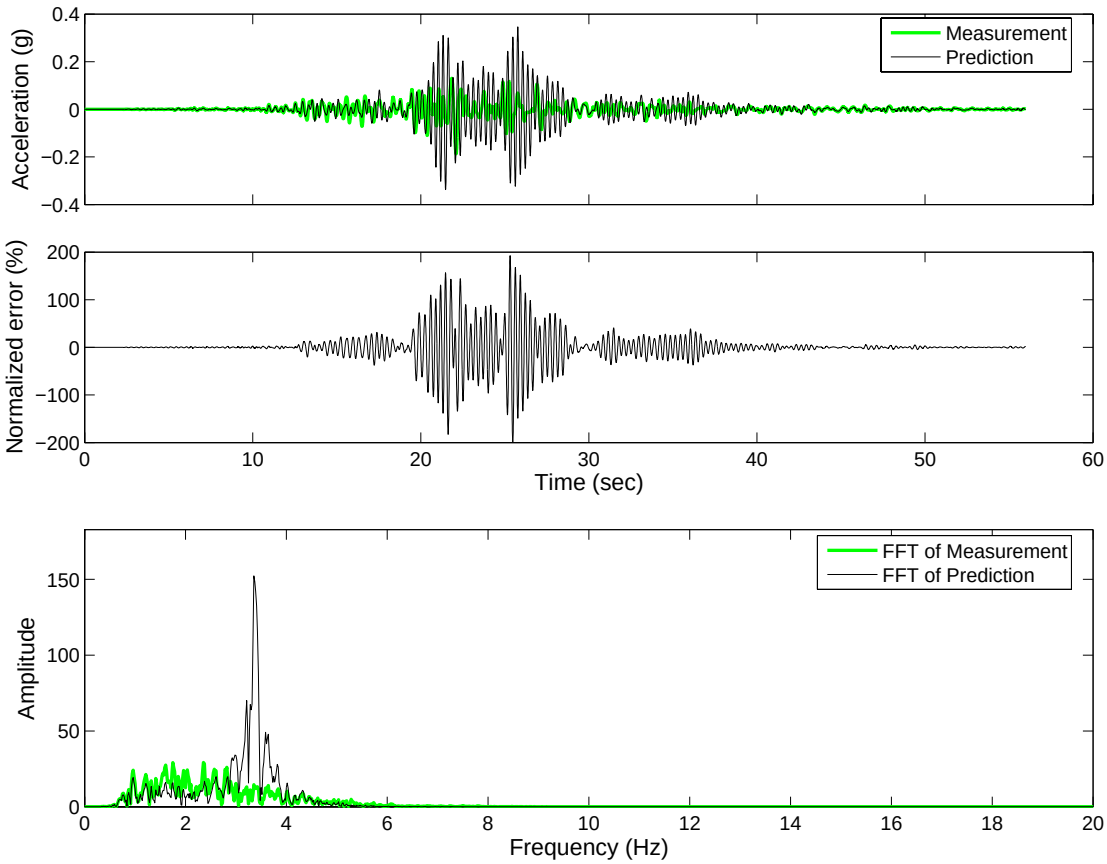


Fig. 2.16 Prediction of the ground surface response to earthquake 16.

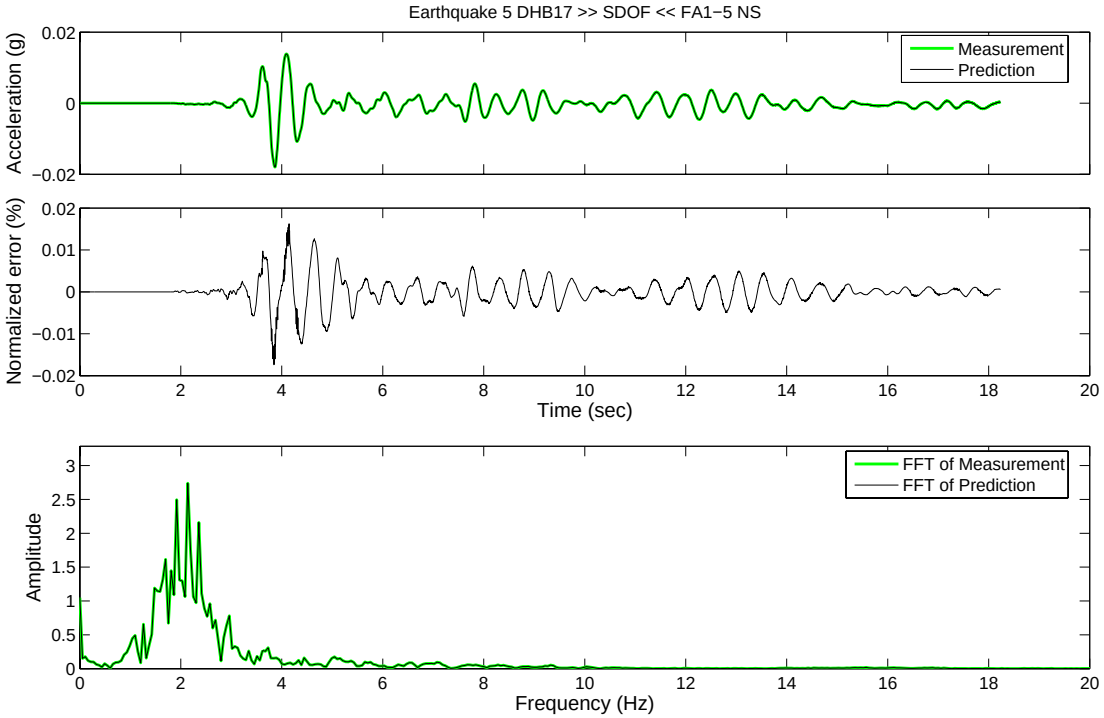


Fig. 2.17 Prediction of the intact SDOF system (scenario 2) response to earthquake 5.

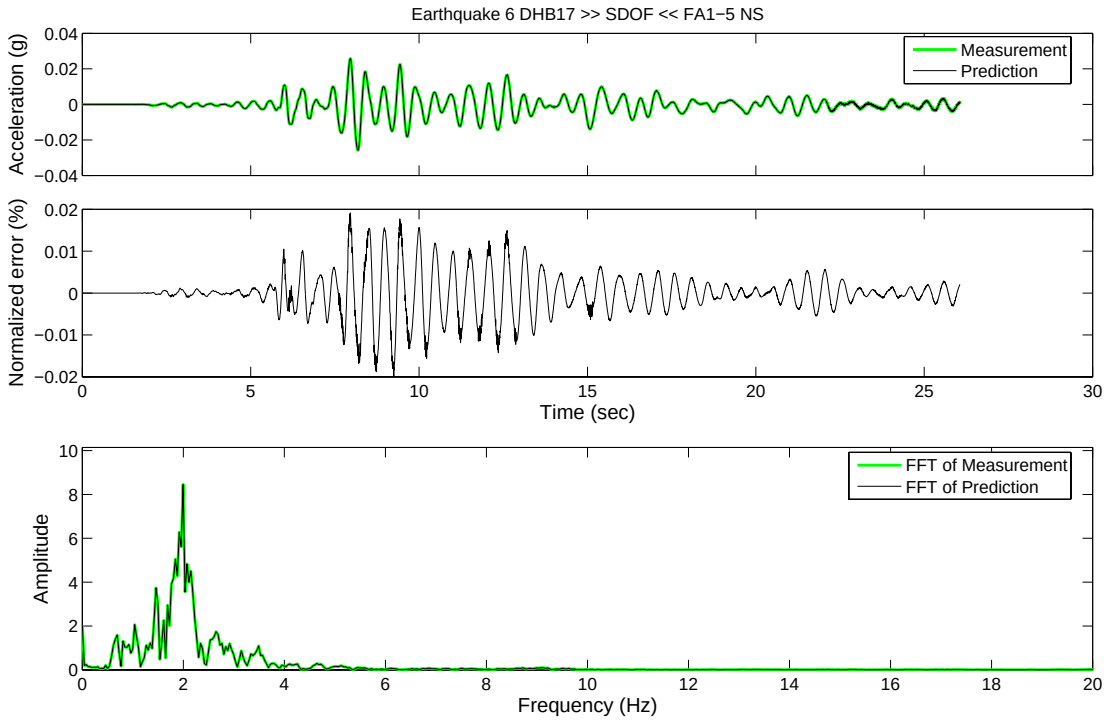


Fig. 2.18 Prediction of the intact SDOF system (scenario 2) response to earthquake 6.

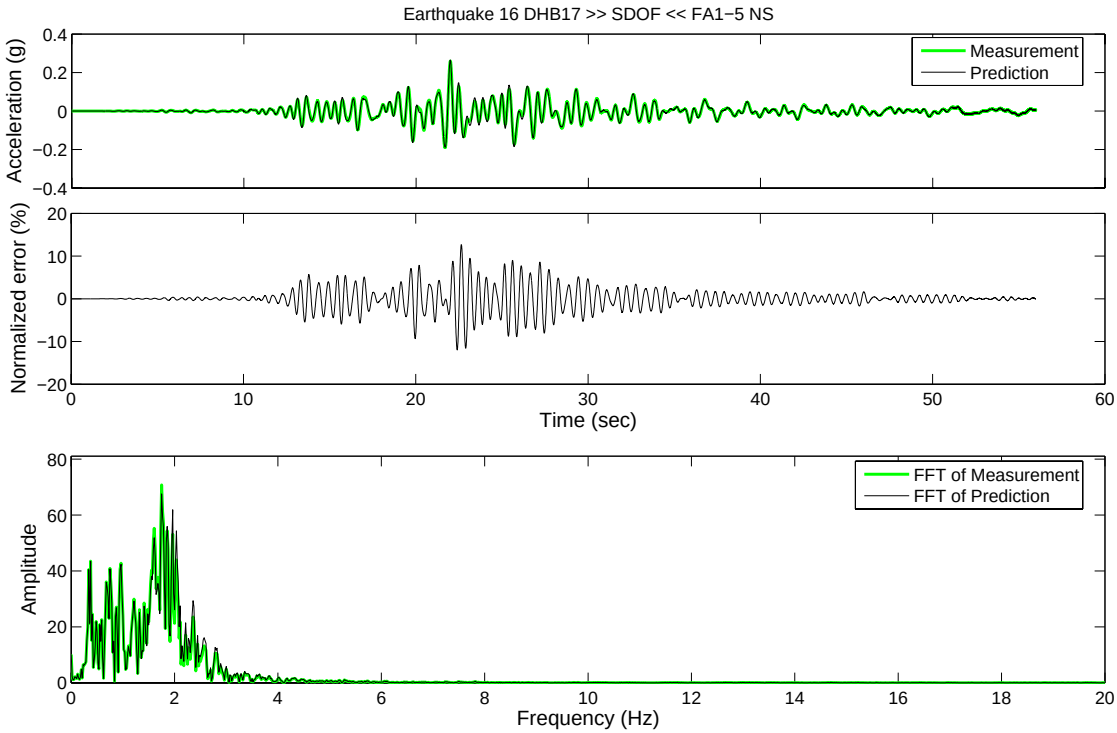


Fig. 2.19 Prediction of the damaged SDOF system (scenario 2) response to earthquake 16.

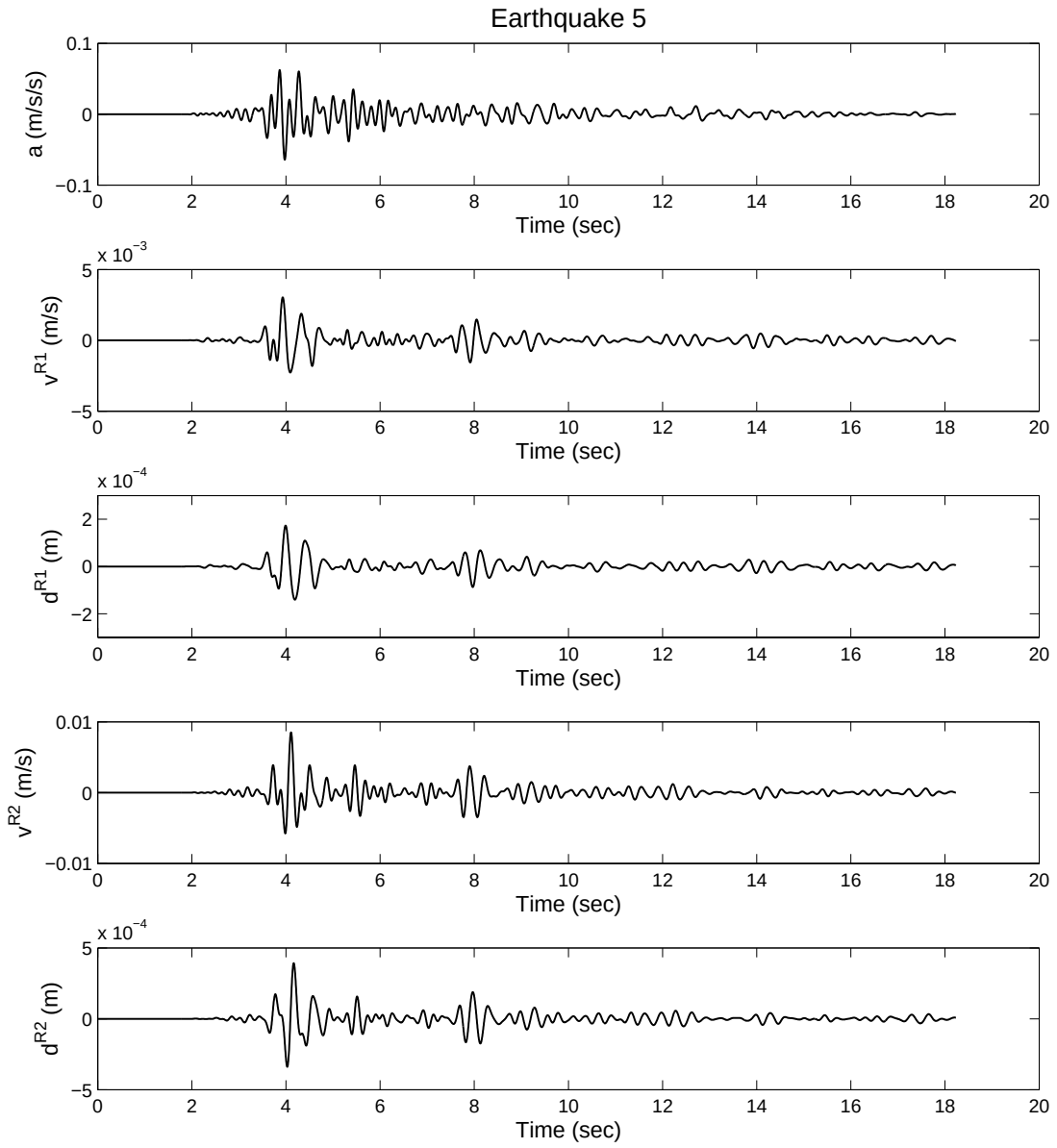


Fig. 2.20 a, v^{R1}, d^{R1}, v^{R2}, and d^{R2} time histories of the soil system between DHB-17 and FA1-5 for response to earthquake 5.

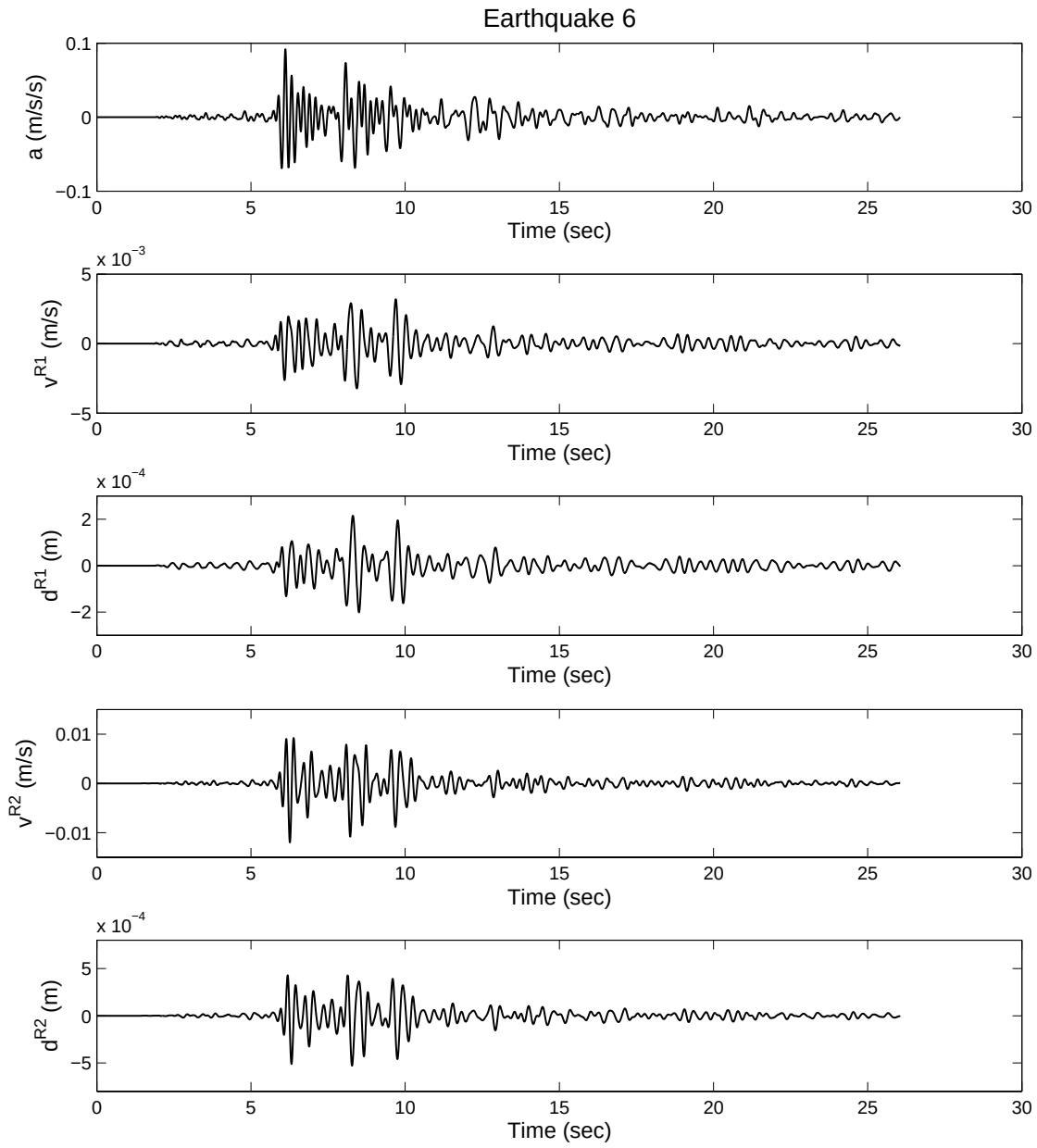


Fig. 2.21 a, v^{R1}, d^{R1}, v^{R2}, and d^{R2} time histories of the soil system between DHB-17 and FA1-5 for response to earthquake 6.

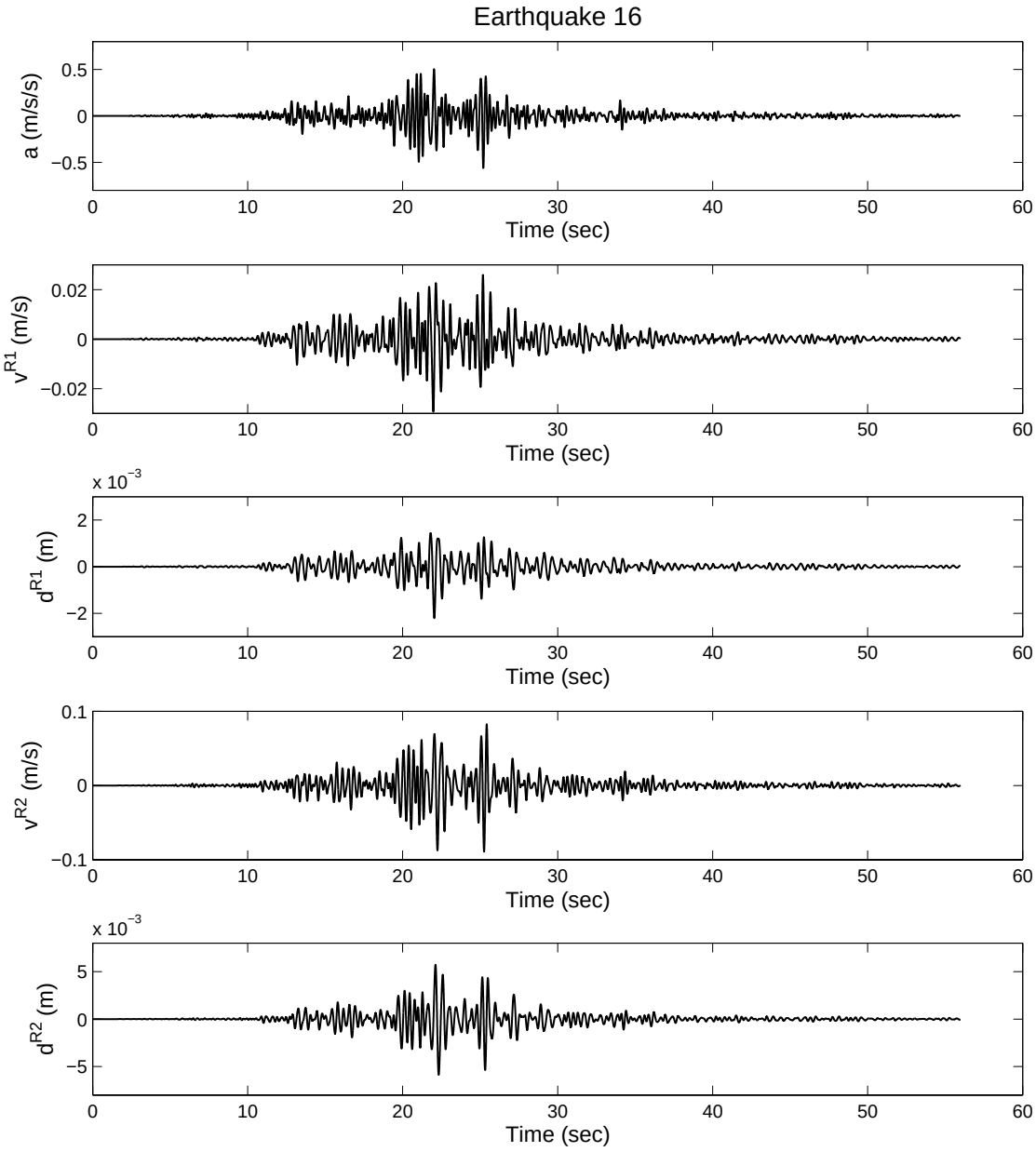


Fig. 2.22 a, v^{R1}, d^{R1}, v^{R2}, and d^{R2} time histories of the soil system between DHB-17 and FA1-5 for response to earthquake 16.

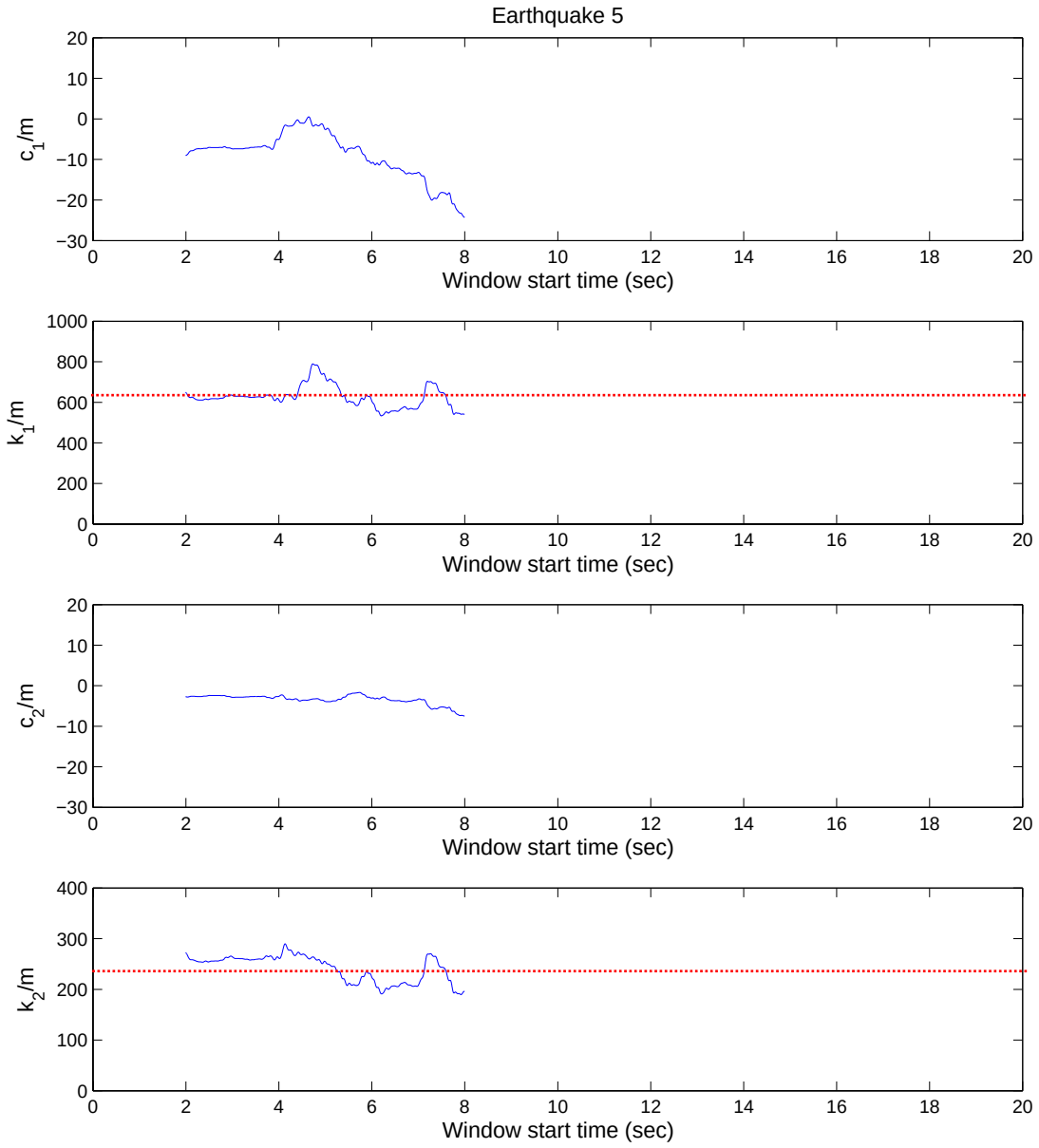


Fig. 2.23 Properties identification of the soil system between DHB-17 and FA1-5 using the analysis framework of scenario 2 and a moving time window of 2.5 second width, based on data of earthquake 5.

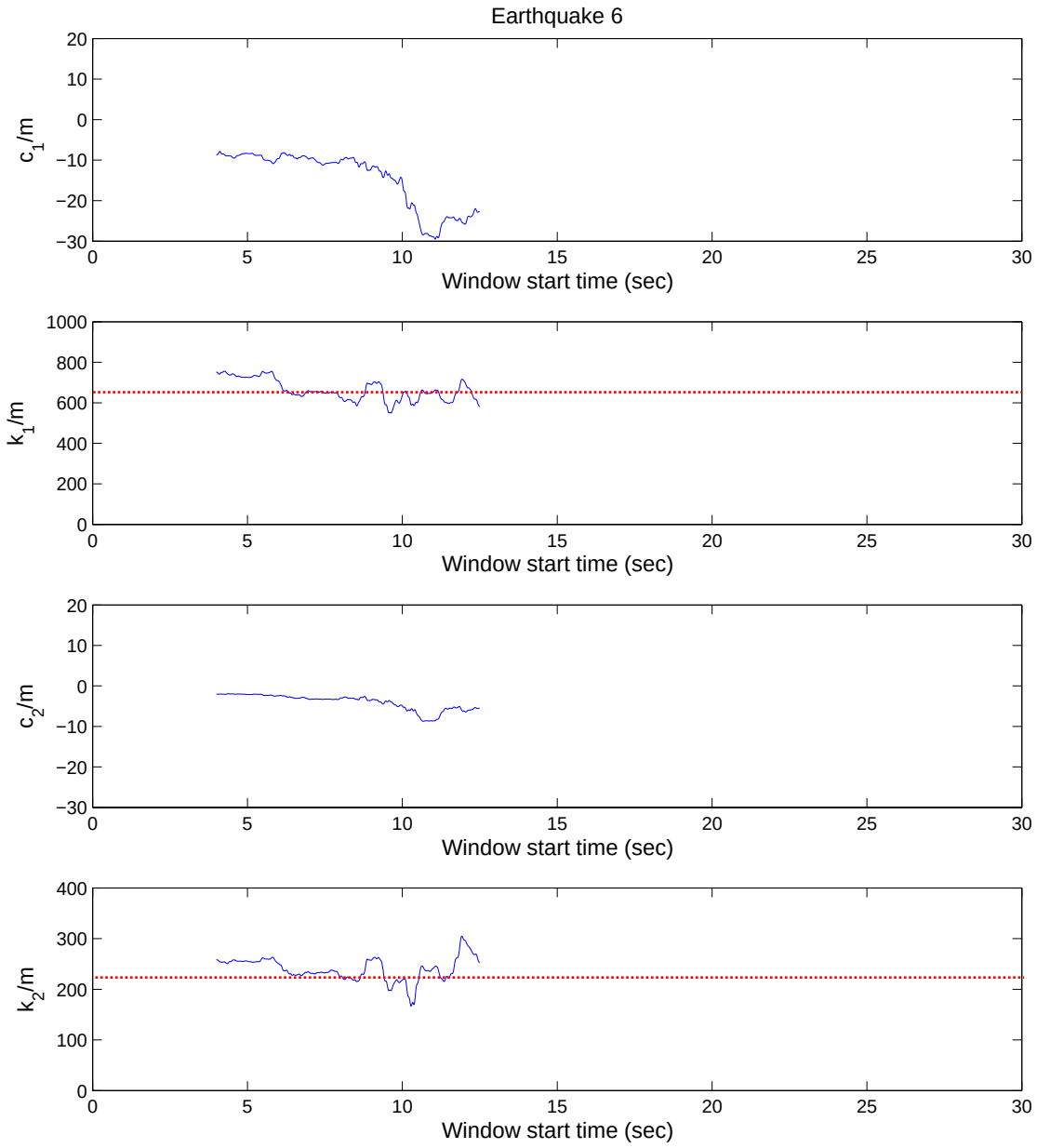


Fig. 2.24 Properties identification of the soil system between DHB-17 and FA1-5 using the analysis framework of scenario 2 and a moving time window of 2.5 second width, based on data of earthquake 6.

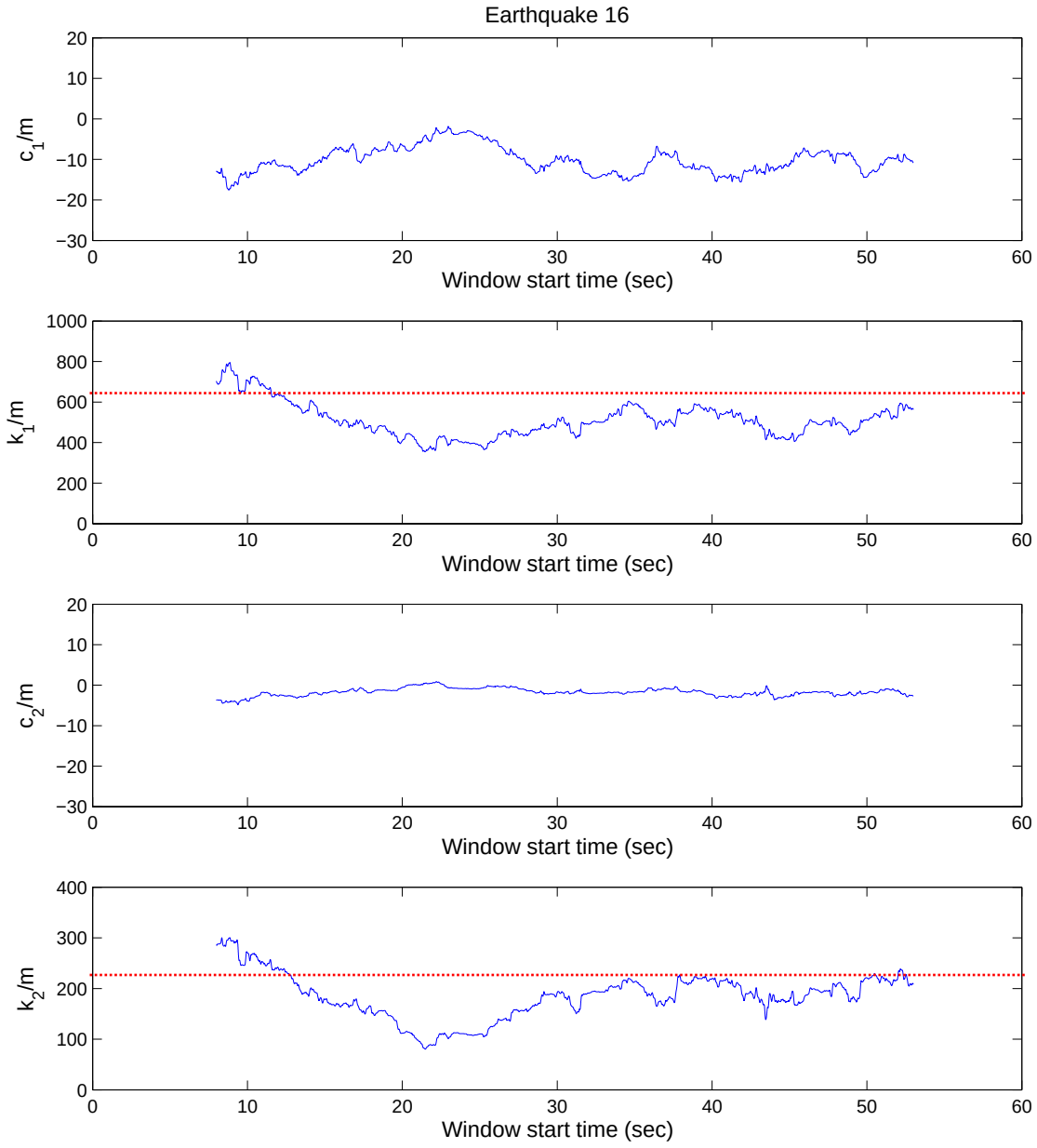


Fig. 2.25 Properties identification of the soil system between DHB-17 and FA1-5 using the analysis framework of scenario 2 and a moving time window of 2.5 second width, based on data of earthquake 16.

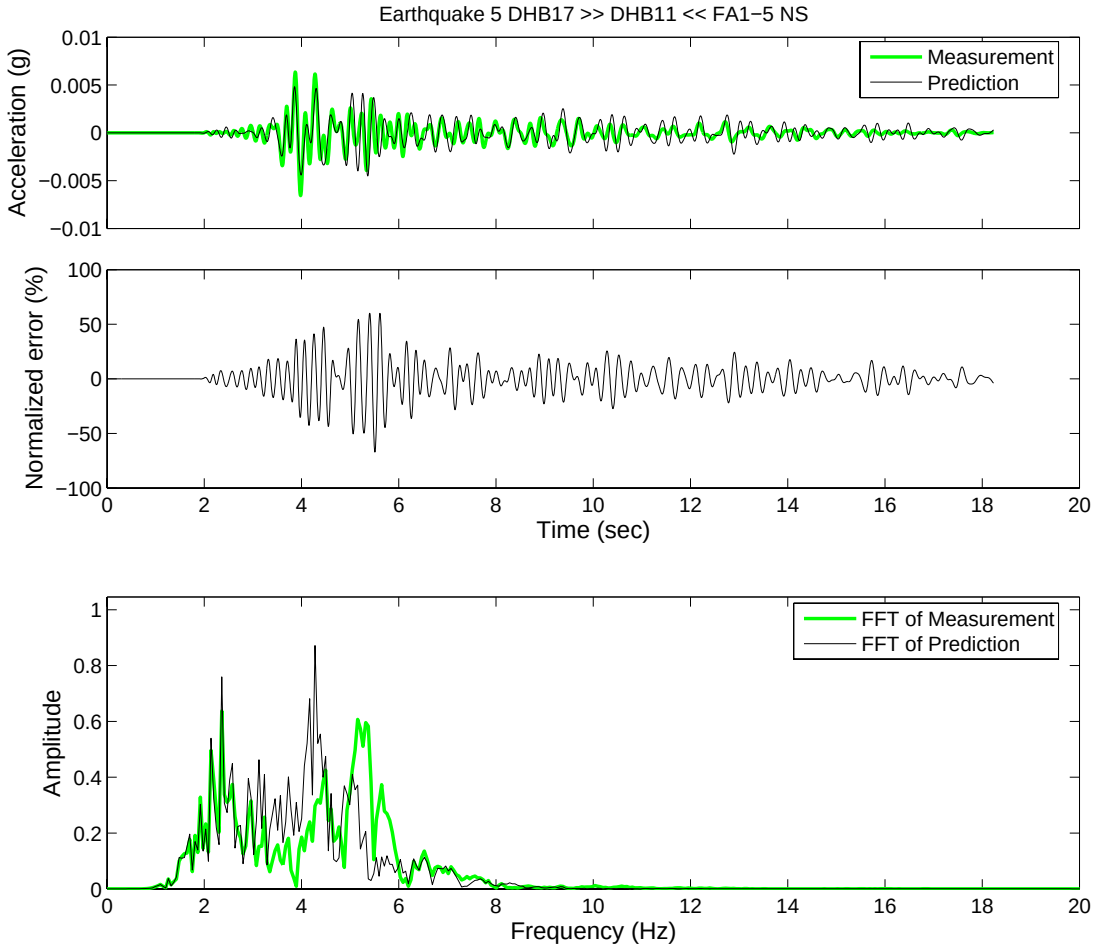


Fig. 2.26 Prediction of the ground response at the DHB-11 station to earthquake 5.

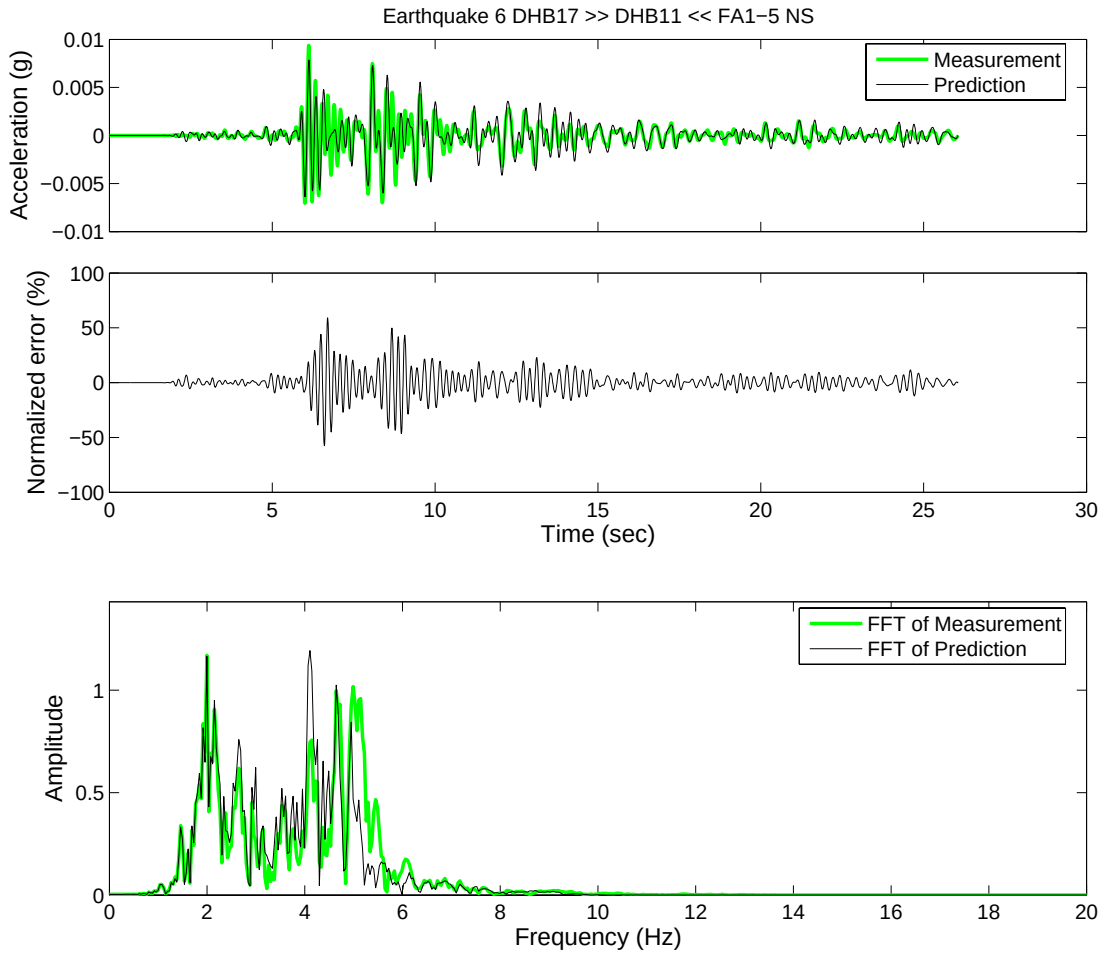


Fig. 2.27 Prediction of the ground response at the DHB-11 station to earthquake 6.

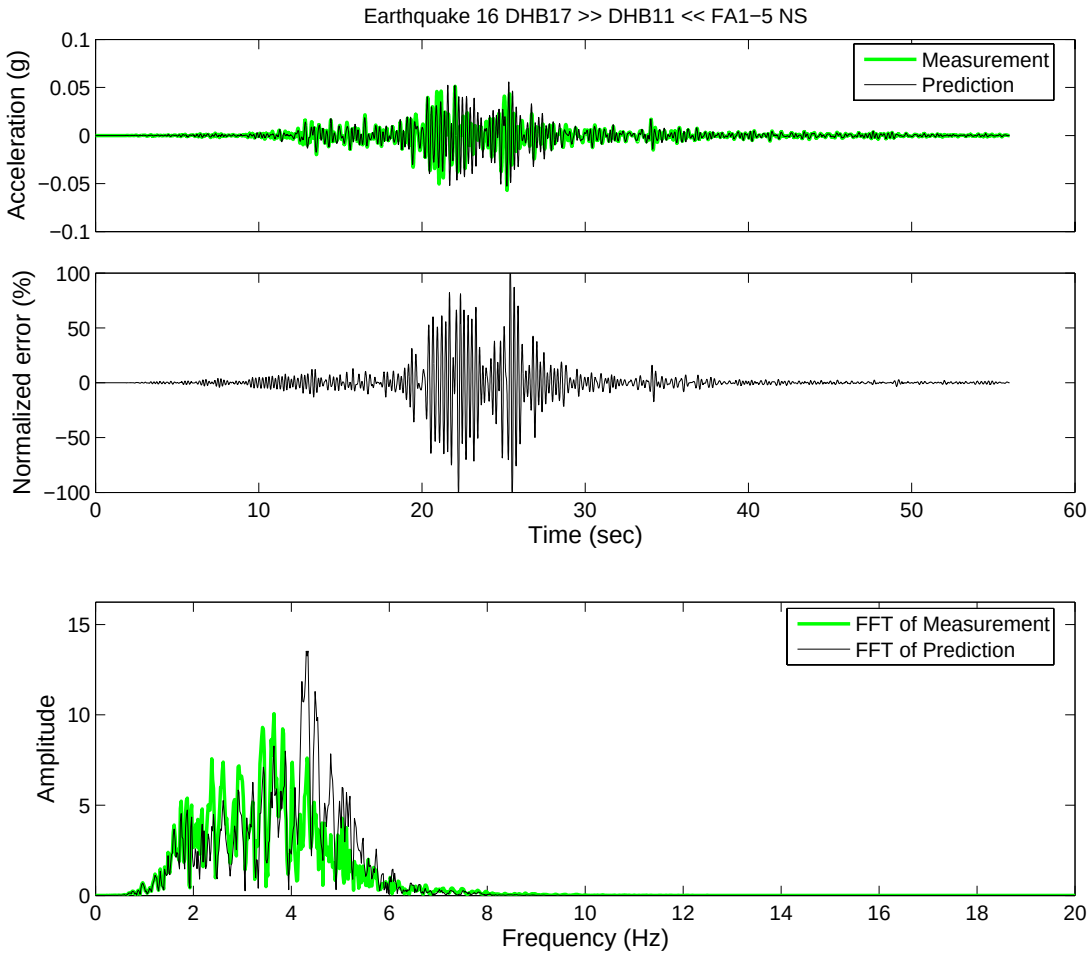


Fig. 2.28 Prediction of the ground response at the DHB-11 station to earthquake 16.

2.8 References

Elgamal, A., Zeghal, M., Tang, H. T., and Stepp, J. C. (1995). "Lotung Downhole Array. I: Evaluation of Site Dynamic Properties." *Journal of Geotechnical Engineering*, 121(4), 350-362.

Electric Power Research Institute (EPRI) (1993). "Guidelines for Determining Design Basis Ground Motions, Volume 1: Method and Guidelines for Estimating Earthquake Ground Motion in Eastern North America." *Rep. No. TR-102293*, Electric Power Research Institute, Palo Alto, CA.

Kramer, S. L. (1996). *Geotechnical Earthquake Engineering*, Prentice-Hall, Englewood Cliffs, New Jersey.

Newmark, N. M. (1959). "A Method of Computation for Structural Dynamics." *Journal of the Engineering Mechanics Division*, ASCE, 1959, 67-94.

Tang, H. (1987). "Large-Scale Soil Structure Interaction." *Rep. No. NP-5513-SR*, Electric Power Research Institute, Palo Alto, CA.

3 A STATISTICAL INFERENCE APPROACH FOR STRUCTURAL DAMAGE DETECTION USING NARX NEURAL NETWORKS

In this chapter, a statistical inference approach for structural damage detection using NARX (Nonlinear AutoRegressive with eXogenous inputs) neural networks (approach B in Chapter 1) is developed. Two applications of this approach based on experimental data are presented. In Section 3.1, vibration-based structural damage identification is briefly introduced, including the challenges and the motivation of this study. The analysis framework of this approach is then described, including detailed information on the NARX network configuration and training, and the procedure used to compute a damage indicator based on change in variance of the network prediction error. Finally, two demonstration applications are presented.

3.1 Introduction

Health monitoring (damage identification) of civil structures has received a growing level of interest from numerous research groups using a variety of analytical and experimental techniques (Chang 1997, 2005). Major efforts have been focused on exploring the potential of identification based on changes in vibration characteristics (Doebling et al. 1996; Sohn et al. 2003).

Although vibration-based damage identification methods have been in wide use for mechanical and aerospace structures, their applications for civil structures remain a challenge (Doebling et al. 1996; Farrar and Jauregui 1996; Farrar and Doebling 1997; Humar et al. 2003; Sohn et al. 2003). One major difficulty is that damage data of an actual civil structure is typically unavailable or scarce due to the

long and gradual degradation progress and the uniqueness of each individual civil structural system (including the site condition). Hence, many proposed approaches employ numerical models to simulate different potential damage states in order to generate necessary data. This necessities a sophisticated finite element model, which requires labor intensive tuning and results in significant uncertainties induced by user interaction and modeling errors (Sohn et al., 2001a). In view of this limitation, researchers also explore the potential of inferring damage from changes in modal parameters (or their derivatives), which are identified from measured dynamic response using modal analysis techniques. However, it was shown that damage in a large-scale civil structure, typically a local phenomenon, does not significantly influence the low-frequency system response, which is the predominant content measurable by current in-situ test techniques (Farrar and Jauregui 1996; Farrar and Doebling 1997; Humar et al. 2003; Sohn et al. 2003).

In view of aforementioned difficulties, significant research efforts have been directed to develop damage detection approaches that do not require numerical modeling or modal analysis. Recent studies show that a combination of time-series-prediction techniques and statistical inference methods is a promising solution (Masri et al. 1996; Nakamura et al. 1998; Sohn et al. 2001; Sohn and Farrar 2001). The basic idea is that for each structure/substructure of interest, a time-series-prediction model is first developed to predict measured system response at the baseline (intact) state. Thus, the system dynamic characteristics can be implicitly identified and represented by the model. Without significant change (damage) occurring in the structure, the prediction error of the model will remain a stable statistical distribution. Thus, change in the

prediction error distribution can be monitored, evaluated, and utilized as a sensitive damage indicator.

In this regard, different time-series-prediction techniques have been employed, including neural networks (e.g., Masri et al. 1996; Nakamura et al. 1998; Wu et al. 2002; Xu et al. 2003), AR-ARX models (e.g., Sohn et al. 2001; Sohn and Ferrar 2001; Sohn et al. 2003; Lei et al. 2003; Nair et al. 2003), and response surface models (e.g., Iwasaki et al. 2002, 2003; Casciati et al. 2003a, b, c). Among others, neural networks are a popular technique, providing strong capabilities for approximating continuous linear/nonlinear systems (Bishop 1995). For instance, Conte et al. (1994) successfully developed neural networks to learn and simulate the linear elastic dynamic behavior of multi-story buildings. Kao et al. (2003) used experimental data of a full scale 3-story 3-bay RCS frame to verify the feasibility of using neural networks to represent nonlinear system.

In this study, the NARX (Nonlinear AutoRegressive with eXogenous inputs) neural networks (Leonatris and Billings 1985; Chen and Billings 1989; Korbicz and Janczak 1996; Demuth and Beale 1998) are employed to predict structural response measured by a sensor from the measurements of neighboring sensors. Thereafter, a statistical inference procedure is developed to detect structural damage based on change in variance of the network prediction error.

3.2 Analysis Framework

The proposed damage detection approach assumes that the investigated structure may be monitored by a heterogeneous sensor array (e.g., accelerometers,

strain gages…). Within this context, the approach can be applied in the following steps (Fig. 3.1):

(1) Based on the spatial distribution of the sensors, substructures in the system of interest are defined. Each substructure includes a set of sensors, with a central sensor considered as the "master" and the neighboring sensor considered as "slaves".

(2) Using a selected external excitation (e.g., shaker-induced white-noise excitation), a dynamic test of the intact structure is performed and the system dynamic response is recorded. For each substructure, an associated NARX neural network (Korbicz and Janczak 1996; Demuth and Beale 1998) is developed to predict the measured response at the master senor from those of the slave sensors. Thus, the dynamic characteristics of the substructure is approximately and implicitly identified and represented by the associated network. Both the network configurations (weights and biases, Bishop 1995) and the time history of network prediction error are archived as a reference baseline state. Note that it is desirable to archive such data for different environmental and operational conditions in order to build a baseline database consisting of many reference states. For a laboratory experiment, one reference state may be sufficient as the environmental and operational conditions are relatively stable.

(3) Perform the same dynamic test periodically on the structure and record system response. For each test, a reference of the closest environmental and operational conditions is selected from the baseline state database (this is

skipped if there is only one reference). For each substructure, the archived network is employed to predict the dynamic response of the master sensor and a new time history of prediction error is obtained. Comparing this new time history with the archived baseline state, a damage indicator is computed based on changes in the variance.

(4) Integrate information from all computed indicators in order to infer the occurrence, location, and relative severity of damage in the structural system.

(5) If no damage is detected, return to step 3. Otherwise, a warning will be issued. In this case, further in-situ inspection is needed to unveil the actual situation and if necessary, the damaged structure must be retrofitted. Thereafter, return back to step 2 to update the baseline state database and continue the monitoring process.

3.3 NARX Neural Network

3.3.1 Network Configuration

As mentioned above, each substructure is monitored by a master sensor and several slave sensors (the number denoted by M). The structural response at the master sensor mainly depends on: (1) the dynamic characteristics of the substructure, and (2) the applied external excitation. Obviously, the structural response measured by the slave sensors also contains information about the external excitation. In this sense, the problem can be formulated as a MISO (Multiple Inputs, Single Output) nonlinear system. As such, the system can be defined by the following NARX model (Leonatris and Billings 1985; Chen and Billings 1989):

$$y(t) = f(\mathbf{x}(t)) \tag{3.1}$$

and

$$\begin{aligned}\mathbf{x}(t) &= [x_i(t)] \\ &= [y(t-n_y)\ldots y(t-1)\,u^1(t-n_u) \\ &\ldots u^1(t-1)\,u^1(t)\ldots u^M(t-n_u)\ldots u^M(t-1)\,u^M(t)]\end{aligned} \tag{3.2}$$

where $u^m(t)$ denotes the mth input (response measured by the mth slave sensor) at time step t, $y(t)$ denotes the output (response measured by the master sensor) at time step t, n_u and n_y are the input and output order, and f is a nonlinear function representing the system.

Herein, the function f is approximated by a Multi-Layer Perceptron (MLP) as Bishop (1995) shows that such networks, with sigmoidal activation functions, provide strong capabilities for representing continuous nonlinear systems. The resulting system is known as a NARX network (Korbicz and Janczak 1996; Demuth and Beale 1998), having one input layer of $M \times (n_u + 1) + n_y$ units, one hidden layer, and an output layer of single unit. The number of hidden units is set to the same number of input units, thereby ensuring adequate representation capability while controlling the network size.

The feed forward network mapping from the input vector $\mathbf{x}(t) = [x_i(t)]$ to the output $\hat{y}(t)$ is defined by

$$\hat{y}(t) = \sum_{j=1}^{M\times(n_u+1)+n_y} w_j^{(2)} g\left(\sum_{i=1}^{M\times(n_u+1)+n_y} w_{ji}^{(1)} x_i(t) + w_{j0}^{(1)}\right) + w_0^{(2)} \tag{3.3}$$

Here, $w_{ji}^{(1)}$ denotes weight going from input unit *i* to hidden unit *j*, $w_{j0}^{(1)}$ denotes bias for hidden unit *j*, $g(\cdot)$ denotes activation function for hidden units, $w_j^{(2)}$ denotes weight

going from hidden unit j to the single output unit, and $w_0^{(2)}$ denotes bias for the single output unit.

As shown, the output layer is linear, and a hyperbolic tanh is adopted as the activation function $g(\cdot)$ of hidden units defined by (LeCun et al. 1998)

$$g(a_j) = 1.7159 \tanh(2a_j / 3) \tag{3.4}$$

where $a_j = \sum_{i=1}^{M\times(n_u+1)+n_y} w_{ji}^{(1)} x_i(t) + w_{j0}^{(1)}$ is the weighted sum of inputs for hidden unit j.

3.3.2 Network Training

Prior to network training, the minimum-to-maximum range of measured response at each sensor is normalized to [-1, 1]. For each substructure, a sequence of input-output patterns $\{y(t) \quad \mathbf{x}(t)\}$ can then be sampled from these normalized time histories. These patterns are randomly partitioned into a training set (80% of the total patterns) and a validation set (20% of the total patterns). Based on the training set, the standard backpropagation algorithm is adopted for network training by minimizing the squared error between the network output $\hat{y}(t)$ and the corresponding target $y(t)$

$$E = \frac{1}{2}\sum_t [y(t) - \hat{y}(t)]^2 \tag{3.5}$$

In order to best utilize the knowledge contained in the data, the training set are repeatedly used with each training loop over all patterns defined as an epoch. After each epoch, the average errors of the training and validation sets are computed. The optimal network configuration is selected according to the minimum error of the validation set so as to avoid overfitting (Bishop 1995; Hastie et al. 2001).

3.4 Damage Indicator

After a NARX network is successfully trained, the dynamic characteristics of the corresponding substructure are implicitly represented by the network. Now, the trained network may be employed to predict the structural response under different states. Herein, the prediction error of the baseline state at time step t is denoted by $e(t)$, $t = 1,\ldots N_e$, where N_e is the time history length. Similarly, the prediction error of an investigated state at time step t is denoted by $\varepsilon(t)$, $t = 1,\ldots N_\varepsilon$, where N_ε is the time history length. Without significant change in the substructure (i.e., occurrence of damage), the trained network should deliver a consistent performance in prediction, and $e(t)$ and $\varepsilon(t)$ would be expected to follow similar statistical distributions. In other words, change in the statistical distribution of the prediction error can be utilized as a damage indicator.

As the prediction error generally follows a distribution with the mean value around zero, most efforts have been directed to assess changes in the variance (or standard deviation). For instance, Sohn and Farrar (2001) evaluated such change by the F test, which assumes that both $e(t)$ and $\varepsilon(t)$ follow normal distributions. However, this normality assumption is hard to justify in practice. In view of this fact, Sohn and Farrar (2001) suggested performing the F hypothesis test against a threshold value from a modified F distribution. Herein, this problem is addressed in an alternative way that weakens the strong normality requirement, only assuming that $e(t)$ and $\varepsilon(t)$ follow stable distributions. Based on this assumption, for each substructure, a damage indicator can be computed using the following steps:

(1) Reshuffle the time step order of the $e(t)$ and $\varepsilon(t)$ time histories in order to eliminate the correlation between neighboring prediction errors.

(2) Divide the reshuffled $e(t)$ and $\varepsilon(t)$ time histories into segments of equivalent lengths (the number of time steps in each segment is denoted by n, the number of $e(t)$ segments is denoted by $N_p = N_e / n$, and the number of $\varepsilon(t)$ segments is denoted by $N_q = N_\varepsilon / n$).

(3) Thus, for each segment, the sequence of prediction errors ($e(t)$ or $\varepsilon(t)$) is approximately independent and identically distributed, and their sum can be computed as $p = \sum_{t=1}^{n} e(t)$ and $q = \sum_{t=1}^{n} \varepsilon(t)$. According to the Central Limit Theory (Spiegel 1992), both p and q approach normal distributions for large n values (herein, $n = 20$ is used).

(4) Compute the damage indicator D as the sample variance ratio of p and q

$$D = \frac{\sigma^2(q)}{\sigma^2(p)} \tag{3.6}$$

Based on D, the similarity of $e(t)$ and $\varepsilon(t)$ can be indirectly evaluated by testing the null hypothesis H_0: $\sigma^2(q) = \sigma^2(p)$ against the one-side alternative H_1: $\sigma^2(q) > \sigma^2(p)$. It can be shown that D follows the F-distribution with $N_q - 1$ and $N_p - 1$ degrees-of-freedom under the null hypothesis (Miller 1997). Thus, given a confidence level α, the theoretical threshold value $F^{\alpha}_{N_q - 1, N_p - 1}$ can be found. If D exceeds this threshold, the null hypothesis H_0 is rejected, indicating a significant change in the substructure.

Note that the computation of D for each substructure only requires local information and inter-sensor data transmission within the substructure. This is desirable in practical implementation as it allows distributed or parallel computing and facilitates large-scale monitoring. In addition, although the computation of D is independent, the damage indicators can be compared to each other as long as the same α, N_p, and N_q are used. In addition, it is expected to see that a higher D indicates that the corresponding substructure has undergone a more significant change (damage) or that the substructure is closer to the damage location. Based on this rule, the location and relative severity of damage can be inferred by integrating information from all computed indicators.

3.5 Application Example 1: 8-DOF Mass-Spring System

3.5.1 Experimental Setup

An 8-DOF system has been designed and constructed for damage identification studies at the Los Alamos National Laboratory (Sohn and Farrar 2001). The system (Fig. 3.2) consists of eight translating masses (each is an aluminum disk 25.4mm thick and 76.2mm in diameter with a central hole) connected by springs. All masses slide on a highly polished steel rod that limits movement to translation along the rod (Fig. 3.2). The DOFs, springs, and masses are numbered from the right end to the left end (Fig. 3.2). The nominal value of mass 1 is 559.3g, and the nominal value for masses 2-8 is 419.4g. Using a 215N peak force electro-dynamic shaker, random excitation was applied to mass 1 and recorded by a force transducer. The system response was recorded by 8 accelerometers, each mounted on the mass of the same number (Fig.

3.2). More detailed information on the experimental setup, shaker, and data acquisition is described in Sohn and Farrar (2001).

Using this setup, a series of experiments (303 in total) was conducted, encompassing scenarios of linear/nonlinear damage of different severities occurring at different locations between adjacent masses. The undamaged configuration of the system is the state with an identical linear spring constant (56.7kN/m) for all springs.

Linear damage is defined as a change in the system stiffness characteristics and simulated by replacing an original spring with another of lower stiffness. The severity of linear damage is controlled by the percentage reduction in the spring constant. Nonlinear damage is defined as an occurrence of impact between two neighboring masses, simulating the impact from closing of a crack during vibration. Fig. 3.3 shows that the nonlinear damage is induced by placing a bumper between two neighboring masses so that the motion of a mass is limited relative to its neighbor. The impact occurs when the bumper mounted on one mass hits the other mass, and the degree of damage is controlled by the amount of relative motion allowed before the impact (defined as the initial clearance).

In the following section, the results of ten representative experimental scenarios as summarized in Table 3.1 are presented, and similar results are obtained for all others. In these experiments, random excitations were generated by the shaker with the root mean square (RMS) amplitude level of input being 5V. Each recorded time history was sampled at 500Hz and consisted of 4096 points.

3.5.2 Application

Following the proposed approach (Fig. 3.1), sensors in the system are first numbered as shown in Table 3.2, and eight substructures are then defined as shown in Fig. 3.2 and Table 3.3. Herein, scenario 1 is employed as the baseline state to develop a NARX network for each substructure for identification purposes. Thereafter, these networks are applied to scenarios 2-10 for damage inference purposes. The related parameters of this application are summarized in Table 3.4.

For each substructure, the associated network is employed to predict the structural response measured by the master sensor. Fig. 3.5 shows the comparison of network predictions and corresponding sensor measurements of structural response at the baseline state, along with the residual errors. It is seen that the prediction of each network closely matches the corresponding sensor measurement throughout all time histories. Thus, it can be concluded that the dynamic properties of each substructure at the baseline state has been properly identified and represented by the associated NARX network.

The residual prediction error ($e(t)$ or $\varepsilon(t)$) time history is then generated (Fig. 3.5) for each substructure/sensor and scenario. In addition, the time step order in each time history is randomly reshuffled such that the values of neighboring steps are independent. For instance, the results related to substructure/sensor 1 at the baseline state are presented in Fig. 3.6, showing that the residual prediction errors of two successive steps are weakly correlated after reshuffling.

Each reshuffled $e(t)$ or $\varepsilon(t)$ time history is divided into segments of equivalent length ($n = 20$), and the sum of each segment (p_i or q_j) is computed (expected to follow a normal distribution). For instance, Fig. 3.7 shows the comparison of the histogram of p of substructure/sensor 1 at the baseline state and the theoretical normal distribution with the same mean value and standard deviation, showing a satisfactory match.

If the dynamic properties of a substructure undergo no significant change, q is expected to have the same distribution as p . For instance, the results related to substructure/sensor 7 for scenarios 1, 2, 8, 9 and 10 (Table 3.1) are shown in Fig. 3.8. It is seen that for scenario 2 with no damage, q depicts a close distribution to p , that of the baseline (scenario 1). As to scenarios 8-10 with damage in substructure 7, the distributions of q are significantly different from p . In addition, the difference increases with the severity of damage, particularly in the variance of distribution.

Based on p and q , the damage indicator D is computed for each substructure using Eq. 3.6. Fig. 3.9 shows the results for scenarios 2-10. In each subplot, the horizontal axis is the substructure ID, and the vertical axis is damage indicator. In addition, log scale is employed for the vertical axis in order to emphasize changes within the relatively low value range, around the threshold line.

It is seen that for scenario 2 without damage, the eight computed damage indicators are all below the threshold, indicating no damage. As to scenarios 3-10 with linear/nonlinear damage, each displays computed damage indicators exceeding the

threshold. In other words, the occurrences of damage in these scenarios are all successfully detected.

In addition, the location of damage can be inferred by integrating information from all damage indicators. For instance, scenario 3 corresponds to linear damage between masses 1 and 2 (spring 1). Fig. 3.9 shows the damage indicators for substructures 1 and 2 exceeding the threshold and significantly larger than the others. According to their configurations (Table 3.3), both substructures 1 and 2 include spring 1. Hence, it can be concluded that spring 1 has undergone damage. In addition, it can be inferred that spring 2 has no damage since the damage indicator for substructure 3, which includes spring 2, is lower than the threshold.

Similarly, damage locations in scenarios 4-10 can all be successfully inferred based on the computed damage indicators. Note that when damage is significant (e.g., scenarios 4-9 in this application), substructures without damage may also display damage indicators exceeding the threshold. However, the largest damage indicators are still associated with those substructures with damage, denoting its location.

Finally, scenarios 8-10 represent nonlinear damage at the same location (Table 3.1) with different severity, and the substructures including damage are 7 and 8. Comparing the results (Fig. 3.9), it is seen that higher level damage (i.e., smaller initial clearance, Table 3.1) corresponds to larger damage indicators. In other words, the relative severity of damage can be inferred from the relative magnitude of the damage indicator.

3.6 Application Example 2: 3-Story Frame Structure

3.6.1 Experimental Setup

A three-story frame structure model as shown in Fig. 3.10 was built at the Los Alamos National Laboratory for structural health monitoring problem studies (Sohn et al. 2003). The structure was constructed of Unistrut columns and aluminum floor plates (Fig. 3.10a). The floors are 0.5in thick plate with two-bolt connections to baskets on the columns (Figs. 3.10b, c), and the base is a 1.5in thick plate with support brackets to hold the columns (Fig. 3.10a). For each floor/base plate, the four corners are numbered from A to D as shown in Fig. 3.10b. The structure sits on four air mount isolators in order to allow free horizontal movements (Fig. 3.10a). In addition, a shaker was coupled to the structure by a 6in long stinger connected to a tapped hole close to corner D of the base plate (3.75in away, Fig. 3.10d) so that both translational and torsional motions can be excited.

In this experiment, damage was simulated in the floor-column joints (Figs. 3.10b, c) through the loosening of the preload applied by the bolts at the joints. The joints are named by the floor number and the corner label. For instance, 1A indicates that the joint is located at the corner A of floor 1. All bolted connections are tightened to a torque value of 60in.lbs in the undamaged state.

Using this setup, a series of experiments (270 in total) has been conducted in 2000, encompassing scenarios of damage of different severities occurring at single/multiple locations. In the following section, the results of ten representative experimental scenarios as summarized in Table 3.5 are presented, and similar results are obtained for all others. It is seen that scenarios 1-3 display no damage, scenarios 4-

7 represent a single damage location at corner 1C or 3A, and scenarios 8-10 correspond to two damage locations at both corners 1C and 3A. Three levels of joint damage are included in these scenarios: level 1 (D10, a torque value of 10in.lbs is left on the bolt), level 2 (D05, a torque value of 5in.lbs is left on the bolt), and level 3 (DBB, the bolt is removed). Obviously, the severity of damage increases with the level number.

For each scenario, a dynamic test of the structure was performed. The RMS voltage of the shaker was 8V, and random excitations were generated. The structural response in the shaking direction was measured by 24 piezo-electric single-axis accelerometers, each mounted on an aluminum block that is attached to the structure by hot glue. Two accelerometers were placed at each joint with one attached to the floor and the other attached to the column (Fig. 3.9b). Each recorded time history was sampled at 1600Hz and consisted of 8192 points. More detailed information on this experiment is described in Sohn et al. (2003).

3.6.2 Application

For this application, the substructures of interest are the twelve floor-column joints. As each joint is monitored by a pair of accelerometers, a NARX network is developed to predict the structural response at the floor sensor (i.e., the master) based on the measurements of the column sensor (i.e., the slave). Herein, scenario 1 is employed as the baseline state to train the networks for identification purposes. Thereafter, these networks are applied to scenarios 2-10 for damage inference purposes. The related parameters of this application are summarized in Table 3.6.

Fig. 3.11 presents the comparison of each sensor measurement and the corresponding network prediction of the structural response at the baseline state, showing a satisfactory match. Thus, it can be concluded that the dynamic properties of each "healthy" joint has been properly identified and represented by the corresponding NARX network.

Fig. 3.12 shows the damage identification results for scenarios 2-10 (Table 3.5). In each subplot, the horizontal axis is the joint ID, and the vertical axis is damage indicator (D , Eq. 3.6). It is seen that for scenarios 2-4 without damage, the computed damage indicators are all below the threshold, indicating no damage in the system. As to scenarios 5-10 with damage, each displays computed damage indicators exceeding the threshold, i.e., the occurrences of damage are all successfully detected.

In addition, it is seen that the damage locations can also be identified based on the computed damage indicators. For scenario 5, as the damage level is low (Table 3.5), only the prediction of the network associated with the damaged joint is affected. Thus, scenario 5 only shows the damage indicator of joint 1C significantly exceeding the threshold (Fig. 3.12), obviously indicating damage occurring at that joint. However, damage of high severity may have an impact in a wider range. For instance, for scenario 6, the more severe damage in joint 1C affects all joints in the first floor such that the damage indicators are all above the threshold. As to scenario 7, since joint 1C undergoes even more severe damage, the impact is system-wide. However, for both scenarios 6 and 7, the damage indicator of joint 1C is significantly higher than all others. Based on this, the location of damage can be identified. Similarly, the damage

locations can be identified for scenarios 8-10 no matter damage is at a single location or more.

Finally, comparing the results of scenarios 5-7 (Fig. 3.12), it is seen that the damage indicator of 1C increases with the level of damage (Table 3.5). In other words, the relative severity of damage can be inferred from the relative magnitude of the damage indicator.

3.7 Summary and Conclusions

In this paper, a structural damage detection approach based on NARX neural networks and statistical inference techniques is proposed. Within this framework, each substructure in a system of interest is monitored by a set of neighboring sensors. A major sensor is selected and an associated NARX network is developed to predict the structural response at this sensor from those measured by the remaining sensors. It is assumed that without significant change in the substructure, the network prediction error should follow a stable statistical distribution. Thus, change in the prediction error variance is evaluated by the modified F test and utilized as a damage indicator.

In order to verify the applicability, this approach is applied to data from two laboratory experiments, an 8-DOF mass-spring system with linear/nonlinear damage and a 3-story frame structure with damage at single or two floor-column joints. Satisfactory results are achieved, showing that: (1) for each substructure, the structural response at the master sensor can be accurately predicted using the trained associated NARX network, (2) the damage indicator is very sensitive and is able to detect the occurrence of damage in an early stage, (3) the damage locations (one or multiple) can also be inferred by integrating information of all computed damage indicators, and (4)

the relative magnitudes of the computed indicators provide information on the relative severities of damage.

3.8 Acknowledgements

Support for this research was provided by the U.S. National Science Foundation, under ITR Grant No. 0205720. This support is gratefully acknowledged. The authors also wish to thank the California Institute for Telecommunications and Information Technology (UCSD Calit2, http://www.calit2.net) for providing fellowship support to this project. Finally, the experimental data studied in this paper were provided by Dr. Francois Hemez and Dr. Charles Farrar at the Los Alamos National Laboratory and Professor Hoon Sohn at the Carnegie Mellon University. This help is most valuable and highly appreciated.

3.9 Tables

Table 3.1 Basic Information on the Ten Experimental Scenarios of the 8-DOF System

Scenario No.	Occurrence of damage	Damage location[1]	Damage type	Stiffness reduction for linear damage (%)	Initial clearance for nonlinear damage (mm)
1	No	-	-	-	-
2	No	-	-	-	-
3	Yes	12	Linear	24	-
4	Yes	56	Linear	24	-
5	Yes	78	Linear	24	-
6	Yes	12	Nonlinear	-	0
7	Yes	56	Nonlinear	-	0
8	Yes	78	Nonlinear	-	0
9	Yes	78	Nonlinear	-	0.2
10	Yes	78	Nonlinear	-	0.4

Note: 1. The damage location is indicated by the IDs of the adjacent masses. For instance, 56 indicates the location is between masses 5 and 6 (Figs. 3.2-4).

Table 3.2 Numbering of Sensors

Sensor ID	Sensor location	Sensor type
0	Mass 1	Force transducer
1	Mass 1	Accelerometer
2	Mass 2	Accelerometer
3	Mass 3	Accelerometer
4	Mass 4	Accelerometer
5	Mass 5	Accelerometer
6	Mass 6	Accelerometer
7	Mass 7	Accelerometer
8	Mass 8	Accelerometer

Table 3.3 Definition of substructures in the 8-DOF System

Substructure ID	Master sensor	Slave sensors
1	1	0, 2
2	2	1, 3
3	3	2, 4
4	4	3, 5
5	5	4, 6
6	6	5, 7
7	7	6, 8
8	8	7

Table 3.4 Parameters of the 8-DOF System Application

Parameter	Value
Number of time steps in each record	4096
Input order of NARX model, n_u	20
Output order of NARX model, n_y	20
Number of network training epochs	50
Length of $e(t)$, N_e	4076
Length of $\varepsilon(t)$, N_ε	4076
Length of each divided segment, n	20
Segment number for $e(t)$, N_p	203
Segment number for $\varepsilon(t)$, N_q	203
Confidence level, α (%)	99

Table 3.5 Information on the Ten Experimental Scenarios of the 3-Story Frame

Scenario No.	Occurrence of damage	Damage location	Damage level
1	No	-	-
2	No	-	-
3	No	-	-
4	No	-	-
5	Yes	1C	D10
6	Yes	1C	D05
7	Yes	1C	DBB
8	Yes	3A	DBB
9	Yes	1C/3A	DBB/DBB
10	Yes	1C/3A	DBB/DBB

Table 3.6 Parameters of the 3-Story Frame Structure Application

Parameter	Value
Number of time steps in each record	8192
Input order of NARX model, n_u	20
Output order of NARX model, n_y	20
Number of network training epochs	50
Length of $e(t)$, N_e	8172
Length of $\varepsilon(t)$, N_ε	8172
Length of each divided segment, n	20
Segment number for $e(t)$, N_p	408
Segment number for $\varepsilon(t)$, N_q	408
Confidence level, α (%)	99

3.10 Figures

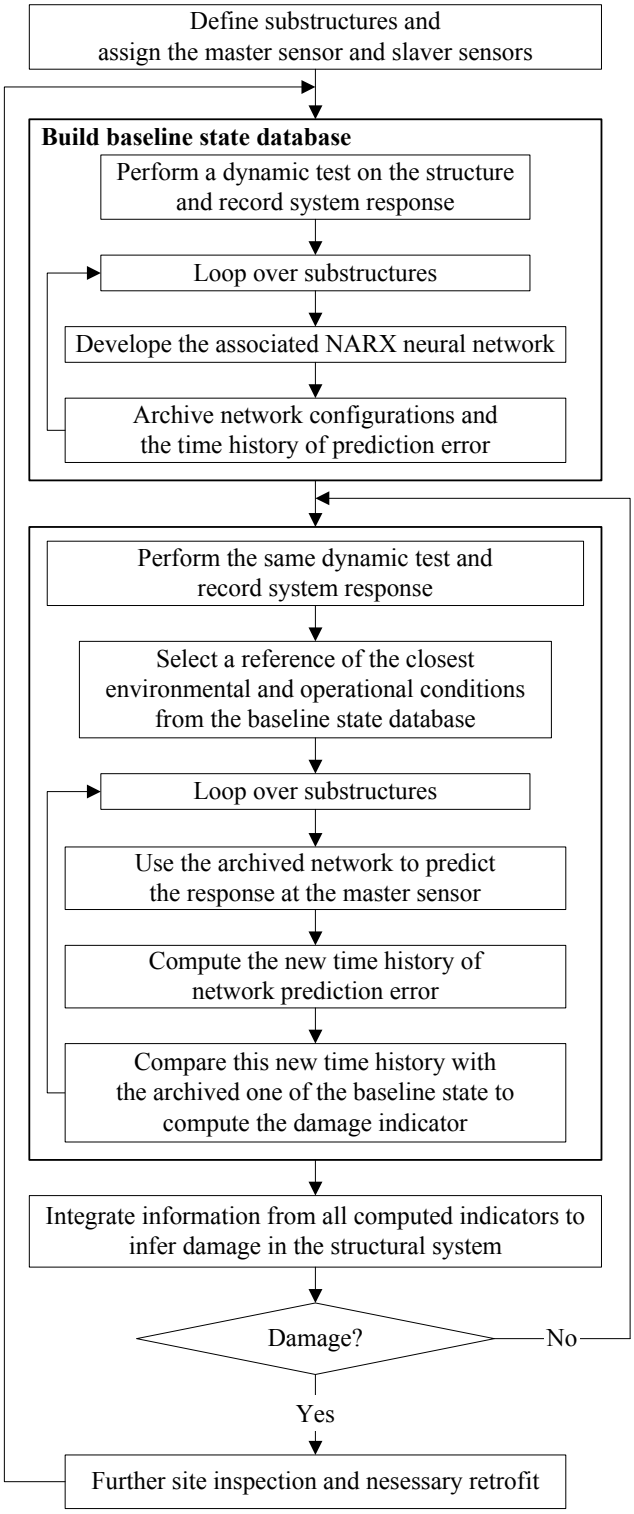


Fig. 3.1 Analysis Framework.

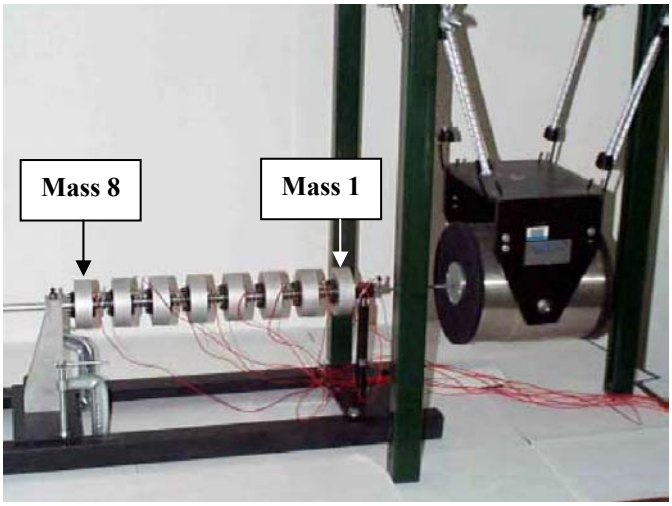


Fig. 3.2 An 8-DOF mass-spring system attached to a shaker with accelerometers mounted on each mass (Sohn and Farrar 2001).

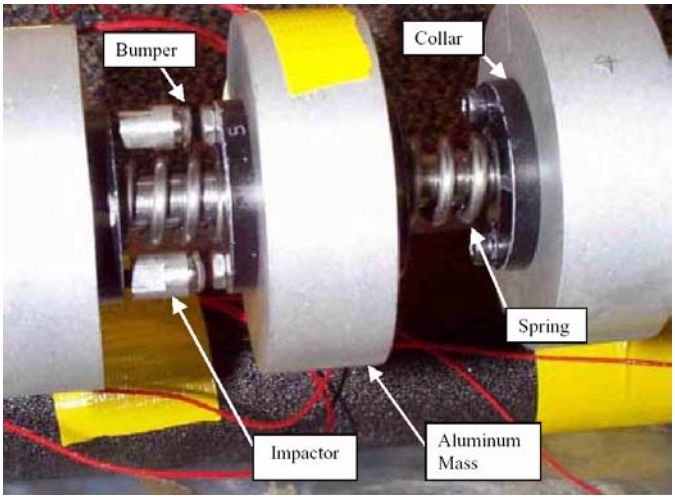


Fig. 3.3 A typical bumper used to simulate nonlinear damage (Sohn and Farrar 2001).

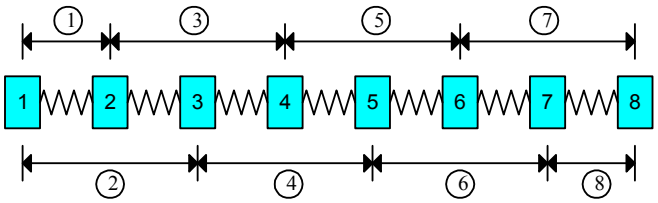


Fig. 3.4 Substructures defined in the 8-DOF system and labeled by the numbers in circles.

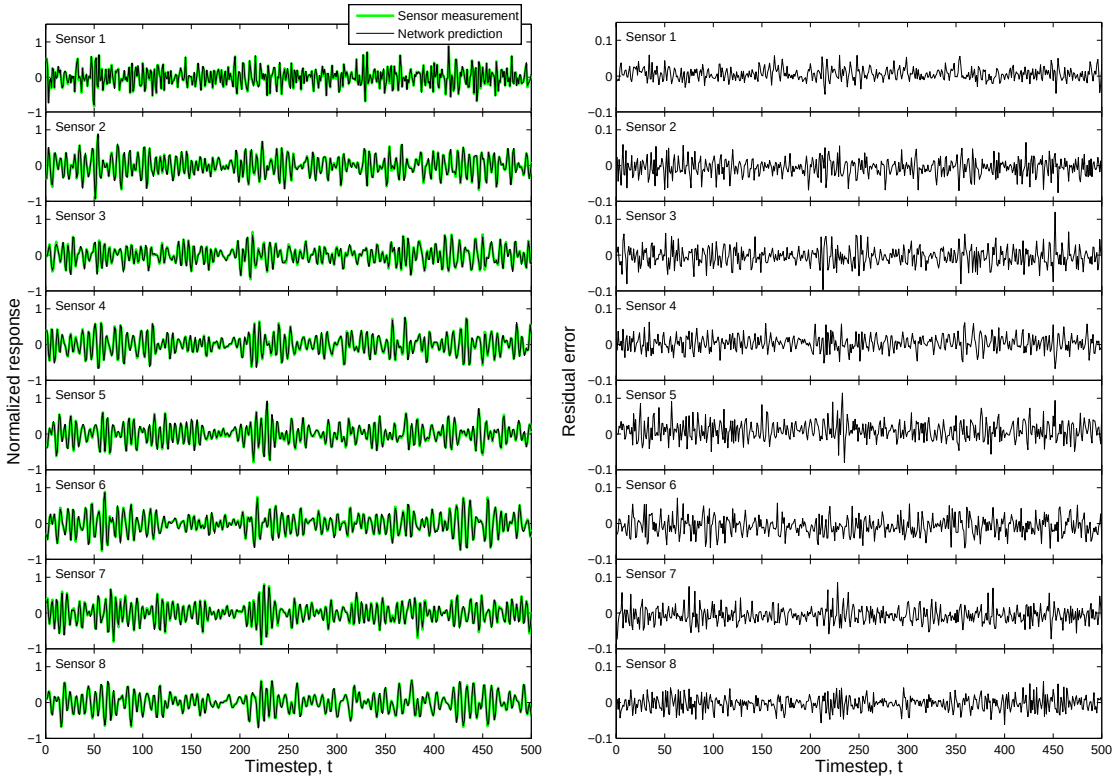


Fig. 3.5 Comparison of network predictions and corresponding sensor measurements of structural response of the 8-DOF mass-spring system at the baseline state, along with the residual errors.

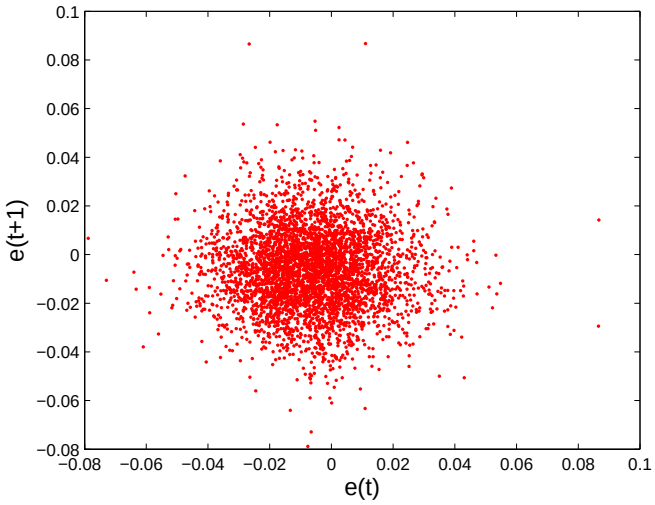


Fig. 3.6 Neighboring prediction errors display very weak correlation after the time step order is randomly reshuffled (substructure/sensor 1 at the baseline state).

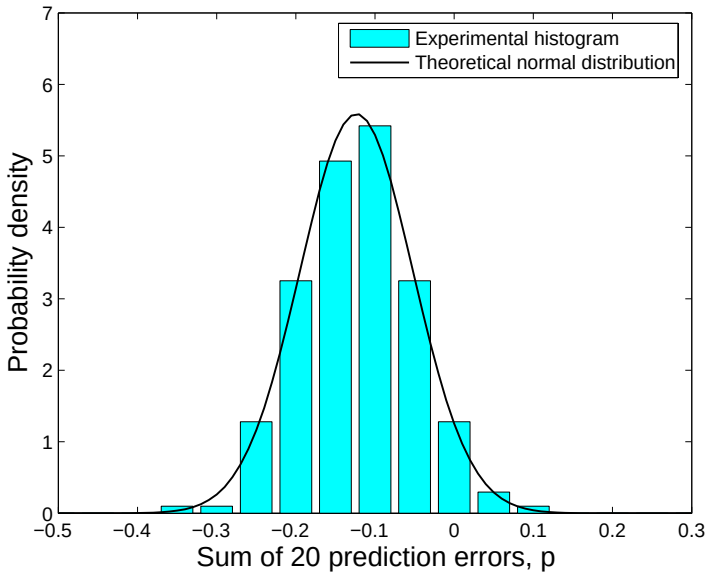


Fig. 3.7 Comparison of the histogram of p and the theoretical normal distribution with the same mean value and standard deviation, for substructure/sensor 1 at the baseline state.

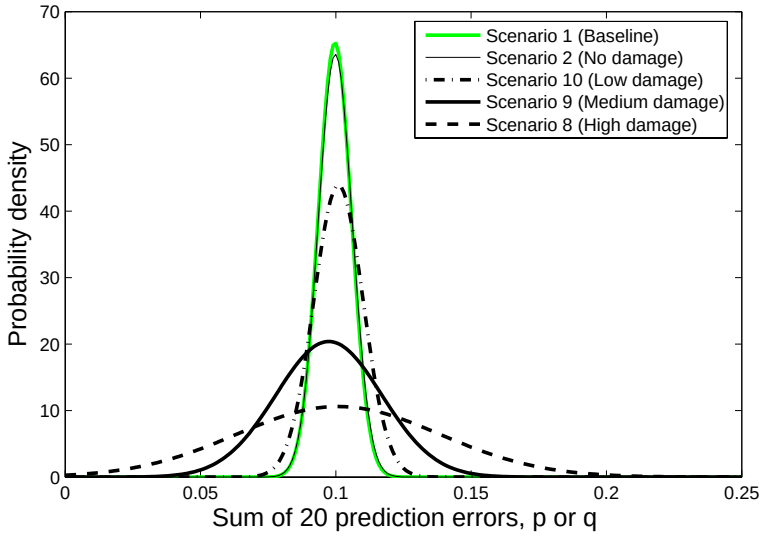


Fig. 3.8 Distributions of p at the baseline state (scenario 1) and q at scenarios 2, 8, 9, and 10, for substructure 7.

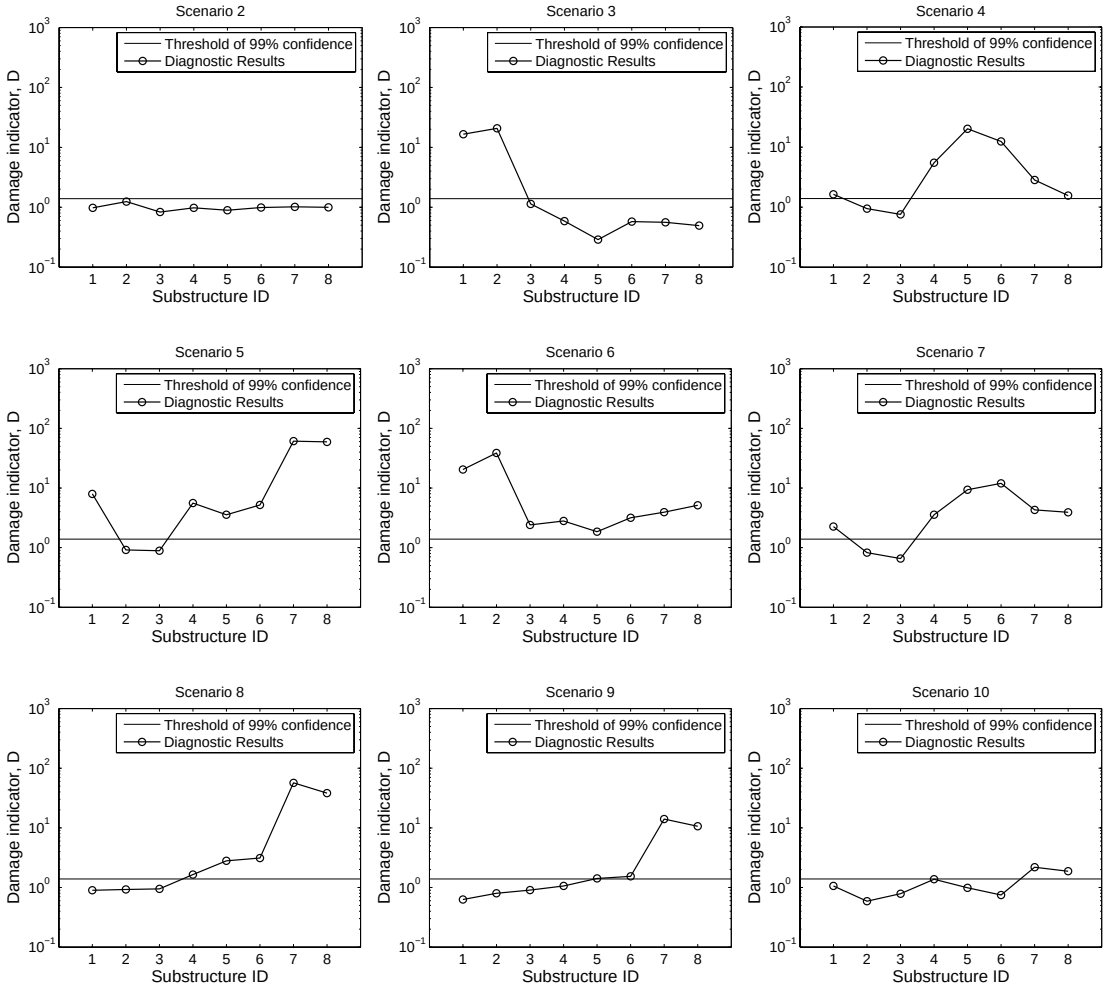
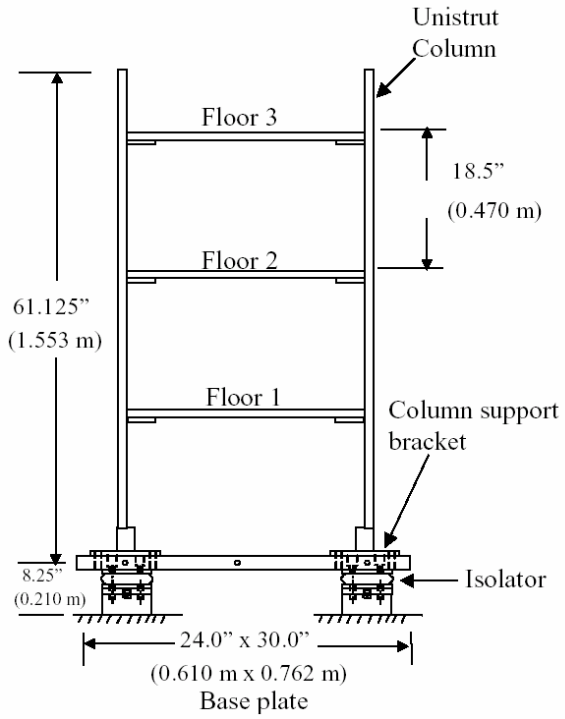
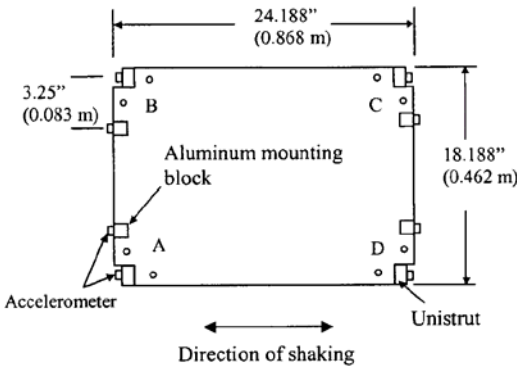


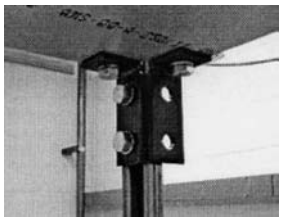
Fig. 3.9 Damage indicators computed for scenarios 2-10 of the 8-DOF mass-spring system, using scenario 1 as the baseline state.



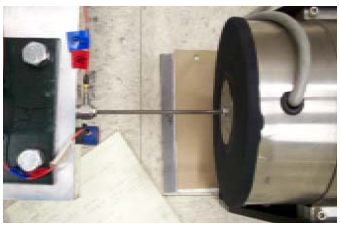
(a) Side view of the structure



(b) Top view of the floor layout



(c) A floor-column joint



(d) The attached shaker

Fig. 3.10 Experimental setup of the 3-story frame structure model (Sohn et al. 2003).

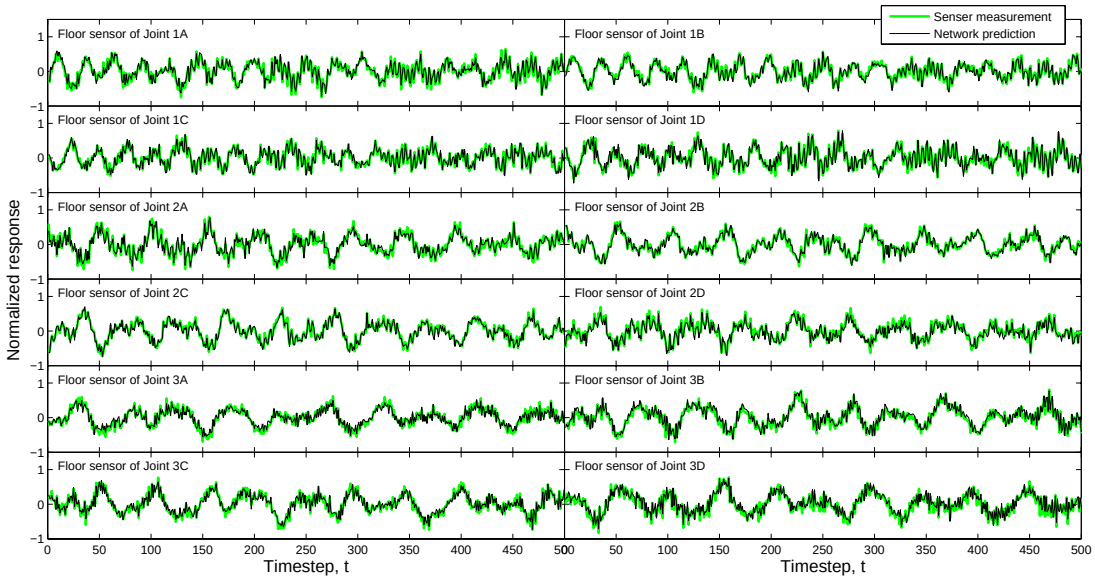


Fig. 3.11 Comparison of network predictions and corresponding sensor measurements of structural response of the 3-story frame structure at the baseline state.

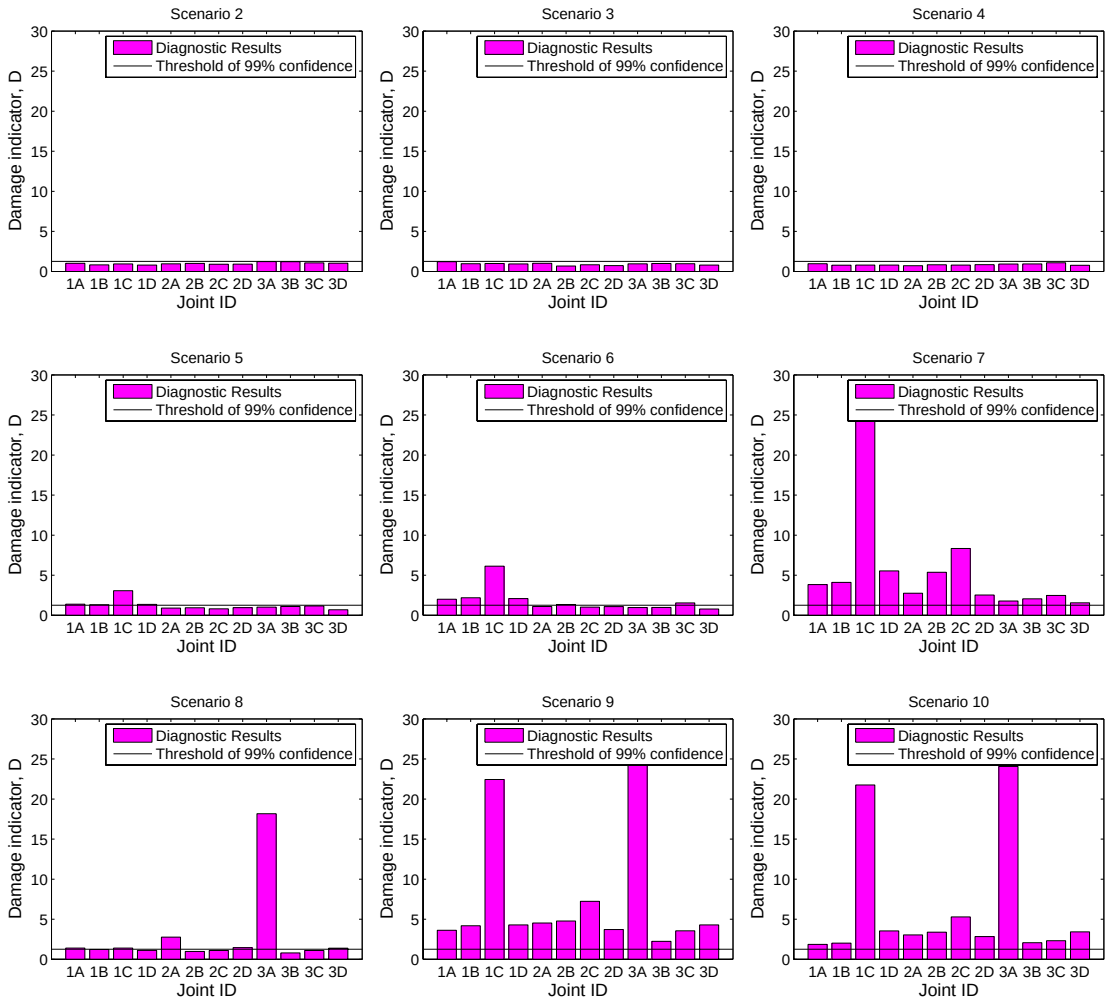


Fig. 3.12 Damage indicators computed for scenarios 2-10 of the 3-story frame structure, using scenario 1 as the baseline state.

3.11 References

Bishop, C. M. (1995). *Neural Networks for Pattern Recognition*, Oxford University Press.

Casciati, F., Casciati, S., and Faravelli, L. (2003a). "Damage Detection via Response Surface Approximations." *Proc. of ICASP9*, San Francisco, CA, 2003.

Casciati, S., Colabrese, E., and Magonette, G. (2003b). "Damage Detection and Localization by Statistical Comparison of Response Time Histories." *Proc. of IWSHM4*, Stanford, CA, 2003.

Casciati, S., Colabrese, E., and Magonette, G. (2003c). "Monitoring and Response Surface Methodology to Detect and Locate Structural Damage." *Proc. of the First International Conference on Structural Health Monitoring and Intelligent Infrastructure (SHMII-1'2003)*, Wu & Abe, eds., 423-429, Tokyo, Japan, November 13-15, 2003.

Chang, F.K., (ed.) (1997). *Proc. of the First International Workshop on Structural Health Monitoring: Current Status and Perspectives*, September 18-20, 1997, Stanford, CA, USA.

Chang, F.K. (ed.) (2005). *Proc. of the 5th International Workshop on Structural Health Monitoring: Advancement and Challenge for Implementation*, September 12-14, 2005, Stanford, CA, USA.

Chen, S. and Billings, S. A. (1989). "Representation of Nonlinear Systems: the NARMAX Model." *Int. J. Control*, 49, 1013-1032.

Conte, J. P., Durrani, A. J., and Shelton, R. O. (1994). "Seismic Response Modeling of Multi-story Buildings Using Neural Networks." *J. of Intelligent Material Systems and Structures*, 5, 392-402.

Demuth, H. and Beale, M. (1998). *Neural Network Toolbox User's Guide, Version 3*, The MathWorks, Inc.

Doebling, S. W., Farrar, C. R., Prime, M. B., and Shevitz, D. W. (1996). "Damage Identification and Health Monitoring of Structural and Mechanical Systems from Changes in Their Vibration Characteristics: A Literature Review." *Report No: LA-13070-MS*, Los Alamos National Laboratory.

Farrar, C. R. and Doebling, S. W. (1997). "Lessons Learned form Applications of Vibration-Based Damage Identification Methods to a Large Bridge Structure." *Proc. of the First International Workshop on Structural Health Monitoring: Current Status and Perspectives*, 351-370, September 18-20, 1997, Stanford, CA, USA.

Farrar, C. R. and Jauregui, D. (1996). "Damage Detection Algorithms Applied to Experimental and Numerical Modal Data from the I-40 Bridge." *Report No: LA-13074-MS*, Los Alamos National Laboratory.

Hastie, T., Tibshirani, R., and Friedman, J. (2001). *The Elements of Statistical Learning: Data Ming, Inference, and Prediction*, Spring-Verlag, New York.

Humar, J. L., Bagchi, A., and Xu, H. (2003). "Challenges in Vibration-based Structural Health Monitoring." *Proc. of the First International Conference on Structural Health Monitoring and Intelligent Infrastructure (SHMII-1'2003)*, Wu & Abe (eds.), 503-511, November 13-15, 2003, Tokyo, Japan.

Iwasaki, A., Todoroki, A., and Sugiya, T. (2002). "Remote Smart Damage Detection via Internet with Unsupervised Statistical Diagnosis." *Proc. of the IUTAM Symposium on Dynamics of Advanced Material and Smart Structures*, Yonezama, Japan, 2002.

Iwasaki, A., Todoroki, A., and Sugiya, T. (2003). "Unsupervised Statistical Damage Diagnosis for SHM of Existing Civil Structure." *Proc. of the First International Conference on Structural Health Monitoring and Intelligent Infrastructure (SHMII-1'2003)*, Wu & Abe, eds., 401-407, Tokyo, Japan, November 13-15, 2003.

Kao, C. Y., Tsang, C. C., Loh, C. C., and Wu, T. H. (2003). "Neural Networks for Nonlinear Identification and Diagnosis of Structures." *Proc. of the First International Conference on Structural Health Monitoring and Intelligent Infrastructure (SHMII-1'2003)*, Wu & Abe (eds.), 619-627, Tokyo, Japan, November 13-15, 2003.

Korbicz, J., and Janczak, A. (1996). "A Neural Network Approach to Identification of Structural Systems." *Proceeding of the IEEE International Symposium on Industrial Electronics, ISIE'96*, June 17-20, 1996, Warsaw, Poland.

LeCun, Y., Bottou, L., Orr, G. B., and Muller, K. R. (1998). "Efficient Backprop." *Neural Networks---Tricks of the Trade*, Springer Lecture Notes in Computer Sciences, 1524, 5-50.

Lei, Y., Kiremidjian, A. S., Nair, K. K., Lynch, J. P., Law, K. H., Kenny, T. W., Carryer, Ed., and Kottapalli, A. (2003). "Statistical Damage Detection Using Time Series Analysis on a Structural Health Monitoring Benchmark Problem." *Proc. of the 9th International Conference on Applications of Statistics and Probabilities in Civil Engineering*, San Francisco, CA, USA, July 6-9, 2003.

Leonatris, I. A. and Billings, S. A. (1985). "Input-Output Parametric Models for Nonlinear System." *Int. J. Control*, 41, 303-344.

Masri, S. F., Nakamura, M., Chassiakos, A. G., and Caughey, T. K. (1996). "Neural Network Approach to Detection of Changes in Structural Parameters." *ASCE, Journal of Engineering Mechanics*, 122(4), 350-360.

Miller, R. G. (1997). *Beyond ANOVA: Basics of Applied Statistics*, New York: Chapman & Hall.

Nair, K. K., Kiremidjian, A. S., Lei, Y., Lynch, J. P., and Law, K. H. (2003). "Application of Time Series Analysis in Structural Damage Evaluation." *Proc. of the First International Conference on Structural Health Monitoring and Intelligent Infrastructure (SHMII-1'2003)*, Wu & Abe, eds., 529-534, Tokyo, Japan, November 13-15, 2003.

Nakamura, M., Masri, S. F., Chassiakos, A. G., and Caughey, T. K. (1998). "A Method for Non-Parametric Damage Detection Through the Use of Neural Networks." *Earthquake Engineering and Structural Dynamics*, 27, 997-1010.

Sohn, H., Allen, D. W., Worden, K., and Farrar, C. R. (2003). "Statistical Damage Classification Using Sequential Probability Ratio Tests." *Structural Health Monitoring*, 2(1), 57-74.

Sohn, H. and Farrar, C. R. (2001). "Damage Diagnosis Using Time Series Analysis of Vibration Signals." *Smart Materials and Structures*, 2001(10), 446-451.

Sohn, H., Farrar, C. R., Hunter, N. F., and Worden, K. (2001a). "Structural Health Monitoring Using Statistical Pattern Recognition Techniques." *Journal of Dynamic Systems, Measurement, and Control*, 123, 706-711.

Sohn, H., Farrar, C. R., Hunter, N. F., and Worden, K. (2001b). "Applying the LANL Statistical Pattern Recognition Paradigm for Structural Health Monitoring to Data from a Surface-Effect Fast Patrol Boat." *Report No: LA-13761-MS*, Los Alamos National Laboratory.

Sohn, H., Farrar, C. R., Hemez, F., Czarnecki, J. J., Shunk, D., Stinemates, D., and Nadler, B. (2003). "A Review of Structural Health Monitoring Literature from 1996-2001." *Report No: LA-13976-MS*, Los Alamos National Laboratory.

Spiegel, M. R. (1992). *Theory and Problems of Probability and Statistics*, New York: McGraw-Hill, pp. 112-113.

Wu, Z. S., Xu, B., and Yokoyama, K. (2002). "Decentralized Parametric Damage Detection Based on Neural Networks." *Computer-Aided Civil and Infrastructure Engineering*, 17, 175-184.

Xu, B., Wu, Z. S., and Yokoyama, K. (2003). "Response Time Series Based Structural Parametric Assessment Approach with Neural Networks." *Proc. of the First International Conference on Structural Health Monitoring and Intelligent Infrastructure (SHMII-1'2003)*, Wu & Abe, eds., 601-609, Tokyo, Japan, November 13-15, 2003.

4 A NEURAL-NETWORK-BASED STATISTICAL INFERENCE APPROACH FOR BRIDGE PIER DAMAGE IDENTIFICATION

In this chapter, the structural damage detection approach developed in Chapter 3 (approach B in Chapter 1) is applied for bridge pier damage identification. This study is based on numerical simulation data generated from a virtual bridge testbed. In Section 4.1, earthquake-induced bridge pier damage and the motivation of this study is introduced. The virtual bridge testbed is then described, including detailed information on FE modeling, damage simulation, and data generation. In the subsequent sections, the analysis framework, neural network development, and damage indicator computation are described. Finally, the damage identification results are presented and discussed.

4.1 Introduction

When a bridge supported on piers (columns) is subjected to destructive earthquake excitation, a typical damage pattern includes formation of plastic hinges at the pier bases. Fig. 4.1 shows a dramatic example of such damage (Hanshin Expressway) during the 1995 Kobe, Japan Earthquake, and Fig. 4.2 depicts a similar pattern (Mingchou Bridge) during the 1999 Ji-Ji, Taiwan Earthquake. After an earthquake, it is essential to rapidly identify the occurrence, location, and severity of damage in each significant bridge of the transportation system.

In practice, highway bridges are typically inspected visually (e.g., Hu et al. 2002). However, the lower section of a bridge pier is often below water or buried under a soil cover, potentially complicating matters. In addition, at low damage levels,

no visible signs may be evident (such as surface cracks or spawling). These situations motivate the development of a sensitive and reliable approach to detect, locate, and assess the severity of damage in bridge piers.

Recently, vibration-based structural damage identification has received a growing level of interest from numerous research groups using a variety of analytical and experimental techniques (Doebling et al. 1996; Sohn et al. 2003; Chang 1997, 2005). Yan and Elgamal (2006a, b) developed a structural damage identification approach, combining neural networks and statistical inference techniques.

Within this framework, each substructure in a system of interest is monitored by a set of neighboring sensors. Therefore, a major sensor is selected and an associated NARX (Nonlinear AutoRegressive with eXogenous inputs) neural network (Korbicz and Janczak 1996; Demuth and Beale 1998) is developed to predict the structural response at this sensor location from the measurements of its neighbors. Thus, dynamic characteristics of the substructure are approximately and implicitly identified and represented by the network. Without significant change in the substructure, the prediction error of the network will follow a stable statistical distribution, and change in prediction error variance is evaluated and utilized as a sensitive damage indicator.

Three successful applications of this approach are presented in Yan and Elgamal (2006a, b), including: (1) identification of linear damage in a shear frame based on simulation data, (2) identification of linear/nonlinear damage in a mass-spring system based on experimental data, and (3) identification of joint damage in a frame structure based on experimental data. Herein, the potential of this approach for

bridge pier damage detection is explored, with the substructures of interest being the pier bases (i.e., the potential locations of plastic hinges).

In view of that actual data from damaged bridges are scare due to the long and gradual degradation progress, a refined three-dimensional (3D) Finite Element (FE) model is herein constructed and employed as a virtual bridge testbed. Using this model, different scenarios of damage at bridge pier bases are simulated in order to generate the necessary data for this study.

4.2 Virtual Bridge Testbed

4.2.1 PEER Humboldt Bay Middle Channel Bridge Testbed

The Humboldt Bay Middle Channel Bridge (HBB, near Eureka in northern California, Fig. 4.3) was selected by the Pacific Earthquake Engineering Research (PEER) Center as a research testbed (Porter 2003, http://peer.berkeley.edu/peertestbeds/humboldt.htm). This testbed has motivated a wide range of studies on advanced numerical simulation and seismic analysis (e.g., Zhang et al. 2005; Elgamal et al. 2006; Yan et al. 2006).

HBB is a 330m long, 9-span structure, supported by 8 single pier bents on foundation pile groups (Fig. 4.3). Herein, the bridge model (Fig. 4.4) is constructed in light of the structural configurations of HBB. The system modeling, damage simulation, and response computations are all performed using OpenSees (Open System for Earthquake Engineering Simulation), an object-oriented, open-source FE analysis framework (http://opensees.berkeley.edu, McKenna and Fenves 2001).

4.2.2 Bridge Modeling

In the model (Fig. 4.4), the bridge superstructure is assumed linear in view of its high stiffness and yield strength relative to the piers. In this regard, the bridge longitudinal girders and transversal brace beams are modeled using 3D linear elastic beam-column elements (Table 4.1). The bridge deck slabs (0.165m thick) are modeled using 3D linear shell elements. Herein, typical mass density ($\rho = 2300\text{kg/m}^3$), Young's Modulus ($E = 2.78 \times 10^7 \text{kPa}$ corresponding to a compressive strength, f_c' of 5ksi), and Poisson's ratio ($\nu = 0.3$) of concrete are used (Wang and Salmon 1992).

Each bridge pier is modeled using five 3D fiber-section force-based beam-column elements with nonlinear fiber materials (Spacone et al. 1996). Discretization of the pier cross-section into concrete and steel fibers is shown in Fig. 4.5a, with confined and unconfined concrete inside and outside the shear reinforcement/stirrups, respectively. The uni-axial Kent-Scott-Park model (Kent and Park 1971; Scott et al. 1982; Mander et al. 1988) with degraded linear unloading/reloading stiffness (Fig. 4.5d) is used to model the concrete (Table 4.2). The reinforcing steel (Table 4.3) is represented (Fig. 4.5e) by a uni-axial bilinear model with kinematic hardening.

Quasi rigid elements (linear elastic beam-column elements with high Young's Modulus and large cross sectional area) are used to model the pier cap beams (Figs. 4.4b, 4.5c) assumed herein to be of adequate strength and high stiffness. The cap beams are connected to the bridge superstructure by perfect hinges using the equalDOF constraint (for translations only) in OpenSees (McKenna and Fenves 2001), assuming no shear key failure.

The modeled bridge foundation system consists of 2×2 pile groups, with 4 vertical circular piles (1.37m/54in diameter). Each pile is modeled using 3D fiber section, force-based beam-column elements with the nonlinear fiber materials defined in Tables 2 and 3 (Figs. 4.5b-e, Spacone et al. 1996). The pile caps are idealized as rigid frames (Figs. 4.4b, 4.5c).

In this model, the boundary condition along the pile foundations is simply defined by fixing the underground sections of each pile (Fig. 4.4a). In addition, the connections between the bridge superstructure ends and abutments are modeled as rollers (Fig. 4.4a), which only allow rotation and longitudinal displacement.

4.2.3 Damage Simulation Using Staged Analysis

Elgamal et al. (2006) and Yan et al. (2006) show that, as a bridge similar to HBB experiences an earthquake with a hazard level of 10% probability of exceedance in 50 years, the peak transversal bending curvature at the pier bases is about $0.001m^{-1}$. Such high curvature will induce nonlinear damage in the pier. In view of this, a damage scenario in the model can be realized using the following staged analysis procedure:

(1) The FE model, only consisting of independent individual bridge piers and foundation pile groups, is first built and the bridge own weight is applied (represented by an axial load of 8MN in each pier).

(2) At each pier top, one cycle of prescribed transversal displacement is statically applied in 200 steps, returning back to zero in the end. Different levels of peak bending moment/curvature can be generated at the pier bases by specifying the maximum displacement level (denoted by *D* herein).

(3) The bridge superstructure FE model is activated to connect all bridge piers.

(4) A white-noise transversal excitation with the root-mean-square (RMS) amplitude level of 0.01g is uniformly applied at each pier base (Fig. 4.5b), and the bridge dynamic response of 20 seconds (2000 time steps, $\Delta t = 0.01\text{sec}$) is computed. For each pier, the time histories of transversal acceleration response at two locations are recorded, simulating presence of two accelerometers (one above and one below the potential location of plastic hinge near the pier base, Fig. 4.4a).

Herein, as the amplitude of the base uniform excitation is relatively small, the structural response remains linear. For the dynamic analysis in Step 4, Rayleigh damping is employed, with damping of about 5% in the frequency range of 1.5-10Hz.

Further, uniform base excitation is employed as the external excitation in this study. When this approach is applied for seismic damage evaluation, the analysis may be performed based on measurements of structural response to aftershocks (small tremors). Alternatively, the white-noise excitation may be induced by small shakers mounted on the bridge deck.

4.2.4 Data Generation

Using the above staged analysis procedure, 4 scenarios (named U1-U4) without damage were generated. In addition, 32 scenarios (named S1-S32) with a single damaged pier (4 scenarios for each pier) were also generated, with the recorded moment-curvature response at the damaged pier base shown in Fig. 4.7. It is seen that as the prescribed value of D increases, both the peak curvature and the area within the hysteretic response loop increase, indicating a higher level of damage. A larger D is

required to induce a similar level of damage in a pier closer to the bridge center, with a larger distance from the pier top to the ground surface (Fig. 4.4a). Furthermore, the scenarios of damage occurring at multiple pier bases simultaneously are considered. For a given number (2-8) of damaged piers, 3 scenarios were generated with randomly selected damaged piers and D values. Thus, a total of 21 scenarios (named M1-M21) with multi damaged piers were generated.

4.3 Analysis Framework

In this study, the neural-network-based statistical inference approach (Yan and Elgamal, 2006a, b) is applied to the simulated scenarios, following the steps described below:

(1) As mentioned earlier, each pier base is monitored by two sensors. Thus, based on the simulation data of scenario U1, an associated NARX neural network (Korbicz and Janczak 1996; Demuth and Beale 1998) is developed to predict the structural response at the upper sensor location from the measurements of the lower sensor. Thus, the dynamic characteristics of the pier base are approximately and implicitly identified and represented by the associated network. Both network configurations (weights and biases, Bishop 1995) and the time history of network prediction error are archived as a reference baseline state.

(2) During the damage identification phase, for each pier base, the archived network is employed to predict the dynamic response at the upper sensor and a new time history of prediction error is obtained. Comparing this new time history with the archived baseline state, a damage indicator is computed based

on changes in prediction error variance.

(3) Integrate information from all computed indicators in order to infer the occurrence, location, and relative severity of damage in the structural system.

4.4 Substructure Identification Using NARX Neural Networks

4.4.1 Network Configuration

As mentioned above, each pier base is monitored by a pair of accelerometers. The structural response at the upper sensor location mainly depends on (1) the dynamic characteristics of the pier and (2) the applied external excitation. Obviously, the structural response measured by the lower sensor also contains information on the external excitation. In this sense, the problem can be formulated as a SISO (Single Input, Single Output) nonlinear system. As such, the system can be defined by the following NARX model (Leonatris and Billings 1985; Chen and Billings 1989):

$$y(t) = f(\mathbf{x}(t)) = f(y(t-n_y), \ldots, y(t-1), u(t-n_u), \ldots, u(t-1), u(t)) \tag{4.1}$$

where $u(t)$ denotes the input (response measured by the lower sensor) at time step t, $y(t)$ denotes the output (response at the upper sensor location) at time step t, n_u and n_y are the input and output order ($n_u = n_y = 20$, herein), and f is a nonlinear function representing the system.

Herein, the function f is approximated by a Multi-Layer Perceptron (MLP) as Bishop (1995) shows that such networks, with sigmoidal activation functions, provide strong capabilities for representing continuous nonlinear systems. The resulting system is known as a NARX network (Korbicz and Janczak 1996; Demuth and Beale 1998), having one input layer of $(n_u + 1) + n_y$ units, one hidden layer, and an output

layer of single unit. The number of hidden units is set to the same number of input units, thereby allowing adequate representation capability while controlling the network size.

The feed forward network mapping from the input vector $\mathbf{x}(t) = [x_i(t)]$ to the output $\hat{y}(t)$ is defined by

$$\hat{y}(t) = \sum_{j=1}^{(n_u+1)+n_y} w_j^{(2)} g\left(\sum_{i=1}^{(n_u+1)+n_y} w_{ji}^{(1)} x_i(t) + w_{j0}^{(1)}\right) + w_0^{(2)} \tag{4.2}$$

Here, $w_{ji}^{(1)}$ denotes weight going from input unit i to hidden unit j, $w_{j0}^{(1)}$ denotes bias for hidden unit j, $g(\cdot)$ denotes activation function for hidden units, $w_j^{(2)}$ denotes weight going from hidden unit j to the single output unit, and $w_0^{(2)}$ denotes bias for the single output unit.

As shown, the output layer is linear, and a hyperbolic tanh is adopted as the activation function $g(\cdot)$ of hidden units defined by (LeCun et al. 1998)

$$g(a_j) = 1.7159 \tanh(2a_j / 3) \tag{4.3}$$

where $a_j = \sum_{i=1}^{(n_u+1)+n_y} w_{ji}^{(1)} x_i(t) + w_{j0}^{(1)}$ is the weighted sum of inputs for hidden unit j.

4.4.2 Network Training

Prior to network training, the minimum-to-maximum range of acceleration response at each sensor is normalized to [-1, 1]. For each pier base, a sequence of input-output patterns $\{y(t) \quad \mathbf{x}(t)\}$ can be sampled from these normalized time histories. These patterns are randomly partitioned into a training set (80% of the total patterns) and a validation set (20% of the total patterns). Based on the training set, the

standard backpropagation algorithm is adopted for network training by minimizing the square error between the network output $\hat{y}(t)$ and the corresponding target $y(t)$

$$E = \frac{1}{2}[y(t) - \hat{y}(t)]^2 \tag{4.4}$$

In order to best utilize the knowledge contained in the data, the training set is repeatedly used with each training loop over all patterns defined as an epoch. After each epoch, the average errors of the training and validation sets are computed. The optimal network configuration is selected according to the minimum error of the validation set so as to avoid overfitting (Bishop 1995; Hastie et al. 2001).

4.4.3 Network Prediction

Fig. 4.7 shows the comparison of network predictions and corresponding sensor measurements of structural response at the baseline state, along with the residual errors. It is seen that the prediction of each network closely matches the corresponding sensor measurement throughout all time histories. Thus, it can be concluded that the dynamic properties of each substructure at the baseline state has been properly identified and represented by the associated NARX network.

4.5 Damage Indicator

For each substructure, the associated NARX network is employed to predict the structural response under different states. Herein, the prediction error of the baseline state at time step t is denoted by $e(t)$, $t = 1,\ldots N_e$, where $N_e = 1980$ is the time history length. Similarly, the prediction error of an investigated state at time step t is denoted by $\varepsilon(t)$, $t = 1,\ldots N_\varepsilon$, where $N_\varepsilon = 1980$ is the time history length. Without significant change in the substructure (i.e., occurrence of damage), the trained network

should deliver a consistent performance in prediction, and $e(t)$ and $\varepsilon(t)$ are expected to follow similar statistical distributions. In other words, change in the statistical distribution of the prediction error can be utilized as a damage indicator.

As the prediction error generally follows a distribution with the mean value around zero, most efforts have been directed to assess changes in the variance (or standard deviation). For instance, Sohn and Farrar (2001) evaluated such change by the F test, which assumes that both $e(t)$ and $\varepsilon(t)$ follow normal distributions. However, this normality assumption is hard to justify in practice. In view of this, Sohn and Farrar (2001) suggested performing the F hypothesis test against a threshold value from a modified F distribution. Herein, this problem is addressed in an alternative way that weakens the strong normality requirement, only assuming that $e(t)$ and $\varepsilon(t)$ follow stable distributions. Based on this assumption, for each substructure, a damage indicator can be computed using the following steps:

(1) Reshuffle the time step order of the $e(t)$ and $\varepsilon(t)$ time histories in order to eliminate the correlation between neighboring prediction errors.

(2) Divide the reshuffled $e(t)$ and $\varepsilon(t)$ time histories into segments of equivalent lengths (the number of time steps in each segment is denoted by n, the number of $e(t)$ segments is denoted by $N_p = N_e / n$, and the number of $\varepsilon(t)$ segments is denoted by $N_q = N_\varepsilon / n$).

(3) Thus, for each segment, the sequence of prediction errors ($e(t)$ or $\varepsilon(t)$) is approximately independent and identically distributed, and their sum can be computed as $p = \sum_{t=1}^{n} e(t)$ and $q = \sum_{t=1}^{n} \varepsilon(t)$. According to the Central Limit

Theory (Spiegel, 1992), both p and q approach normal distributions for large n values (herein, $n = 20$ is used).

(4) Compute the damage indicator D as the sample variance ratio of p and q

$$D = \frac{\sigma^2(q)}{\sigma^2(p)} \tag{4.5}$$

Based on D, the similarity of $e(t)$ and $\varepsilon(t)$ can be indirectly evaluated by testing the null hypothesis H_0: $\sigma^2(q) = \sigma^2(p)$ against the one-side alternative H_1: $\sigma^2(q) > \sigma^2(p)$. It can be shown that D follows the F-distribution with $N_q - 1$ and $N_p - 1$ degrees-of-freedom under the null hypothesis (Miller 1997). Thus, given a confidence level α, the theoretical threshold value $F^{\alpha}_{N_q-1,N_p-1}$ can be found. If D exceeds this threshold, the null hypothesis H_0 is rejected, indicating a significant change in the substructure.

4.6 Results and Discussions

4.6.1 Quantification of Simulated Damage

In order to compare with the network identification results, simulated pier-base damage is first quantified in terms of percentage reduction in the gross cross-section flexural stiffness, which is actually due to the stiffness degradation of concrete fibers (Fig. 4.5).

As the applied base excitation is relatively small, the bridge response remains linear no matter whether damage exists or not. Thus, given an intact/damage pattern, the available gross flexural stiffness of a pier-base cross-section can be determined by computing the slope of the recorded linear moment-curvature response. As such, the

percentage stiffness reduction can be evaluated. Fig. 4.8 shows the evaluation results for the 32 patterns (with a single damaged pier) in Fig. 4.6. The horizontal axis is the peak transversal bending curvature (ϕ_m) induced at a pier base and the vertical axis is the corresponding percentage stiffness reduction (β). It is seen that ϕ_m and β show a strong positive linear correlation (Fig. 4.8), which can be approximately represented by the following bilinear model obtained by linear regression

$$\beta = \begin{cases} 38868\phi_{\mathrm{m}} - 19 & \text{if } \phi_{\mathrm{m}} > 0.0005 \\ 0 & \text{if } \phi_{\mathrm{m}} \le 0.0005 \end{cases} \tag{4.6}$$

Thus, given the ϕ_m of a damaged pier, the corresponding percentage stiffness reduction can be easily obtained using Eq. 4.6.

4.6.2 Damage Identification Results

The networks are now applied to the simulated scenarios for damage inference purposes, and damage indicators are computed using Eq. 4.5. The results are shown in Figs. 4.9-4.11. In these figures, the magnitude of damage indicator is indicated by the column height, the horizontal axis is pier number, and the vertical axis is damage indicator in log-scale in order to emphasize changes within the relatively low value range, around the threshold line. It is seen (Fig. 4.9) that for scenarios U2-4 (no damage), the computed damage indicators are all below the threshold, as expected.

The damage identification results for scenarios S1-S32 with damage in a single pier are shown in Fig. 4.10, where the scenarios of damage in the same pier but of different severities are grouped together. It is seen that for each scenario, only the damage indicator of the damaged pier is significantly larger than the others and exceeds the threshold. Based on this observation, the damaged pier can be identified.

In addition, for each damaged pier, the corresponding stiffness reduction computed using Eq. 4.6 is also shown in Fig. 4.10. It may be seen that the relative level of damage can be inferred from the magnitude of the damage indicator.

The damage identification results for scenarios M1-M21 with damage in multi piers are shown in Fig. 4.11, where shown on the top of each column is the corresponding stiffness reduction computed using Eq. 4.6. It is seen that in general, the pattern of computed damage indicators show a good agreement with the damage condition of piers. Thus, it may be concluded that the proposed approach is also feasible for identification of damage occurring in multi piers simultaneously.

4.7 Summary and Conclusions

In Yan and Elgamal (2006a, b), a structural damage detection approach based on NARX neural networks and statistical inference techniques is proposed. Herein, the potential of this approach is explored to identify earthquake-induced plastic hinges in bridge piers.

In view of that actual data from damaged bridges are scare, a refined 3D FE model is herein constructed and employed as a virtual bridge testbed, along with different simulated damage scenarios. For each scenario, the bridge acceleration response to ambient base excitation is evaluated and recorded at 16 locations (representing accelerometers, two on each pier, with one above and one below the potential location of plastic hinge).

For each pier base, an associated NARX neural network is developed to predict the structural response at the upper sensor location from the measurements of the

lower sensor. Thus, dynamic characteristics of each pier base are approximately and implicitly identified and represented by the network.

Without damage, the prediction error of the network will follow a stable statistical distribution. Herein, change in the prediction error variance is evaluated by the standard F test and utilized as a sensitive damage indicator. Finally, satisfactory results are achieved, showing that the approach can successfully infer the occurrence, location, and relative severity of damage at multi pier bases.

4.8 Acknowledgements

Support for this research was provided by the U.S. National Science Foundation, under ITR Grant No. 0205720. This support is gratefully acknowledged. The authors also wish to thank the California Institute for Telecommunications and Information Technology (UCSD Calit2, http://www.calit2.net) for providing fellowship support to this project.

4.9 Tables

Table 4.1 Model Parameters of 3D Linear Elastic Beam-Column Elements in the Bridge Superstructure

Modeled component	A (m^2)	I_z (m^4)	I_y (m^4)
Longitudinal girder	0.73	0.49	0.0094
Transversal beam	0.1	0.067	0.00017

Table 4.2 Constitutive Model Parameters (Fig. 4.5d) for Concrete Materials Used in Fiber Beam-Column Elements

Concrete01 material model in OpenSees	Confined concrete	Unconfined concrete
Compressive strength (f_c, kPa)	-3.45×10^4 (-5ksi)	-2.76×10^4 (-4ksi)
Strain at compressive strength (ε_c)	-0.004	-0.002
Crushing strength (f_{cu}, kPa)	-2.07×10^4 (-3ksi)	0
Strain at crushing strength (ε_{cu})	-0.014	-0.008

Table 4.3 Constitutive Model Parameters (Fig. 4.5e) for Steel Material Used in Fiber Beam-Column Elements

Steel01 material model in OpenSees	Reinforcing steel
Yield strength (f_y, kPa)	4.14×105 (60ksi)
Initial elastic tangent modulus (E_s, kPa)	2.0×108 (29000ksi)
Hardening ratio (b)	0.008

4.10 Figures



Fig. 4.1 Damage at bridge pier bases occurring during the 1995 Kobe, Japan Earthquake (Thewalt 1995).



Fig. 4.2 Plastic hinge formation at pier bases of Mingchou Bridge during the 1999 Ji-Ji, Taiwan Earthquake (Uang et al. 1999).



Fig. 4.3 Sky view of Humboldt Bay Middle Channel Bridge (Courtesy of Caltrans).

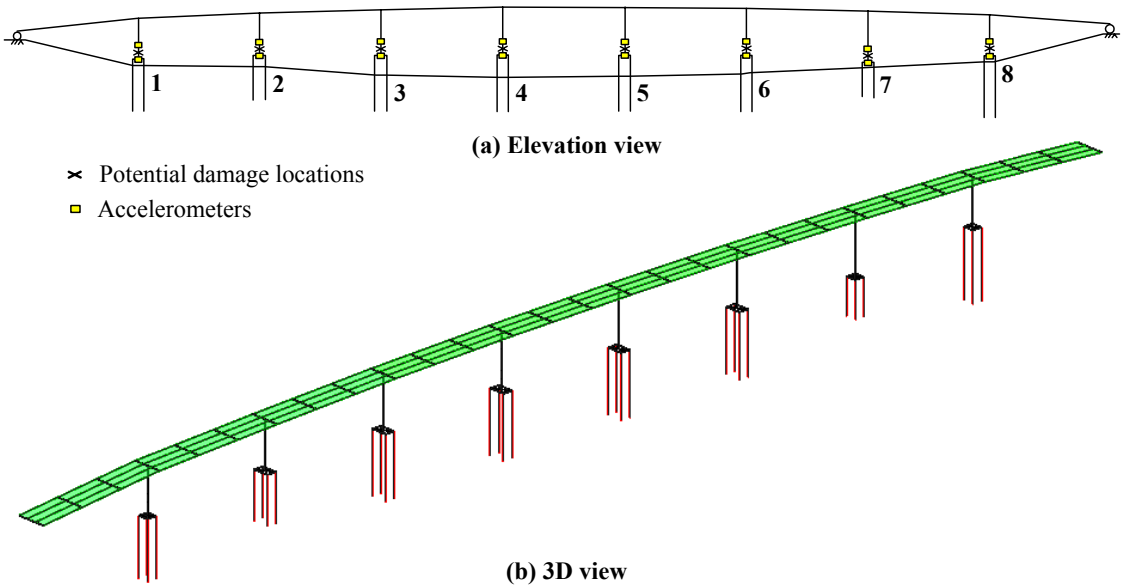


Fig. 4.4 3D FE model of bridge.

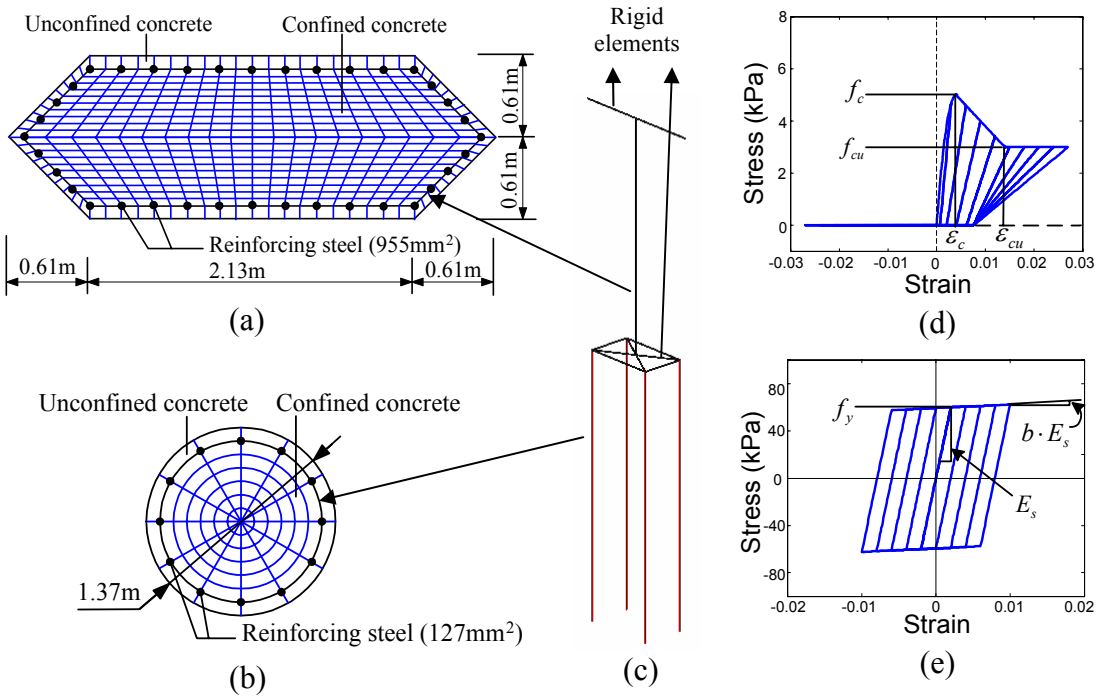


Fig. 4.5 Modeling of piers and pile groups, using fiber-section beam-column elements with uni-axial material constitutive models: (a) fiber discretization of pier cross-section; (b) fiber discretization of pile cross-section; (c) a pier supported by a 2×2 pile group; (d) concrete Kent-Scott-Park model with degraded linear unloading/reloading stiffness; and (e) reinforcing steel bilinear inelastic model with linear kinematic hardening.

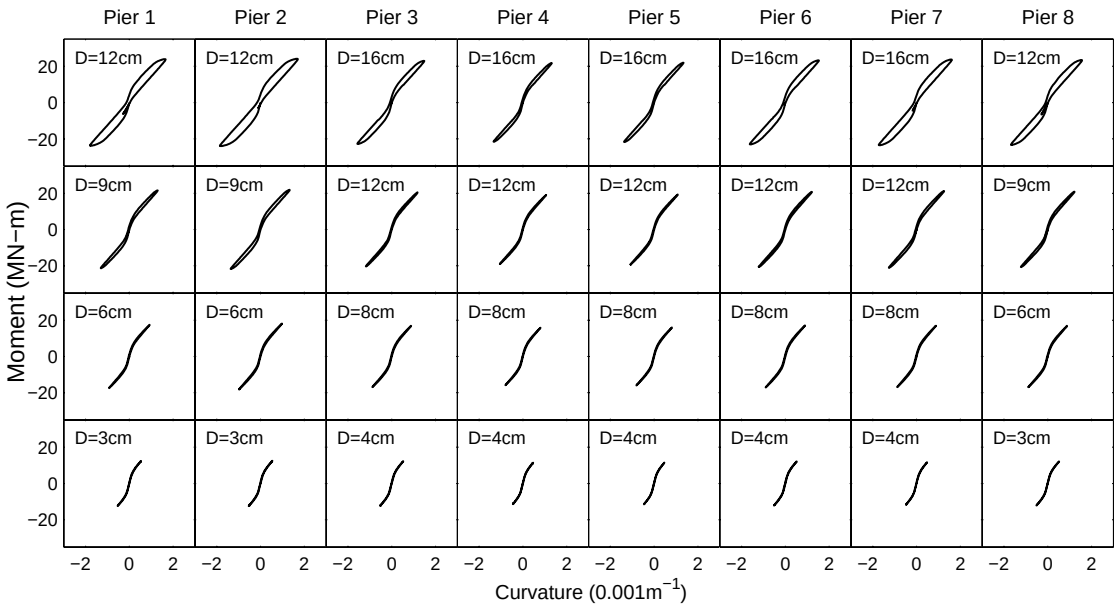


Fig. 4.6 32 patterns with a single damaged pier: (a) transversal moment-curvature response at the damaged pier base, and (b) the maximum pier-top displacement *D*.

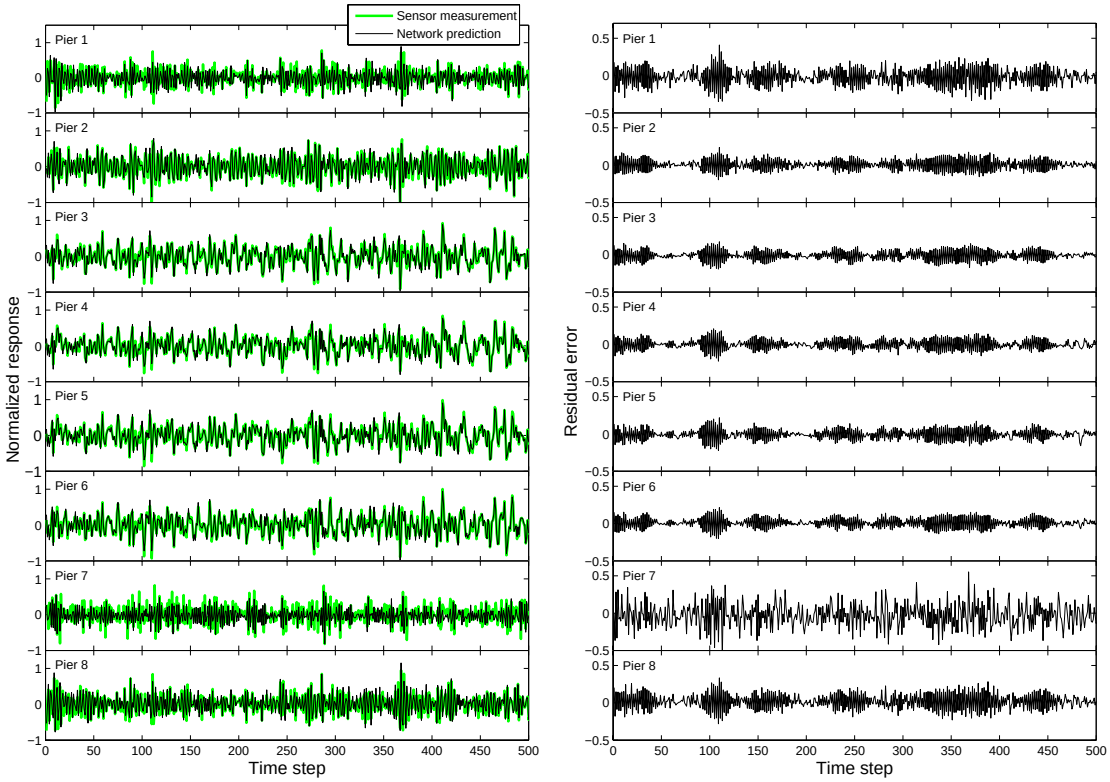


Fig. 4.7 Comparison of network predictions and corresponding actual record of structural response at the upper accelerometers of each pier for scenario U1, along with the residual errors.

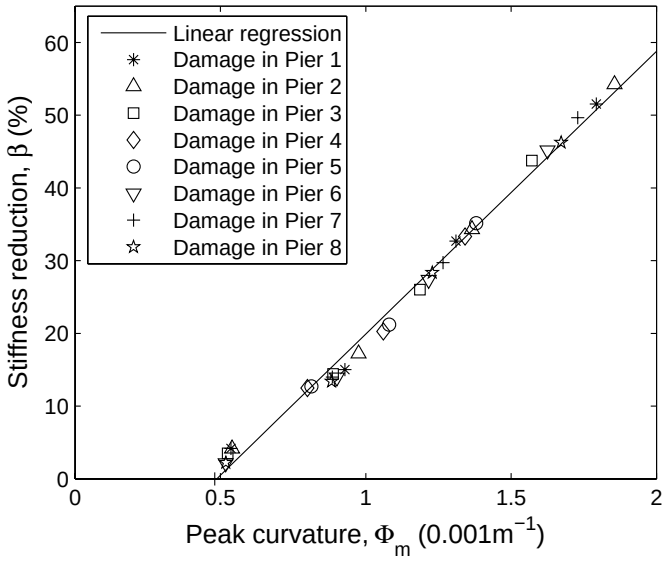


Fig. 4.8 Strong positive linear correlation between the damage-induced peak bending curvature ϕ_m at a pier cross-section near the base and corresponding reduction in gross flexural stiffness β.

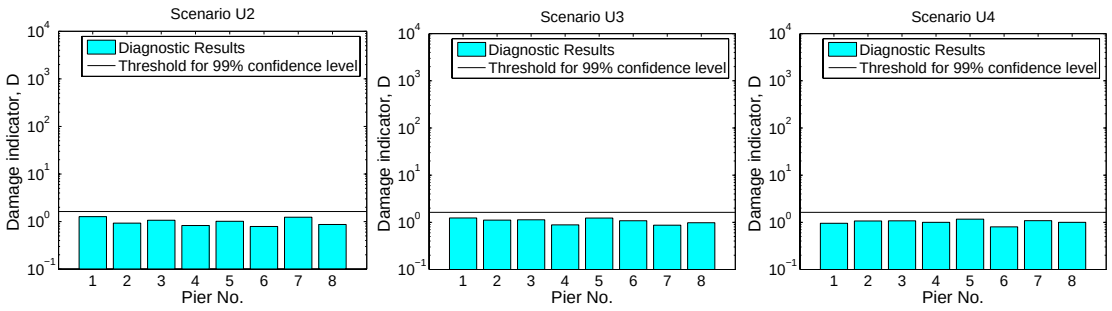


Fig. 4.9 Damage identification results for scenarios U2-U4.

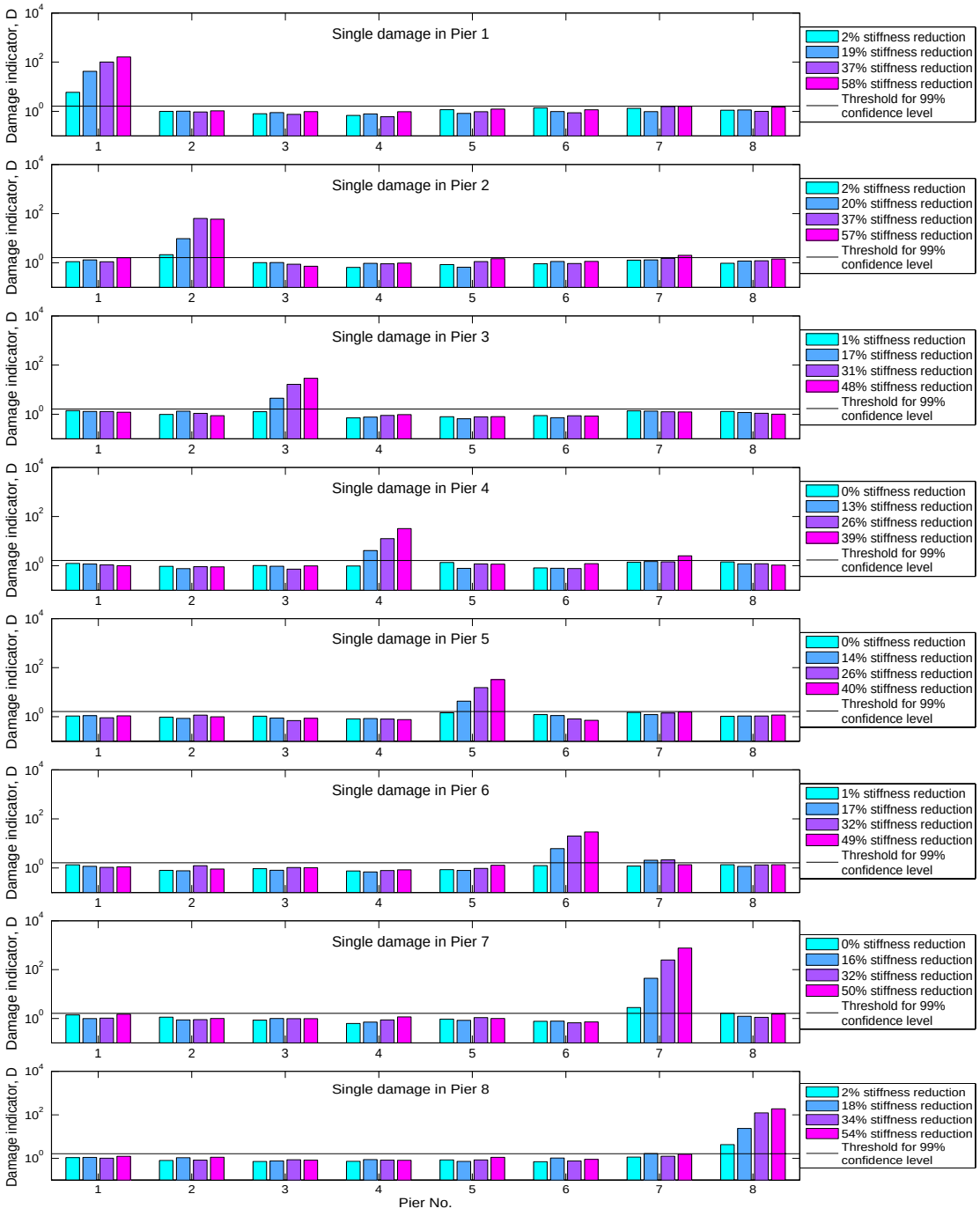
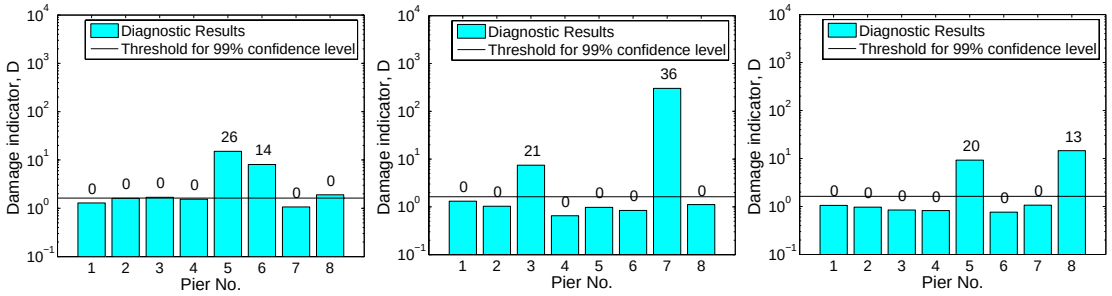
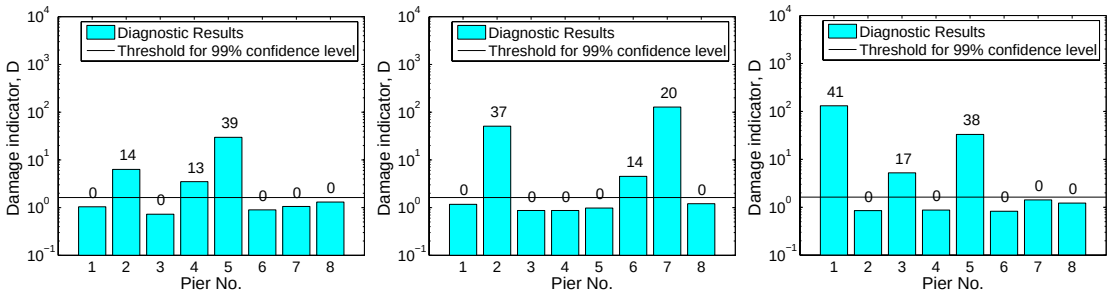


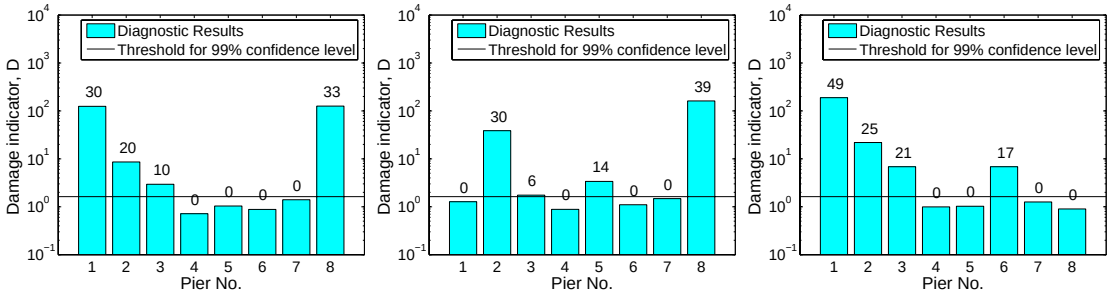
Fig. 4.10 Damage identification results for scenarios S1-S32 with damage in a single pier, along with the corresponding stiffness reduction computed using Eq. 4.6.



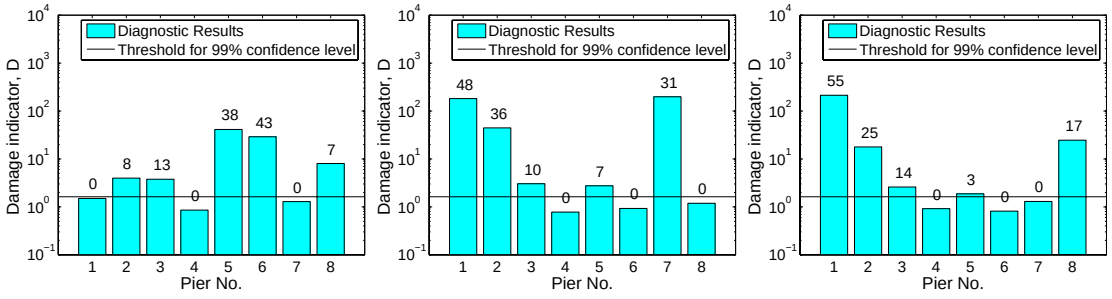
(a) 2 damage piers



(b) 3 damage piers

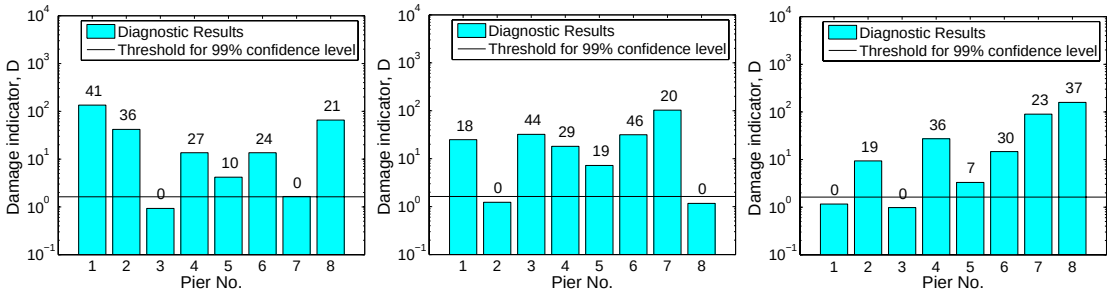


(c) 4 damage piers

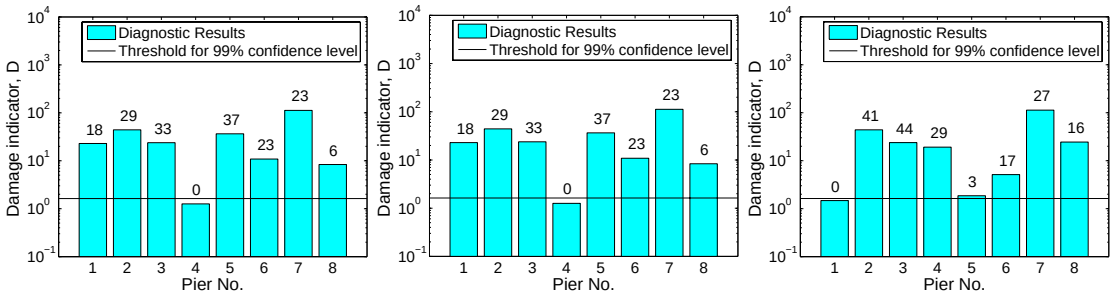


(d) 5 damage piers

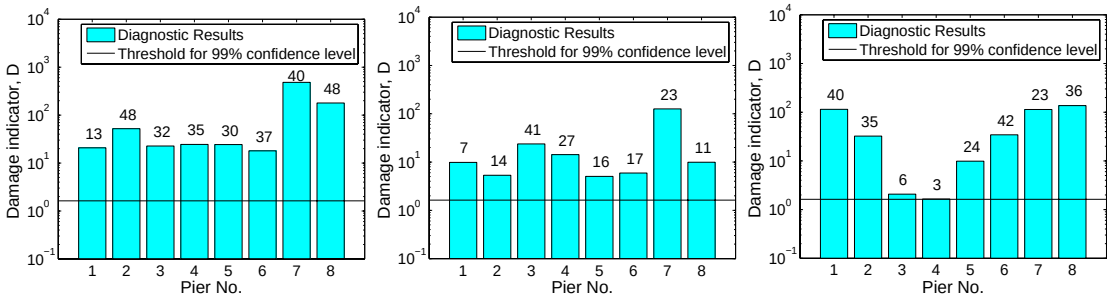
Fig. 4.11 Damage identification results for scenarios M1-M21 with damage in multi piers, along with the corresponding stiffness reduction computed using Eq. 4.6 shown on the top of each column.



(d) 6 damage piers



(e) 7 damage piers



(g) 8 damage piers

Fig. 4.11 Damage identification results for scenarios M1-M21 with damage in multi piers, along with the corresponding stiffness reduction computed using Eq. 4.6 shown on the top of each column.

4.11 References

Bishop, C. M. (1995). *Neural Networks for Pattern Recognition*, Oxford University Press.

Chang, F.K., (ed.) (1997). *Proc. of the First International Workshop on Structural Health Monitoring: Current Status and Perspectives*, September 18-20, 1997, Stanford, CA, USA.

Chang, F.K. (ed.) (2005). *Proc. of the 5th International Workshop on Structural Health Monitoring: Advancement and Challenge for Implementation*, September 12-14, 2005, Stanford, CA, USA.

Chen, S. and Billings, S. A. (1989). "Representation of Nonlinear Systems: the NARMAX Model." *Int. J. Control*, 49, 1013-1032.

Demuth, H. and Beale, M. (1998). *Neural Network Toolbox User's Guide, Version 3*, The MathWorks, Inc.

Doebling, S. W., Farrar, C. R., Prime, M. B., and Shevitz, D. W. (1996). "Damage Identification and Health Monitoring of Structural and Mechanical Systems from Changes in Their Vibration Characteristics: A Literature Review." *Report No: LA-13070-MS*, Los Alamos National Laboratory.

Elgamal, A., Yan. L., Yang, Z., and Conte, J. P. (2006). "Three-Dimensional Bridge-Foundation-Ground System: Part I Computational Model." *Journal of Structural Engineering*, ACSE, submitted for publication, Mar. 2006.

Hastie, T., Tibshirani, R., and Friedman, J. (2001). *The Elements of Statistical Learning: Data Ming, Inference, and Prediction*, Spring-Verlag, New York.

Hu, S. L. J., Hillier, T. S., and Stepanishen, P. (2002). "Data Analysis and Detection Methods for On-line Health Monitoring of Bridge Structures." *Report No: URITC 536112*, University of Rhode Island, Transportation Center.

Kent, D. C., and Park, R. (1971). "Flexural Members with Confined Concrete." *J. Struct. Div., ASCE*, 97(7), 1969–1990.

Korbicz, J., and Janczak, A. (1996). "A Neural Network Approach to Identification of Structural Systems." *Proceeding of the IEEE International Symposium on Industrial Electronics, ISIE'96*, June 17-20, 1996, Warsaw, Poland.

LeCun, Y., Bottou, L., Orr, G. B., and Muller, K. R. (1998). "Efficient Backprop." *Neural Networks---Tricks of the Trade*, Springer Lecture Notes in Computer Sciences, 1524, 5-50.

Leonatris, I. A. and Billings, S. A. (1985). "Input-Output Parametric Models for Nonlinear System." *Int. J. Control*, 41, 303-344.

Mander, J. B., Priestley, M. J. N., and Park, R. (1988). "Theoretical Stress-Strain Model for Confined Concrete." *Journal of the Structural Engineering*, 114(ST8), 1804-1826.

Miller, R. G. (1997). *Beyond ANOVA: Basics of Applied Statistics*, New York: Chapman & Hall.

McKenna, F. T., and Fenves, G. L. (2001). *The OpenSees Command Language Manual, Version 1.2*, Pacific Earthquake Engineering Research Center, University of California, Berkeley.

Scott, B. D., Park, R., and Priestley, M. J. N. (1982). "Stress-Strain Behavior of Concrete Confined by Overlapping Hoops at Low and High Strain Rates." *Journal of the American Concrete Institute*, 79(1), 13-27.

Sohn, H., and Farrar, C. R. (2001). "Damage Diagnosis Using Time Series Analysis of Vibration Signals." *Smart Materials and Structures*, 2001(10), 446-451.

Sohn, H., Farrar, C. R., Hemez, F., Czarnecki, J. J., Shunk, D., Stinemates, D., and Nadler, B. (2001). "A Review of Structural Health Monitoring Literature: 1996-2001." *Report No: LA-13976-MS*, Los Alamos National Laboratory.

Spacone, E., Filippou, F. C., and Taucer, F. F. (1996). "Fibre Beam-Column Model for Non-Linear Analysis of R/C Frames: Part I. Formulation." *Earthquake Engineering and Structural Dynamics*, 25(7), 711-725.

Wang, C. K., and Salmon, C. G. (1992). *Reinforced Concrete Design*, 5th Ed., HarperCollins Publisher Inc., New York, NY.

Yan, L., and Elgamal, A. (2006a). "A Vibration-Based Statistical Inference Approach for Structural Damage Detection." *Proc. of 4th World Conference on Structural Control and Monitoring*, July 11-13, 2006, San Diego, CA, U.S.A.

Yan, L., and Elgamal, A. (2006b). "A Statistical Inference Approach for Structural Damage Detection Using NARX Neural Networks." Journal paper in progress.

Yan, L., Elgamal, A., and Conte, J. P. (2006). "Three-Dimensional Bridge-Foundation-Ground System: Part II. Seismic Response." *Journal of Structural Engineering*, ACSE, submitted for publication, Mar. 2006.

Zhang, Y., Conte, J. P., Yang, Z., Elgamal, A., Bielak, J., and Acero, G. (2005). "Two-Dimensional Nonlinear Earthquake Response Analysis of a Bridge Ground System." *Earthquake Spectra*, submitted for publication, Dec. 2005.

5 A PCA-BASED NEURAL NETWORK APPROACH FOR BRIDGE PIER DAMAGE IDENTIFICATION

In this chapter, the PCA-based neural network approach (approach C in Chapter 1) is also applied for the same bridge pier damage identification problem. This study is also based on numerical simulation data generated using the virtual bridge testbed. In Section 5.1, earthquake-induced bridge pier damage is introduced, and a brief review is provided for the studies on neural-network-based structural damage identification. The analysis framework of this approach is described, along with the information about the virtual bridge testbed. Thereafter, the application is presented in details, including feature extraction using PCA, neural network development, and damage identification results. Finally, summary and conclusions are provided.

5.1 Introduction

When a bridge supported on piers (columns) is subjected to destructive earthquake excitation, a typical damage pattern includes formation of plastic hinges at the pier bases. Fig. 5.1 shows a dramatic example of such damage (Hanshin Expressway) during the 1995 Kobe, Japan Earthquake, and Fig. 5.2 depicts a similar pattern (Mingchou Bridge) during the 1999 Ji-Ji, Taiwan Earthquake. After an earthquake, it is essential to rapidly identify the occurrence, location, and severity of damage in each significant bridge of the transportation system.

In practice, highway bridges are typically inspected visually (e.g., Hu et al. 2002). However, the lower section of a bridge pier is often below water or buried

under a soil cover, potentially complicating matters. In addition, at low damage levels, no visible signs may be evident (such as surface cracks or spawling). These situations motivate the development of a sensitive and reliable approach to detect, locate, and assess the severity of damage in bridge piers.

A large body of structural health monitoring research has been dedicated to the development of vibration-based damage identification methods (Doebling et al. 1996; Masri et al. 2000; Sohn et al. 2001; Chang 2005). Within this framework, the damage patterns are correlated to the changes in structural dynamic response. In this regard, significant efforts have been made to identify the underlying mapping function with the help of supervised learning techniques, including neural networks (Ghaboussi 1993, 1994; Bishop 1995; Doebling et al. 1996; Adeli 2001; Sohn et al. 2001; Chang 2005).

Barai and Pandey (1995, 1997) explored the potential of using neural networks to identify damage in a truss bridge based on changes in vertical displacement time histories generated by a moving load. Liu and Sun (1997) investigated damage-induced changes in strain response of a simply supported three-span beam (bridge). For each vulnerable location, an associated network was trained to assess the severity of local damage based on axial strains generated by a moving load. Feng and Bahng (1999) and Feng et al. (2004) employed neural networks, with natural frequencies and mode shapes as input, to detect damage in bridges with jacketed reinforced concrete columns. Choi and Kwon (2000) developed a two-staged neural network approach to identify damaged members in a truss bridge, where changes in stain response and modal parameters are employed for network training.

The studies mentioned above are based on numerical simulation efforts, as the training of neural networks requires availability of data on potential damage patterns. Such data does not exist or is very scarce for actual structures. In this regard, a calibrated Finite Element (FE) model provides the means for simulating damage patterns and generating the necessary data. In all studies above, linear FE models were employed and damage was prescribed in the form of a reduction in element stiffness.

Different strategies were taken in the above studies for extracting damage-sensitive features from observed structural response in order to control the network input vector size. For approaches employing time history data as input directly, either a large time step (Barai and Panday 1995, 1997) or only peak values (Liu and Sun 1997) were used to reduce the number of input data points. In other situations (Feng and Bahng 1999; Choi and Kwon 2000; Feng et al. 2004), natural frequencies and mode shapes were used as the network input.

In this study, a novel approach is proposed for bridge pier damage identification. In this approach, feature extraction is performed using the Principal Components Analysis (PCA, Jolliffe 1986) technique, as a statistics-based information condensation procedure. Using these features as input, a neural network is then trained to detect and assess the severity of damage in all piers of a bridge simultaneously.

5.2 Analysis Framework

Fig. 5.3 shows the analysis framework of the proposed PCA-based neural network approach, consisting of two phases. In Phase I, a PCA-based neural network is built and trained using simulated damage data, based on the following steps (Fig. 5.3):

(1) For an existing bridge, a FE model is constructed and calibrated to capture the dynamic characteristics of the actual intact structure.

(2) Using the calibrated model, the dynamic response of the intact bridge to a selected external excitation is computed and recorded in terms of acceleration time histories at chosen locations (referred to as the simulated baseline).

(3) A range of potential damage patterns of interest is systematically simulated by reducing stiffness of the pier base elements. For each pattern, the bridge response to the same external excitation is evaluated and recorded.

(4) The damage-induced response deviation from the simulated baseline is computed.

(5) The PCA technique is applied to define a procedure to extract salient features from the computed response deviation.

(6) Using these features as input, a neural network is constructed and trained to detect and assess the severity of damage in all bridge piers simultaneously.

In Phase II, the trained neural network is applied to infer damage based on any observed change in structural response of the actual bridge, using the steps as described below (Fig. 5.3):

(1) An in-situ test is performed to record the dynamic response of the intact bridge to the selected external excitation. The response is recorded and referred to as the measured baseline.

(2) Using the same external excitation, in-situ tests of the bridge are performed periodically or after an earthquake event.

(3) The response deviation from the measured baseline is computed.

(4) Extract features form the computed deviation, using the procedure defined in Step 5 of Phase I.

(5) Apply the trained network to the extracted features to identify the occurrence and severity of damage in all bridge piers simultaneously.

In order to exercise and verify this approach, a refined three-dimensional (3D) FE model (referred to as Model I) is herein constructed and employed to represent an actual bridge as a virtual testbed. In addition, another relatively simple FE model of the same bridge (referred to as Model II) is built and employed to represent a numerical simulation effort. It is desirable to show that using simulated damage data from Model II, a PCA-based neural network can be trained to identify damage induced in Model I.

In the following sections, the FE modeling details of Models I and II are first presented, including information on damage simulation and data generation. Subsequently, the procedure of feature extraction using PCA is given, and the neural network configuration and training is described. The trained network is then tested by damage patterns generated by Models I and II, and the results are reported and discussed.

5.3 Virtual Bridge Testbed

5.3.1 PEER Humboldt Bay Middle Channel Bridge Testbed

The Humboldt Bay Middle Channel Bridge (HBB, near Eureka in northern California, Fig. 5.4) was selected by the Pacific Earthquake Engineering Research Center as a research testbed (http://peer.berkeley.edu/peertestbeds/humboldt.htm, Porter 2003). This testbed has motivated a wide range of studies on advanced

numerical simulation and seismic analysis (e.g., Zhang et al. 2005; Elgamal et al. 2006; Yan et al. 2006).

HBB is a 330m long, 9-span structure, supported by 8 single pier bents on foundation pile groups (Fig. 5.4). Herein, Models I and II are constructed in light of the structural configurations of HBB. The system modeling, damage simulation, and response computations are all performed using OpenSees (Open System for Earthquake Engineering Simulation), an object-oriented, open-source FE analysis framework (http://opensees.berkeley.edu, McKenna and Fenves 2001).

5.3.2 Model I

5.3.2.1 Bridge Modeling

In Model I (Fig. 5.5), the bridge superstructure is assumed linear in view of its high yield strength relative to the piers. In this regard, the bridge longitudinal girders and transversal brace beams are modeled using 3D linear elastic beam-column elements (Table 5.1). The bridge deck slabs (0.165m thick) are modeled using 3D linear shell elements. Herein, typical mass density ($\rho = 2300\text{kg/m}^3$), Young's Modulus ($E = 2.78\times10^7\text{kPa}$ corresponding to a compressive strength, f_c' of 5ksi), and Poisson's ratio ($\nu = 0.3$) of concrete are used (Wang and Salmon 1992).

Each bridge pier is modeled using five 3D fiber-section force-based beam-column elements with nonlinear fiber materials (Spacone et al. 1996). Discretization of the pier cross-section into concrete and steel fibers is shown in Fig. 5.6a, with confined and unconfined concrete inside and outside the shear reinforcement/stirrups, respectively. The uni-axial Kent-Scott-Park model (Kent and Park 1971; Scott et al.

1982; Mander et al. 1988) with degraded linear unloading/reloading stiffness (Fig. 5.6d) is used to model the concrete (Table 5.2). The reinforcing steel (Table 5.3) is represented (Fig. 5.6e) by a uni-axial bilinear model with kinematic hardening.

Quasi rigid elements (linear elastic beam-column elements with high Young's Modulus and large cross sectional area) are used to model the pier cap beams (Figs. 5.5b, 5.6c) assumed herein to be of adequate strength and high stiffness. The cap beams are connected to the bridge superstructure by perfect hinges using the equalDOF constraint (for translations only) in OpenSees (McKenna and Fenves 2001), assuming no shear key failure.

The modeled bridge foundation system consists of 2×2 pile groups, with 4 vertical circular piles (1.37m/54in diameter). Each pile is modeled using 3D fiber section, force-based beam-column elements with the nonlinear fiber materials defined in Tables 5.2 and 5.3 (Fig. 5.6b-e, Spacone et al. 1996). The pile caps are idealized as rigid frames (Figs. 5.5b, 5.6c).

In this model, the boundary condition along the pile foundations is simply defined by fixing the underground sections of each pile (Fig. 5.5a). In addition, the connections between the bridge superstructure ends and abutments are modeled as rollers (Fig. 5.5a), which only allow rotation and longitudinal displacement.

5.3.2.2 Damage Simulation Using Staged Analysis

Elgamal et al. (2006) and Yan et al. (2006) show that, as a bridge similar to HBB experiences an earthquake with a hazard level of 10% probability of exceedance in 50 years, the peak transversal bending curvature at the pier bases is about $0.001m^{-1}$. Such high curvature will induce nonlinear damage in the pier. In view of this, a

damage pattern in Model I can be realized using the following staged analysis procedure:

(1) The FE model, only consisting of independent individual bridge piers and foundation pile groups, is first built and the bridge own weight is applied (represented by an axial load of 8MN in each pier).

(2) At each pier top, one cycle of prescribed transversal displacement is statically applied in 200 steps, returning back to zero in the end. Different levels of peak bending moment/curvature can be generated at the pier bases by specifying the maximum displacement (denoted by D herein).

(3) The bridge superstructure FE model is activated to connect all bridge piers.

(4) Using the loadPattern remove feature in OpenSees (McKenna and Fenves 2001), a static force of 100kN transversally applied at the bridge center (Fig. 5.5b) is suddenly removed. Thereafter, the bridge undergoes free vibration and the structural dynamic response during the first 5 seconds (250 time steps of $\Delta t = 0.02\,\text{sec}$) is computed and recorded in terms of the transversal acceleration time histories at pier tops (Fig. 5.5a).

Herein, the selected external excitation is a transversal impulsive force applied at the bridge center, as simulated in step 4. For in-situ implementation, such an excitation can be generated by the impact of a hammer or the sudden release of a tension cable (e.g., Delaunay et al. 1999). In addition, as the impact force is relatively small, the structural response remains linear and can be easily normalized by the impact force amplitude. For the dynamic analysis in Step 4, Rayleigh damping is employed, with damping of about 5% in the frequency range of 1.5-10Hz.

5.3.2.3 Data Generation

Using the above staged analysis procedure, 32 patterns with a single damaged pier (4 for each pier) were first generated. For each pattern, the moment-curvature response at the damaged pier base is recorded as shown in Fig. 5.7. It is seen that as the prescribed value of D increases, both the peak curvature and the area within the hysteretic response loop increase, indicating a higher level of damage. In addition, it is noted that a larger D is required to induce a similar level of damage in a pier closer to the bridge center, which has a larger distance from the pier top to the ground surface (Fig. 5.5a).

In addition, the scenario of damage occurring at multi pier bases simultaneously is considered. For a given number (2-8) of damaged piers, 4 patterns were generated with randomly selected damaged piers and D values. Thus, a total of 28 patterns with multi damaged piers were generated using Model I. Later, both these 28 patterns and the 32 patterns with a single damaged pier will be used to test the trained neural network.

5.3.3 Model II

5.3.3.1 Bridge Modeling

Compared to Model I, Model II has the same configurations for the bridge superstructure, pier cap beams, and pile caps, the same boundary conditions, and the same numerical damping (Fig. 5.5). However, in Model II, the bridge piers and piles are simply modeled using 3D linear elastic beam-column elements (Table 5.4) with $E = 2.78 \times 10^7$ kPa and $\nu = 0.3$.

5.3.3.2 Model Calibration

Model II presented herein has been well calibrated to capture to the dynamic characteristics of Model I. Table 5.5 shows the comparison of the first 9 natural frequencies of these two models, which shows a great agreement with all relative difference less than 3%. In addition, the same transversal impulse excitation is applied to Model II and the dynamic response of the intact bridge is evaluated and compared with that of Model I. Fig. 5.8 shows the pier-top acceleration time histories of Model II (representing the simulated baseline state, Fig. 5.3) can well match those of Model I (representing the measured baseline state, Fig. 5.3).

5.3.3.3 Damage Simulation

In Model II, damage at a pier base is simply prescribed by partially reducing the stiffness (E) of the lowest pier element (1/5 of the total pier length). As an incipient plastic hinge might only partially reduce stiffness, damage severities of up to 60% are considered. For each damaged pier in a simulated pattern, the stiffness reduction is generated as an independent random value statistically following a uniform distribution between 0 and 60%.

5.3.3.4 Data Generation

Since the bridge has 8 piers, the total number of potential combinations of damaged piers is $\sum_{n=1}^{8} C_8^n = 255$. For each combination, 10 random damage patterns were generated. For every pattern, the bridge response to the applied impulse excitation was evaluated. As shown in Table 5.6, the simulated damage patterns (2550 in total) were divided into a training set (60% of the patterns, 6 for each combination), validation set (20% of the patterns, 2 for each combination), and test set (20% of the

patterns, 2 for each combination).

5.4 Feature Extraction Using PCA

As mentioned earlier, for every damage pattern, the bridge dynamic response to the impulse excitation is recorded in terms of the transversal acceleration time histories (250 time steps) at the 8 pier tops. The damage-induced deviation in the dynamic response can then be computed by subtracting the simulated/measured baseline (Fig. 5.8) from the simulated/measured structural response. Thus, using change in each time step as a feature, each damage pattern is described by a high-dimensional row feature vector $\mathbf{x}$ composed of 2000 entities (denoted by M).

Considering that only changes in $\mathbf{x}$ contain essential information of damage existence, location, and severity, it is desirable to capture this information using as few features as possible. In this regard, the efficient statistics-based feature extraction approach PCA (Jolliffe 1986) is adopted. PCA reduces the dimension of a data set by transforming the original possibly correlated features into a new set of uncorrelated features, so-called Principal Components (PCs).

Given the damage patterns in the training set (the total number denoted by N , Table 5.6), a $N \times M$ data matrix $\mathbf{X}$ is constructed. In this matrix, the *n*th row vector $\mathbf{x}^n = [x_1^n \ldots x_M^n]$ is the feature vector of the *n*th pattern, and each column represents one original feature (change in a time step in this study). The PCA of $\mathbf{X}$ is implemented following the standard procedure summarized below (Jolliffe 1986).

A new $N \times M$ data matrix $\mathbf{Z}$ is constructed in such a way that each feature is mean centered (i.e., remove overall average so as to retain the difference only), where the *n*th row vector $\mathbf{z}^n$ is computed as

$$\mathbf{z}^n = \mathbf{x}^n - \bar{\mathbf{x}} \tag{5.1}$$

where $\bar{\mathbf{x}} = \sum_{n=1}^{N} \mathbf{x}^n / N$. Thereafter, a $M \times M$ covariance matrix of the original features is evaluated as

$$\mathbf{V} = \mathbf{Z}^{\mathrm{T}}\mathbf{Z} \tag{5.2}$$

Descending ordered eigenvalues ($\lambda_1, \lambda_2 ... \lambda_M$) and their corresponding eigenvectors ($\boldsymbol{\alpha}_1, \boldsymbol{\alpha}_2 ... \boldsymbol{\alpha}_M$) of $\mathbf{V}$ are then computed, with the eigenvectors normalized to unit length. As such, the *i*th PC is the *i*th eigenvector associated with the *i*th largest eigenvalue. Thus, the PCs may be viewed as normalized basic shapes that represent damage-induced changes in the acceleration time histories (Hasselman et al. 1998).

Jolliffe (1986) shows that the *i*th eigenvalue λ_i is a valid measure of variance accounted for by the *i*th PC (as a new feature). Hence, when the data set is represented by the first *k* PCs, the retained variance of the original data set can be evaluated by the expression

$$\sum_{j=1}^{k} \lambda_j / \sum_{i=1}^{M} \lambda_i \tag{5.3}$$

The results show that the first 23 PCs retain 99.9% variance in the original data set. Consequently, PCA is seen to be quite efficient, compressing feature number from 2000 to 23 with only 0.1% loss of the total variance. Given the feature vector $\mathbf{x} = [x_1 \ldots x_M]$ of a damage pattern, a new feature vector $\mathbf{f} = [f_1 \ldots f_{23}]$ can then be computed using

$$\mathbf{f} = \left(\mathbf{x} - \bar{\mathbf{x}}\right)[\boldsymbol{\alpha}_1 \, \boldsymbol{\alpha}_2 \cdots \boldsymbol{\alpha}_{23}] \tag{5.4}$$

Finally, prior to using f as the input vector of neural network, the minimum-to-maximum range of each feature (f_i) is normalized to [-1, 1].

5.5 Neural Network for Damage Identification

In this study, a two-layered back-propagation neural network is employed to identify damage in all piers simultaneously. Bishop (1995) has shown that such networks using sigmoidal activation functions have strong capabilities for approximating continuous nonlinear functions.

Using the normalized feature vector $\mathbf{f}$ as input, the network has 23 input units and 8 linear output units (each corresponding to one pier). As recommended by LeCun et al. (1998), the number of hidden units is set to twice the number of input units (i.e., 46), thereby ensuring the network has adequate representing capability and to control the size of the neural network as well.

The feed forward network mapping from the input feature vector $\mathbf{f} = [f_i]$ to the output vector $\mathbf{y} = [y_k]$ is defined by (Bishop 1995)

$$y_k = \sum_{j=1}^{46} w_{kj}^{(2)} g(\sum_{i=1}^{23} w_{ji}^{(1)} f_i + w_{j0}^{(1)}) + w_{k0}^{(2)} \tag{5.5}$$

Here, $w_{ji}^{(1)}$ denotes the weight going from input feature *i* to hidden unit *j*, $w_{j0}^{(1)}$ denotes bias for hidden unit *j*, $g(\cdot)$ denotes the activation function for hidden units, $w_{kj}^{(2)}$ denotes the weight going from hidden unit *j* to output *k*, and $w_{k0}^{(2)}$ denotes bias for output unit *k*.

A hyperbolic tanh, as recommended by LeCun et al. (1998), is adopted as the activation function $g(\cdot)$ of hidden units

$$b_j = g(a_j) = 1.7159 \tanh(2a_j / 3) \tag{5.6}$$

where $a_j = \sum_{i=1}^{23} w_{ji}^{(1)} f_i + w_{j0}^{(1)}$ is the weighted sum of the inputs of hidden unit *j*, and b_j is the activation of hidden unit *j*.

Herein, each network output represents the stiffness reduction at one pier base and the corresponding target (t_k, desired output) is coded using

$$t_k = (\beta_k - 30) / 30 \tag{5.7}$$

where β_k is the actual percentage of stiffness reduction at the *k*th pier base. As such, the value range of each target (t_k) is normalized to [-1, 1]. Inversely, given a network output y_k, the identified percentage of stiffness reduction at the *k*th pier base (θ_k) can be computed.

The standard backpropagation algorithm (Bishop 1995) is adopted for network training by minimizing the standard sum-of-squares error given by

$$E = \frac{1}{2} \sum_{k=1}^{8} (y_k - t_k)^2 \tag{5.8}$$

Using data in the training and validation sets (Table 5.6), the standard backpropagation algorithm (Bishop 1995) is adopted for network training in this study. In order to best utilize the knowledge contained in available data, the damage patterns in the training set are repeatedly used and each training loop over all patterns is called an epoch. After each epoch, the errors of both the training set and the validation set are computed. Finally, the optimal network configuration is selected according to the minimum error of the validation set so as to avoid overfitting (Bishop 1995; Hastie et al. 2001).

5.6 Test Results and Discussion

5.6.1 Damage Patterns Generated Using Model II

In order to evaluate the performance, the trained network is first tested by the damage patterns in the test set (Table 5.6), which were generated using Model II. The results are shown in Fig. 5.9. The horizontal axis is the actual stiffness reduction, and the vertical axis is the stiffness reduction identified by the network. All results associated with a specific pier are presented in the corresponding subplot, in which each dot represents a pattern. It is seen that all dots fall closely to the diagonal lines, which indicate perfect identification. For all piers, the average error of the identified stiffness reduction is less than 1%, which is satisfactory.

5.6.2 Damage Patterns Generated Using Model I

For this approach, the ultimate goal is to use the trained network to identify damage occurring in the actual bridge (Model I herein). In this regard, the trained network need to be further tested by damage patterns generated using Model I so as to verify the efficiency of this approach.

5.6.2.1 Quantification of Damage in Model I

In order to compare with the network identification results, damage in Model I need to be also quantified in terms of percentage reduction in the gross cross-section flexural stiffness. Herein, the applied impulse excitation is relatively small so the bridge response remains linear no matter whether damage exists or not. Thus, given an intact/damage pattern, the gross flexural stiffness of a pier-base cross-section can be determined by computing the slope of the recorded linear moment-curvature response. Thereafter, the percentage stiffness reduction can be evaluated. Fig. 5.10 shows the

evaluation results for the 32 patterns (with a single damage pier) in Fig. 5.7. The horizontal axis is the peak transversal bending curvature (ϕ_m) induced at a pier base and the vertical axis is the corresponding percentage stiffness reduction (β). It is seen that ϕ_m and β show a strong positive linear correlation (Fig. 5.10), which can be approximately represented by the following bilinear model obtained by linear regression

$$\beta = \begin{cases} 38868\phi_{\mathrm{m}} - 19 & \text{if } \phi_{\mathrm{m}} > 0.0005 \\ 0 & \text{if } \phi_{\mathrm{m}} \le 0.0005 \end{cases} \tag{5.9}$$

Thus, given the ϕ_m of a damaged pier in Model I, the corresponding percentage stiffness reduction can be easily obtained using Eq. 5.8.

5.6.2.2 Patterns with a Single Damaged Pier

Now, the trained network is applied to the 32 patterns with a single damaged pier generated using Model I (Fig. 5.7) and the results are reported in Fig. 5.11. The horizontal axis is the stiffness reduction computed using Eq. 5.9, and the vertical axis is the stiffness reduction identified by the network. Fig. 5.11 shows that the network performs well as all results fall around the diagonal line, which indicates perfect identification. It is also noted that for high level damage, the network tends to conservatively overestimate the severity. The reason might be that in addition to stiffness reduction, nonlinear damage in Model I also induce residual deformation into the piers. This factor is not considered in the damage simulation using linear Model II.

5.6.2.3 Patterns with Multi Damaged Piers

Finally, the network is tested by the 28 patterns with multi damaged piers generated using Model I. The results are shown in Fig. 5.12, where the horizontal axis is pier num and the vertical axis is stiffness reduction. It is seen that for all patterns, the identified damage shows a good agreement with the actual value computed using Eq. 5.9. No matter how many piers are damaged, the network can always successfully identify the existence and severity of damage in all piers simultaneously. It is also observed that the network tends to overestimate the severity of damage, especially for high level damage, consistent with the phenomenon shown Fig. 5.11. For all piers, the average error of the identified stiffness reduction is less than 5%, which is small and acceptable.

5.7 Summary and Conclusions

A PCA-based neural network approach is developed to identify earthquake-induced plastic hinges in bridge piers (Fig. 5.1). Within this framework, network training requires data on potential damage patterns can be provided by numerical (FE) simulations. Herein, a refined 3D nonlinear FE model of HBB is employed to represent an actual bridge as a virtual testbed. In addition, another relatively simple linear FE model of the same bridge is built to represent the numerical simulation effort. Using these two models, the approach is exercised and the following conclusions can be made from this study:

(1) As an existing bridge is subjected to a relatively small excitation, the structural dynamic response remains linear. Within this context, it is viable to model the structure as linear and prescribe damage in the form of element stiffness

reduction. Thus, the simulation procedure can be significantly simplified and the computing time can be saved as well.

(2) For the efficiency of this approach, it is vital to have the employed numerical model well calibrated to capture the dynamic characteristics of the actual bridge.

(3) Based on simulation data, PCA is an efficient tool to extract essential features from damage-induced changes in the structural dynamic response (e.g., acceleration time histories).

(4) Using the PCA-extracted features as input, a neural network can be trained to detect and access the severity of damage in all piers simultaneously. In addition, the knowledge learned from the simulated damage patterns can be applied to infer damage in the actual bridge.

5.8 Acknowledgements

Support of this research is provided by the U.S. National Science Foundation, under ITR Grant No. 0205720. This support is gratefully acknowledged. The authors wish to thank Mr. Patrick Hipley, Dr. Cliff Roblee, Dr. Charles Sikorsky, Mr. Thomas Shantz, and Mr. Mark Yashinsky of Caltrans for providing all the requested information regarding the Humboldt Bay Middle Channel Bridge. Professor Gregory Fenves and Dr. Frank McKenna of U.C. Berkeley and Professor Michael Scott of Oregon State University helped with the OpenSees modeling and analysis phase. This assistance was most valuable and is highly appreciated.

5.9 Tables

Table 5.1 Model Parameters of 3D Linear Elastic Beam-Column Elements in the Bridge Superstructure

Modeled component	A (m^2)	I_z (m^4)	I_y (m^4)
Longitudinal girder	0.73	0.49	0.0094
Transversal beam	0.1	0.067	0.00017

Table 5.2 Constitutive Model Parameters (Fig. 5.6d) for Concrete Materials Used in Fiber Beam-Column Elements

Concrete01 material model in OpenSees	Confined concrete	Unconfined concrete
Compressive strength (f_c, kPa)	-3.45×10^4 (-5ksi)	-2.76×10^4 (-4ksi)
Strain at compressive strength (ε_c)	-0.004	-0.002
Crushing strength (f_{cu}, kPa)	-2.07×10^4 (-3ksi)	0
Strain at crushing strength (ε_{cu})	-0.014	-0.008

Table 5.3 Constitutive Model Parameters (Fig. 5.6e) for Steel Material Used in Fiber Beam-Column Elements

Steel01 material model in OpenSees	Reinforcing steel
Yield strength (f_y, kPa)	4.14×10^5 (60ksi)
Initial elastic tangent modulus (E_s, kPa)	2.0×10^8 (29000ksi)
Hardening ratio (b)	0.008

Table 5.4 Model Parameters of the 3D Linear Elastic Beam-Column Elements of Piers and Piles in Model II

Modeled component	A (m^2)	I_z (m^4)	I_y (m^4)
Pier	3.1	1.72	0.34
Pile	1.474	0.173	0.173

Table 5.5 Comparison of Natural Frequencies of Models I and II

	Natural frequency (Hz)				
	1st	2nd	3rd	4th	5th
Model I	0.719	1.495	1.730	2.120	2.663
Model II	0.738	1.500	1.728	2.114	2.664
Difference	2.6%	0.3%	0.1%	0.3%	0.04%
	Natural frequency (Hz)				
	6th	7th	8th	9th	
Model I	2.677	2.684	2.733	3.344	
Model II	2.678	2.684	2.734	3.352	
Difference	0.04%	0%	0.04%	0.2%	

Table 5.6 Number of Damage Patterns in Each Dataset Generated Using Model II

Dataset	Pattens for each potential combination of damaged piers	Total
Training set	6	1530
Validation set	2	510
Test set	2	510
Total	10	2550

5.10 Figures



Fig. 5.1 Damage at bridge pier bases occurring during the 1995 Kobe, Japan Earthquake (Thewalt 1995).



Fig. 5.2 Plastic hinge formation at pier bases of Mingchou Bridge during the 1999 Ji-Ji, Taiwan Earthquake (Uang et al. 1999).

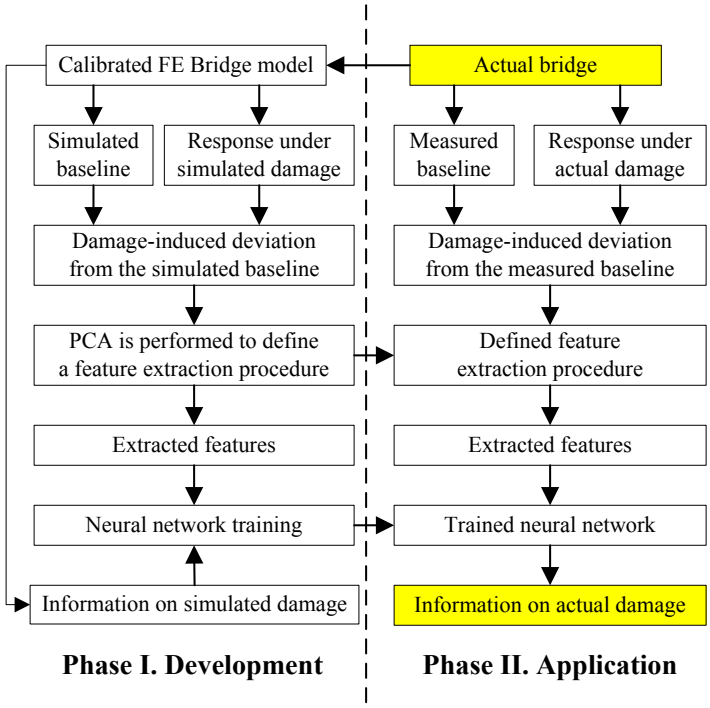


Fig. 5.3 Analysis framework of the employed PCA-based neural network approach.



Fig. 5.4 Sky view of Humboldt Bay Middle Channel Bridge (Courtesy of Caltrans).

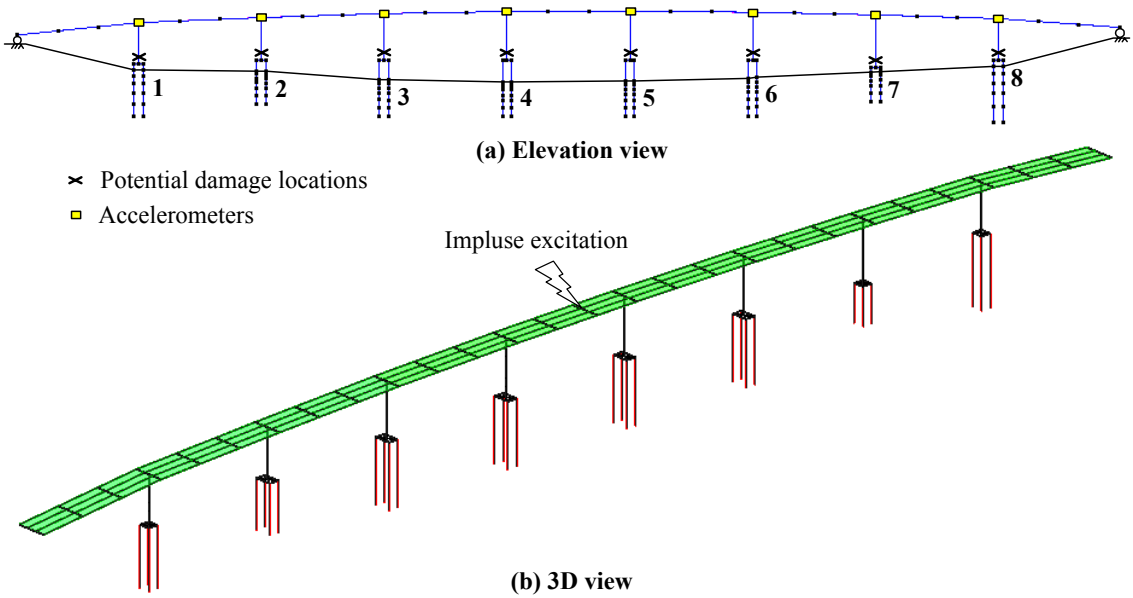


Fig. 5.5 3D FE model of bridge.

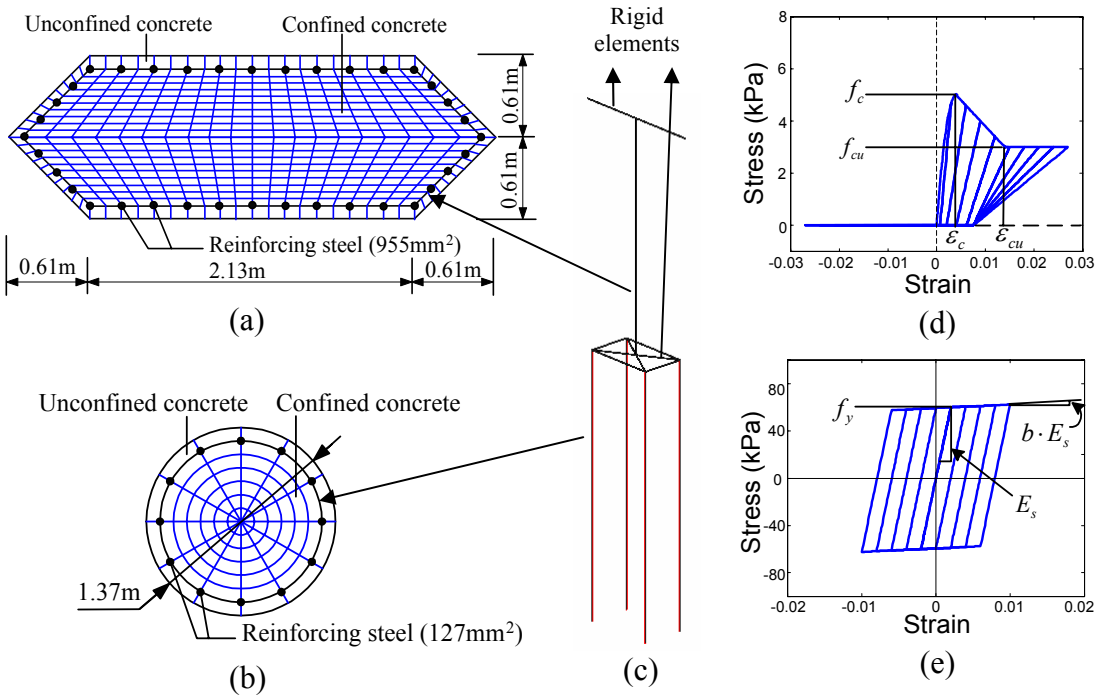


Fig. 5.6 Modeling of piers and pile groups in Model I, using fiber-section beam-column elements with uni-axial material constitutive models: (a) fiber discretization of pier cross-section; (b) fiber discretization of pile cross-section; (c) a pier supported by a 2×2 pile group; (d) concrete Kent-Scott-Park model with degraded linear unloading/reloading stiffness; and (e) reinforcing steel bilinear inelastic model with linear kinematic hardening.

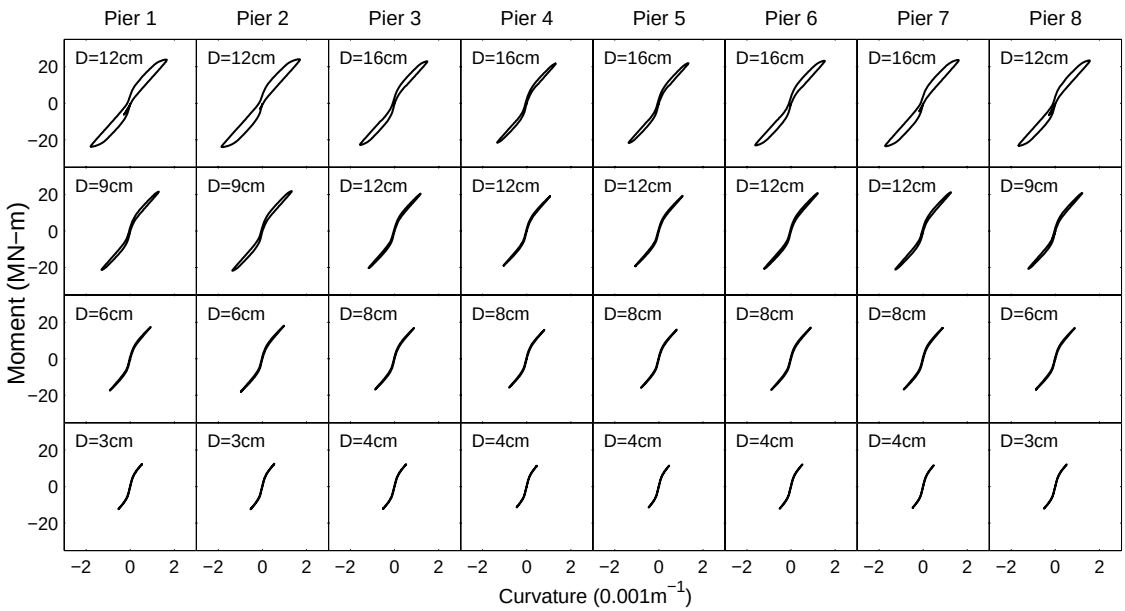


Fig. 5.7 32 patterns with a single damaged pier generated using Model I: (a) transversal moment-curvature response at the damaged pier base and (b) the maximum pier-top displacement *D*.

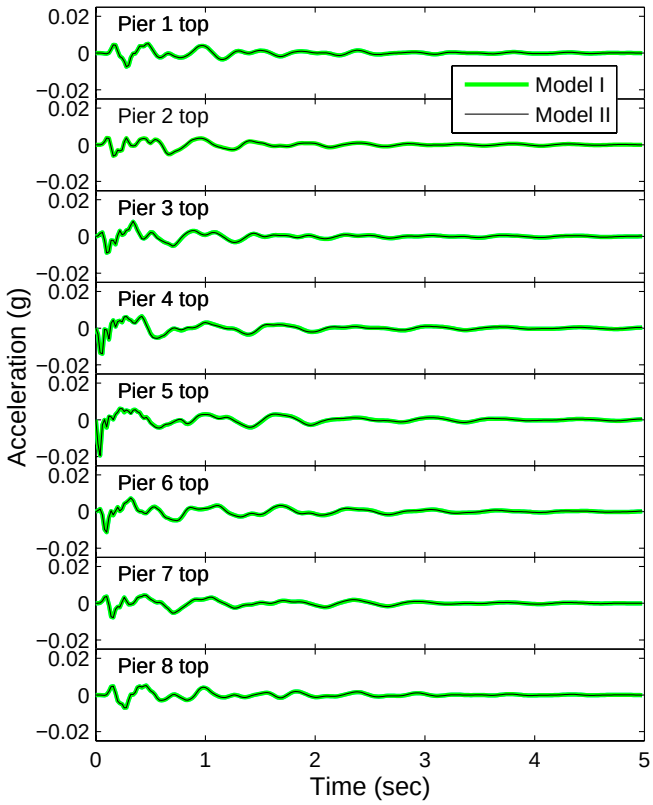


Fig. 5.8 Baseline pier-top acceleration response comparison of Models I and II.

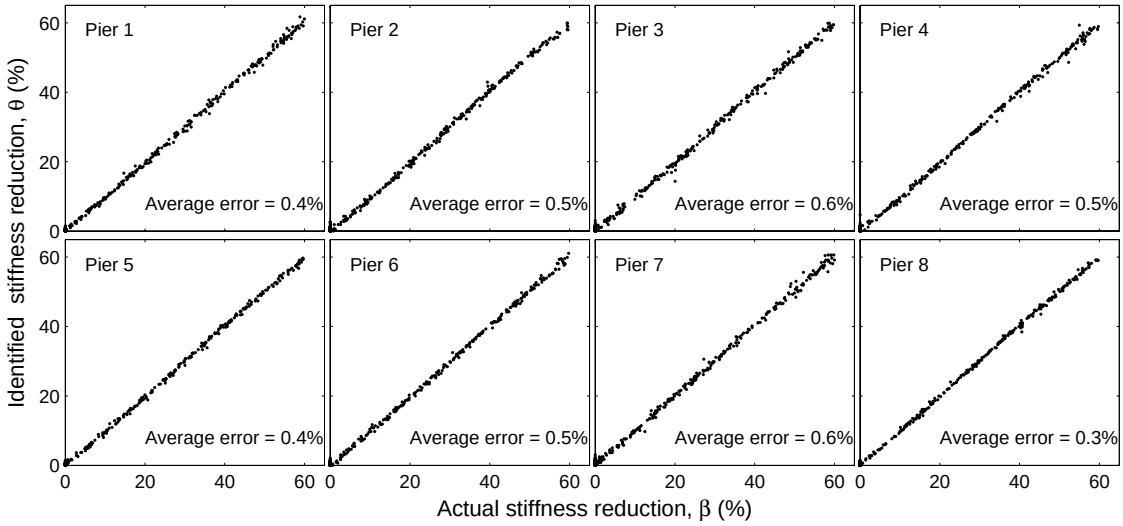


Fig. 5.9 Test results of applying the trained neural network to identify the damage patterns in the test set (Table 5.6) generated using Model II.

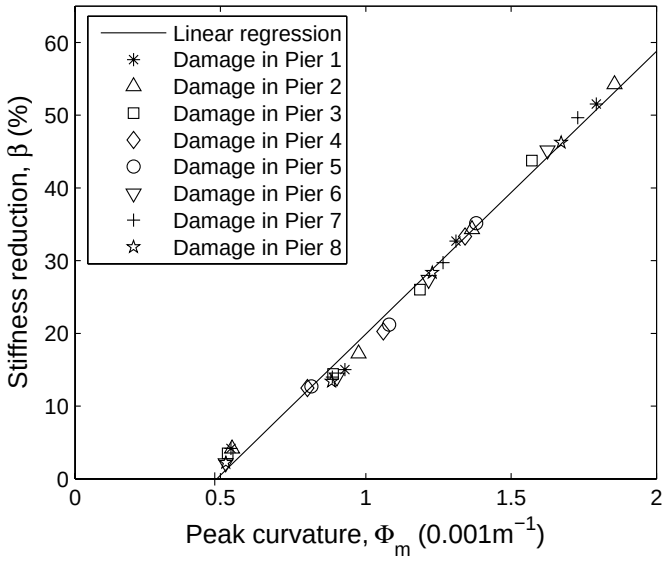


Fig. 5.10 Strong positive linear correlation between the damage-induced peak bending curvature ϕ_m at a pier cross-section near the base and corresponding reduction in gross flexural stiffness β.

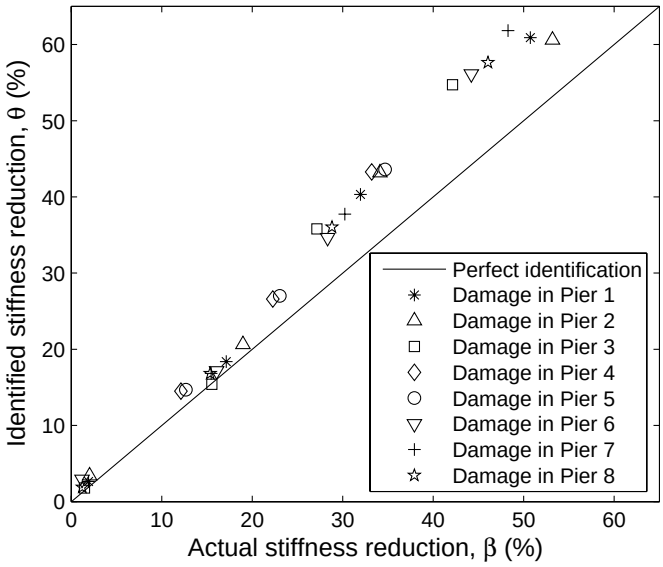


Fig. 5.11 Test results of applying the trained neural network to identify the 32 patterns with a single damaged pier (Fig. 5.7) generated using Model I.

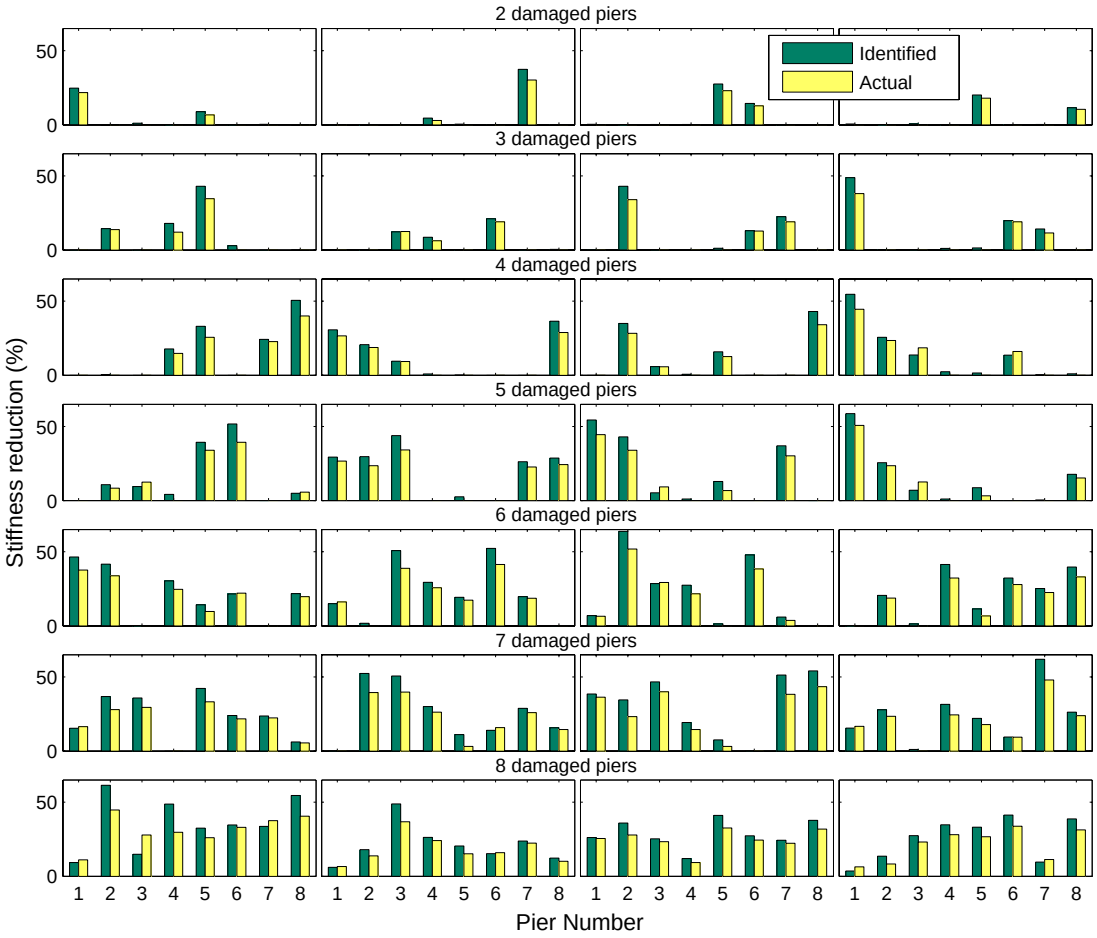


Fig. 5.12 Test results of applying the trained neural network to identify 28 patterns with multi damaged piers generated using Model I.

5.11 References

Adeli, H. (2001). "Neural Networks in Civil Engineering: 1989-2000." *Computed-Aided Civil and Infrastructure Engineering*, 16(2001): 126-142.

Barai, S. V., and Panday, P. C. (1995). "Vibration Signature Analysis Using Artificial Neural Networks." *Journal of Computing in Civil Engineering*, 9(4): 259-265.

Barai, S. V., and Panday, P. C. (1997). "Time-Delay Neural Networks in Damage Detection of Railway Bridges." *Advances in Engineering Software*, 28: 1-10.

Bishop, C. M. (1995). *Neural Networks for Pattern Recognition*, Oxford University Press.

Chang, F. K. (ed.) (2005). *Proceedings of the 5th International Workshop on Structural Health Monitoring 2005: Advancements and Challenges for Implementation*, Stanford, CA, September 12-14, 2005.

Choi, M. Y., and Kwon, I. B. (2000). "Damage Detection System of a Real Steel Truss Bridge by Neural Networks." *Proc. of the Smart Structure and Materials 2000: Smart Systems for Bridges, Structures and Highways*, Newport Beach, CA, USA, 3988: 295-306.

Delaunay, D., Grillaud, G., Bietry, J., and Sacre, C. (1999). "Wind Response of Long Span Bridges: In-Situ Measurements and Modal Analysis." *Proc. IMAC 17, the Int. Modal Analysis Conference*, Kissimmee, FL, 719-725.

Doebling, S. W., Farrar, C. R., Prime, M. B., and Shevitz, D. W. (1996). "Damage Identification and Health Monitoring of Structural and Mechanical Systems from Changes in Their Vibration Characteristics: A Literature Review." *Report No: LA-13070-MS*, Los Alamos National Laboratory.

Elgamal, A., Yan. L., Yang, Z., and Conte, J. P. (2006). "Three-Dimensional Bridge-Foundation-Ground System: Part I Computational Model." *Journal of Structural Engineering*, ACSE, submitted for publication, Mar. 2006.

Feng, M., and Bahng, E. (1999). "Damage Assessment of Bridge with Jacketed RC Column Using Vibration Test." *Proc. of the Smart Structure and Materials 1999: Smart Systems for Bridges, Structures and Highways*, SPIE, 3671, 316-327.

Feng, M., Kim, D. K., Yi, J. H., and Chen, Y. (2004). "Baseline Models for Bridge Performance Monitoring." *Journal of Engineering Mechanics*, 130(5): 562-569.

Ghaboussi, J. (1993). "An Overview of the Potential Applications of Neural Networks in Civil Engineering." *Proc. of the Structures Congress'93*, ASCE, Irvine, CA.

Ghaboussi, J. (1994). "Some Applications of Neural Networks in Structural Engineering." *Proc. of the Structures Congress'94*, ASCE, Atlanta, GA.

Hasselman, T. K., Anderson, M. C., and Gan, W. (1998). "Principal Components Analysis for Nonlinear Model Correlation, Updating and Uncertainty Evaluation." *Proc. of the 16th International Modal Analysis Conference*, SPIE, Santa Barbara, CA.

Hastie, T., Tibshirani, R., and Friedman, J. (2001). *The Elements of Statistical Learning: Data Ming, Inference, and Prediction*, Spring-Verlag, New York.

Hu, S. L. J., Hillier, T. S., and Stepanishen, P. (2002). "Data Analysis and Detection Methods for On-line Health Monitoring of Bridge Structures." *Report No: URITC 536112*, University of Rhode Island, Transportation Center.

Jolliffe, I. T. (1986). *Principal Components Analysis*, Spring-Verlag, New York.

Kent, D. C., and Park, R. (1971). "Flexural Members with Confined Concrete." *J. Struct. Div., ASCE*, 97(7), 1969–1990.

LeCun, Y., Bottou, L., Orr, G. B., and Muller, K. R. (1998). "Efficient Backprop." in *Neural Networks-Tricks of the Trade*, Springer Lecture Notes in Computer Sciences, 1524: 5-50.

Liu, P. L., and Sun, S. C. (1997). "The Application of Artificial Neural Networks on the Health Monitoring of Bridges." *Proc. of the 1st International workshop on structural Health Monitoring: Structural Health Monitoring: Current Status and Perspectives*, Stanford University, Palo Alto, CA, 103-110.

Mander, J. B., Priestley, M. J. N., and Park, R. (1988). "Theoretical Stress-Strain Model for Confined Concrete." *Journal of the Structural Engineering*, 114(ST8), 1804-1826.

Masri, S. F., Smyth, A. W., Chassiakos, A. G., Caughey, T. K., and Hunter, N. F. (2000). "Appliction of Neural Networks for Detection of Changes in Nonlinear Systems." *Journal of Engineering Mechanics*, 2000(July), 666-676.

McKenna, F. T., and Fenves, G. L. (2001). *The OpenSees Command Language Manual, Version 1.2*, Pacific Earthquake Engineering Research Center, University of California, Berkeley.

Porter, K. A. (2003). "An Overview of PEER's Performance-Based Earthquake Engineering Methodology." *Proc. Ninth International Conference on Applications of Statistics and Probability in Civil Engineering (ICASP9)*, Civil Engineering Risk and Reliability Association (CERRA), San Francisco, CA.

Scott, B. D., Park, R., and Priestley, M. J. N. (1982). "Stress-Strain Behavior of Concrete Confined by Overlapping Hoops at Low and High Strain Rates." *Journal of the American Concrete Institute*, 79(1), 13-27.

Sohn, H., Farrar, C. R., Hemez, F., Czarnecki, J. J., Shunk, D., Stinemates, D., and Nadler, B. (2001). "A Review of Structural Health Monitoring Literature: 1996-2001." *Report No: LA-13976-MS*, Los Alamos National Laboratory.

Spacone, E., Filippou, F. C., and Taucer, F. F. (1996). "Fibre Beam-Column Model for Non-Linear Analysis of R/C Frames: Part I. Formulation." *Earthquake Engineering and Structural Dynamics*, 25(7), 711-725.

Thewalt, C. R. (1995). "Failed Column Showing Splice Failures." The Earthquake Engineering Online Archive, University of California, Berkeley, CA.
< http://nisee.berkeley.edu/elibrary/ >

Uang, C. M., Elgamal, A., Li, W. S., and Chou, C. C. (1999). "Ji-Ji, Taiwan Earthquake of September 21, 1999: A Brief Reconnaissance Report." *Department Report*, Department of Structural Engineering, University of California, San Diego, CA.

Wang, C. K., and Salmon, C. G. (1992). *Reinforced Concrete Design*, 5th Ed., HarperCollins Publisher Inc., New York, NY.

Yan, L., Elgamal, A., and Conte, J. P. (2006). "Three-Dimensional Bridge-Foundation-Ground System: Part II. Seismic Response." *Journal of Structural Engineering*, ACSE, submitted for publication, Mar. 2006.

Zhang, Y., Conte, J. P., Yang, Z., Elgamal, A., Bielak, J., and Acero, G. (2005). "Two-Dimensional Nonlinear Earthquake Response Analysis of a Bridge Ground System." *Earthquake Spectra*, submitted for publication, Dec. 2005.

6 NEURAL NETWORKS AND PRINCIPAL COMPONENTS ANALYSIS FOR STRAIN-BASED VEHICLE CLASSIFICATION

In this chapter, the combination of neural networks and PCA is employed to develop a strain-based vehicle classification approach, based on the strain-video dataset from the UCSD bridge-deck testbed (Fraser et al. 2002; Fraser 2006). In the following sections, a brief review on vehicle classification/identification approaches is first provided. The bridge-deck testbed and strain-video data are introduced, followed by results from a preliminary analysis. Thereafter, the strain-based vehicle classification approach is presented in detail, including information on the analysis framework, feature extraction using PCA, neural network development, analysis results and discussions.

6.1 Introduction

A large database has been complied of traffic crossing over a set of bridge-deck panels on campus at the University of California, San Diego (UCSD). Deck strains caused by traffic, along with synchronized video clips have been archived (over 400,000 records). As such, this dataset allows for relating a measured strain signal to the corresponding vehicle characteristics. Availability of video greatly enhances the range of extractable knowledge, allowing the "input" loading to be systematically correlated to the "output" strains. This archived and readily available dataset (http://healthmonitoring.ucsd.edu) may be of use for a wide range of data fusion, computer vision, and machine learning investigations.

In this study, the recorded dataset is used to develop a strain-based vehicle classification approach, as a machine learning application. A neural network technique (Bishop 1995) in combination with Principal Components Analysis (PCA, Jolliffe 1986) is employed. The developed approach serves as a demonstration of possible applications using such a video and strain-sensor dataset.

Recently, a variety of algorithms have been proposed to identify vehicle class, weight, and speed. For instance, vehicle parameters are derived from traffic-induced signatures of Inductive Loop Detectors (ILDs, e.g., Athol 1965; Sun and Ritchie 2000; Oh et al. 2001; Sun et al. 2003). Based on recent advances in computer vision, image analysis techniques have also been applied to develop vehicle classification systems (e.g., Lu 1989; Yuan et al. 1994; Achler and Trivedi 2004; Chang et al. 2004). Augmentation of such image approaches with strain data (reflecting vehicle load) can only provide for added accuracy and versatility.

6.2 UCSD Bridge-Deck Testbed and Strain-Video Database

Four bridge-deck panels (measuring 4.58m in length and 4×2.29m in width) were installed in 1996 along a roadway on the UCSD campus (located between the two white lines in Fig. 6.1, Zhao 1999). Three of those panels were built of composite materials and instrumented to verify durability and potential for long-term usage (Zhao 1999). During 1999-2001, periodic measurements (including data from the 16 gages, Fig. 6.2) demonstrated satisfactory performance as anticipated.

In 2002, the site was adopted as a Testbed for continuous monitoring (Fraser et al. 2002; Elgamal et al. 2003; Fraser 2006). In addition to the 16 strain gages (Fig. 6.2), a video camera was integrated into the monitoring system to gather image information

of traffic (Fraser 2006). Through the data acquisition system, live data from the strain gages and the video camera were synchronized and stored in a temporary buffer. A computer (Perl) program was then applied to the strain data to identify events of vehicles crossing the deck. For each event, a record was archived into a database, composed of 16 strain time histories (one from each gage, with a duration of 2000 time steps, $\Delta t = 0.005\,\text{sec}$) and 40 video images (4 per second). From October 2003 to April 2005, over 400,000 vehicle records were archived in the database, with worldwide access through the website http://healthmonitoring.ucsd.edu. The records include a wide variety of vehicle types ranging from 2-axle passenger cars to 5-axle semi-trailer trucks.

As summarized in Sun et al. (2003), different categorization schemes have been adopted in recent vehicle classification studies. In these schemes, the numbers of classes range from 3 (e.g., Wei et al. 2003) to 7 (e.g., Sun and Ritchie 2000; Sun et al. 2003). According to a Federal Highway Administration (FHWA) standard, vehicles are categorized into the six classes, passenger cars, motorcycles, buses, other 2-axle 4-tire vehicles (including vans, pickup trucks, and SUVs), single-unit 2-axle 6-tire or more trucks, and combination trucks. In this study, a similar categorization scheme is defined to sort vehicles into the 5 classes (Table 6.1, Fig. 6.3), Small vehicles, Medium trucks, Buses/Large trucks, 3-axle trucks, and Combination trucks.

As most of the strain gages are located on the Eastbound lane (Fig. 6.2), this study only focuses on records of vehicles traveling in this direction (about 300,000 of the available 400,000). Furthermore, for this relatively simple structural system, the strains recorded by the different gages were found to be highly correlated. In view of

this fact, only the strain data of Gage A (near the mid-span, Fig. 6.2) are utilized in this study.

Following the classification scheme of Table 6.1, a subset of about 9,000 records (Table 6.2) was manually labeled by visual inspection of the archived images. The labeled records of each vehicle class are divided (Table 6.2) into a training set (50% of the records), validation set (20% of the records), and test set (30% of the records) composed of randomly selected records.

6.3 Preliminary Analysis

6.3.1 Characteristics of Traffic-Induced Strain Response

The nature and characteristics of the recorded traffic-induced strain time histories are first investigated. Fig. 6.4 shows a representative record corresponding to a 4-axle semi-trailer truck (1F+2M+1R, Table 6.1). When a vehicle axle crosses the deck, the strain response increases significantly. In this record (Fig. 6.4), 4 major peaks are visible in the time history, each corresponding to an axle. In addition, the spacing of these peaks is consistent with the distance between the axles. For instance, the 2nd peak is very close to the 3rd peak as these axles are closely spaced, and the magnitude of each strain peak (Fig. 6.4) primarily depends on the axle weight (Fraser 2006).

A Matlab program is applied to each strain time history to automatically identify the four basic parameters, ε_P (maximum peak strain), T_S (time of the first axle reaching the deck), T_E (time of the last axle leaving the deck), and $D = T_E - T_S$ (time taken by a vehicle to cross the deck, Fig. 6.4). The value of D depends on both the vehicle speed and the wheelbase (distance between the first and last axles). In this

sense, these two parameters are coupled. As the variation of recorded speed in this testbed is relatively small (due to the 25 mile-per-hour speed limit), the parameter D is actually heavily influenced by the wheelbase.

6.3.2 Vehicle Classification Based on Bayesian Inference

For each vehicle class, a normalized histogram of maximum peak stain (ε_P) and event duration (D) is generated for the training set records of Table 6.2. These histograms are shown in Fig. 6.5, where the vertical axis represents normalized count (i.e., records in a bin divided by the total number in class). It is seen that the distributions of C_1, C_2, and C_3 display little scatter, while both C_4 and C_5 show a large ε_P variation denoting that peak axle weight in these two truck classes falls within a wide range. In addition, the longer C_5 wheelbases clearly result in larger D values. Finally, Fig. 6.5 shows that the distributions of C_3 and C_4 overlap as a significant number of vehicles in these two classes are similar in peak axle weight and wheelbase length (Fig. 6.3).

Based on these normalized histograms (Fig. 6.5), the ε_P-D joint probability distribution function for each vehicle class, $\Pr(\varepsilon_P, D \mid C_k)$ is estimated. The posterior probability of a vehicle record belonging to class C_k given ε_P and D ($\Pr(C_k \mid \varepsilon_P, D)$, denoted by p_k) can be inferred using Bayes' Rule (Russell and Norvig 1995):

$$p_k = \Pr(C_k \mid \varepsilon_P, D) = \frac{\Pr(\varepsilon_P, D \mid C_k)\Pr(C_k)}{\Pr(\varepsilon_P, D)} = \frac{\Pr(\varepsilon_P, D \mid C_k)\Pr(C_k)}{\sum_{j=1}^{5}[\Pr(\varepsilon_P, D \mid C_j)\Pr(C_j)]} \quad (6.1)$$

where, in this simple framework, $\Pr(C_k)$ is 1/5, $k = 1, 2...5$, assuming equal prior probability for all classes.

Thus, a preliminary classification can be made by sorting vehicles into the class associated with the highest posterior probability (p_k) computed using Eq. 6.1. Table 6.3 shows the classification results for the test set of Table 6.2 using this Bayesian inference approach. In general, the success rates are not high except for C_1 and most failures are misclassifications between neighboring classes mainly due to the overlap of the ε_P - D distributions (Fig. 6.5). Particularly, the heavy overlap of C_4 with its neighbors (C_3 , C_5) reduces the success rate to about 50%. Clearly, the parameters ε_P and D alone do not provide sufficient information for vehicle classification. Consequently, the approach based on PCA and the neural network technique is employed in the next section.

6.4 Analysis Procedure

The classification approach adopts a statistical pattern recognition paradigm (Bishop 1995), consisting of feature extraction and neural network development. For this supervised learning application, training, validation, and test sets must be available, with the approach implemented according to the following steps (Fig. 6.6):

(1) For each traffic-induced strain time history, T_S and T_E are identified (Fig. 6.4).

(2) The strain response between T_S and T_E is re-sampled to generated a normalized time history composed of $M = 500$ time steps. For instance, Fig. 6.7 shows the original and normalized strain time histories for 8 representative vehicle records.

(3) As an information condensation technique, PCA is applied to extract the essential features of each normalized strain time history (27 features herein, denoted by $f_1, f_2 ... f_i ... f_{27}$).

(4) The minimum-to-maximum range of each feature f_i is set to [-1, 1], resulting in normalized features denoted by f_i'.

(5) For each record, the neural network input vector is now defined by $\mathbf{F} = [f_1' f_2' \ldots f_{27}']$.

(6) Using $\mathbf{F}$ as the input, a two-layered back-propagation neural network is constructed and trained to infer the posterior probabilities of vehicle classes ($\Pr(C_k \mid \mathbf{F})$, denoted by y_k, $k = 1, 2...5$). As such, a vehicle record is sorted into the class associated with the highest posterior probability, a value that can be interpreted as the confidence of classification.

In steps 3 and 4, only vehicle records in the training set are employed to define the feature extraction procedure. The defined procedure is then applied to the validation and test sets so that comparable features can be extracted. Thus, the neural network training is based on the training set, and the validation set is utilized to determine the optimal network configuration (Bishop 1995). Finally, the test set is used to objectively evaluate the trained network performance.

As shown in Table 6.2, the number of labeled records for each class is significantly different as buses and personal vehicles are predominant on campus. Such unbalanced data structure might potentially induce bias in network training. In order to address this issue, two scenarios of data configuration are studied. In scenario

1, the training, validation, and test sets of Table 6.2 are employed. Copies of randomly selected records are added to classes C_1, C_2, C_4, and C_5, to match the 1663 records of class C_3. In scenario 2, only 600 randomly selected labeled records from each class are employed on account of the sparsely populated class C_4 (with 607 records only). In this case, the training, validation, and test sets are composted of 400, 100, and 100 randomly selected records, respectively. In this study, the proposed approach is applied to both scenarios 1 and 2 for comparison purposes.

6.5 Feature Extraction Using PCA

The shape of the strain time history contains information (Fig. 6.4) related to the axle number, distribution, and weights. Considering that only the difference between strain time history shapes is useful for classification, it is desirable to capture this information using as few features as possible. In this regard, the efficient statistics-based feature extraction approach PCA (Jolliffe 1986) is adopted. PCA reduces the dimension of a data set by transforming the original possibly correlated features into a new uncorrelated set, so-called Principal Components (PCs). These PCs are ordered so that the first few retain most of the variance displayed by the original features.

6.5.1 Computational Procedure

For a training set of N records, a $N \times M$ data matrix $\mathbf{X}$ can be constructed. In this matrix, the *n*th row vector $\mathbf{x}^n = [x_1^n \ldots x_M^n]$ is the normalized strain time history of the *n*th record (Fig. 6.7), and the elements of each column represent one original

feature (a normalized time step in this study). The PCA of **X** is implemented following the procedure summarized below (Jolliffe 1986).

A new $N \times M$ data matrix **Z** is constructed in such a way that each feature is mean centered (to remove the overall average and retain the difference only), with the *n*th row vector $\mathbf{z}^n$ computed as

$$\mathbf{z}^n = \mathbf{x}^n - \bar{\mathbf{x}} \tag{6.2}$$

where $\bar{\mathbf{x}} = \sum_{n=1}^{N} \mathbf{x}^n / N$. Thereafter, a $M \times M$ covariance matrix of the original features is evaluated as

$$\mathbf{V} = \mathbf{Z}^{\mathrm{T}}\mathbf{Z} \tag{6.3}$$

Descending ordered eigenvalues ($\lambda_1, \lambda_2 ... \lambda_M$) and the corresponding eigenvectors ($\boldsymbol{\alpha}_1, \boldsymbol{\alpha}_2 ... \boldsymbol{\alpha}_M$) of **V** are then computed and normalized to unit length. As such, the *i*th PC is the *i*th eigenvector associated with the *i*th largest eigenvalue. Thus, the PCs may be viewed as basic shapes that can be used to represent the normalized strain time histories (Hasselman et al. 1998), and from which the original records can be reconstructed.

Jolliffe (1986) shows that the *i*th eigenvalue λ_i is a valid measure of variance accounted for by the *i*th PC (as a new feature). Hence, when the data set is represented by the first *k* PCs, the retained variance of the original data set can be evaluated by the expression

$$\sum_{j=1}^{k} \lambda_j / \sum_{i=1}^{M} \lambda_i \tag{6.4}$$

Furthermore, for a given normalized strain time history $\mathbf{x} = [x_1 \dots x_M]$, a new row feature vector $\mathbf{f} = [f_1 \dots f_k]$ can be computed by

$$\mathbf{f} = (\mathbf{x} - \bar{\mathbf{x}})[\boldsymbol{\alpha}_1 \, \boldsymbol{\alpha}_2 \cdots \boldsymbol{\alpha}_k] \tag{6.5}$$

Inversely, for a given $\mathbf{f}$ vector, the corresponding strain time history can be reconstructed by

$$\tilde{\mathbf{x}} = \mathbf{f}[\boldsymbol{\alpha}_1 \, \boldsymbol{\alpha}_2 \cdots \boldsymbol{\alpha}_k]^{\mathrm{T}} + \bar{\mathbf{x}} \tag{6.6}$$

6.5.2 PCA Representation

For illustration, the PCA results for scenario 1 are presented in Figs. 6.8-6.10. Fig. 6.8a shows the computed eigenvalues of the covariance matrix $\mathbf{V}$, dropping rapidly as the number increases. This implies that most variance in the data set is represented by the first few PCs. The same conclusion can be also inferred from Fig. 6.8b, which shows the percent of variance accounted for using the first k PCs (Eq. 6.4). As the number k of employed PCs increases, the represented variance increases accordingly, and reaches as much as 99% with $k = 27$. Consequently, PCA is seen to be efficient, compressing the feature number from 500 to 27 with only 1% loss of the total variance in the original data set.

Fig. 6.9 shows the computed $\mathbf{f}$ vectors (with $k = 27$ in Eq. 6.5) for the 8 representative vehicle records of Fig. 6.7. It is seen that the projected values (f_i) for the first few dominant PCs are significantly larger, and $\mathbf{f}$ vectors of each class are distinctly different. The $\mathbf{f}$ vectors of the last four records display some similarity (Fig. 6.9), as they all represent combination trucks (class C_5).

In order to illustrate adequacy of the selected $k = 27$ PCs, Fig. 6.10 shows the reconstructed strain time histories for the 8 representative vehicle records of Fig. 6.7, using Eq. 6.6. It is seen (for $k = 5$ and $k = 27$) that as the number of employed PCs increases, the reconstructed curves closely match the original measurements. A satisfactory representation is achieved using the first 27 PCs. A similar outcome was also observed for scenario 2 where more than 99% variance of the dataset was represented by the first 27 PCs.

6.6 Neural Network Development

In this vehicle classification study, a two-layered back-propagation neural network is employed as the statistical pattern classifier. Bishop (1995) shows that such a network, with sigmoidal activation functions, provides strong capabilities for approximating continuous nonlinear systems.

6.6.1 Network Configuration

The network with input vector $\mathbf{F} = [F_i]_{1\times q}$ is comprised of q input units and 5 output units (each corresponding to a vehicle class, Table 6.1). As recommended by LeCun et al. (1998), the number of hidden units is set to twice the number of input units (i.e., $2q$), thereby allowing adequate representation capability while controlling the neural network size.

The feed forward network mapping from the input feature vector $\mathbf{F} = [F_i]_{1\times q}$ to the output vector $\mathbf{y} = [y_k]_{1\times 5}$ is defined by (Bishop 1995):

$$y_k = g\left(\sum_{j=1}^{2q} w_{kj}^{(2)} h\left(\sum_{i=1}^{q} w_{ji}^{(1)} F_i + w_{j0}^{(1)}\right) + w_{k0}^{(2)}\right) \tag{6.7}$$

where, $w_{ji}^{(1)}$ denotes weight going from input unit i to hidden unit j, $w_{j0}^{(1)}$ denotes bias for hidden unit j, $h(\cdot)$ denotes activation function for hidden units, $w_{kj}^{(2)}$ denotes weight going from hidden unit j to output unit k, $w_{k0}^{(2)}$ denotes bias for output unit k; and $g(\cdot)$ denotes activation function for output units.

In order to speed-up convergence of the network training phase, a hyperbolic tanh is adopted as the activation function $h(\cdot)$ of hidden units defined by (LeCun et al. 1998; Dailey et al. 2002):

$$h(a_j) = 1.7159 \tanh(2a_j / 3) \tag{6.8}$$

where $a_j = \sum_{i=1}^{q} w_{ji}^{(1)} F_i + w_{j0}^{(1)}$ is the weighted sum of inputs for hidden unit j.

In addition, it is desirable that the network output vector $\mathbf{y} = [y_k]_{1\times 5}$ represents the posterior probabilities of classes given the input vector, with $0 \le y_k \le 1$ and $\sum_{k=1}^{5} y_k = 1$. For this purpose, the "softmax" function (Bridle 1990; Dailey et al. 2002) is used as the activation function $g(\cdot)$ of output units defined by:

$$y_k = g(c_k) = \exp(c_k) / \sum_{m=1}^{5} \exp(c_m) \tag{6.9}$$

where $c_k = \sum_{j=1}^{2q} w_{kj}^{(2)} h(a_j) + w_{k0}^{(2)}$ is the weighted sum of inputs for output unit k.

6.6.2 Network Training

The error function for network training is defined as the cross entropy between each pair of network output vector $\mathbf{y} = [y_k]_{1\times 5}$ and its target vector $\mathbf{t} = [t_k]_{1\times 5}$ (Bishop 1995; Dailey et al. 2002):

$$E = -\sum_{k=1}^{5} [t_k \ln(y_k / t_k)] \tag{6.10}$$

where $t_k = 1$ if the corresponding vehicle record belongs to class C_k, and $t_k = 0$ otherwise. Thus, a perfect match between the network output and its target will lead to $E = 0$.

Using data in the training and validation sets, the standard backpropagation algorithm (Bishop 1995) is adopted for network training (minimization of *E*), with each training loop known as an epoch. After each epoch, the average cross entropy errors of the training and validation sets are computed. The optimal network configuration is selected according to the minimum error of the validation set so as to avoid overfitting (Bishop 1995; Hastie et al. 2001).

Bishop (1995) and Dailey et al. (2002) show that a neural network of the above configuration is essentially a statistical model. In addition, minimization of *E* is a parametric optimization process by the maximum likelihood method. As such, the outputs (y_k) of the trained network can be interpreted as the posterior probabilities of vehicle classes given the input, $\Pr(C_k \mid \mathbf{F})$.

6.7 Neural Network Results

In scenario 1, the network is trained and tested by the data sets of Table 6.2, and the results are shown in Table 6.4. It is seen that, compared to the earlier preliminary classification (Table 6.3), the success rates have been significantly improved. The trained network performs satisfactorily, achieving a high success rate for all classes, ranging from 93.4% for C_4 to 98.7% for C_5.

Fig. 6.11 shows the histograms of classification confidence (the largest y_k computed by Eq. 6.7) for the success/failure cases of the test set. It is seen that the vast

majority of successful classifications are made with reasonably high confidence (very close to 1 in Fig. 6.11a), while low confidence is associated with most of the small number of misclassifications (Fig. 6.11b). This denotes that when the network encounters an uncertain vehicle record, a warning may be issued in terms of low confidence.

As mentioned earlier, scenario 2 employs a balanced small subset of the available labeled data. Results for this case (Table 6.5) generally show success rates that are in the neighborhood of those of scenario 1 (Table 6.4). Thus, it appears that the unbalanced data structure of scenario 1 (augmented by additional copies) was of little impact on the final network performance. It may also be inferred that labor for manual labeling could have been significantly reduced as the additional records in scenario 1 do not notably improve the results.

In order to include the insights of the Bayesian inference preliminary analysis, a third scenario is also studied, using the data configuration of scenario 1. In this scenario, the network input vector is defined as $\mathbf{F} = [p_1\ p_2 \ldots p_5\ f_1'\ f_2' \ldots f_{27}']$, where $p_1\ p_2 \ldots p_5$ represent information on the parameters ε_P and D (Figs. 6.4 and 6.5). The results are shown in Table 6.6, where marginal change in success rates is observed compared to the above scenarios (Tables 6.4 and 6.5).

6.7.1 Discussion

It is noted that most failures (Tables 6.4-6.6) are misclassifications between neighboring classes that are not completely resolved using the employed features. Although relatively few, unexpected misclassifications have also occurred between

classes such as C_5 and C_1 or C_2. Closer inspection of these cases revealed that a C_5 record for instance (Figs. 6.4 and 6.7) was processed erroneously as to its start and end times (T_S and T_E). In some instants, the flat interval between front and back axles (e.g., the last 2 cases of Fig. 6.7) dictated a T_E that ignored the back axle segment of the record. This issue highlights possible challenges associated with distinction between signals from different subsequent crossing vehicles. Very close vehicles in heavy traffic situations will necessitate increased reliance on information from the recorded video.

6.7.2 Application to the Entire Database

In order to classify all records in the database, the trained neural network of scenario 3 was employed. A total of about 300,000 eastbound traffic records were automatically classified. The classification results are shown in Table 6.7. For each vehicle class, 100 random records were checked to evaluate the network overall performance, and the results (Table 6.8) are in general agreement with Table 6.6.

Thus, the trained network is found to be effective in sorting the entire database. Within the context of this relatively simple structural system, similar favorable results would be anticipated for new strain-only data, without the need for additional video images.

6.8 Summary and Conclusions

A large database has been acquired and complied of traffic crossing over a bridge deck on campus at the University of California, San Diego (UCSD). Over the course of 1.5 years, deck strains caused by traffic, along with time-synchronized video

images have been archived (400,000 records). This readily available dataset (http://healthmonitoring.ucsd.edu) may be of use for a wide range of data fusion, computer vision, and machine learning studies.

Herein, this dataset is used to develop a strain-based vehicle classification approach, as a machine learning application. To achieve this goal, the PCA technique is first applied to extract essential features from the strain time histories and a two-layered back-propagation neural network is employed as the statistical pattern classifier. In this regard, availability of the video images provides essential information for developing the needed labeled datasets. The test results of the trained neural network are satisfactory, showing that the PCA-based neural network was generally successful in attaining the desired goal.

6.9 Acknowledgements

The material in this chapter is prepared as a paper draft for publication, and the author is the primary researcher. This material is also based on the contributions of (1) Dr. Michael Fraser, who developed the UCSD bridge-deck testbed and the employed dataset (Fraser 2006), (2) Professor Ahmed Elgamal, the Ph.D. advisor of author, (3) Dr. Tony Fountain, who provided insightful advice on the research, and (4) Kendra Oliver, who helped in the data labeling.

Support of this research is provided by the U.S. National Science Foundation, Grant No. 0205720. This support is gratefully acknowledged. The authors wish to thank the California Institute for Telecommunications and Information Technology (UCSD Calit2, http://www.calit2.net) for providing fellowship support to this project. The authors are grateful to Professors Vistasp Karbhari and Frieder Seible of UCSD,

for providing access to the bridge-deck panels. Finally, the authors wish to acknowledge Mr. Minh Phan for his major contributions in development of the health monitoring web portal (http://healthmonitoring.ucsd.edu).

6.10 Tables

Table 6.1 Definition of Vehicle Classes

Vehicle class	Notation	Number of axles	Distribution of axles[1]	Vehicle types	FHWA vehicle categories
Small vehicles	C_1	2	1F+1R	Passenger car, minivan, van, SUV, pickup truck	Passenger car, other 2-axle 4-tired vehicles
Medium trucks	C_2	2	1F+1R	Medium single-unit 2-axle trucks	Other 2-axle 4-tired vehicles
Buses/Large trucks	C_3	2	1F+1R	Buses, large single-unit 2-axle trucks	Bus, single-unit 2-axle 6-tire or more trucks
3-axle trucks	C_4	3	1F+2R	Single-unit 3-axle trucks	Single-unit 2-axle 6-tire or more trucks
Combination trucks	C_5	3-5	1F+1M+1R 1F+2M+1R 1F+1M+2R 1F+2M+2R	Semi-trailer trucks, trucks with trailer	Combination trucks

Note: 1.F-Front, M-Middle, R-Rear. (For instance: 1F+2M+1R indicates a vehicle with one front axle, two middle axles grouped together, and one rear axle.)

Table 6.2 Numbers of Labeled Records

Vehicle class	Total	Training set	Validation set	Test set
C_1	2709	1354	541	814
C_2	1089	544	217	328
C_3	3326	1663	665	998
C_4	607	303	121	183
C_5	1044	522	208	314

Table 6.3 Preliminary Classification Results for the Test Set of Table 6.2 Using Bayesian Inference

Actual vehicle class	Class given by Bayesian inference					Success rate (%)
	C_1	C_2	C_3	C_4	C_5	
Small vehicles, C_1	762	46	3	1	2	93.6
Medium trucks, C_2	11	242	52	15	8	73.8
Buses/Large trucks, C_3	6	136	725	59	72	72.6
3-axle trucks, C_4	0	15	51	92	25	50.3
Combination trucks, C_5	1	5	14	45	249	79.3

Table 6.4 Classification Results for the Test Set Using the Trained Network (Scenario 1)

Actual vehicle class	Class given by the trained neural network					Success rate (%)
	C_1	C_2	C_3	C_4	C_5	
Small vehicles, C_1	795	19	0	0	0	97.7
Medium trucks, C_2	6	307	13	1	1	93.6
Buses/Large trucks, C_3	1	47	933	13	4	93.5
3-axle trucks, C_4	0	3	6	171	3	93.4
Combination trucks, C_5	2	1	1	0	310	98.7

Table 6.5 Classification Results for the Test Set Using the Trained Network (Scenario 2)

Actual vehicle class	Class given by the trained neural network					Success rate (%)
	C_1	C_2	C_3	C_4	C_5	
Small vehicles, C_1	97	3	0	0	0	97
Medium trucks, C_2	1	87	12	0	0	87
Buses/Large trucks, C_3	0	2	97	0	1	97
3-axle trucks, C_4	0	2	5	93	0	93
Combination trucks, C_5	2	1	0	0	97	97

Table 6.6 Classification Results for the Test Set Using the Trained Network (Scenario 3)

Actual vehicle class	Class given by the trained neural network					Success rate (%)
	C_1	C_2	C_3	C_4	C_5	
Small vehicles, C_1	791	23	0	0	0	97.2
Medium trucks, C_2	3	304	20	1	0	92.7
Buses/Large trucks, C_3	0	29	943	23	3	94.5
3-axle trucks, C_4	0	1	5	174	3	95.1
Combination trucks, C_5	0	3	2	0	309	98.4

Table 6.7 Classification Results for the Entire Database Using the Trained Network of Scenario 3

	Class given by the trained neural network				
	C_1	C_2	C_3	C_4	C_5
Number of records	161,323	36,184	125,929	3,954	3954

Table 6.8 Random Check of Classification Results for the Entire Database Using the Trained Network of Scenario 3

Actual vehicle class	Class given by the trained neural network					Success rate (%)
	C_1	C_2	C_3	C_4	C_5	
Small vehicles, C_1	99	1	0	0	0	99
Medium trucks, C_2	3	93	3	0	1	93
Buses/Large trucks, C_3	0	13	87	0	0	87
3-axle trucks, C_4	0	2	3	94	1	94
Combination trucks, C_5	0	0	1	0	99	99

6.11 Figures



Fig. 6.1 UCSD bridge-deck panels testbed (Fraser et al. 2002).

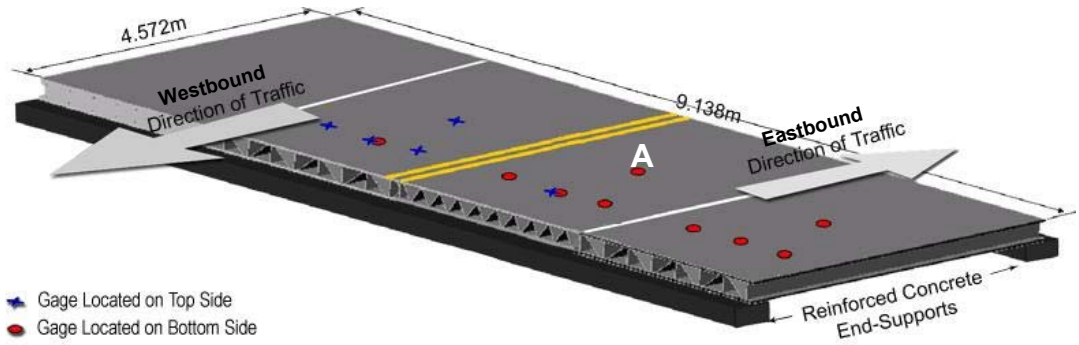


Fig. 6.2 Strain gage locations on the bridge-deck panels (Fraser et al. 2002).



Small vehicles, C_1



Medium trucks, C_2



Buses/Large trucks, C_3



3-axle trucks, C_4



Combination trucks, C_5

Fig. 6.3 Examples of vehicle types in each class.

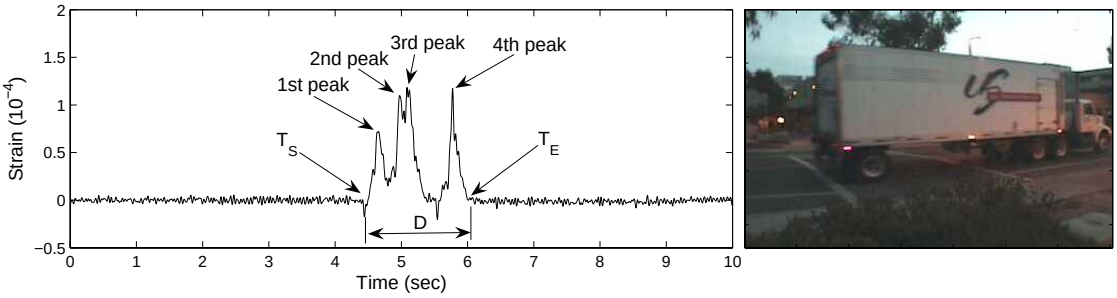


Fig. 6.4 Characteristics of traffic-induced strain response time histories.

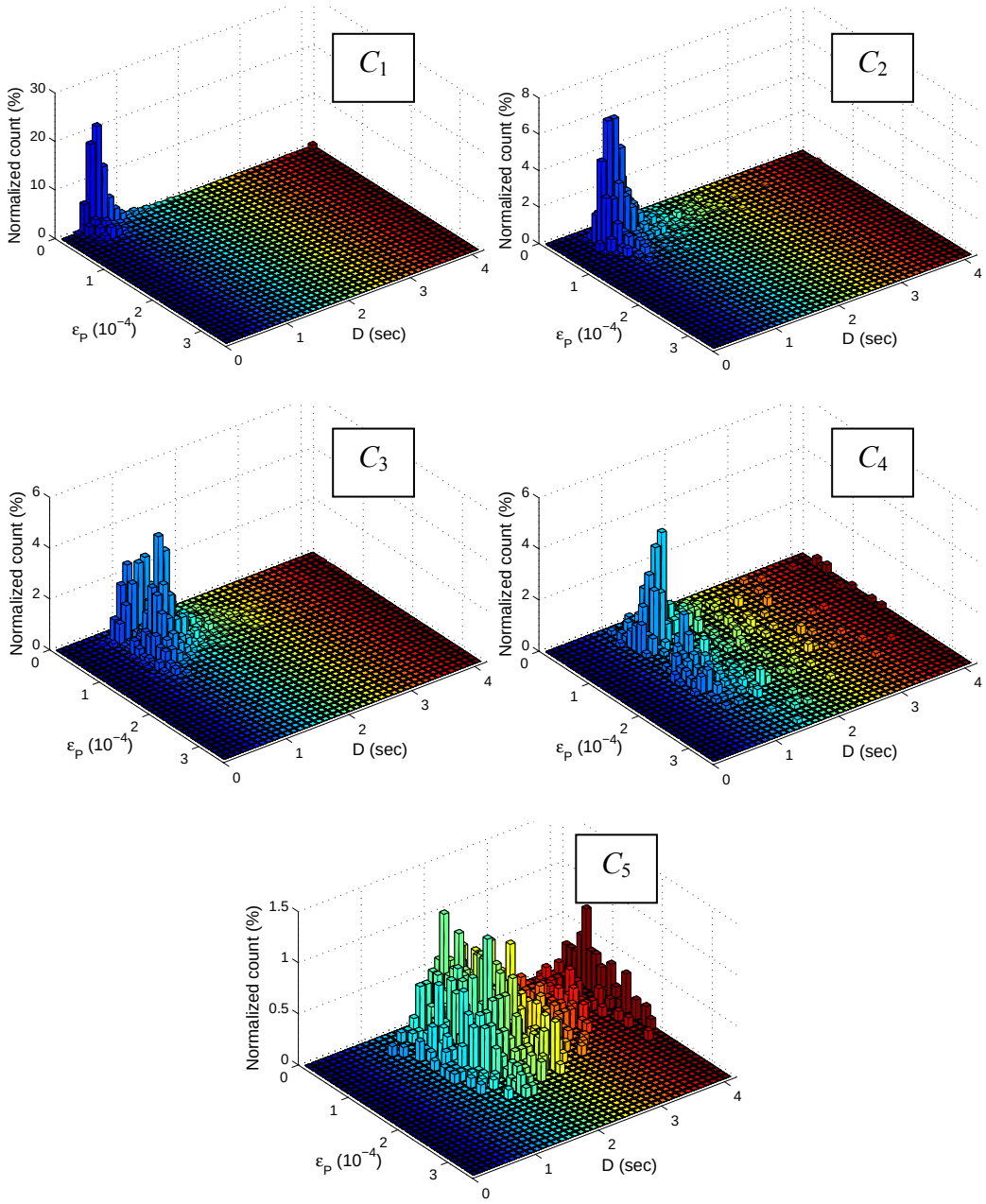


Fig. 6.5 Normalized histograms of maximum peak strain (ε_P) and event duration (D) of each vehicle class (records in the training set of Table 6.2).

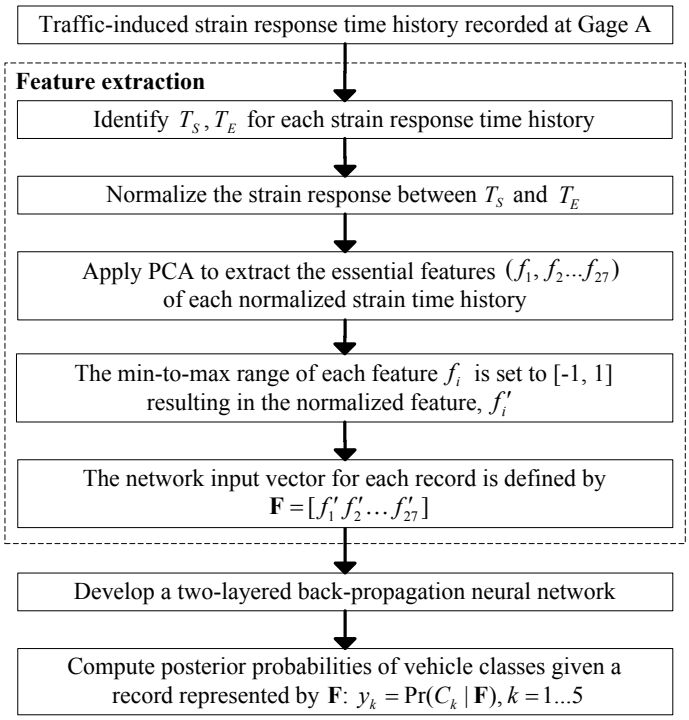


Fig. 6.6 Flowchart of analysis procedure.

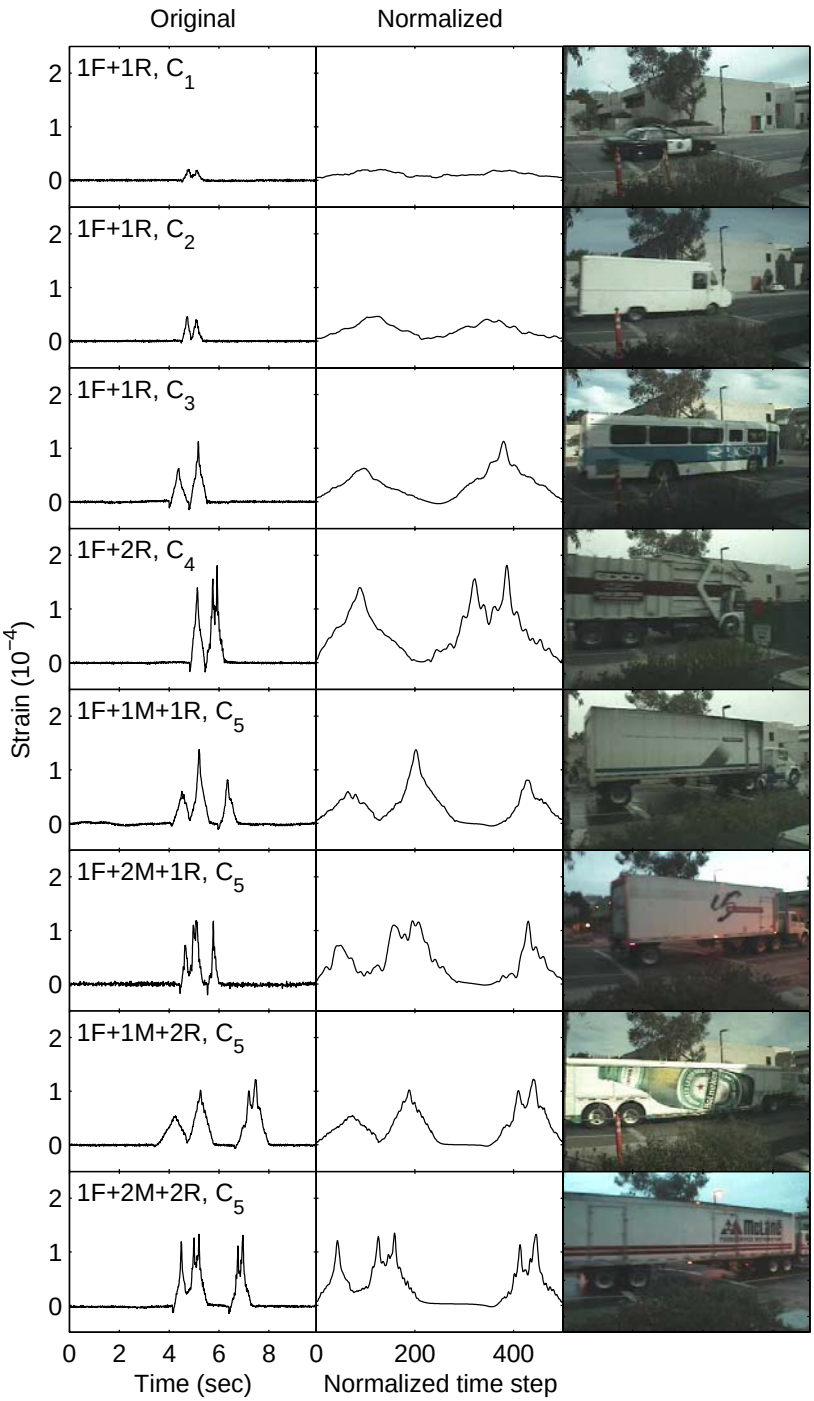


Fig. 6.7 Original and normalized strain time histories for 8 representative vehicle records of different classes and axle distributions (Table 6.1).

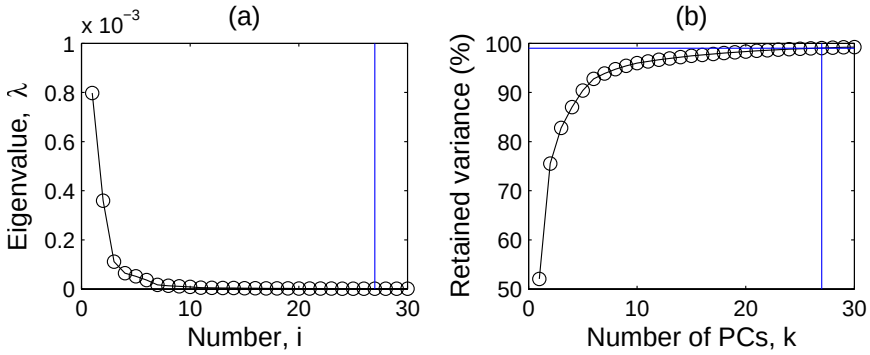


Fig. 6.8 PCA of the training set of scenario 1: (a) eigenvalues of covariance matrix **V**, (b) retained variance using the first *k* PCs.

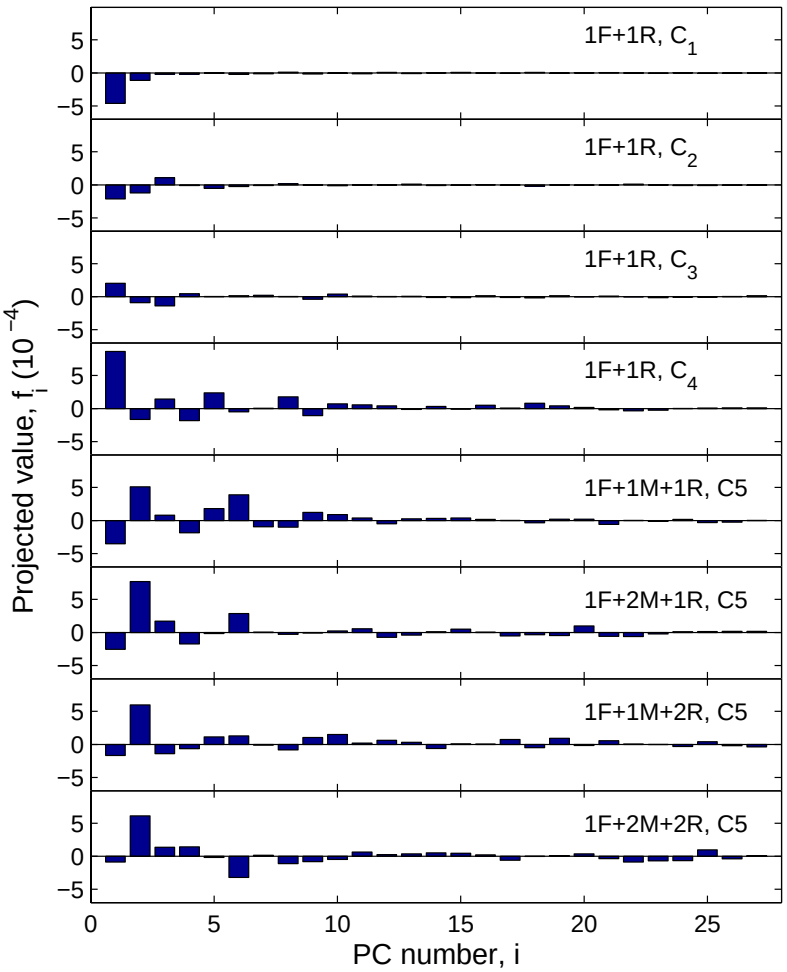


Fig. 6.9 Computed **f** vectors of the 8 representative vehicle records in Fig. 6.7.

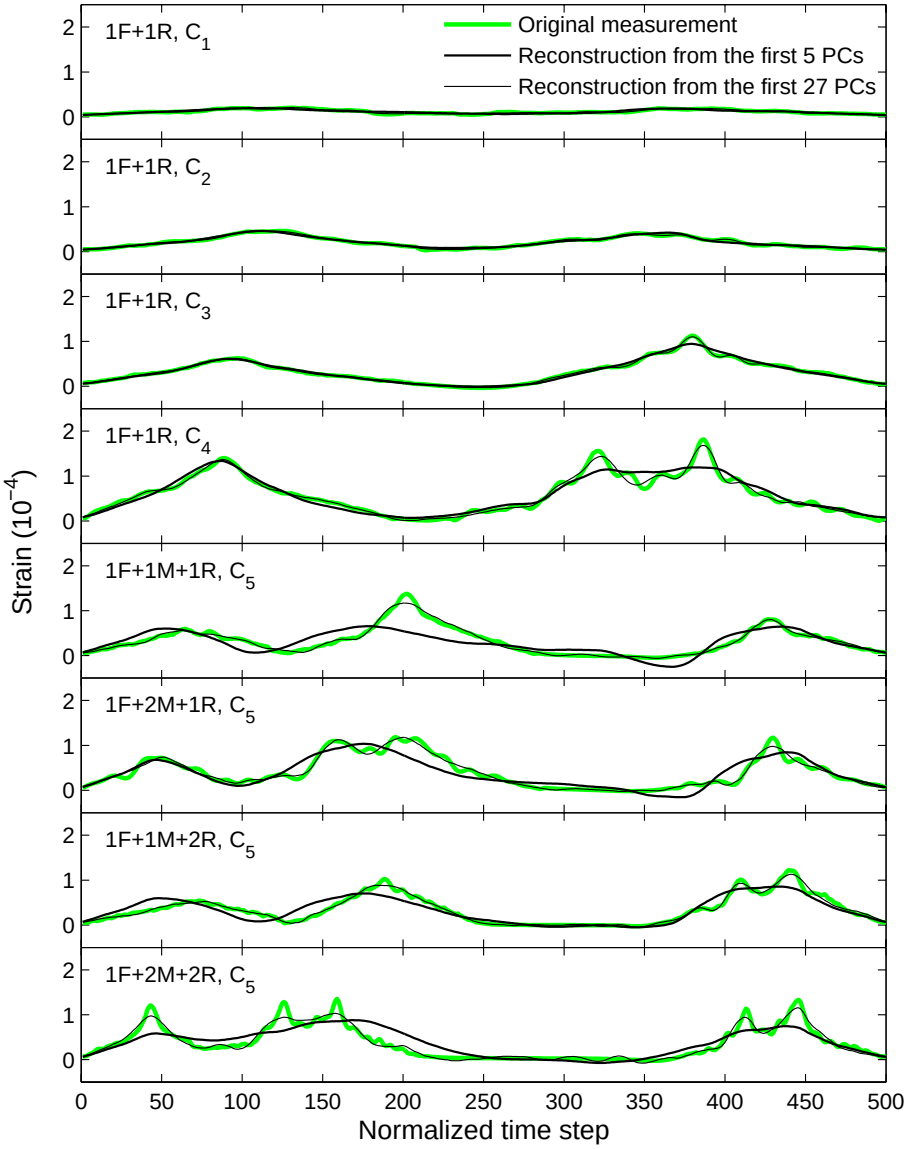


Fig. 6.10 Reconstructed strain time histories of the 8 representative vehicle records in Fig. 6.7 using the first 5 and 27 PCs (k = 5 and 27 respectively).

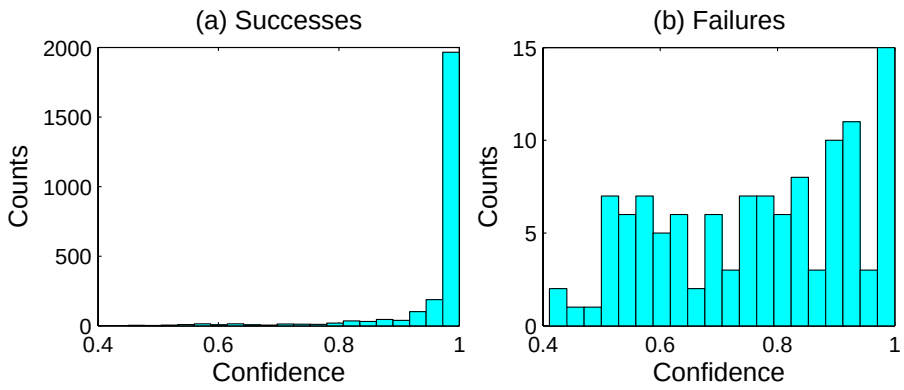


Fig. 6.11 Histograms of classification confidence for successes and failures.

6.12 References

Achler, O. and Trivedi, M. (2004). "Camera Based Vehicle Detection, Tracking, and Wheel Baseline Estimation Approach." *7th International IEEE Conference on Intelligent Transportation Systems (ITSC 2004)*, Washington D.C., October 3-6.

Athol, P. (1965). "Interdependence of Certain Operational Characteristics Within a Moving Traffic Stream." *Highway Research Record*, HRB, National Research Council, Washington D.C., 72, pp 58-87.

Bishop, C. M. (1995). *Neural Networks for Pattern Recognition*, Oxford University Press.

Bridle, J. S. (1990). "Probabilistic Interpretation of Feedforward Classification Network Outputs, with Relationships to Statistical Pattern Recognition." *Neurocomputing: Algorithms, Architectures, and Applications*, F.F. Soulie and J. Herault, eds., Springer-Verlag, New York, 227-236.

Chang, R., Gandhi, T., and Trivedi, M. (2004). "Vision Modules for a Multi-Sensory Bridge Monitoring Approach." *7th International IEEE Conference on Intelligent Transportation Systems (ITSC 2004)*, Washington D.C., October 3-6.

Dailey, M. N., Cottrell, G. W., Padgett, C., and Adolphs, R. (2002). "Empath: A Neural Network that Categorizes Facial Expression." *Journal of Cognitive Neuroscience*, 14(8), 1158-1173.

Elgamal, A., Conte J. P., Masri, S., Fraser, M., Fountain, T., Gupta, A., Trivedi, M., and El Zarki, M. (2003). "Health Monitoring Framework for Bridges and Civil Infrastructure." *Proccedings of the 4th International Workshop on Structural Health Monitoring*, Stanford University, Stanford, CA, September 15-17.

Fraser, M., Elgamal, A., Conte, J. P., Karbhari, V., Zhao, L., and Seible, F. (2002). "Pilot Health Monitoring for Composite Bridge-deck Panels." *Proceedings of the Third Middle East Symposium on Structural Composites for Infrastructure Applications*, Aswan, Egypt. December 17-20.

Fraser, M. (2006). "Development and Implementation of an Integrated Framework for Structural Health Monitoring." *Ph.D. Dissertation*, Department of Structural Engineering, University of California, San Diego, La Jolla, CA.

Hasselman, T. K., Anderson, M. C., and Gan, W. (1998). "Principal Components Analysis for Nonlinear Model Correlation, Updating and Uncertainty Evaluation." *Proc. of the 16th International Modal Analusi Conferecne, SPIE*, Santa Barbara, CA.

Hastie, T., Tibshirani, R., and Friedman, J. (2001). *The Elements of Statistical Learning: Data Mining, Inference, and Prediction*, Springer Series in Statistics, Springer-Verlag, New York, NY.

Jolliffe, I. T. (1986). *Principal Components Analysis*, Spring-Verlag, New York.

LeCun, Y., Bottou, L., Orr, G. B., and Muller, K. R. (1998). "Efficient Backprop." *Neural Networks - Tricks of the Trade*, Springer Lecture Notes in Computer Sciences, 1524, 5-50.

Lu, Y. (1989). "Vehicle Classification Using Infrared Image Analysis." *ASCE Journal of Transportation Engineering*, 118(2), 223-240.

Oh, S., Ritchie, S. G., and Oh, C. (2001). "Real Time Traffic Measurement from Single Loop Inductive Signatures." *Report No. UCI-ITS-WP-01-15*, Institute of Transportation Studies, Department of Civil & Environment Engineering, University of California, Irvine.

Russell, S. J., and Norvig, P. (1995). *Artificial Intelligence: A Modern Approach*, Prentice Hall, Upper Saddle River, NJ.

Sun, C. and Ritchie, S. G. (2000). "Heuristic Vehicle classification Using Inductive Signatures on Freeways." *Paper Number 00-3273*, preprint in Transportation Research Board Annual Meeting, Washington, DC.

Sun, C. and Ritchie, S. G., and Oh. S. (2003). "Individual Classifying Artificial Network for Vehicle Type Categorization." *Computer-Aided Civil and Infrastructure Engineering*, 2003(18), 161-172.

Wei, C. et al. (1996). "Vehicle Classification Using Advanced Techniques." *Transportation Research Record*, 1551, 45-50.

Yuan, X. et al. (1994). "Computer Vision System for Automatic Vehicle Classification." *ASCE Journal of Transportation Engineering*, 120(6), 861-876.

Zhao, L. (1999). "Characterization of Deck-to-Girder Connections in FRP Composite Superstructures." *Ph.D. Dissertation*, Department of Structural Engineering, University of California, San Diego, La Jolla, CA.

7 SUMMARY AND CONCLUSIONS

For structural health monitoring based on large, dense, and heterogeneous sensor networks, it is vital to develop efficient techniques to process and analyze the massive amount of sensor data in order to extract essential information (e.g., structural damage condition, traffic loading condition on bridges, and so forth). The efforts in this dissertation were primarily dedicated to this direction, including studies on structural damage identification and traffic pattern recognition. In these studies, traditional analysis tools for structural engineering (e.g., finite element based simulation) were utilized, and the potential of machine learning techniques has been extensively explored. Based on these studies, three different structural damage identification approaches (referred to as approach A, B, and C, respectively) and one vehicle classification approach were developed. In section 7.1, each structural damage identification approach is summarized, including the applications and the key conclusions/findings. In addition, a comparison of approaches A, B, and C is also provided, along with suggestions for future research. Finally, the study on vehicle classification is summarized in section 7.2.

7.1 Structural Damage Identification

7.1.1 Approach A

Approach A adopts a decentralized analysis framework, within which substructures in the monitored system of interest are defined according to the sensor spatial distribution. Therefore, each substructure is represented by a dynamic model,

and the system properties are periodically identified based on sensor measurements for monitoring purposes.

In this dissertation, approach A was applied to seismic downhole data to monitor changes in soil layer properties (Chapter 2). In the presence of a vertical array of downhole and surface accelerometers, the soil layer between selected sensors was modeled crudely as an equivalent lumped mass SDOF system. Two scenarios were investigated: (1) soil layer between a selected downhole sensor and the surface sensor, and (2) soil layer within the range of three neighboring sensors. For each scenario, an analysis framework based on Newmark time integration was then developed to identify the equivalent SDOF system based on measured seismic ground response.

This proposed approach was first verified using simulation data generated from numerical SDOF models, and then applied to the Lotung, Taiwan seismic downhole array data. Promising results were achieved and the key conclusions are:

(1) Strong earthquake induced changes in soil layer properties can be captured using the proposed approach.

(2) The identified equivalent SDOF model can be employed to predict ground response at the corresponding sensor location, and the prediction error is a sensitive indicator and may be utilized to infer changes in the soil layer properties.

(3) For such an approach based on dynamic models, it is easy to provide insightful explanations for analysis results, but it is hard to extend its efficiency to complex scenarios.

7.1.2 Approach B

Approach B is essentially a decentralized structural damage identification technique. In a structural system, distributed substructures of interest are first defined, each of which is monitored by a set of neighboring sensors. Therefore, for each substructure, a master sensor is selected and an associated NARX neural network is developed to predict the structural response at this sensor location from the measurements of its neighbors. Thus, dynamic characteristics of the substructure are approximately and implicitly identified and represented by the network. Without significant change in the substructure, the prediction error of the network follows a stable statistical distribution. Change in the prediction error variance is then evaluated and utilized as a sensitive damage indicator. Finally, information from all computed indicators is integrated in order to infer the occurrence, location, and relative severity of damage in the structural system.

The feasibility and efficiency of this approach was first verified using data from two Los Alamos laboratory experiments (Chapter 3): (1) identification of linear/nonlinear damage in an 8-DOF mass-spring system, and (2) identification of joint damage in a 3-story frame structure. Thereafter, the approach was employed to develop a method for bridge pier damage identification (Chapter 4), using simulation data generated from a virtual bridge testbed. The key conclusions/findings from these studies are:

(1) The combination of time-series-prediction techniques and statistical inference methods is a promising solution for structural damage identification.

(2) The dynamic characteristics of each substructure can be represented by the trained associated NARX network since it can accurately predict the structural response at the master sensor.

(3) Using this approach, the occurrence and relative severity of damage occurring at multiple locations can be simultaneously identified.

(4) The efficiency of this approach requires that the applied external excitation follows the same pattern every time.

(5) The analysis framework of this approach is flexible and scalable. Thus, it may be applied to different structural damage identification problems, from critical component monitoring using a few sensors to global structural health monitoring using a large scale dense sensor network.

(6) The computation of this approach is decentralized, only requiring substructure-wide data transmission, and can be completed at the sensor level. Thus, it is suitable to be implemented within a smart sensor framework (Lynch et al. 2001; Spencer et al. 2004).

7.1.3 Approach C

Approach C adopts a statistical pattern recognition paradigm. Within this framework, a range of damage patterns of interest is provided by numerical simulation, the PCA technique is employed for feature extraction, and a neural network is developed for damage pattern identification. Herein, approach C is also applied to the same bridge pier damage identification problem (Chapter 5). In this study, the refined 3D nonlinear FE model of HBB was employed to represent an actual bridge as a virtual testbed. In addition, another relatively simple linear FE model of the same

bridge was built to represent the numerical simulation effort. Using these two models, the approach was exercised and the key conclusions/findings are:

(1) For the efficiency of this approach, the employed numerical (FE) model must be well calibrated in order to capture the dynamic characteristics of the actual bridge.

(2) As an existing bridge is subjected to a relatively small excitation, the structural dynamic response remains linear. Within this context, it is viable to model the structure as linear and prescribe damage in the form of element stiffness reduction. Thus, the simulation procedure can be significantly simplified and computing time can be saved as well.

(3) PCA is an efficient tool to extract essential features from damage-induced changes in the structural dynamic response (e.g., acceleration time histories).

(4) Using the PCA-extracted features as input, a neural network can be trained to detect and assess the severity of damage in all piers simultaneously. In addition, the knowledge learned from the simulated damage patterns can be applied to infer damage in the actual bridge.

7.1.4 Comparison of Approaches A, B, and C

A comparison of approaches A, B, and C is summarized in Table 7.1. It is seen that approach A requires that each substructure defined in the monitored system can be characterized by a dynamic model. This may impose a challenge to applications related to complex structures (including boundary conditions). Obviously, the main benefit from the dynamic model is that insightful explanations can be provided to the analysis results.

Table 7.1 also shows that approach B offers many desirable features: (1) no requirement on a dynamic model, (2) no requirement on damage data and numerical simulation, (3) decentralized computation, and (4) flexibility and scalability. Thus, it is well suited for implementation within a smart sensor framework, which integrates embedded microprocessors and wireless communication links (Fig. 7.1, Lynch et al. 2001; Spencer et al. 2004). Such a decentralized approach will process sensor data and extract useful information locally at the sensor level, which may provide significant advantages to data communication, storage, and management. The major disadvantages of approach B are: (1) it is hard to directly relate the computed statistical damage indicators to physical properties, and (2) the exact level of damage cannot be identified.

As to approach C, the efficiency highly depends on the numerical model used for damage pattern simulation. This will often dictate a sophisticated finite element model, with labor intensive tuning and possible uncertainties induced by modeling errors. Further, as the scenarios of damage of different types occurring at multiple locations simultaneously are considered, time-consuming and expensive simulation will be required in order to encompass all possible damage patterns.

7.1.5 Suggestions for Future Research

Based on above discussions, it may be concluded that approach B provides significant advantages for practical implementation. Thus, it is desirable to further explore the potential of approach B, and implement it within a smart sensor framework (Lynch et al. 2001; Spencer et al. 2004). Furthermore, as the studies in this dissertation were based on either laboratory experimental data or numerical simulation

data, the effects of operational and environmental conditions were not investigated. This is also a critical issue that needs to be addressed in future research.

7.2 Traffic Pattern Recognition

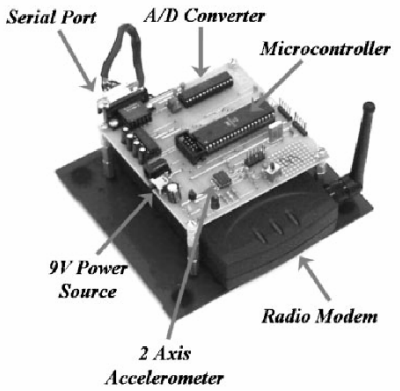
Finally, the combination of neural networks and PCA was also employed to develop a strain-based vehicle classification approach (Chapter 6), which may be used to provide information on traffic loading conditions. This study was based on the strain-video data recorded at the UCSD bridge-deck testbed. Within this framework, the PCA technique was first applied to extract essential features from the strain time histories and a neural network was employed as the statistical pattern classifier. In this regard, availability of the video images provided essential information for developing the needed labeled datasets. The test results of the trained neural network were satisfactory, showing that the PCA-based neural network was generally successful in attaining the desired goal.

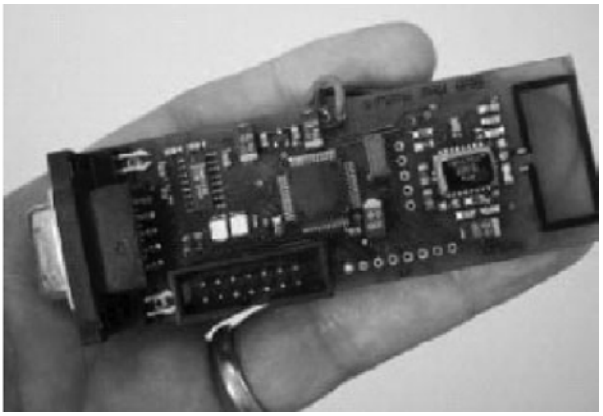
7.3 Tables

Table 7.1 Comparison of Structural Damage Identification Approaches A, B, and C

	Approach A	Approach B	Approach C
Requirement on dynamic models	Yes	No	Yes
Requirement on data of damage states	No	No	Yes
Requirement on numerical simulation	No	No	Yes
Sensitivity to changes in the applied external excitation	No	Yes	Yes
Identification of damage occurrence	Yes	Yes	Yes
Identification of damage location	Yes	Yes	Yes
Identification of damage level	Yes	No	Yes
Decentralized computation	Yes	Yes	No
Flexible and Scalable	No	Yes	No

7.4 Figures





(Lynch et al. 2001) (EYES project 2002)

Fig. 7.1 Prototype smart sensors.

7.5 References

Energy Efficient Sensor Networks (EYES 2002). http://eyes.eu.org/

Lynch, J. P., Law, K. H., Kiremidjian, A. S., Kenny, T. W., Carryer, E., and Partridge, A. (2001). "The Design of a Wireless Sensing Unit for Structural Health Monitoring." *3rd International Workshop on Structural Health Monitoring*, Stanford, CA, 2001,1041–1050.

Spencer Jr. B. F., Ruiz-Sandoval, M. E., and Kurata, N. (2004). "Smart Sensor Technology: Opportunities and Challenges." *Structural Control and Health Monitoring*, 11: 349-368.

APPENDIX A

THREE-DIMENSIONAL BRIDGE-FOUNDATION-GROUND SYSTEM: PART I. COMPUTATIONAL MODEL

Soil-structure interaction may play a major role in the seismic response of a bridge structure. Specifically, a significant reduction in soil stiffness and strength may result in permanent displacement of the abutments and foundations, thus imposing important kinematic conditions to the bridge structure. A study of such phenomena is undertaken based on three-dimensional (3D) nonlinear dynamic finite element (FE) modeling and analysis. A bridge-foundation-ground model is developed based on the structural configuration and local soil conditions of the Humboldt Bay Middle Channel Bridge, near Eureka in northern California. The FE model and nonlinear solution strategy are built in the open-source software platform OpenSees of the Pacific Earthquake Engineering Research (PEER) Center. Appendix A presents the modeling details of the bridge structure, foundation, and surrounding soil system. The adopted spatial definition of seismic excitation is described, along with the employed nonlinear static and dynamic staged analysis procedure. Results of the seismic response analysis performed and potential scenarios of detrimental kinematic constraints dictated by the inelastic ground deformations are discussed in Appendix B.

A.1 Introduction

Seismically-induced ground deformation effects on foundations and structures continue to be a major concern. During the Hokkaido-Nansei-Oki, Japan earthquake (July 12, 1993), the most common patterns of damage to bridges were caused by

ground failures such as liquefaction and lateral spreading (Yanev 1993). Similar observations were reported after other recent events including the 1989 Loma Prieta Earthquake (Baldwin and Sitar 1991; Seed et al. 1990) and the 1995 Kobe Earthquake (Sitar 1995; JGS 1996, 1998).

The 3D nature of bridge response imposes significant computational challenges. For instance:

(1) The spatial extent of the bridge-foundation-ground system is large, typically in the hundreds or thousands of meters, necessitating an appropriate finite element (FE) mesh to provide adequate modeling resolution.

(2) In view of the highly nonlinear properties of the foundation ground, elaborate hysteretic constitutive models of soil materials are needed.

(3) The seismic response analysis is conducted in the time-domain, with many thousands of time steps and iterations.

(4) Spatial definition of the input seismic excitation and soil boundary conditions remain an area of ongoing research.

(5) Pre-processing and output visualization in 3D FE analysis can be quite tedious and time consuming.

These challenges impose high demands on software efficiency and hardware performance (e.g., high speed CPU, and large memory). Nevertheless, recent efforts on 3D modeling and analysis (linear) are being reported (Ju 2004).

Building on prior 2D modeling and simulation studies (Conte et al. 2002; Zhang et al. 2003, 2005), a pilot 3D FE modeling effort is presented in this paper for nonlinear seismic response analysis of bridge-foundation-ground systems. Modeling

focuses on a virtual bridge-foundation-ground system inspired from the PEER (Pacific Earthquake Engineering Research Center) Humboldt Bay Middle Channel Bridge Testbed (http://www.peertestbeds.net/humboldt.htm). However, some key features of the actual bridge are not modeled (e.g., spliced regions at the base of the piers), and therefore various aspects of the actual response mechanisms may not be captured by the present model. Modeling and computations are performed using the PEER open-source software framework OpenSees (Open System for Earthquake Engineering Simulation, http://opensees.berkeley.edu) for simulation applications in earthquake engineering using advanced FE methods.

Herein, the bridge model characteristics are described, along with the underlying foundation and ground properties. An elasto-plastic soil model simulates hysteretic behavior and permanent soil deformations. Challenges associated with the spatial definition of the seismic input are addressed. In Appendix B, the simulation results and potential scenarios of detrimental kinematic constraints imposed by the inelastic ground deformations are discussed.

A.2 Case Histories of Ground-Bridge Damage

A dramatic illustration of damage due to ground deformation is depicted in Fig. A.1. Settlement and movement of the abutment towards the bridge resulted in compressive axial forces acting on the superstructure and a buckling-type deformation pattern (Steinbrugge 2002). Such large ground deformations can result in total destruction and collapse of the structural system (e.g., Showa Bridge during the Niigata 1964 earthquake, JNCEE 1965).

Generally, significant damage to bridges can result from much lower levels of ground deformation. In May 1960, a series of large earthquakes ($M_w = 9.5$) shook southern Chile (USGS 2003), causing serious damage to a bridge crossing the Rio Valdivia (Figs. A.2 and A.3). Fig. A.2 shows the east abutment lurching towards the river (Steinbrugge 2002). Fig. A.3 displays the associated approach ramp settlement (Steinbrugge 2002).

During the 1994 Northridge Earthquake, damage to bridge abutments was reported throughout the epicentral region (EERI 1995; UC and NISEE 2002a, b). The observed damage included shear key cracking and failure, spalling of abutment backwalls and wingwalls, approach ramp settlement (Fig. A.4), and approach slab buckling.

A.3 PEER Humboldt Bay Middle Channel Bridge Testbed

PEER initiated a number of testbed projects to synthesize the research products into a coherent methodology and to demonstrate and exercise this methodology (http://peer.berkeley.edu, Porter 2003). The Humboldt Bay Middle Channel Bridge (Caltrans, personal communication, 2000), near Eureka in northern California (Fig. A.5) was selected as one of these testbeds. Herein, the reported modeling effort is undertaken based on the bridge structural configuration, local soil conditions and site seismicity. The bridge (Fig. A.5) is a 330m long, 9-span structure, supported on the cap beams of single pier bents with both longitudinal and transversal shear keys to prevent unseating (Fig. A.6). Two expansion joints are located on the top of piers 3 and 6 as shown in Fig. A.7. The abutments and piers are supported on pile-group foundations (Fig. A.7).

Three of the eight foundations (1, 7 and 8 in Fig. A.7) are composed of an approximately 3.5×4m pile group with 4 interior vertical square piles (0.356m/14in width) and 12 exterior batter square piles (0.356m/14in width) with the pile cap (1.22m in thickness) below ground surface (Fig. A.6e). The remaining five pile groups (2-6 in Fig. A.7, approximately 3.5×5m each) are composed of 5 vertical circular piles (1.37m/54in diameter) with the pile cap above ground, surrounded by 2.9m high concrete skirts to prevent direct impact from marine navigation (Fig. A.6d). Each bridge abutment is supported on two rows of circular piles (Fig. A.7, about 1.2×10m in size), with 7 front batter piles (0.356m/14in diameter), and 5 rear vertical piles (0.356m/14in diameter).

The average slope of the river channel from the banks to its center is about 7% (4 degrees). The foundation soil is composed mainly of dense fine-to-medium sand, organic silt, and stiff clay layers. Thin layers of loose and soft clay are located near the ground surface.

A.4 Finite Element Analysis Framework/Platform: OpenSees

System modeling and response computations are performed using OpenSees, an object-oriented, open-source FE analysis framework (McKenna 1997; McKenna and Fenves 2001). The current version of OpenSees includes an extensive library of structural and soil material models, as well as a number of structural (e.g., beam-column, shell) and continuum elements.

In the bridge-foundation-ground model, different types of elements are employed to represent the foundation and superstructure such as:

(1) 3D linear elastic beam-column element (Bathe 1996).

(2) 3D nonlinear (material and geometric) beam-column element with a Gauss-Lobato integration rule (five integration points) as implemented in OpenSees by Souza (2000). This element employs a flexibility approach with force-based interpolation functions that strictly satisfy equilibrium of internal forces along the element (Spacone et al. 1996). The cross section associated with this element is discretized into fibers (steel rebar, confined/unconfined concrete) with uni-axial material constitutive models (McKenna and Fenves 2001).

(3) Four-node linear elastic shell element (MITC4) with a bilinear isoparametric formulation in combination with a modified shear interpolation to improve thin-plate bending performance (Bathe 1996).

(4) Hexahedra solid element (8-node brick, Bathe 1996).

(5) Linear/nonlinear ZeroLength element implemented in OpenSees by Fenves and co-workers (http://opensees.berkeley.edu). This element connects two coincident nodes with linear/nonlinear translational/rotational springs.

A.5 Finite Element Model

Generally, effort is directed towards (Fig. A.8): (1) inclusion of a representative soil domain around the bridge structure, and (2) investigation of the resulting soil-structure interaction/deformation effects. The 3D mesh of this bridge-foundation-ground system (Fig. A.8) is generated and visualized using the pre/post-processor software GiD (http://gid.cimne.upc.es, Diaz and Amat 1999). This FE model (Fig. A.8) includes 30237 nodes, 1140/280 linear/nonlinear beam-column elements, 81 linear shell elements, 23556 solid brick elements, 1806 zero-length elements, and

2613 equalDOF constraints (McKenna and Fenves 2001). The simulated soil domain in this model is 650m long, 151m wide and 74.5m deep.

The large-scale FE model described above necessitates the use of a special sparse solver to allow in-core execution using a PC with 3 Gigabytes of RAM. This sparse solver was developed by Mackay et al. (1991) and Law and Mackay (1993) and implemented in OpenSees by Peng (2002). The solver is based on a row-oriented storage schema that takes full advantage of the stiffness matrix sparsity (Peng 2002).

A.5.1 Bridge Superstructure

The main longitudinal bridge I-girders and transversal brace I-beams (Fig. A.6) are modeled using the 3D linear elastic beam-column element (Table A.1). The bridge deck slabs (0.165m thick) are modeled using the 3D linear shell element. Herein, typical mass density ($\rho = 2300\text{kg/m}^3$), Young's Modulus ($E = 2.78\times10^7\,\text{kPa}$ corresponding to a compressive strength, f_c' of 5ksi), and Poisson's ratio ($\nu = 0.3$) of concrete are used (Wang and Salmon 1992).

In order to model the presence of expansion joints above the third and sixth piers, the bridge deck is divided into three continuous sub-sections. In the present model, these sections are simply connected by perfect hinges using the equalDOF constraint (for translations only) in OpenSees (McKenna and Fenves 2001).

A.5.2 Bridge Piers

The bridge piers are modeled using the 3D fiber-section force-based beam-column element with nonlinear fiber materials. Discretization of the pier cross-section into concrete and steel fibers is shown in Fig. A.9a, with confined and unconfined concrete inside and outside the shear reinforcement/stirrups, respectively. The uni-

axial Kent-Scott-Park model (Kent and Park 1971; Scott et al. 1982; Mander et al. 1988) with degraded linear unloading/reloading stiffness (Fig. A.9e) is used to model the concrete (Table A.2). The reinforcing steel (Table A.3) is represented (Fig. A.9f) by a uni-axial bilinear model with kinematic hardening (equivalent to 1-D J_2 plasticity model with linear kinematic and no isotropic hardening). Compared to the confined concrete (Table A.2), the unconfined concrete material is characterized by a lower compressive strength, lower crushing strength, and lower strain ductility. Fig. A.10 shows the cyclic moment-curvature response of the cross-section of the bridge piers under constant axial load of 8MN ($\cong 0.08 f_c' A_g$, where A_g denotes the gross cross-section area) representative of the action of gravity. It is seen that the pier has a much higher flexural capacity in the transversal direction (28MN-m) than the longitudinal direction (11MN-m).

Quasi rigid elements (linear beam-column elements with high Young's Modulus of 3.0×10^{10}kPa and a square cross sectional area of $4m^2$) are used to model the pier cap beams (Figs. A.9c-d) assumed herein to be of adequate strength and high stiffness. The cap beams are connected to the bridge superstructure by perfect hinges using the equalDOF constraint (for translations only) in OpenSees (McKenna and Fenves 2001), assuming no shear key failure.

A.5.3 Pile Groups

As mentioned earlier, the bridge piers are supported on pile foundations (Fig. A.7), consisting each of 5 circular piles (1.37m/54in diameter) or 16 square piles (0.365m/14in width). In the FE model, in order to reduce the complexity of 3D mesh generation, 2×2 pile groups are employed (Table A.4), with 4 vertical circular piles

(1.37m/54in diameter, Figs. A.9c-d). Each pile is modeled using the 3D fiber section, force-based beam-column element with the nonlinear fiber materials defined in Tables A.2 and A.3 (Fig. A.9b). Furthermore, rigid beam-column links, normal to the pile longitudinal axis (Figs. A.9c-d) are used to represent the actual size of the pile cross-section (below ground). Fig. A.11 shows the cyclic moment-curvature response of this circular pile cross-section under constant axial load of 2MN ($\cong 0.04 f_c' A_g$) representative of the action of gravity. Since the pile is circular, it has the same flexural capacity (1.5MN-m) in the longitudinal and transversal directions.

The modeling of pile caps depended on the location. The 1.53m thick pile caps (below piers 2-6) above ground (Fig. A.7) are idealized as rigid frames (Fig. A.9c), and the inertial properties of these massive pile caps are represented by 4 lumped masses of 33×10^3kg at the four corner nodes. The 1.22m thick pile caps (below piers 1, 7, 8) below ground (Fig. A.7) are modeled by a layer of solid elements (with linear elastic properties corresponding to uncracked concrete) to represent the actual geometric configuration (Fig. A.9d).

A.5.4 Abutments and Soil Domain

Fig. A.12 shows the employed idealized shear wave velocity profile of the underlying soil. This profile is defined according to the data (also shown in Fig. A.12) measured by oil suspension logging at borehole 1 of the Caltrans Samoa Bridge Geotechnical downhole array, about 0.25 miles north-west of the bridge (C. Roblee, personal communication, 2002).

As shown in Figs. A.8 and A.12, the soil profile is idealized into a surface crust layer, and five underlying sub-layers (Table A.5). Layer 1 (Fig. A.8) varies in

thickness from 4.9m at the center of the river channel to 7.3m at the banks. This layer is modeled as a relatively soft soil material in order to study the effects of lateral soil spreading on the bridge foundation and superstructure (typical situation of a river deposited soft stratum). Shear strength of this soft layer is defined to be 10kPa, a representative value for young San Francisco Bay mud (Bonaparte et al. 1979; Goldman 1969; Rogers and Figuers 1991).

Below the bridge abutments and approach ramps, stiffness and strength of this soft soil layer are increased locally (to 25kPa) in order to support the relatively high approach-ramp stresses (Fig. A.13). In addition, abutment piles are represented by a block of linear (elastic) elements ($E = 5 \times 10^5$ kPa , $\nu = 0.25$, Fig. A.13) representative of the original pile-soil system stiffness, so as to reduce the FE model complexity. The abutment slope towards the river channel is 40 degrees, and the approach ramp average side slope is 30 degrees (Fig. A.13). In the present model, the connections between the abutments and the bridge superstructure ends are simply modeled as perfect hinges using the equalDOF constraints (for translations only) in OpenSees (McKenna and Fenves 2001). Obviously, more refined modeling of this important bridge component would potentially provide additional useful insights.

A.5.4.1 Soil Constitutive Model

The foundation soil is modeled as a nonlinear hysteretic material (Prevost 1978; Parra 1996) with a Von Mises multi-surface (Iwan 1967; Mroz 1967) kinematic plasticity model (Fig. A.14). In this regard, focus is on reproduction of the soil hysteretic elasto-plastic shear response (including permanent deformation).

A detailed description of this model (PressureIndependMultiYield) along with the user interface can be found online at http://opensees.berkeley.edu or http://cyclic.ucsd.edu/opensees. The latter site also includes a number of sample examples for testing purposes.

In this model, the nonlinear shear stress-strain back-bone curve is represented by a hyperbolic relation (Kondner 1963) defined by two material constants: low-strain shear modulus and ultimate shear strength (Table A.5).

A.5.5 Boundary Conditions

A.5.5.1 Lateral Mesh Boundaries

Near ground surface, soil response to earthquake motion is assumed to be predominantly caused by vertically propagating shear waves (e.g., Idriss and Sun 1993; Elgamal et al. 1995; Kramer 1996). Thus, in the free field (away from the superstructure), the lateral soil domain response is expected to closely match that of a conventional shear-beam (Kramer 1996). In this regard, the longitudinal/transversal mesh lateral boundaries (at any given depth) are constrained to undergo the same vertical and longitudinal/transversal motions, using the equalDOF constraint in OpenSees. These lateral boundaries are located as far as possible from the superstructure so as to decrease any effect of these boundary conditions on the bridge response (Fig. A.8).

A.5.5.2 Along Model Base

For computational efficiency, it is desirable to limit the depth of the soil domain. Herein, the FE mesh base is placed away from the foundation system at a depth of 74.5m from ground surface (Fig. A.8). Conventionally, during seismic

excitation, soil strata below this depth may be represented by a transmitting boundary. In this study, the Lysmer-Kuhlemeyer (1969) boundary is applied along the model base so as to handle spurious reflections of waves at the soil mesh base. At each node along the base, three dashpots are activated in the x, y, and z directions, and incident seismic wave excitation is defined by three dynamic equivalent nodal forces.

In order to prescribe these dynamic forces along the FE model base, the following procedure is adopted (Zhang et al. 2003, 2005): (1) along the base, essentially rigid springs are activated during the initial stage of static own-weight load application, (2) after application of own weight, the force in each spring is recorded, and (3) before dynamic excitation, the rigid springs are replaced by the forces, allowing for perfect static equilibrium and application of the seismically induced base-force time histories.

For implementation, the spring and dashpot in each direction are coupled and modeled by using the ZeroLength element in OpenSees. In addition, the spring removal is realized by using the material updating feature in OpenSees to reduce the spring stiffness to zero.

A.6 Definition of Input Excitation

As part of the Humboldt Bay Middle Channel Bridge PEER testbed activities, the September 16, 1978 Tabas earthquake record (Hartzell and Menodza 1991) was selected as a potential site-specific rock outcrop motion at a hazard level of 10% probability of exceedance in 50 years (Somerville and Collins 2002). This Tabas Earthquake record is employed in this study to derive an incident earthquake motion along the FE mesh base.

In order to obtain the corresponding incident wave motion at the model base, deconvolution of the Tabas rock outcrop lateral ground motions is achieved using Shake91 (Idriss and Sun 1993). Deconvolution is performed in two stages (Fig. A.15): (1) the rock outcrop motion is first deconvolved downwards to bedrock ($V_s = 900\text{m/s}$) at 217m depth, assuming the same overlying soft rock throughout (Fig. A.16 shows the shear modulus reduction and damping curves for this soft rock), and (2) using the bedrock motion, we adopt the soil shear wave profile above bedrock as shown in Fig. A.15 (after C. Roblee, personal communication, 2002) to propagate this base motion upwards. For simplicity, the shear modulus reduction and damping curves of sand as shown in Fig. A.17 are employed in this analysis phase (Silva 2003).

The above process allows for definition of an incident motion at the FE model base (74.5m depth). Fig. A.18 shows the achieved results. In the longitudinal and transversal directions, the peak acceleration of the incident motion at the FE model base is 0.255g and 0.233g, compared to the original 0.439g and 0.373g peak acceleration of the ground surface rock outcrop motion, respectively. Finally, incident vertical motion at the FE model base (peak acceleration of 0.185g) is simply assumed to be half that of the original ground surface Tabas record (Kramer 1996).

A.7 Solution Procedure

A staged analysis procedure is adopted with gravity loads applied first (statically) followed by dynamic earthquake excitation (Zhang et al. 2005). These two analysis stages are discussed below.

A.7.1 Stage I. Application of Self Weight

Gravity is applied first to the soil domain FE mesh, with linear material properties (E and ν given in Table A.5). As mentioned earlier, along the FE model base, essentially rigid springs (1.0×10^{10}kN/m spring constant) are placed in the longitudinal, transversal and vertical directions (Fig. A.19). Subsequently, a series of static nonlinear analyses is performed as the soil properties are updated to nonlinear (using the material state update feature in OpenSees), layer by layer from the base upwards. Thereafter, the superstructure own weight is added, acting on the existing soil domain mesh. After static equilibrium is obtained, the supporting base spring forces are recorded.

A.7.2 Stage II. Earthquake Dynamic Analysis

Using the material stiffness update feature in OpenSees, the supporting base springs are replaced by the recorded forces so that the entire system remains in equilibrium. The transmitting boundary dashpots (see Appendix I, Lysmer and Kuhlemeyer 1969) are included along with these static forces (Fig. A.19). Using this approach, 5000 time steps ($\Delta t = 0.005\,\text{sec}$) of transient dynamic nonlinear analysis are executed to evaluate the system response during 25 seconds of earthquake shaking. In this computation, the incremental-iterative integration scheme employs the Newmark-β time-stepping method in combination with the modified Newton-Raphson algorithm, using the initial stiffness matrix (after application of gravity) of the system for all steps and iterations. For the large-scale nonlinear computational model presented here, updating of the initial stiffness matrix to the tangent stiffness matrix, even once per step, significantly increases the computational time.

A.8 Free-Field Ground Response

Fig. A.20 shows a comparison of ground motion (acceleration time history) at different depths (0m, 2m, 9.33m, and 44.5m) between a 1D soil column (shear beam modeled with the same nonlinear soil layers as the 3D mesh) and the 3D mesh (location 1 in Fig. A.8). This comparison verifies that the soil domain is large enough and the free-field is not significantly affected by the presence of the bridge and the surrounding topography.

In addition, the amplification response spectra (i.e., ratio of 5% damped linear elastic response spectra) of ground motion at location 1 (free-field) compared to that of model base (vertically below location 1) is investigated to assess the underlying motion amplification effects (peaks around 1Hz for longitudinal and transversal shaking, and around 3Hz for vertical shaking, in Fig. A.21). For comparison, a preliminary linear study of this soil profile shows that the first four lateral resonant frequencies (in each horizontal direction) are at 1.3, 2.6, 4.3, and 6.0Hz. It is seen in Fig. A.21 that for the horizontal shaking (corresponding to shear waves), high-frequency components are significantly reduced (mainly, amplification near the first site resonance at about 1Hz). However, for the vertical excitation (Fig. A.21), significant amplification is observed over a wide frequency range.

A.9 Summary and Conclusions

In order to study the effect of seismically-induced ground deformation on bridge system response, a 3D nonlinear FE bridge-foundation-ground model is developed. The open-source software framework OpenSees is used to construct the model, in light of the structural configuration and site seismicity of the Humboldt Bay

Middle Channel Bridge PEER Testbed. Combining advanced structural and geotechnical seismic response simulation capabilities, OpenSees shows its potential as a flexible and powerful modeling and analysis tool. The employed pre/post-processor GiD is also an essential component. Herein, 3D linear frame and shell elements are used to model the bridge superstructure in view of its large yield strength relative to the piers, but the supporting piers and piles are modeled by 3D fiber section, force-based frame elements with nonlinear constitutive laws.

Based on downhole measurements of shear wave velocity, the soil profile is idealized into a surface crust layer and five underlying sub-layers. The top sub-layer is selected as a relatively soft material in order to study the effect of lateral inelastic ground deformation on the bridge foundation, piers and superstructure. The soil is modeled as a nonlinear material with a Von Mises multi-surface kinematic plasticity model so as to reproduce hysteretic elasto-plastic shear response (including permanent deformation). The longitudinal/transversal mesh lateral boundaries (at any given depth) are constrained to undergo the same vertical and longitudinal/transversal motions. Energy transmission and seismic input along the base of the computational soil domain are allowed using the classical Lysmer-Kuhlemeyer formulation. A staged nonlinear dynamic analysis procedure is adopted to evaluate the system seismic response. Details of the simulation results are presented in Appendix B, along with discussions on the potential detrimental kinematics of bridge-ground kinematic interaction.

A.10 Acknowledgements

The material in this appendix is prepared as a paper draft for publication, and the author is the primary researcher. This material is also based on the contributions of (1) Professor Ahmed Elgamal, the Ph.D. advisor of author, (2) Dr. Zhaohui Yang, who helped in the numerical modeling of soil system using OpenSees, and (3) Prof. Joel P. Conte, who helped in the numerical modeling of the bridge structural system using OpenSees, and in the editing process.

Support of this work is provided by the Earthquake Engineering Research Centers Program of the National Science Foundation, under Award Number EEC-9701568 through the Pacific Earthquake Engineering Research Center (PEER), and NSF Grants (No. CMS0084616 and CMS0200510). This support is gratefully acknowledged. The authors wish to thank Mr. Patrick Hipley, Dr. Cliff Roblee, Dr. Charles Sikorsky, Mr. Thomas Shantz, and Mr. Mark Yashinsky of Caltrans for providing all the requested information regarding the Humboldt Bay Middle Channel Bridge. Professor Gregory Fenves and Dr. Frank McKenna of U.C. Berkeley and Professor Michael Scott of Oregon State University helped with the OpenSees modeling and analysis phase. Professor Kincho Law and Dr. Jun Peng (Stanford University) were instrumental in providing their sparse solver and assisting in every way. This assistance was most valuable and is highly appreciated.

A.11 Appendix I

The nodal coefficient of lateral and vertical dashpots may be defined by (Lysmer and Kuhlemeyer 1969) $C = \rho v A$, where ρ (1900kg/m3) and v (550m/s laterally and 1400m/s vertically) are estimated as the average values of mass density

and shear wave (laterally) or compression wave (vertically) velocity of underlying soil layers between the FE model base and bedrock, and A is the surface boundary area attributed to the node.

With the dashpots, dynamic base excitation is imposed along the FE model base in terms of three equivalent nodal forces in the longitudinal, transversal and vertical directions, respectively. In a given direction, the force is defined by (Lysmer and Kuhlemeyer 1969) $F_i(t) = 2\rho v A v_i(t)$, where $v_i(t)$ is the corresponding velocity component of the incident earthquake motion at the FE model base.

A.12 Tables

Table A.1 Model Parameters of Linear Elastic Beam-Column Element

	A (m^2)	I_z (m^4)	I_y (m^4)
Longitudinal I-girder	0.73	0.49	0.0094
Transversal brace I-beam	0.1	0.067	0.00017

Table A.2 Constitutive Model Parameters (Fig. A.9e) for Concrete Material Used in Fiber Beam-Column Element

Concrete01 material model in OpenSees	Confined concrete	Unconfined concrete
Compressive strength (f_c, kPa)	-3.45×10^4 (-5ksi)	-2.76×10^4 (-4ksi)
Strain at compressive strength (ε_c)	-0.004	-0.002
Crushing strength (f_{cu}, kPa)	-2.07×10^4 (-3ksi)	0
Strain at crushing strength (ε_{cu})	-0.014	-0.008

Table A.3 Constitutive Model Parameters (Fig. A.9f) for Steel Material Used in Fiber Beam-Column Element

Steel01 material model in OpenSees	Reinforcing steel
Yield strength (f_y , kPa)	4.14×10^5 (60ksi)
Initial elastic tangent modulus (E_s , kPa)	2.0×10^8 (29000ksi)
Hardening ratio (b)	0.008

Table A.4 Pile Spacing of the Idealized 2×2 Pile Groups (1.37m Diameter) in the FE Model

	Longitudinal spacing (m)	Transversal spacing (m)
Pile group of 16 0.356m square piles (1, 7, 8 in Fig. A.7)	2.67	2.67
Pile group of 5 1.37m diameter piles (2-6 in Fig. A.7)	2.67	4.00

Table A.5 Soil Layer Properties (Fig. A.8)

Soil layer in Fig. A.8	Mass density (kg/m^3)	Shear modulus G (kPa)	Poisson's ratio	Shear strength s_u (kPa)
Abutment soil	2000	30000	0.4	30
Crust layer	1500	60000	0.4	40
Layer 1	1300	19000	0.4	10
Improved approach foundation	1500	25000	0.4	25
Layer 2	1500	60000	0.4	40
Layer 3	1800	196000	0.4	75
Layer 4	1900	335000	0.4	75
Layer 5	1900	475000	0.4	75

A.13 Figures



Fig. A.1 Damage to the Toyokoro wooden bridge at Toyokoro, Tokachi District, Hokkaido during Tokachi-Oki, Japan earthquake ($M_w = 8.10$, on March 4, 1952). As the abutment pushed forward, the bridge buckled (Steinbrugge 2002).



Fig. A.2 Damaged east abutment of bridge crossing the Rio Valdivia in the Chile Earthquake of May, 1960 (Steinbrugge 2002).



Fig. A.3 Settlement at east abutment of bridge across Rio Valdivia in the Chile Earthquake of May, 1960 (Steinbrugge 2002).



Fig. A.4 Abutment settlement, at Nordhoff Way Bridge over the Southern Pacific Railroad after Northridge Earthquake (UC and NISEE 2002a).



Fig. A.5 Sky view of Humboldt Bay Middle Channel Bridge (Courtesy of Caltrans).

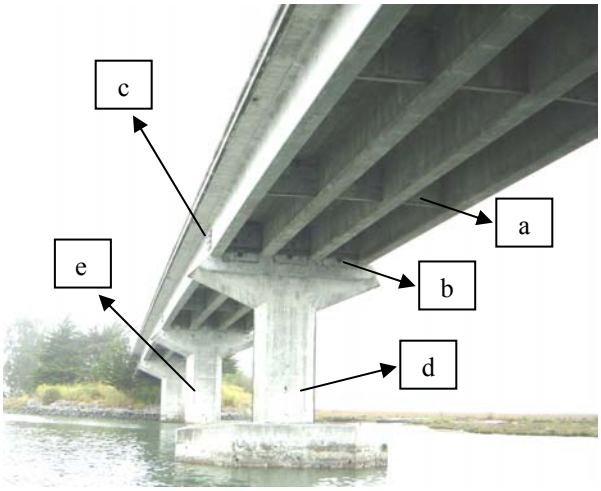


Fig. A.6 Close-up photo of Humboldt Bay Middle Channel Bridge (taken by authors on August 16, 2002) shows the following structural details. (a) transversal brace I-beam between main longitudinal I-girders; (b) longitudinal shear keys at the connection between superstructure and cap beam; (c) expansion joint on top of the sixth pier; (d) the sixth pier supported by a pile group with pile cap above ground and concrete skirt around it; and (e) the seventh pier supported by a pile group with pile cap below ground surface.

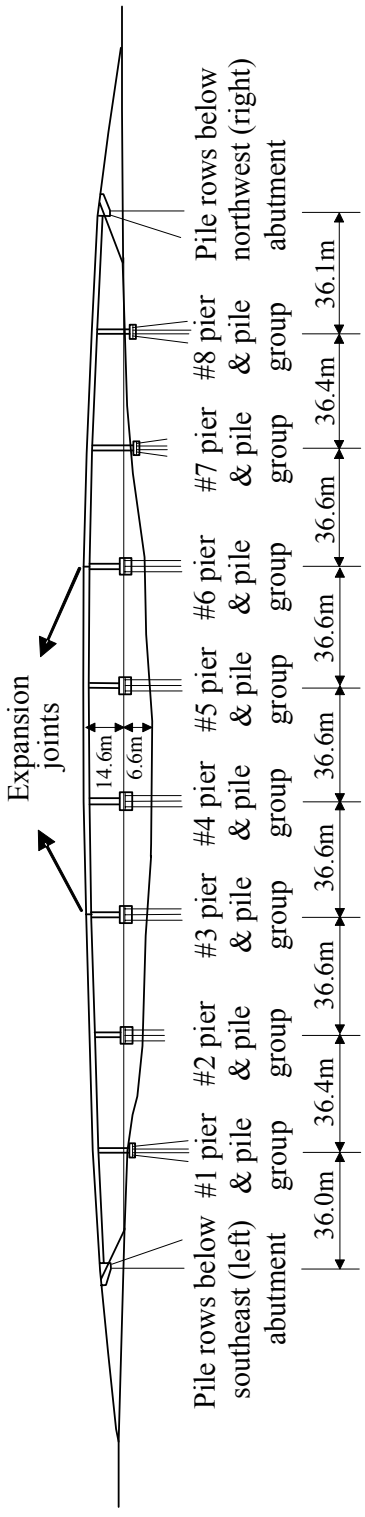


Fig. A.7 Global elevation view of bridge superstructure, piers, and foundation system.

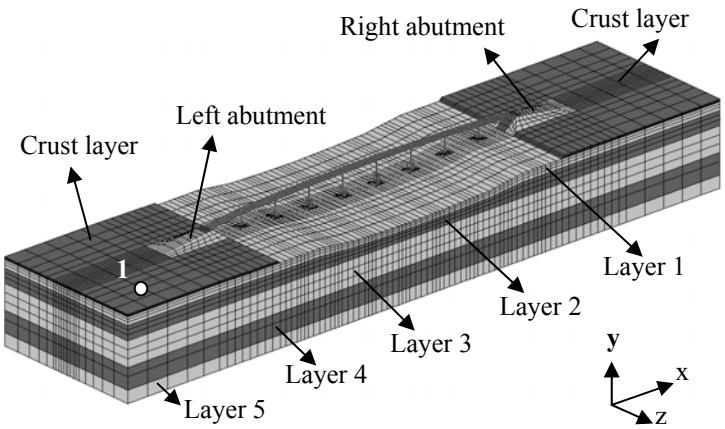


Fig. A.8 3D FE model of bridge and idealized soil profile.

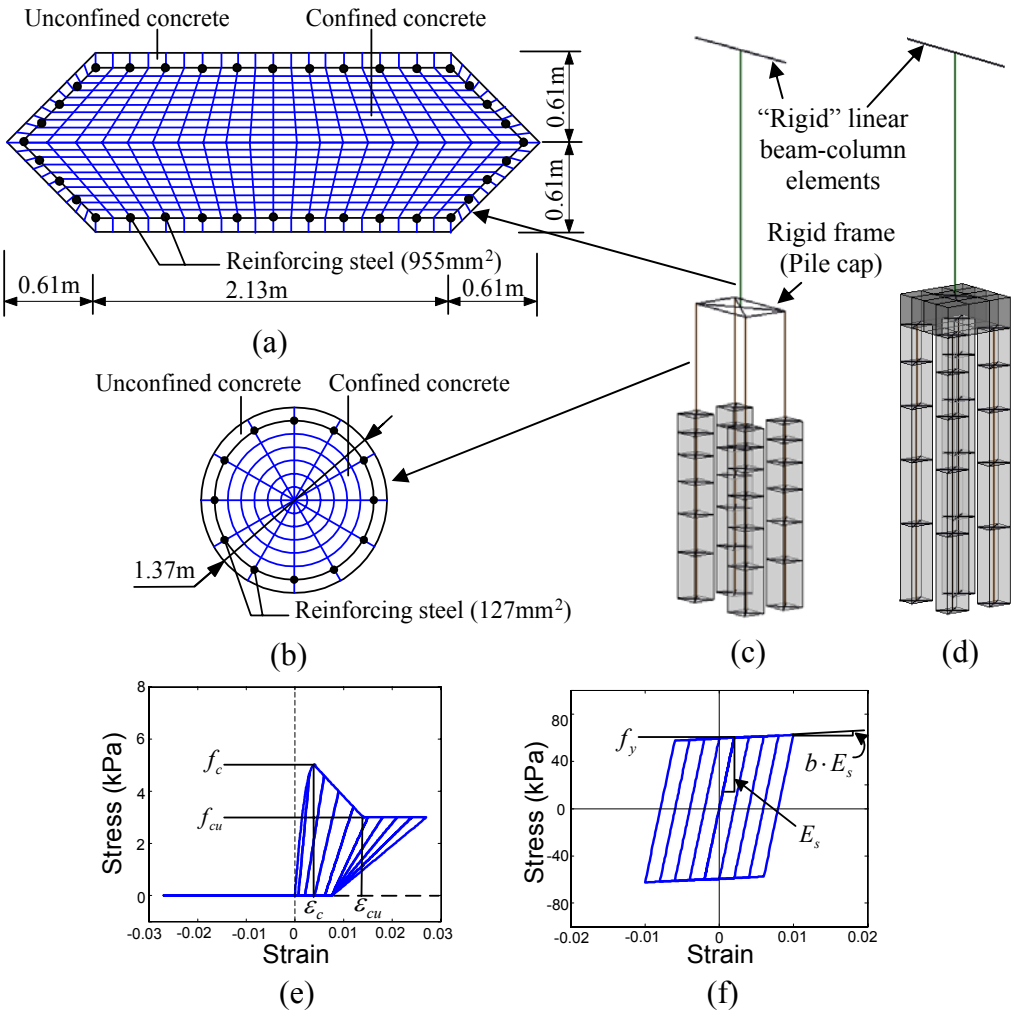


Fig. A.9 Modeling of pier and pile group using fiber-section beam-column element with uni-axial material constitutive models: (a) fiber discretization of pier cross-section; (b) fiber discretization of pile cross-section; (c) pile group with pile cap above ground; (d) pile group with pile cap below ground surface; (e) concrete Kent-Scott-Park model with degraded linear unloading/reloading stiffness; and (f) reinforcing steel bilinear inelastic model with linear kinematic hardening.

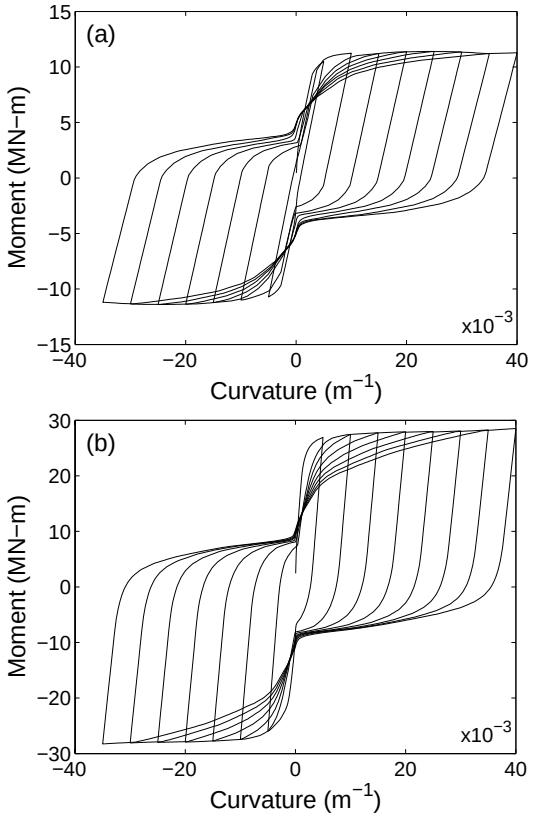


Fig. A.10 Cyclic moment-curvature response of pier cross-section under constant axial load due to gravity of 8MN ($\cong 0.08 f_c' A_g$): (a) longitudinal bending, and (b) transversal bending

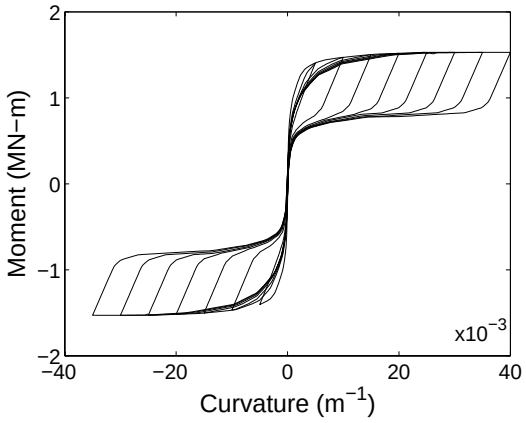


Fig. A.11 Cyclic moment-curvature response of circular pile cross-section under constant axial load due to gravity of 2MN ($\cong 0.04 f_c' A_g$).

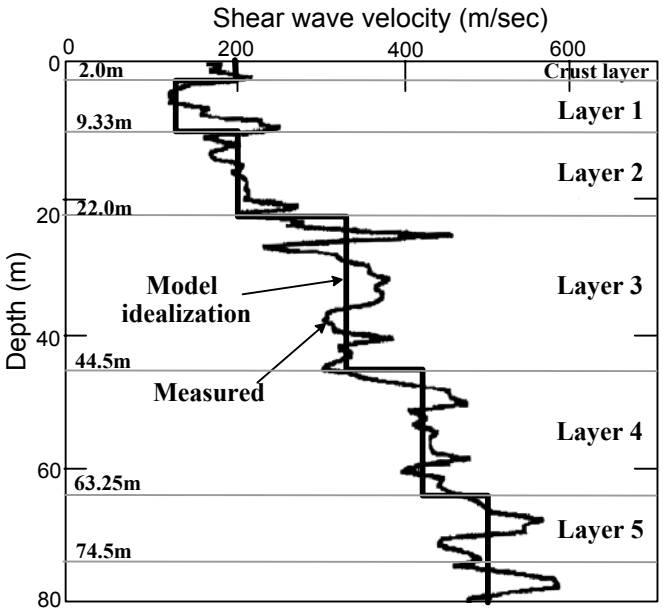


Fig. A.12 Idealized soil shear wave velocity profile (Fig. A.8, free-field) and measured soil shear wave velocity of borehole 1 at Caltran's Samoa Bridge Geotechnical downhole array, about 0.25 mile north-west of northwest abutment of Humboldt Bay Middle Channel Bridge (C. Roblee, personal communication, 2002).

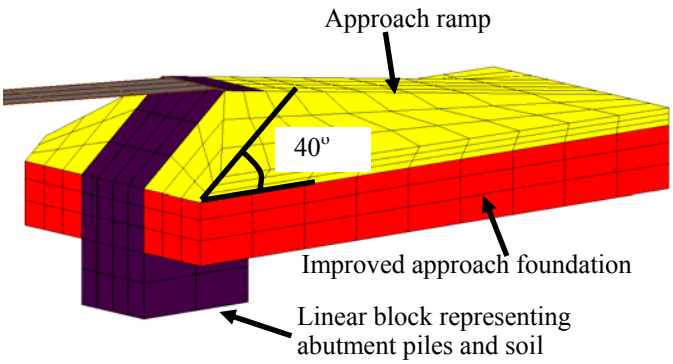


Fig. A.13 Details of abutment and approach ramp zone.

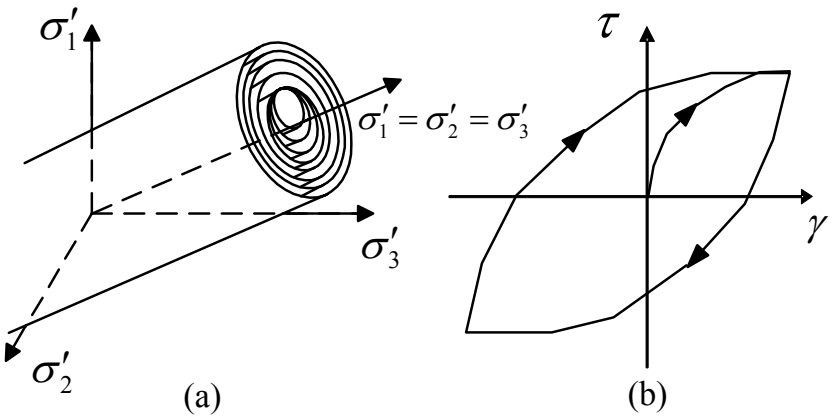


Fig. A.14 Yield surfaces and hysteretic shear response of the employed soil model.

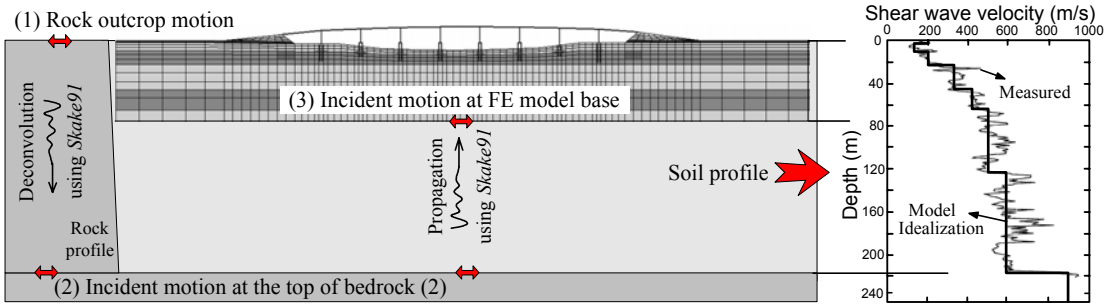


Fig. A.15 Deconvolution of rock outcrop motion using Shake91 (Idriss and Sun 1993).

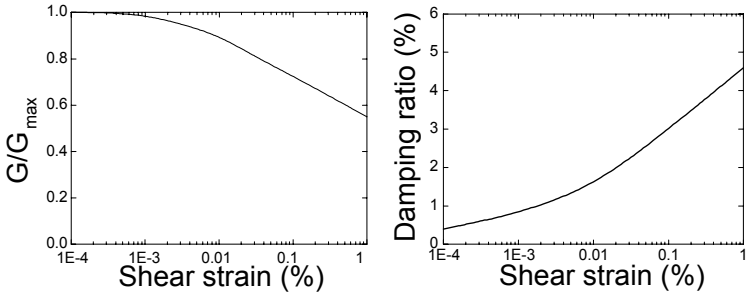


Fig. A.16 Shear modulus reduction and damping curves of rock in Shake91 Manual (Idriss and Sun 1993) used for the deconvolution analysis phase.

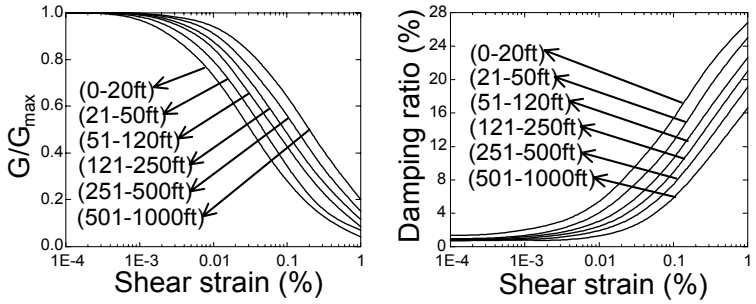
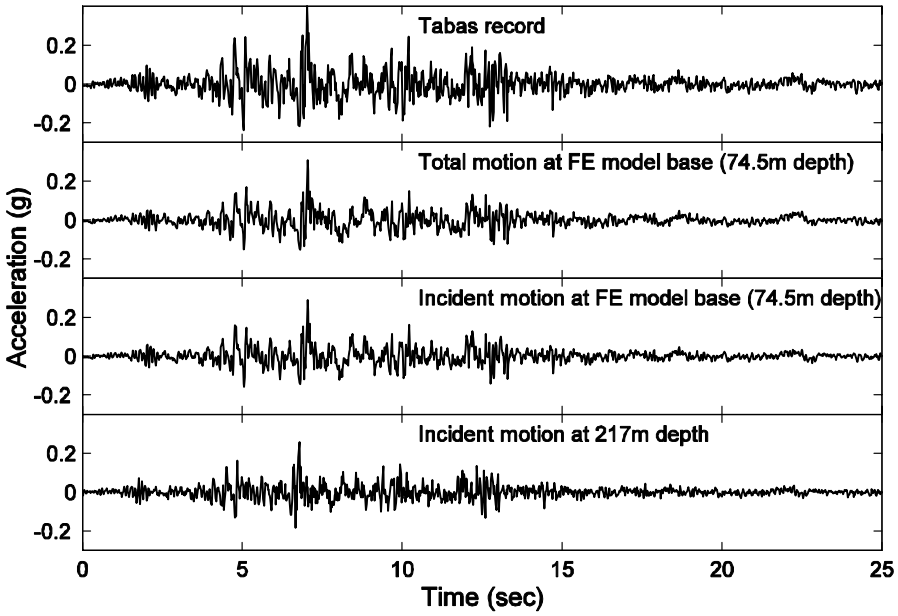
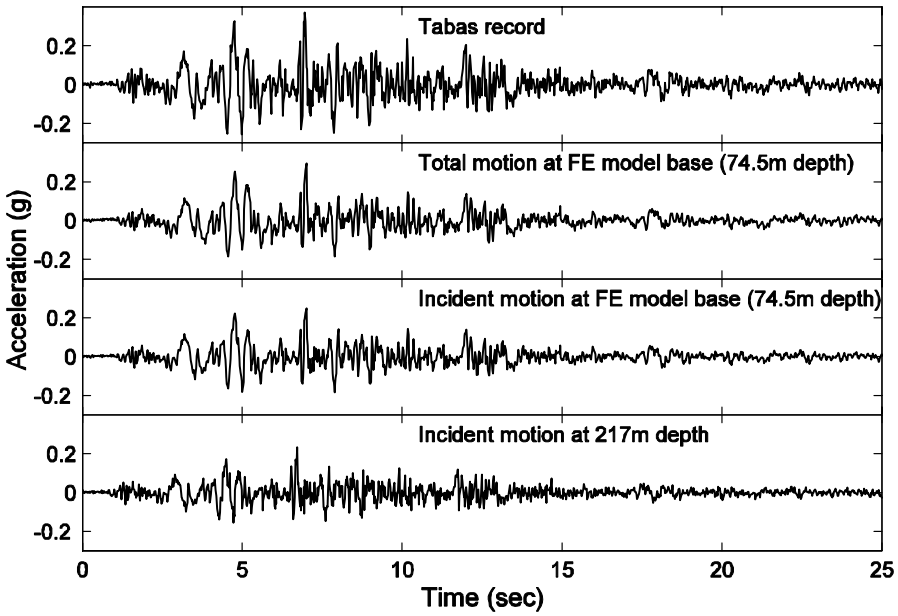


Fig. A.17 Shear modulus reduction and damping curves of sand according to soil depth (Silva 2003) used in the upward propagation analysis phase



(a) Longitudinal direction



(b) Transversal direction

Fig. A.18 Results of deconvolution: acceleration time histories of the original rock outcrop motion (location 1 in Fig. A.15), bedrock incident motion (location 2 in Fig. A.15), incident and total motion at FE model base (location 3 in Fig. A.15).

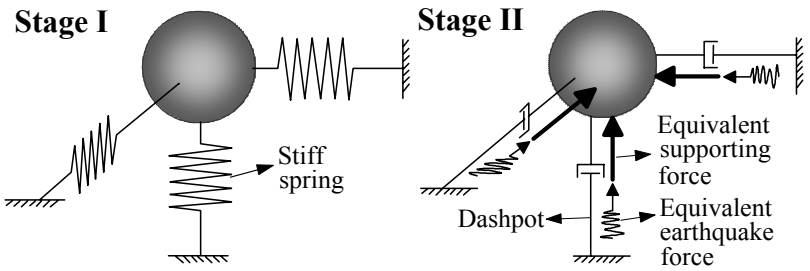
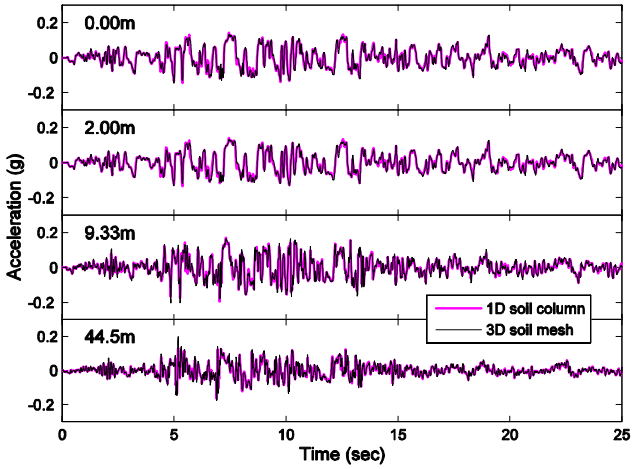
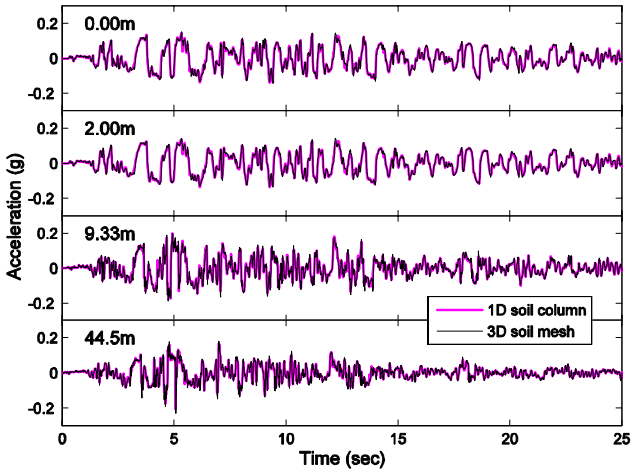


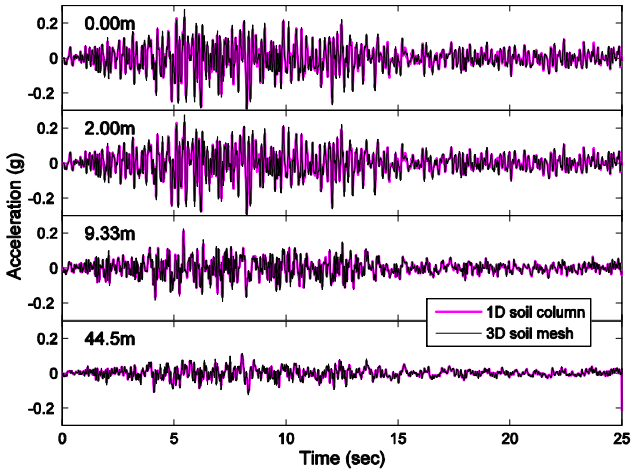
Fig. A.19 Schematic of updated boundary condition applied at a node along the FE model base (Stage I, application of own weight, and Stage II, earthquake dynamic analysis).



(a) Longitudinal direction



(b) Transversal direction



(c) Vertical direction

Fig. A.20 Free-field ground motion comparison of 1D soil column and the 3D soil mesh (location 1 in Fig. A.8).

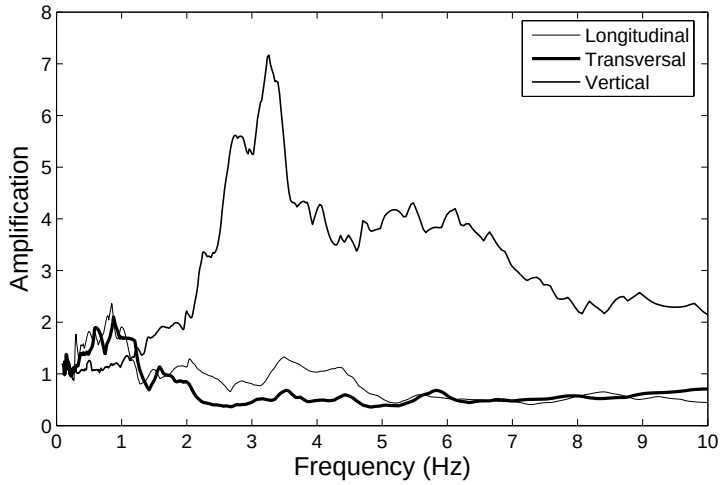


Fig. A.21 Amplification response spectrum of ground motion at location 1 (free-field) in Fig. A.8.

A.14 References

Baldwin, J. E. II, and Sitar, N. (eds.) (1991). "Loma Prieta Earthquake: Engineering Geologic Perspectives." *Special Publication No. 1*, Association of Engineering Geologists, San Francisco, CA.

Bathe, K. J. (1996). *Finite Element Procedures*, Prentice-Hall Inc., New Jersey.

Bonaparte, R., and Mitchell, J. K. (1979). *The Properties of San Francisco Bay Mud at Hamilton Air Force Base, California*, University of California, Berkeley.

Conte, J. P., Elgamal, A., Yang, Z., Zhang, Y., Acero, G., and Seible, F. (2002). "Nonlinear Seismic Analysis of a Bridge Ground System." *Proc. of the 15th ASCE Engineering Mechanics Conference (EM 2002)*, Columbia University, New York, NY.

Diaz, N. D., and Amat, P. S. (1999). *GiD the Personal Pre/Postprocessor User Manual Version 5.0*, CIMNE, Barcelona, Spain.

Earthquake Engineering Research Institute (EERI). (1995). "Northridge Report Vol. 1." *Earthquake Spectra*, Vol. 11, Supplement C, Chapter 6.

Elgamal, A., Zeghal, M., and Parra, E. (1995). "Identification and Modeling of Earthquake Ground Response." *First International Conference on Earthquake Geotechnical Engineering, IS-TOKYO'95*, Tokyo, Japan, 3, 1369-1406.

Goldman, H. B. (ed.) (1969). "Geologic and Engineering Aspects of San Francisco Bay Fill." *Special Report 97*, California Division of Mines and Geology.

Hartzell, S. H., and Mendoza, C. (1991). "Application of an Iterative Least-Squares Waveform Inversion of Strong-Motion and Teleseismic Records to the 1978 Tabas, Iran Earthquake." *Bull. Seism. Soc. Am.*, 81, 3-5-331.

Idriss, I. M., and Sun, J. I. (1993). *User's Manual for SHAKE91 : a Computer Program for Conducting Equivalent Linear Seismic Response Analyses of Horizontally Layered Soil Deposits,* Center for Geotechnical Modeling, Dept. of Civil and Environmental Engineering, University of California, Davis, CA.

Iwan, W. D. (1967). "On a Class of Models for the Yielding Behavior of Continuous and Composite Systems." *J. Applied Mechanics, ASME*, 34, 612-617.

Japan National Committee on Earthquake Engineering (JNCEE). (1965). "Niigata Earthquake, 1964." *Proceedings of the 3rd World Conference in Earthquake Engineering*, 3, 78-105.

Japanese Geotechnical Society (JGS). (1996). *Special Issue on Geotechnical Aspects of the January 17, 1995 Hyogoken-Nanbu Earthquake*, *Soils and Foundations Journal*, Tokyo, Japan.

Japanese Geotechnical Society (JGS). (1998). *Special Issue on Geotechnical Aspects of the January 17, 1995 Hyogoken-Nanbu Earthquake, No.2, Soils and Foundations Journal*, Tokyo, Japan.

Ju, S. H. (2004). "Three-Dimensional Analysis of Wave Barriers for Reduction of Train-Induced Vibrations." *Journal of Geotechnical and Geoenvironmental Engineering, ASCE*, 04(7), 740-748.

Kent, D. C., and Park, R. (1971). "Flexural Members with Confined Concrete." *J. Struct. Div., ASCE*, 97(7), 1969–1990.

Kondner, R. L. (1963). "Hyperbolic Stress–Strain Response: Cohesive Soils." *J. Soil Mech. Found. Div.*, 89(1), 115–143.

Kramer, S. L. (1996). *Geotechnical Earthquake Engineering*, Prentice-Hall, Englewood Cliffs, New Jersey.

Law, K. H., and Mackay, D. R. (1993). "A Parallel Row-Oriented Sparse Solution Method for Finite Element Structural Analysis." *International Journal for Numerical Method in Engineering*, 36, 2895-2919.

Lysmer, J., and Kuhlemeyer, R. L. (1969). "Finite Dynamic Model for Infinite Media." *J. Eng. Mech. Div., ASCE*, 95(EM4), 859-877.

Mackay, D. R., Law, K. H., and Raefsky, A. (1991). "An Implementation of a Generalized Sparse/Profile Finite Element Solution Method." *Computers & Structures*, 41, 723-737.

Mander, J. B., Priestley, M. J. N., and Park, R. (1988). "Theoretical Stress-Strain Model for Confined Concrete." *Journal of the Structural Engineering*, 114(ST8), 1804-1826.

McKenna, F. T. (1997). "Object-Oriented Finite Element Programming: Frameworks for Analysis, Algorithms and Parallel Computing." *Ph.D. Dissertation*, University of California, Berkeley.

McKenna, F. T., and Fenves, G. L. (2001). *The OpenSees Command Language Manual, Version 1.2*, Pacific Earthquake Engineering Research Center, University of California, Berkeley.

Mroz, Z. (1967), "On the Description of Anisotropic Work Hardening." *J. Mechanics and Physics of Solids*, 15, 163-175.

Parra, E. (1996). "Numerical Modeling of Liquefaction and Lateral Ground Deformation Including Cyclic Mobility and Dilation Response in Soil Systems." *Ph.D. Dissertation*, Dept. of Civil Engineering, Rensselaer Polytechnic Institute, Troy, NY.

Peng, J. (2002). "An Internet-Enabled Software Framework for the Collaborative Development of a Structural Analysis Program." *Ph.D. Dissertation*, Department of Civil and Environment Engineering, Stanford University, Stanford, CA.

Porter, K. A. (2003). "An Overview of PEER's Performance-Based Earthquake Engineering Methodology." *Proc. Ninth International Conference on Applications of Statistics and Probability in Civil Engineering (ICASP9)*, Civil Engineering Risk and Reliability Association (CERRA), San Francisco, CA.

Prevost, J. H. (1978). "Plasticity Theory for Soil Stress-Strain Behavior." *Journal of the Engineering Mechanics Division*, 104(5), 1177-1194.

Rogers, J. D., and Figuers, S. H. (1991). "Engineering Geologic Site Characterization of the Greater Oakland–Alameda Area, Alameda and San Francisco Counties, California." *Report*, National Science Foundation.

Scott, B. D., Park, R., and Priestley, M. J. N. (1982). "Stress-Strain Behavior of Concrete Confined by Overlapping Hoops at Low and High Strain Rates." *Journal of the American Concrete Institute*, 79(1), 13-27.

Seed, R. B., Dickenson, S. E., Riemer, M. F., Bray, J. D., Sitar, N., Mitchell, J. K., Idriss, I. M., Kayen, R. E., Kropp, A., Harder, L. F. Jr., and Power, M. S. (1990). "Preliminary Report on the Principal Geotechnical Aspects of the October 17, 1989, Loma Prieta Earthquake." *Report No. UCB/EERC-90/05*, Earthquake Engineering Research Center, Berkeley, CA.

Silva, W. (2003). "Soil Response to Earthquake Ground Motion." *Research Project RP2556-07 Final Report*, Woodward-Clyde Consultants, Walnut Creek, CA.

Sitar, N. (ed.) (1995). "Geotechnical Reconnaissance of the Effects of the January 17, 1995, Hyogoken-Nanbu Earthquake, Japan." *Report No. UCB/EERC-95/01*, Earthquake Engineering Research Center, Berkeley, CA.

Spacone, E., Filippou, F. C., and Taucer, F. F. (1996). "Fibre Beam-Column Model for Non-Linear Analysis of R/C Frames: Part I. Formulation." *Earthquake Engineering and Structural Dynamics*, 25(7), 711-725.

Somerville, P., and Collins, N. (2002). "Ground Motion Time Histories for the Humboldt Bay Bridge." *Report*, prepared for the PEER Methodology Testbeds Project, URS Corporation, Pasadena, CA.

Souza, R. M. (2000). "Force-based Finite Element for Large Displacement Inelastic Analysis of Frames." *Ph.D. Dissertation*, University of California, Berkeley.

Steinbrugge, K. V. (2002). *The Karl V. Steinbrugge Slide and Photograph Collection World Earthquakes and Earthquake Engineering*, Earthquake Engineering Research Center, <http://nisee.berkeley.edu/eqiis.html>.

University of California (UC), and National Information Service for Earthquake Engineering (NISEE) (2002a). *Earthquake Image Information System*, <http://nisee.berkeley.edu/eqiis.html>.

University of California (UC), and National Information Service for Earthquake Engineering (NISEE) (2002b). "Northridge California Earthquake January 17, 1994." <http://nisee.berkeley.edu/northridge/northridge.html>.

US Geological Survey (USGS). (2003). "Largest Earthquake in the World: Chile 1960 May 22 19:11:14 UTC Magnitude 9.5." Earthquake Hazards Program, <http://neic.usgs.gov/neis/eq_depot/usa/1960_05_22_articles.html>.

Wang, C. K., and Salmon, C. G. (1992). *Reinforced Concrete Design*, 5th Ed., HarperCollins Publisher Inc., New York, NY.

Yanev, P. (1993). "Hokkaido Nansei-Oki Earthquake of July 12, 1993." *EQE Review*, 1993(Fall).

Zhang, Y., Yang, Z., Bielak, J., Conte, J. P., and Elgamal, A. (2003). "Treatment of Seismic Input and Boundary Conditions in Nonlinear Seismic Analysis of a Bridge Ground System." *Proc. of the 16th ASCE Engineering Mechanics Conference (EM 2003)*, University of Washington, Seattle, WA.

Zhang, Y., Conte, J. P., Yang, Z., Elgamal, A., Bielak, J., and Acero, G. (2005). "Two-Dimensional Nonlinear Earthquake Response Analysis of a Bridge Ground System." *Earthquake Spectra*, submitted for publication, Dec. 2005.

APPENDIX B

THREE-DIMENSIONAL BRIDGE-FOUNDATION-GROUND SYSTEM: PART II. SEISMIC RESPONSE

In Appendix A, a three-dimensional (3D) model of a bridge-foundation-ground system is presented. The challenges are discussed, and the employed material constitutive models are described. Details are presented regarding the employed software framework, modeling effort, spatial definition of seismic excitation, and staged analysis procedure. In Appendix B, the seismic response simulation results are reported, along with potential scenarios of detrimental bridge-ground kinematic interaction effects. The overall system response behavior is examined, as well as local deformations/stresses at selected critical locations. It is seen that permanent ground deformation may induce settlement and longitudinal/transversal displacements of the abutments and deep foundations. The relatively massive approach ramps may also contribute to this simulated damage condition, which imposes large stresses on the bridge foundations, supporting piers, and superstructure.

B.1 Introduction

Motivated by the structural configuration, local soil conditions and site seismicity of the Humboldt Bay Middle Channel Bridge, a large-scale 3D Finite Element (FE) model of the bridge-foundation-ground system is developed (Appendix A). In the following sections of this paper, details of the simulation results are presented, along with discussions of potential detrimental effects of bridge-ground kinematic interaction.

B.2 Global Response Behavior of the Bridge-Foundation-Ground System

Fig. B.1a shows the residual deformation (3D view in exaggerated scale) of the entire bridge-foundation-ground system after earthquake shaking. The elevation and plan views of this deformation are shown in Figs. B.1b-c, where the arrows indicate the directions of soil flow, heave, settlement, and lateral spreading. As observed in historical earthquake events (Appendix A), Fig. B.1 presents typical damage scenarios such as settlement of abutment fill, soil lateral spreading along the river bank, and the resulting deformation of the bridge foundation system and superstructure. Superimposed on local deformations is a minor global lateral shift (0.04m longitudinally and 0.05m transversally) along the ground surface (upper 6 meters), resulting from yielding in the underlying 4.9-7.3m thick soft bay-mud layer (Appendix A).

Along the river banks (Figs. B.1b-c), the yielded soil flows down-slope towards the center of the river channel, and the maximum soil lateral movement at both river banks reaches approximately 0.28m. Furthermore, the soil flowing towards the center of channel elevates the river bed by about 0.1m near the banks and about 0.05m at the center (Fig. B.1b).

The mass of the approach ramps results in ground settlement (Fig. B.1) of about 0.3m at the left abutment and 0.4m at the right abutment). Similar damage scenarios were also observed in historical earthquake events (e.g., Rio Valdivia Bridge in 1960 Chile Earthquake, Steinbrugge 2002; Nordhoff Way Bridge in 1994 Northridge Earthquake, UC and NISEE 2002). Such large settlement of approach ramps will impede traffic and result in malfunction after the earthquake. Finally, Fig.

B.1c indicates transversal lateral spreading of the approach ramps (maximum of about 0.05 m), highlighting the 3D nature of soil deformation.

B.3 Spatial Ground Motion Variability

Computed ground surface motion at 3 representative locations (1-3, indicated by black dots in Fig. B.1c) from the free-field to the center of the river channel are compared. Fig. B.2 shows the acceleration time history comparison in the longitudinal, transversal, and vertical directions, respectively. In the vicinity of the river channel center, higher peak accelerations and more high frequency components (Fig. B.3) are observed. For instance (Figs. B.2a-b), peak acceleration at location 1 in Fig. B.1c (free field) is only about 0.12-0.14g, while peak acceleration at the center (location 3 in Fig. B.1c) reaches 0.22-0.25g (almost double).

Hence, it appears that surface ground motion can be noticeably different along the bridge spatial extent. Such a spatial variability of the surface ground motion may have some implications in simulation studies where the superstructure is studied without an underlying soil domain. Potential mechanisms behind this observed difference are discussed in the next section.

B.4 Soil Response

B.4.1 Free Field Response

Soil shear stress-strain response at different depths of location 1 in Fig. B.1c (free field) is shown in Fig. B.4a. Response at 5 different depths is shown: 1m (middle of the crust layer), 8m, 20m, 40m, and 70m (base of layers 1, 2, 3, and 5). Near the base (70m depth), some yielding may be observed at high shear stress levels, providing a sort of base isolation mechanism at this base soil layer. The bay-mud weak

soil layer in the free field (8m depth) experiences large inelastic deformations. Consequently, only low levels of shear stress are transmitted to the crust layer (see Fig. B.4a at 1m depth).

These low levels of shear stress in the surficial crust layer (free-field) also correlate to the observed lower ground surface acceleration peaks at location 1, as compared to location 3 near the river channel center (Figs. B.2a-b). In this regard, inertial shear loads in the upper crust layer (which is only present in the free-field) are limited by yielding in the underlying bay-mud. This conclusion is further confirmed by results of separate studies (not presented here) based on 1D nonlinear shear beam models of the free-field and channel-center soil profile.

B.4.2 Ground Response near Abutments

Soil shear stress-strain behavior at different depths of location 4 in Fig. B.1c (next to the right abutment) is shown in Fig. B.4b. Compared to Fig. B.4a, much higher levels of inelastic shear strain are observed in the 8m-20m depth range. The bridge approach ramp/abutment system near the channel slope has clearly induced additional soil deformations at this location compared to the free-field situation of Fig. B.4a. Additional locations around the left/right abutments are also checked, and the simulation results show similar accumulated levels of shear strain in the soil (also significantly larger than in the free field).

B.5 Response of Bridge Structure

Fig. B.5a shows the elevation view of structural and embankment soil/abutment deformation (exaggerated by a factor of 50). Lateral spreading causes the bridge pile groups to move towards the river channel center (maximum lateral

permanent displacement of about 0.1m at pile group 1). In addition to settlement, the abutments are slightly tilted (about 1 degree), reminiscent of the Rio Valdivia Bridge response (Steinbrugge 2002; Fig. A.2 in Appendix A).

The plan view of structural deformation (exaggerated by a factor of 150) is depicted in Fig. B.5b. It is observed that the permanent transversal displacement is non-uniform ranging from 0.01m (between the first and second pile groups) to 0.12m (near the right abutment). Generally, Fig. B.5 highlights the significance of 3D analysis, and the inelastic ground deformation imposed on the bridge foundations.

Fig. B.6 shows the earthquake excitation at 3 representative locations of the bridge superstructure supports (left abutment, Pier 2 base and Pier 4 base). Consistent with the results shown in Fig. B.2, locations closer to the river channel center show larger amplitudes (by as much as 50%) and higher frequency content for the horizontal motions (Fig. B.7).

Fig. B.8 shows acceleration time histories at 3 different locations along the bridge superstructure (left end, Pier 2 top, and Pier 4 top) in the longitudinal, transversal, and vertical directions, respectively. The longitudinal acceleration responses at these locations are very similar due to the high axial stiffness of the superstructure (Fig. B.8a). Away from the bridge ends, transversal motion is clearly amplified (Fig. B.8b). Compared to the pier base horizontal response (Figs. B.6a-b), the motion is amplified with relatively little high frequency response (i.e., high frequency components are filtered out by the bridge structure). The corresponding acceleration amplification spectra (i.e., ratio of acceleration response spectrum at an inspected location over that at a reference location) referenced to the base of Pier 4

(Fig. B.9) show significant peaks up to about 2.5Hz (horizontal motions) due to the bridge vibration relative to its base, and no appreciable amplification for the vertical motion. A resonance at about 1Hz is seen to clearly dominate the longitudinal bridge response.

B.6 Response of Bridge Piers

In our modeling effort, the bridge deck system is assumed linear elastic and essentially rigid (Appendix A), maintaining the relative distance between the pier tops. However, spacing between the pile caps (at the pier bases) changes significantly due to soil lateral spreading (Fig. B.5a). Therefore, permanent (residual) shear forces and bending moments are induced in the bridge piers.

Fig. B.10a shows the longitudinal displacement time histories of representative piers. At the end of shaking, the bridge superstructure undergoes an overall residual displacement of 0.125m. The difference in displacement between any two pile caps increases continuously in time (Fig. B.10a), resulting in permanent pier top-to-bottom relative displacement of as much as 0.07m for Pier 2 and 0.09m for Pier 7.

As might be expected, much lower levels of permanent deformation are observed in the transversal direction (Fig. B.10b). However, during earthquake excitation, the top-to-bottom relative displacement of the piers is still quite large (as much as that in the longitudinal direction). This is a consequence of the relatively flexible configuration of the bridge superstructure in the transversal direction, in spite of the much higher moment of inertia of the piers cross-section in this direction as compared to the longitudinal direction (Appendix A).

The computed relative top-to-bottom displacements of bridge piers induce large bending moments and shear forces. Since the bridge piers are fixed to the pile caps at the base and connected to the superstructure through shear keys (modeled as internal hinges), the maximum bending moment occurs at the base of each pier (Fig. B.11). Fig. B.11a shows the moment-curvature response and bending moment time histories in the piers base cross-sections, in the longitudinal plane. It is observed that the outer piers have higher flexural response with a peak value exceeding 5MN-m (about 45% of the longitudinal bending moment capacity of the pier, Appendix A). In addition, significant residual moments due to soil lateral spreading are observed at the end of earthquake shaking, especially in the outer piers, consistent with the overall permanent deformation response of the bridge-foundation-ground system (Figs. B.1, B.5). From the moment-curvature response, a low level of nonlinearity (partial yield) is observed with the reinforced steel unyielded and a minor (hair crack) level of damage in the concrete (Acero et al. 2006).

As to pier bending in the transversal direction, the results are shown in Fig. B.11b. The unrestrained cantilever-type transversal response is driven by inertia effects and no significant residual moments and flexural deformations are observed at the end of the earthquake. The bending moment response in the transversal direction is about twice as high as in the longitudinal direction (Fig. B.11a), with the peak moment reaching 15MN-m, about 50% of the transversal moment capacity of the pier (Appendix A). However, the curvature response at the base of the piers is smaller in the transversal direction than in the longitudinal direction due to the significantly higher stiffness in the transversal direction (Appendix A).

Pier-top shear force time histories are shown in Fig. B.12. Maximum longitudinal shear force reaches about 400kN, with a maximum residual value of about 250kN (resisted by the shear key mechanism). In the transversal direction, dynamic loading effects are more significant with peak shear force reaching 1.0MN.

Finally, pier-base axial force time histories are shown in Fig. B.13, where peak-to-peak fluctuations are less than 50% of the axial force due to gravity alone. In addition, it is seen that the earthquake induces some permanent axial force reduction in piers 2 and 7 (Fig. B.13). The reason is that pile groups 2 and 7 (underneath piers 2 and 7) are shorter piles than all others, causing larger settlements at these locations (Fig. B.5a).

B.7 Response of Bridge Pile Foundations

As described earlier (Appendix A), the bridge foundations are modeled as 2×2 pile groups. Fig. B.14 shows the axial force-strain response and force time histories at the top of the four piles in group 4, along with a diagram describing the top view of the pile group and the relative positions of the numbered piles. It is seen that the axial forces in all piles have significant fluctuation and the axial forces in the piles on the different sides of the bridge (piles 1 and 3 versus piles 2 and 4 in Fig. B.14) vary in opposite way. This is because during the earthquake, the cantilever configuration of the bridge superstructure in the transversal direction causes the pile caps to rock transversally, inducing opposite variations (increase/decrease) of the axial force in the piles on different sides of the bridge. Compared to the pier axial force response shown in Fig. B.13, the pile axial force responses in Fig. B.14 clearly exhibit much additional low frequency content due to the pile cap rocking. These low frequency response

components of individual piles cancel out as the axial forces of all 4 piles are summed up (see top-right corner of Fig. B.14) to balance the axial force from the superposed pier and the vertical inertia force of the pile cap.

Fig. B.15 shows the axial force-strain response and axial force time histories (at the top) of four single representative piles (with the same position of pile 1 in Fig. B.14) from pile groups 2, 4, 5 and 7, respectively. Figs. B.14 and B.15 show small tensile excursions of the axial force occurring in all piles, associated with a significant stiffness reduction. This marked change of stiffness reflects the lack of concrete participation (zero strength and zero stiffness) in tension, according to the employed material constitutive model for concrete (Appendix A).

Fig. B.16a shows the moment-curvature response in the longitudinal direction and moment time histories at the top of the same piles as in Fig. B.15, with peak moment exceeding 1MN-m (2/3 of the moment capacity of the pile, Appendix A). Residual flexural deformations appear particularly in the outer pile groups (No. 2 and 7) consistent with the overall residual deformation pattern of the bridge (Figs. B.1b, B.5a). For pile group 7 with the pile cap embedded in the soil (Appendix A), moment in the representative pile does not change sign during the earthquake due to lateral soil spreading towards the center of the river channel.

Fig. B.16b shows moment-curvature response in the transversal direction and moment time histories at the top of the same four single representative piles. For the single representative piles in pile groups 4 and 5 (middle of the bridge), peak moments exceed 1.5MN-m and are near the flexural capacity of the piles (Appendix A). The moment-curvature response exhibits significant nonlinearities and large flexural

ductilities (ratio of maximum absolute curvature to effective yield curvature, Conte et al. 2002) in excess of 10.

As mentioned earlier, the axial force in each pile undergoes significant fluctuations due to rocking of the pile cap induced by the dynamic response of the bridge in the transversal direction (see Figs. B.14, B.15). The pronounced asymmetric bending response of each pile in the transversal direction (Fig. B.16b) is explained by the facts that (1) the flexural capacity depends significantly on the axial force and (2) the axial force and transversal bending moment at the top of a given single pile reach their local maximum/minimum at the same time (see Figs. B.15 and B.16b). In other words, at each cycle of rocking response in the transversal direction, a given pile section undergoes (1) a local maximum bending (in one direction) and maximum compressive force (which increases the bending capacity), followed by (2) a local maximum bending (in the other direction) and minimum compressive force (which decreases the bending capacity). This pattern of response occurs within the upper 8m or so of each pile where the axial force approaches the tensile state. Finally, it is noted that the pile flexural response in the longitudinal direction (Fig. B.16a) also exhibits higher peak bending response at instances of higher compressive axial force.

B.8 Response of Bridge Superstructure

As shown earlier, the bridge abutments undergo permanent displacements due to soil lateral spreading. Fig. B.17a shows that the longitudinal displacement (d_x) of the abutment top finally reaches 0.15/0.10m at the left/right abutment, respectively. Thus, soil lateral spreading causes the abutments to move towards each other producing compressive axial force (P) along the bridge superstructure (Fig. B.17b).

In this figure, it is also seen that longitudinal shaking induces axial force fluctuations in the superstructure, reaching a peak compression force of 1.3MN, which is relatively small (approximately $0.05 f_c' A$, where f_c' and A are defined in Appendix A). Case histories suggest that compression of the bridge superstructure due to soil lateral spreading has caused structural failure (e.g., buckling in bridge deck system, Steinbrugge 2002 and Fig. A.1 in Appendix A). At the end of the earthquake, there are residual (permanent) compressive axial forces of 0.5/0.6MN in the girders of the two end spans.

Fig. B.17a also shows that the settlement (d_y) at the end of the earthquake reaches as much as 0.15/0.21m at the left/right abutment, respectively, which is significantly larger than the settlements of the bridge piers as shown in Fig. B.5a. The above observed abutment displacement (both vertical and longitudinal) is seen to increase the vertical shear force (V) and longitudinal bending moment (M_z) in the bridge girders (Fig. B.17b). Longitudinal moment in the shown bridge girders increases gradually during the earthquake and is nearly doubled in the end. The maximum flexural stress ($\sigma_{x,\max}$) in the girder corresponding to the maximum longitudinal bending moment of 6MN-m (Fig. B.17b) is $\sigma_{x,\max} = M_z y / I_z = 14.7\text{MPa} = 0.43 f_c'$ ($y = 1.2\text{m}$ is half of the girder depth, I_z and f_c' are defined in Appendix A), which is significant. The maximum vertical shear force in the bridge girders is 0.6MN (Fig. B.17b), which is significant compared to the nominal shear strength carried by the concrete (V_c) of a bridge girder. As prescribed in the ACI (1989) code, $V_c = 2\sqrt{f_c'} b_w d = 1.23 \times 10^5 \text{lbs} = 0.55\text{MN}$ ($b_w = 9\text{in}$ and $d = 97\text{in}$ are the

width of the web and the effective depth of a bridge girder). In addition, a close inspection of the high frequency fluctuations in the vertical shear force response (with peak-to-peak variation of as much as 0.25MN, Fig. B.17b) shows that it is mainly driven by the vertical earthquake motion, highlighting the necessity of considering 3D earthquake excitation.

B.9 Summary and Conclusions

An investigation of the 3D seismic response of a bridge-foundation-ground system is undertaken. Of interest are the potential dynamic and permanent deformation mechanisms dictated by the underlying ground domain. Among the main observations are:

(1) Soil nonlinear response, and in particular the yield strength, can impose limits on the acceleration that can be transferred to upper soil layers due to base-isolation effects.

(2) Changes in properties of the upper surficial soil layers along the bridge length may dictate significantly different time histories of dynamic excitation at the various support points of the bridge (i.e., bases of piers and abutments).

(3) Soil lateral spreading primarily towards the center of the underlying river channel must be taken into consideration in order to determine the level of permanent (residual) deformations and corresponding internal forces in the bridge structure, especially in the piers and foundation piles, which are difficult to predict without modeling the soil domain explicitly.

(4) In the longitudinal direction, the bridge structure may be subjected to significant residual loads due to this lateral spreading mechanism of the

foundation. The inertial effects of the abutments and approach ramps also play an important role in this response mechanism.

(5) In the transversal direction, the cantilever configuration of the bridge superstructure induces significant dynamic loads that must be resisted by the bridge piers and underlying pile foundations. In particular, the outside piles of a pile group foundation will experience dynamic axial tensile force excursions that must be carefully assessed.

(6) Finally, approach ramp deformations and abutment displacements are shown to permanently and significantly increase flexural forces in the bridge superstructure, potentially affecting the bridge operability after the earthquake.

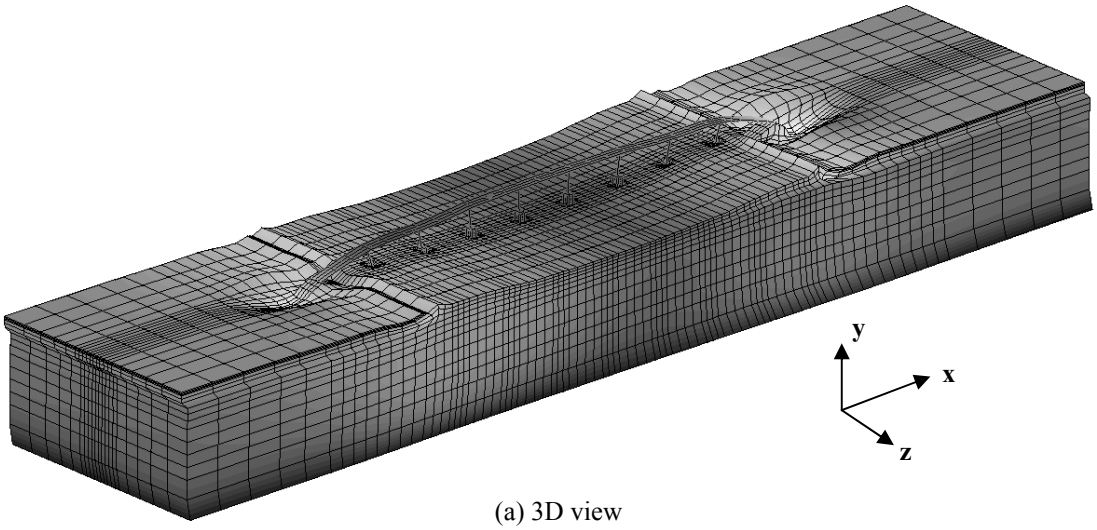
B.10 Acknowledgements

The material in this appendix is prepared as a paper draft for publication, and the author is the primary researcher. This material is also based on the contributions of (1) Professor Ahmed Elgamal, the Ph.D. advisor of author, and (2) Prof. Joel P. Conte, who helped with editing and insightful explanations of the analysis results.

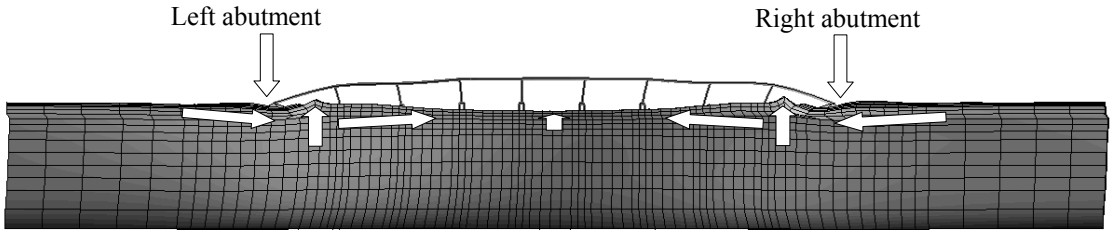
Support of this work is provided by the Earthquake Engineering Research Centers Program of the National Science Foundation, under Award Number EEC-9701568 through the Pacific Earthquake Engineering Research Center (PEER), and NSF Grants (No. CMS0084616 and CMS0200510). This support is gratefully acknowledged. The authors wish to thank Mr. Patrick Hipley, Dr. Cliff Roblee, Dr. Charles Sikorsky, Mr. Thomas Shantz, and Mr. Mark Yashinsky of Caltrans for providing all the requested information regarding the Humboldt Bay Middle Channel Bridge. Professor Gregory Fenves and Dr. Frank McKenna of U.C. Berkeley and

Professor Michael Scott of Oregon State University helped with the OpenSees modeling and analysis phase. Professor Kincho Law and Dr. Jun Peng (Stanford University) were instrumental in providing their sparse solver and assisting in every way. This assistance was most valuable and is highly appreciated.

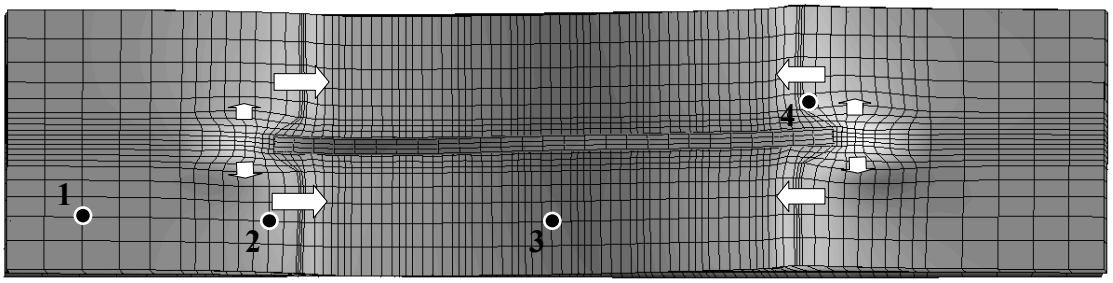
B.11 Figures



(a) 3D view

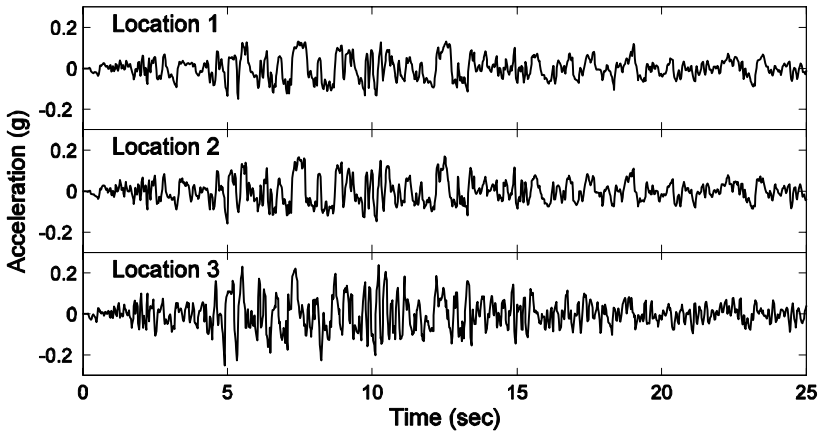


(b) Elevation view (arrows indicating soil flow, heave, settlement)

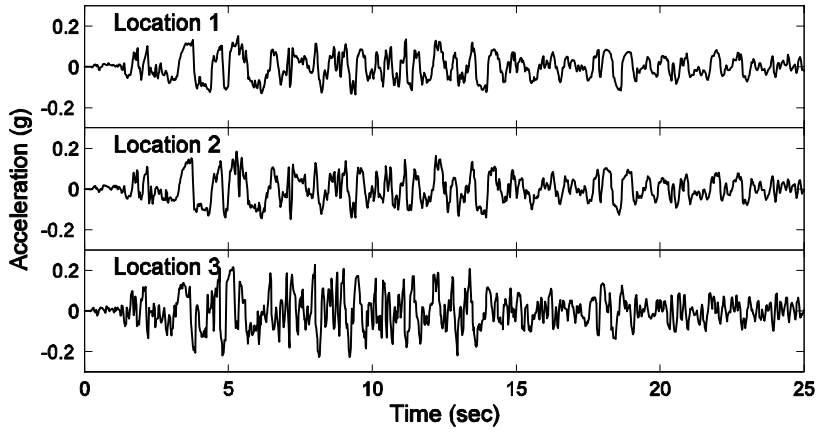


(c) Plan view (arrows indicating lateral spreading of abutment fill and river bank)

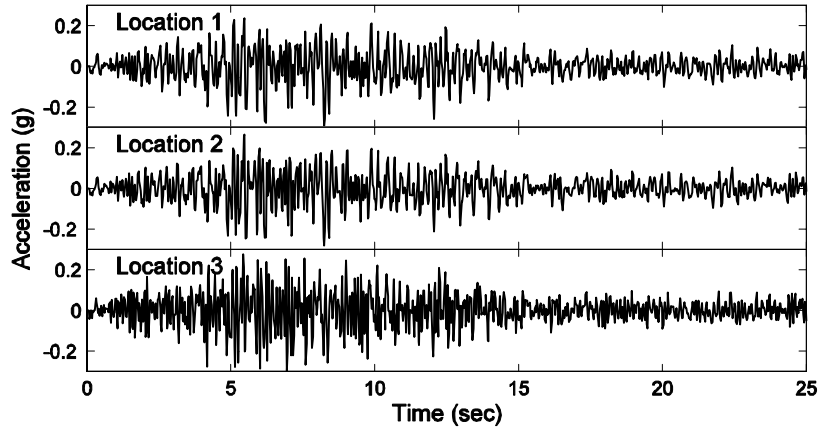
Fig. B.1 3D, elevation, and plan views of residual deformation (displacement scaled by a factor of 50) of the bridge-foundation-ground system after earthquake shaking.



(a) Longitudinal direction



(b) Transversal direction



(c) Vertical direction

Fig. B.2 Ground surface acceleration time history comparison for locations 1-3 in Fig. B.1c.

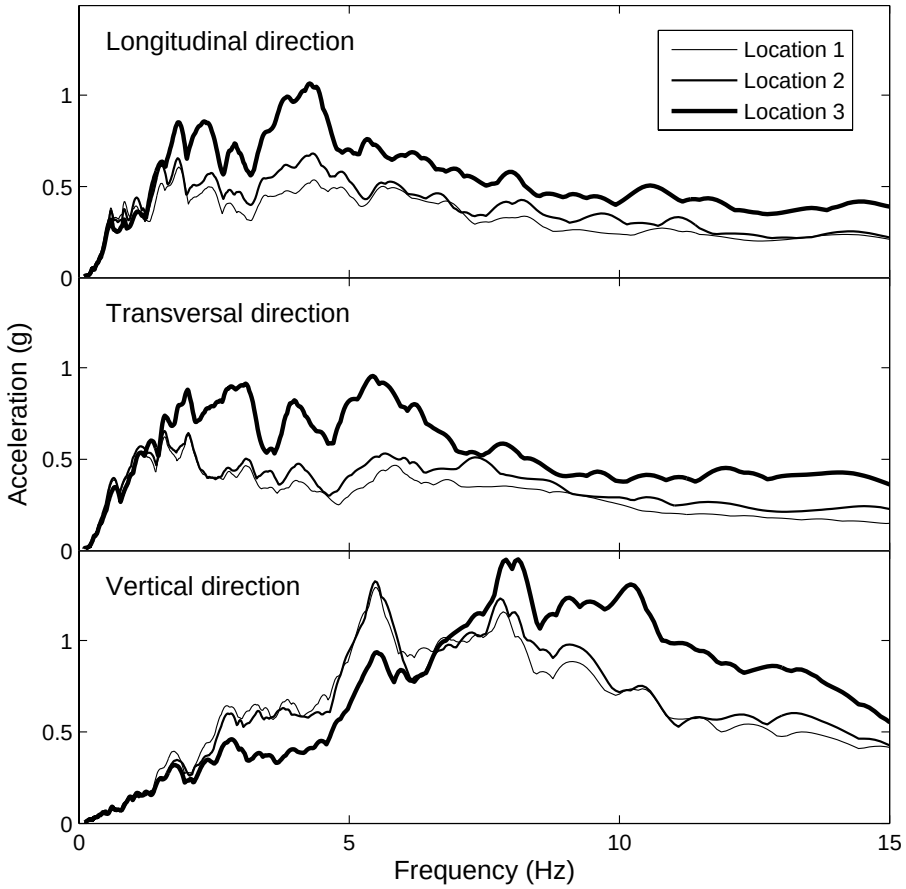
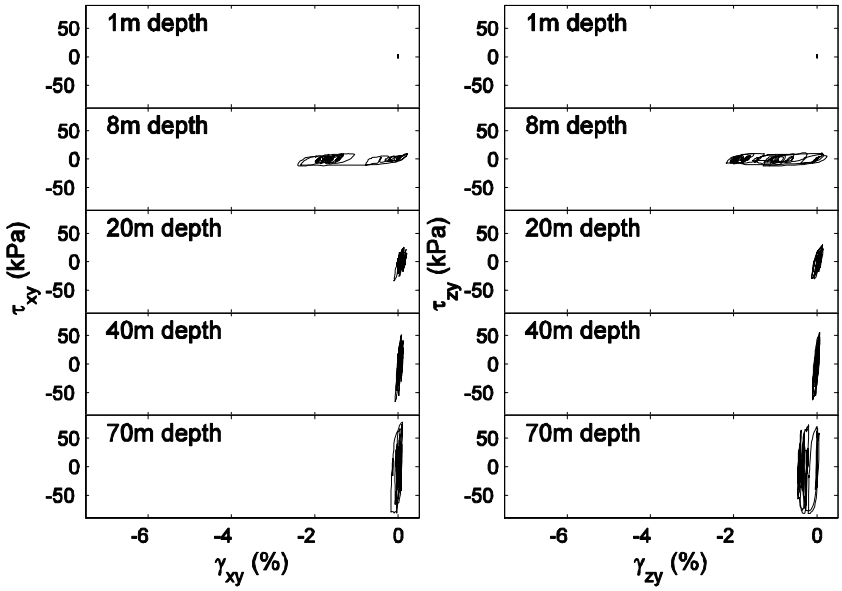
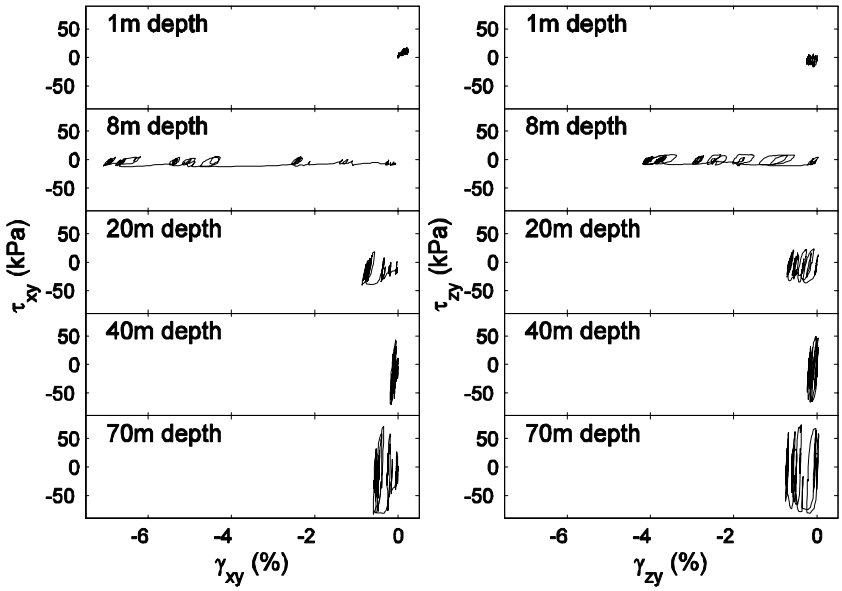


Fig. B.3 Linear elastic acceleration response spectra (5 percent damped) comparison for locations 1-3 in Fig. B.1c.

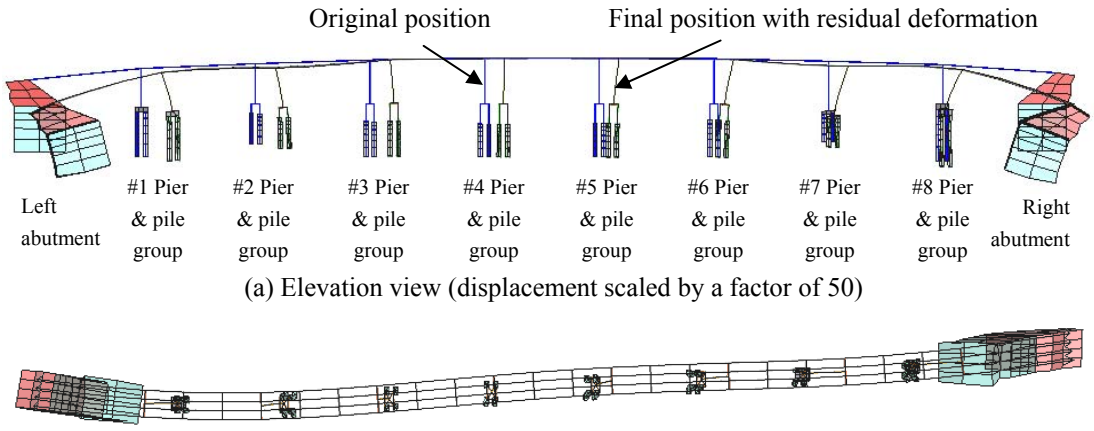


(a) location 1 in Fig. 1c (free field)



(b) location 4 in Fig. 1c (next to the right abutment)

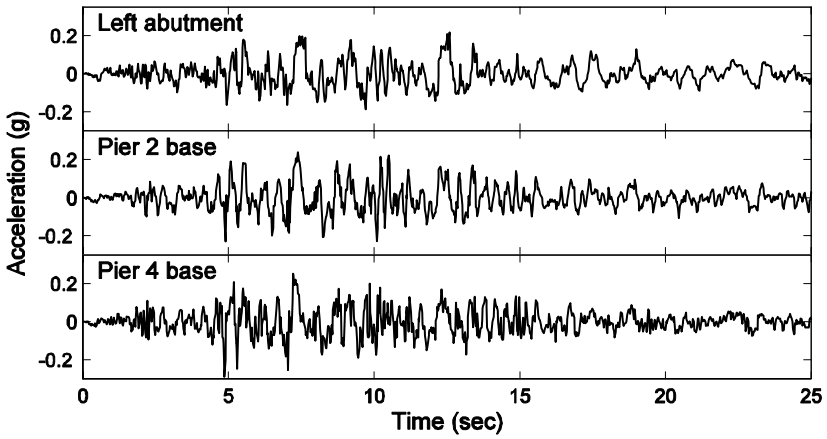
Fig. B.4 Longitudinal (xy) and transversal (zy) shear stress-strain response at different depths of locations 1 and 4 in Fig. B.1c.



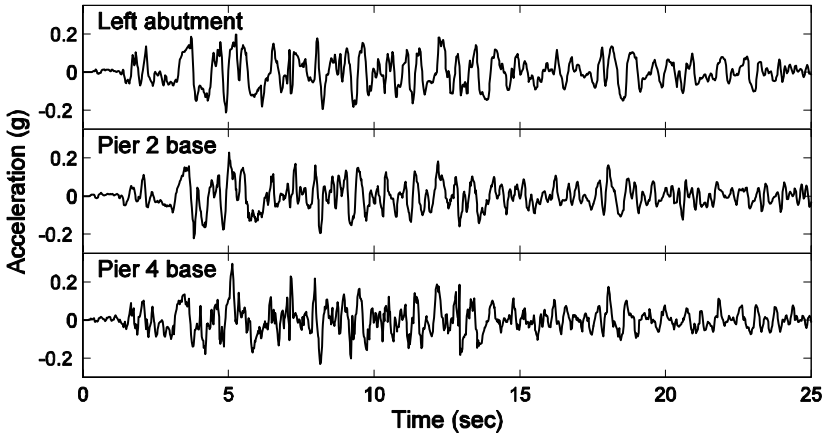
(a) Elevation view (displacement scaled by a factor of 50)

(b) Plan view (displacement scaled by a factor of 150)

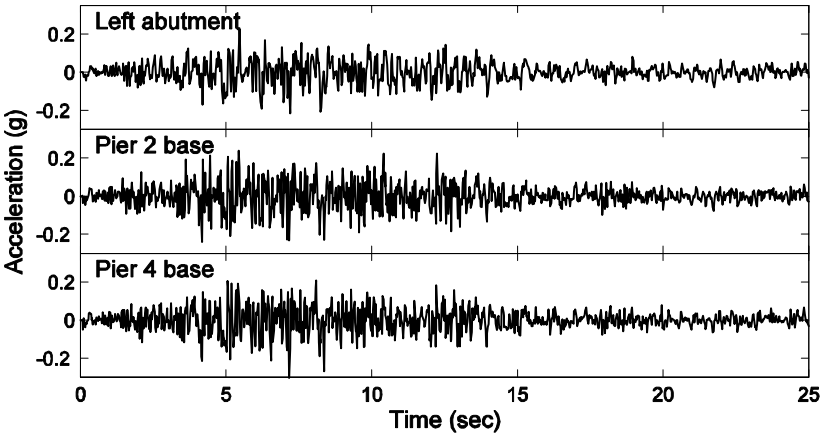
Fig. B.5 Elevation and plan views of the bridge, pier, pile foundation, and abutments after earthquake shaking.



(a) Longitudinal direction



(b) Transversal direction



(c) Vertical direction

Fig. B.6 Acceleration time histories at representative locations of bridge piers and abutments.

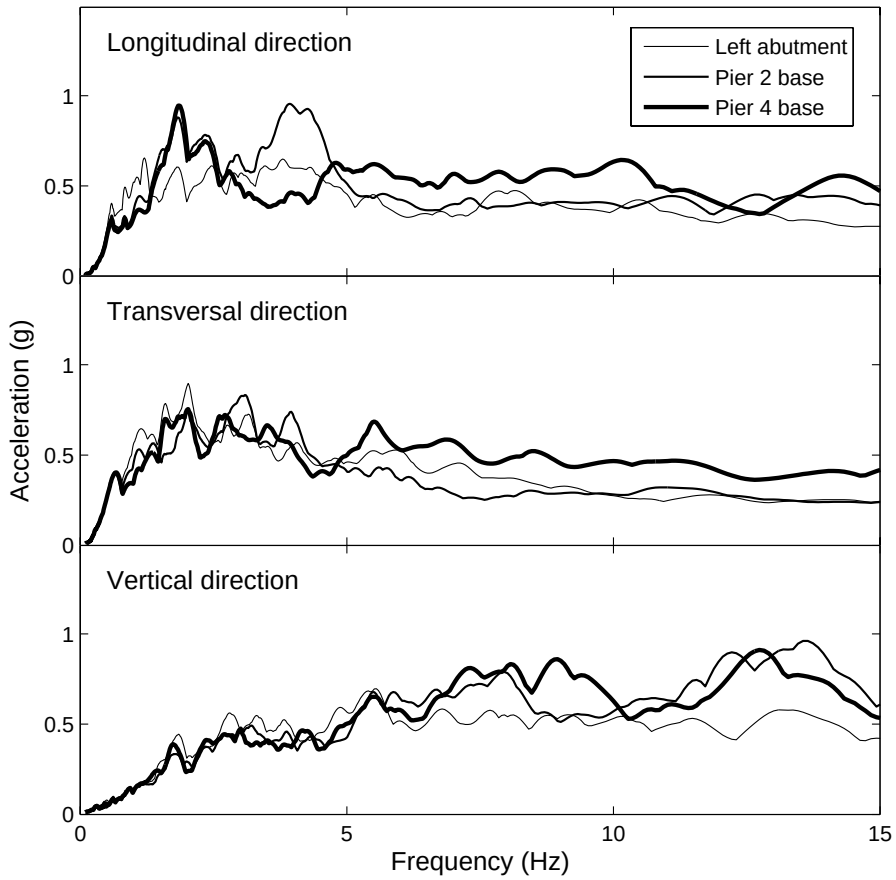
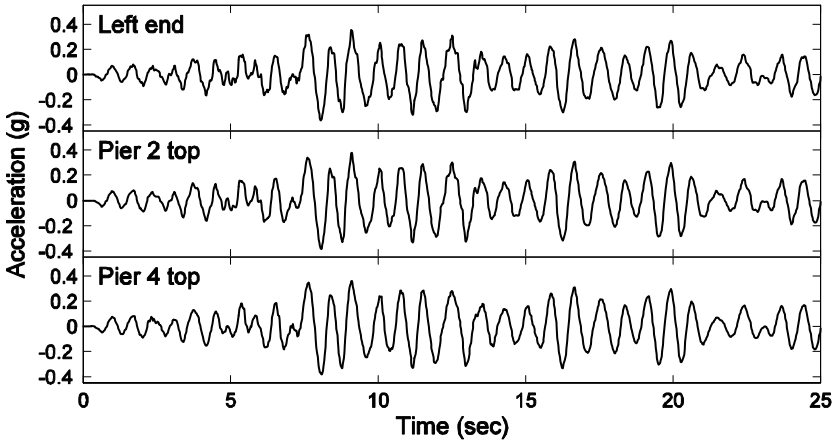
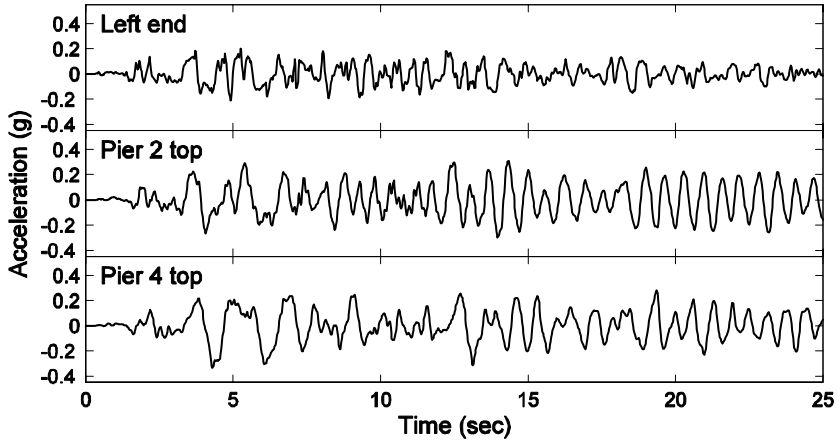


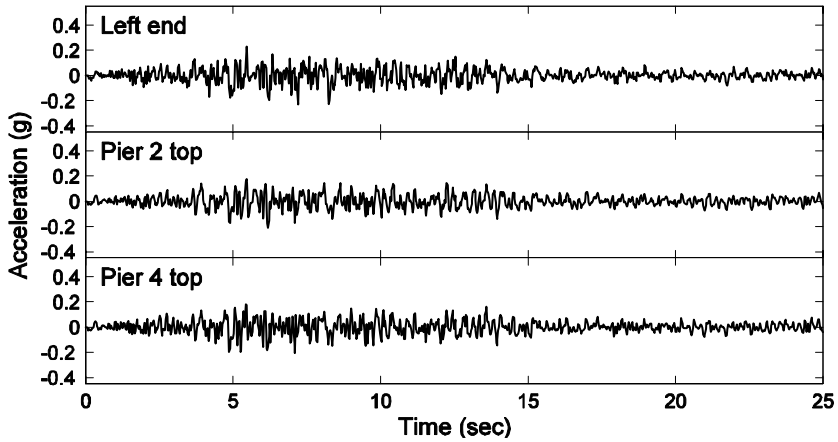
Fig. B.7 Linear elastic acceleration response spectra (5 percent damped) comparison for 3 representative locations of bridge piers and abutments.



(a) Longitudinal direction



(b) Transversal direction



(c) Vertical direction

Fig. B.8 Acceleration time histories at 3 locations along the bridge superstructure.

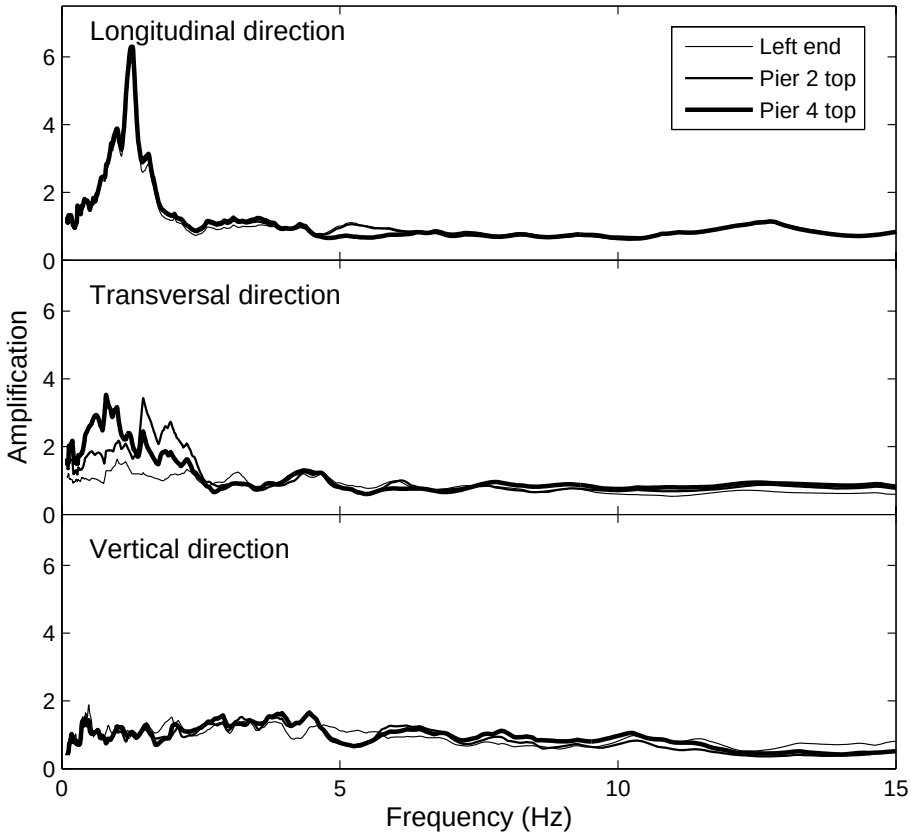
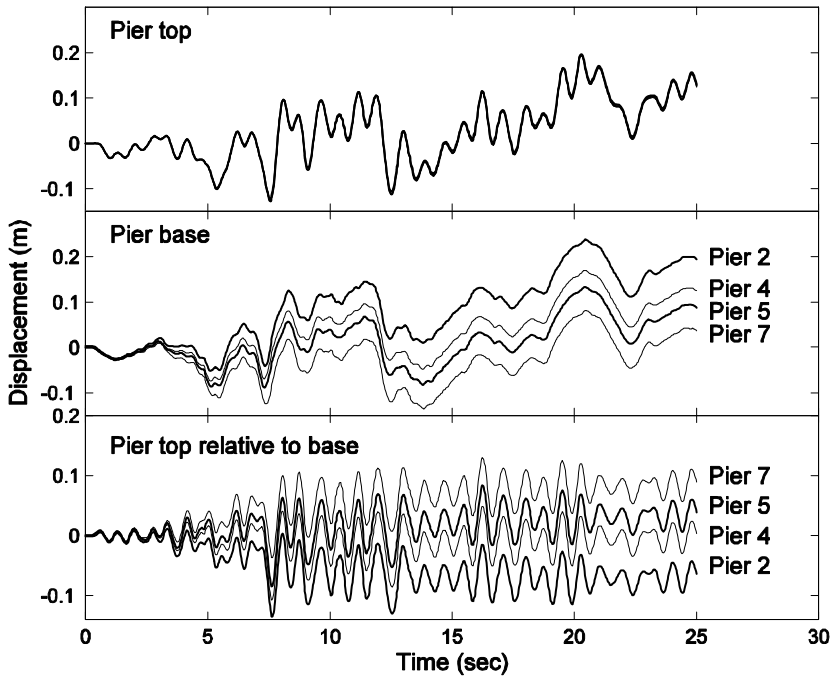
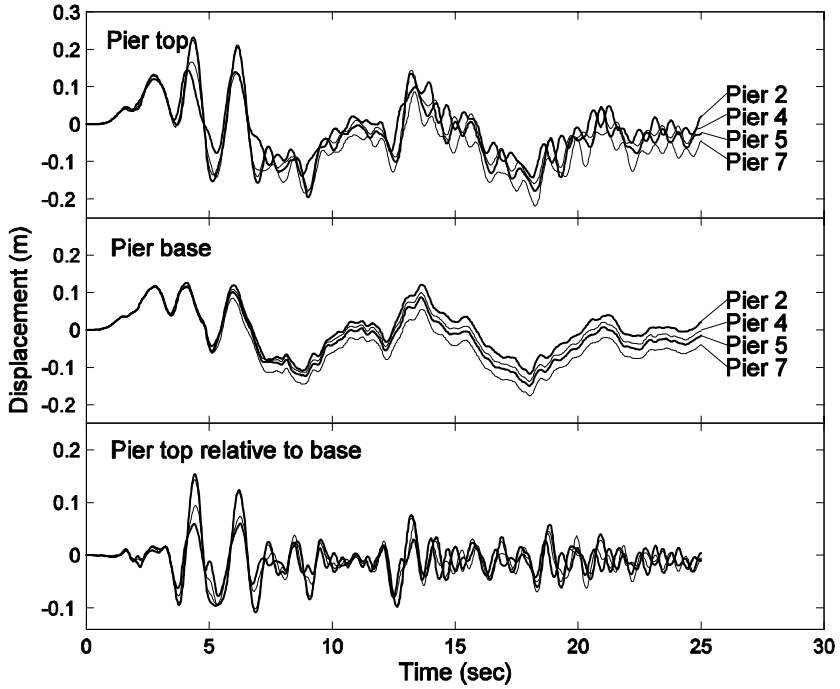


Fig. B.9 Linear elastic acceleration amplification spectra (5 percent damped) comparison at 3 representative locations along bridge superstructure (referenced to the base of Pier 4).

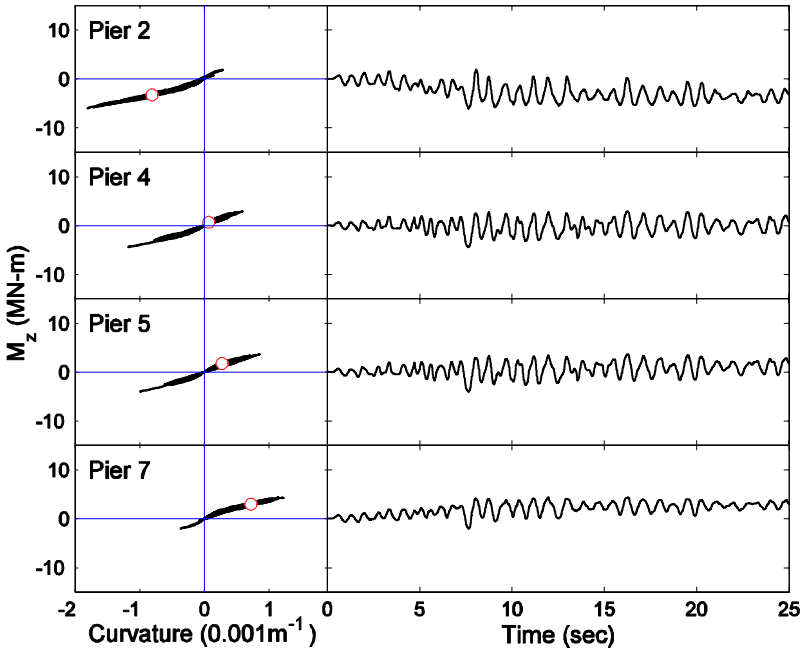


(a) Longitudinal direction

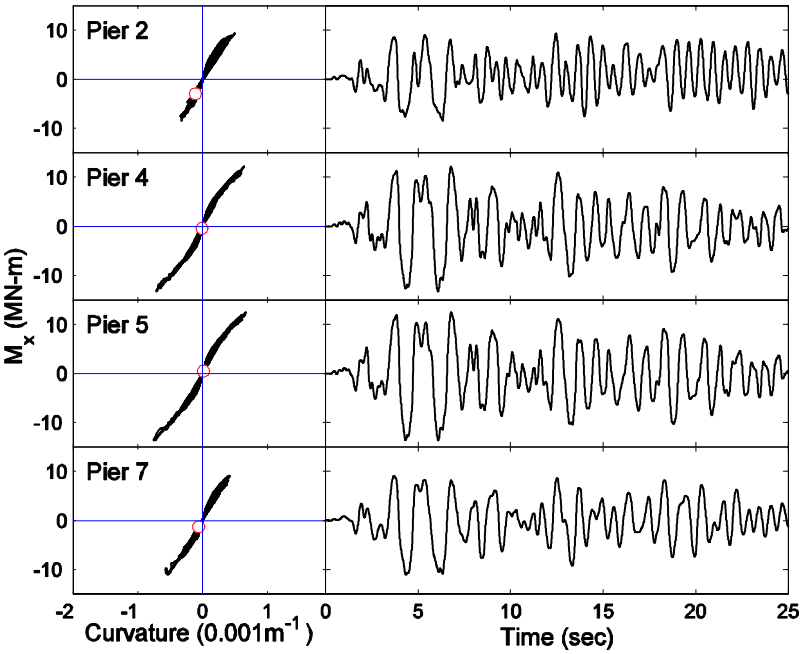


(b) Transversal direction

Fig. B.10 Displacement time histories at bridge pier tops and bases.



(a) Longitudinal direction



(b) Transversal direction

Fig. B.11 Moment-curvature response and moment time histories at pier bases, with residual moment-curvature indicated by a white circle.

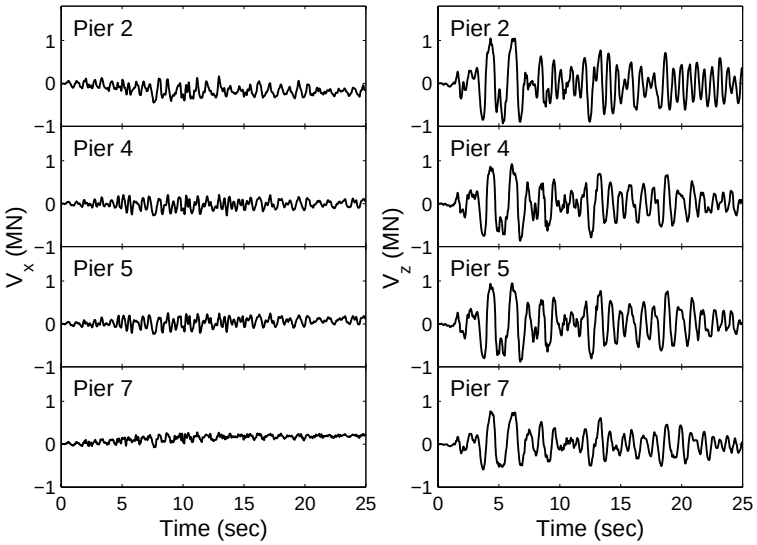


Fig. B.12 Longitudinal (x) and transversal (z) shear force time histories at pier tops.

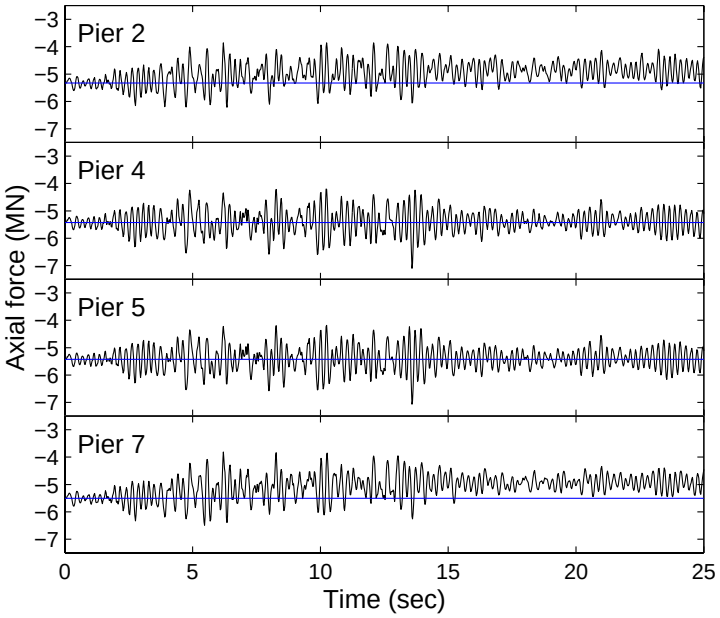


Fig. B.13 Pier-base axial force time histories

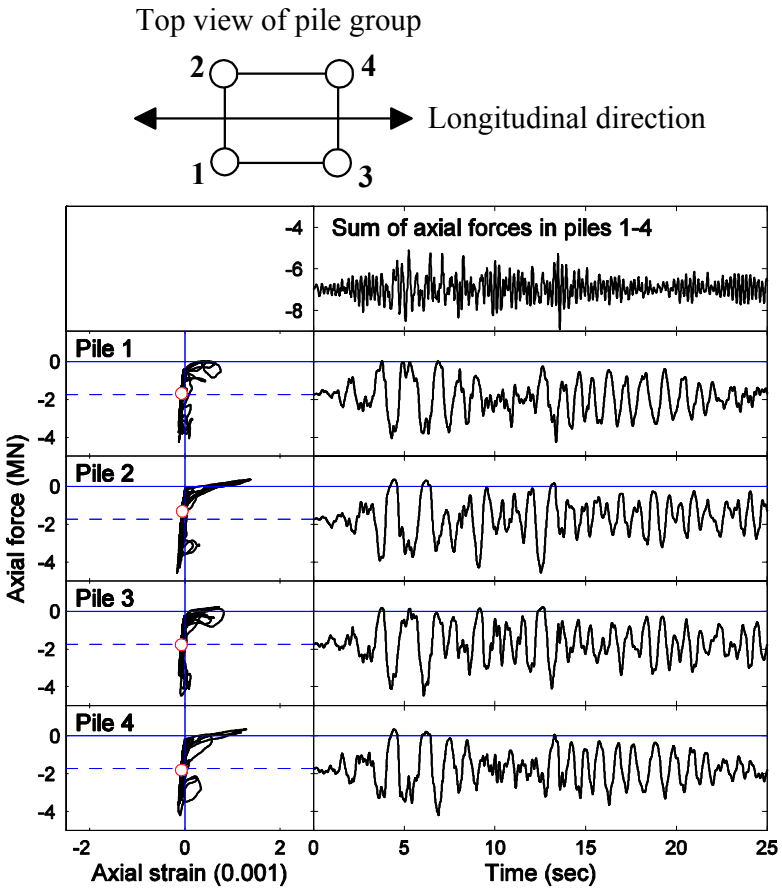


Fig. B.14 Axial force response of piles in group 4: (1) a diagram showing the top view of the pile group and the numbering of piles, (2) Axial force-strain response and force time histories of each pile, with residual force-strain indicated by a white circle, and (3) the sum of the axial forces in all 4 piles.

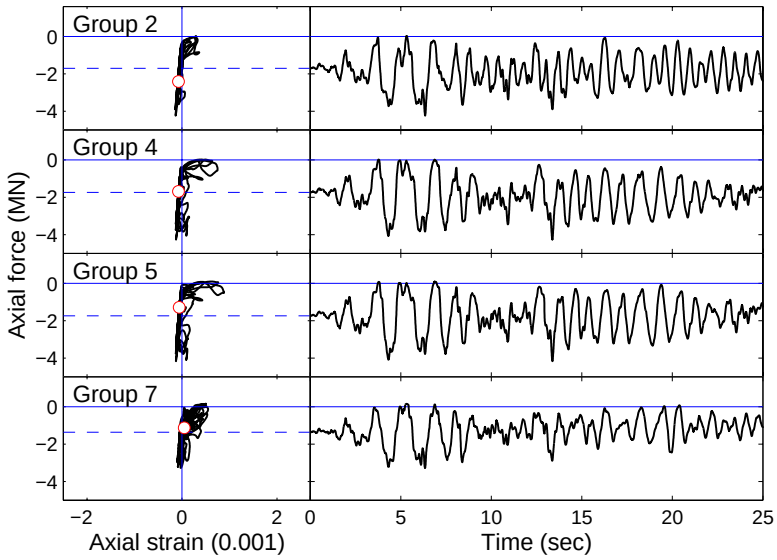
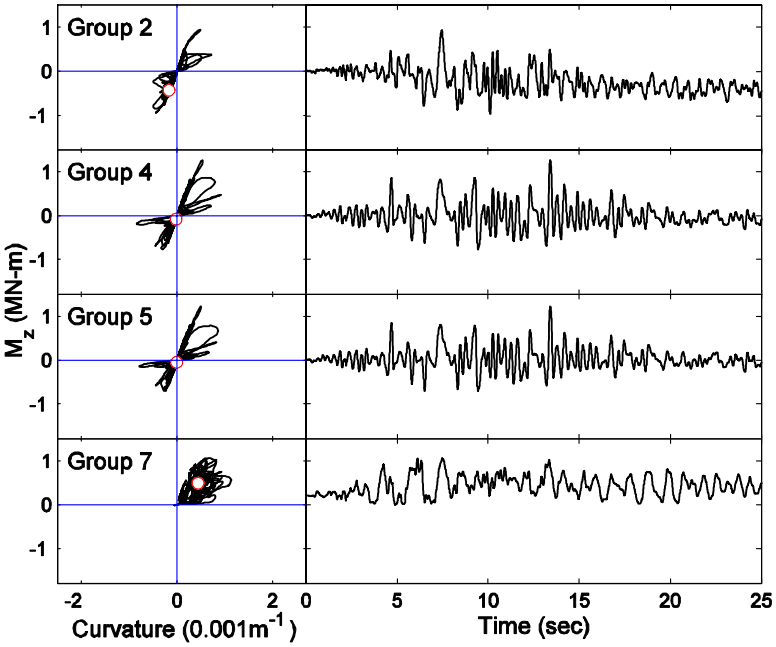
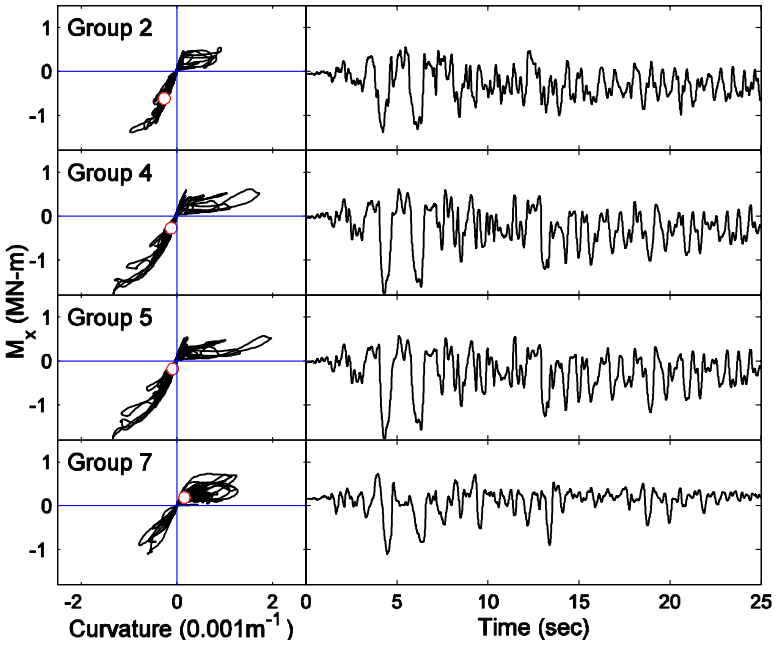


Fig. B.15 Axial force-strain response and axial force time histories at the top of single representative piles (with the same position of pile 1 in Fig. B.14), with residual force-strain indicated by a white circle.

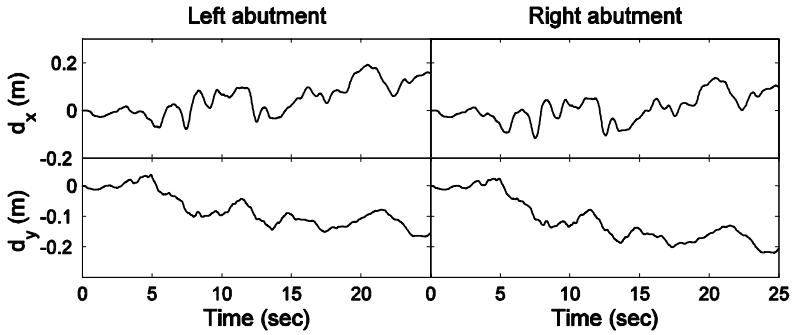


(a) Longitudinal direction

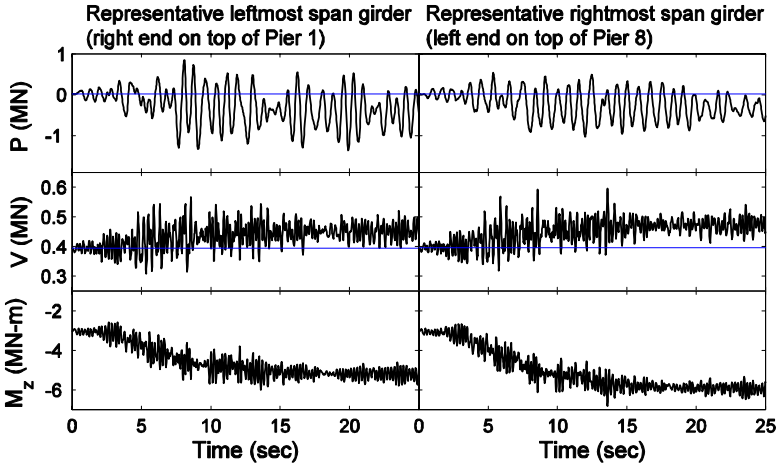


(b) Transversal direction

Fig. B.16 Moment-curvature response and moment time histories at the top of single representative piles (with the same position of pile 1 in Fig. B.14), with residual moment-curvature indicated by a white circle.



(a) Abutment displacement



(b) Bridge response

Fig. B.17 Correlation between abutment displacement and bridge response: (a) longitudinal displacement d_x, and settlement d_y at abutment tops; (b) axial force P, vertical shear force V, and longitudinal moment M_z in bridge girders.

B.12 References

Acero, G. J., Restrepo, J. I., Conte, J. P., and Zhang, Y. (2006). "Seismic Response of Columns with Unconfined Lap-splices." ACI Structural Journal (in progress).

American Concrete Institute (ACI). (1989). *Building Code Requirements for Reinforced Concrete (ACI 318-89) and Commentary*, American Concrete Institute, Detroit.

Conte, J. P., Elgamal, A., Yang, Z., Zhang, Y., Acero, G., and Seible, F. (2002). "Nonlinear Seismic Analysis of a Bridge Ground System." *Proc. of the 15th ASCE Engineering Mechanics Conference (EM 2002)*, Columbia University, New York, NY.

Steinbrugge, K. V. (2002). *The Karl V. Steinbrugge Slide and Photograph Collection World Earthquakes and Earthquake Engineering*, Earthquake Engineering Research Center, <http://nisee.berkeley.edu/eqiis.html>.

University of California (UC), and National Information Service for Earthquake Engineering (NISEE) (2002). *Earthquake Image Information System*, <http://nisee.berkeley.edu/eqiis.html>.